FAA-72-54

REPORT NO. FAA-RD-73-172

AIRCRAFT L-BAND BALLOON-SIMULATED SATELLITE EXPERIMENTS
Volume II: CW Multipath Test Results and Analyses

J. Liu
J. Kraemer
S. Karp

NOVEMBER 1973

FINAL REPORT

Prepared for

U.S. DEPARTMENT OF TRANSPORTATION
FEDERAL AVIATION ADMINISTRATION
Systems Research and Development Service
Washington DC 20591

Technical Report Documentation Page

1. Report No.	2. Government Accession No.	3. Recipient's Catalog No.
FAA-RD-73-172		

4. Title and Subtitle	5. Report Date
AIRCRAFT L-BAND BALLOON-SIMULATED SATELLITE EXPERIMENTS Volume II: CW Multipath Test Results and Analyses	November 1973
	6. Performing Organization Code
7. Author(s) J. Liu, J. Kraemer, S. Karp	8. Performing Organization Report No. DOT-TSC-FAA-72-34
9. Performing Organization Name and Address U.S. Department of Transportation Transportation Systems Center Kendall Square Cambridge MA 02142	10. Work Unit No. (TRAIS) FA311/R5110
	11. Contract or Grant No.
12. Sponsoring Agency Name and Address U.S. Department of Transportation Federal Aviation Administration Systems Research and Development Service Washington DC 20591	13. Type of Report and Period Covered Final Report January 1971-June 1972
	14. Sponsoring Agency Code

15. Supplementary Notes

Volume I gives a description of the experiment design and operation, and presents results of the voice tests.

16. Abstract

Volume II contains the CW test results of an experiment run to simulate a satellite-to-aircraft channel at L-band. The program was initiated when the ATS-5 Satellite failed to achieve a wholly successful synchronous orbit and started to tumble. Using balloons to simulate the satellite, tests were run with the FAA CV880 aircraft. Although the geometry restricted the tests to low elevation angles and tangential paths, they were sufficient to obtain representative results.

The data reduction focused primarily on satisfactorily characterizing the combined direct and multipath returns. The results of this characterization indicated that, for the narrow bandwidth considered, the diffuse reflection from the surface appears Gaussian with independent in-phase and quadrature-phase components as attested to by a Ricean-distributed combined envelope return. The absence of a specular return was noted at elevation angles as low as 5 degrees and for Sea State I. Komolgorov-Smirnov tests were used to check for homogeneity and to test for a Ricean Distribution. Further analysis indicated a negative correlation between the envelope returns of the vertically and horizontally polarized signals.

17. Key Words	18. Distribution Statement
Multipath; Balloon Tests; Aerosat; Satellite ATC; Satellite Channel Characterization	DOCUMENT IS AVAILABLE TO THE PUBLIC THROUGH THE NATIONAL TECHNICAL INFORMATION SERVICE, SPRINGFIELD, VIRGINIA 22151.

19. Security Classif. (of this report)	20. Security Classif. (of this page)	21. No. of Pages	22. Price
Unclassified	Unclassified	196	

Form DOT F 1700.7 (8-72) Reproduction of completed page authorized

PREFACE

The work described in this report was performed in the context of an overall program at the Transportation Systems Center designed to support the FAA in preparation for the Experimental and Evaluation(E&E) phase of the AEROSAT program. This program is sponsored jointly by the Federal Aviation Administration and the Office of the Secretary.

Basic experimental data has been obtained to aid the design of voice, data and ranging modems and to support the selection of multiple access control formats.

The authors would like to thank Messrs. Louis Frasco and H. David Goldfein for their help in the formulation stages of the data analysis and reduction. We also would like to thank Mr. Orville Dodson for his assistance in programming the various subroutines required and in handling the production runs.

TABLE OF CONTENTS

LIST OF ILLUSTRATIONS

LIST OF ILLUSTRATIONS (CONT.)

LIST OF ILLUSTRATIONS (CONT.)

LIST OF TABLES

1. INTRODUCTION

Satellite systems are presently being designed for oceanic air traffic control (ATC) applications. In the design of these ATC systems, the propagation characteristics of the satellite-to-aircraft link are of vital concern. This report addresses multipath problems.

Existing experimental data on multipath over the satellite-to-aircraft channel at L-Band is insufficient to enable adequate channel characterization for system design purposes. Two experiments have been sponsored, therefore, by DOT to measure the characteristics of multipath signals over the oceanic satellite-to-aircraft link. One of these experiments uses the NASA ATS-5 satellite and is currently being performed by the Boeing Corporation under sponsorship of the DOT/FAA.[1] The other flight experiment, sponsored by DOT/TSC, utilized a high altitude balloon to simulate the satellite terminal. This document reports on the results of CW measurements in balloon-simulated satellite-to-aircraft tests. The experiment set-up and description is also discussed in detail in Section 2 of this report. The main attention in this report is given to the analysis of CW test results in an effort to provide a statistical characterization of channels representative of those of interest in aeronautical oceanic ATC satellite systems.

During the analysis phase, it was found that the data were contaminated by noise generated in the test equipment. Efforts in data reduction were, therefore, diverted to isolate the source of this noise, the nature of the noise, its effects on the data and methods to remove it from the data. These results are also presented in Section 2. Theoretical models of the balloon-simulated satellite-to-aircraft channel are discussed in Section 3. In Section 4 some of the experimental results are presented. In Section 5 the results of the data are interpreted and conclusions and recommendations are presented. *The reader who is primarily concerned with a summary of conclusions can be referred directly to Section 5.* Included in several appendixes are various detailed

discussions pertinent to "quick look" analyses, the distortion effects of noise and equipment problems, data reduction and filtering sub-routines, antenna and oscillator issues and material on calibration. Appendix A has the results of analyses performed on analog tapes used in the European tests.

The channel which we are considering is commonly referred to as a fading dispersive channel. To understand the relevant parameters which describe this channel, it is useful to visualize what is physically occurring. There are no deleterious effects on the direct path since there is no propagation through the various ionized layers of the atmosphere in the balloon geometry. Thus we concentrate on the reflected or multipath parameters. If the ocean were perfectly smooth, it would be possible to reflect off it as if it were a mirror with some associated dielectric constant. Since the ocean is spherical, some defocusing would occur and slightly decrease the received power. This is considered a purely "specular" reflection.

As the surface becomes roughened, energy is scattered out of the specular path and away from the receiver, causing a decrease in the specular component. At the same time, energy is scattered toward the receiver from regions which normally would not contribute energy. Hence the emergence of a "diffuse" reflection. At any instant of time, the various contributions to the diffuse component traverse different paths and cause "echoes" at the receiver. The time spread of the echoes is called the "delay spread" and is an important parameter to be measured.

As time progresses, the echo structure varies due to motions of the transmitter and receiver. The variations create a time dependence in the echo structure referred to as Doppler fading. Because of the geometry, each contribution to the echo structure can have a different Doppler shift and hence the "Doppler spread" is a measure of the fading rate: another important parameter.

In the narrow bandwidth case, many echoes can overlap at any time and hence, by arguments involving the central limit theorem,

one expects this to be a Gaussian random process. If this can be established, all the statistical information would be contained in the delay-Doppler power spectral density (or delay-Doppler scatter function). If not Gaussian, this latter quantity is still a useful function for use in design, but must be accompanied by detailed statistics. In the current experiment, we focus primarily on establishing the Gaussian nature of the diffuse component (Ricean envelope) and the strength of the specular reflection. In addition, polarization and the cross-coupling of these modes are also monitored.

2. EXPERIMENT DESCRIPTION

Two balloon-aircraft experiments were performed in 1971 by DOT/TSC, one in May 1971 at Pt. Mugu, California, and the other during September and October 1971 over the Bay of Biscay off the coast of France.[2] In these experiments, signals were transmitted from the balloon to an instrumented aircraft. Direct path and multipath signals were measured and recorded on board the aircraft during the course of the tests.

This report presents analyses of some of the CW data taken in these balloon experiments. The information contained in the CW data relevant to the design of communication and ranging systems is also summarized and discussed. Since the balloon-to-aircraft channel is only an approximation of the actual satellite-to-aircraft channel, inherent limitations were placed on the flight profiles. Thus, all flights were constrained to 5° to 15° elevation angles (due to balloon altitude) along tangential paths relative to the balloon. These constraints limited our ability to extract information concerning Doppler effects and the angular dependence of diffuse reflections.

The balloon-simulated satellite-to-aircraft experimental data are presented in this section. For purposes of analysis, segments of the data were selected and processed. These segments were analyzed in depth in order to gain a thorough understanding of the data from an examination of detailed characteristics. Thus, although 250 minutes of data were available for analysis, approximately 20 minutes were actually reported on. With the experimental conditions of the channel reasonably constant (i.e., same sea states and test geometry), the conclusions drawn on the basis of the selected data segments are representative. Confidence levels regarding conclusions are high, and generalizations can therefore be inferred. Subsequent efforts in data reduction beyond the analyses contained in this report need not re-examine these characteristics. Rather, other statistical parameters should be analyzed from the available data, especially those pertaining to the temporal

properties of multipath fading.

It will become evident later in this section that the experimental data contains coherent noise generated by the equipment. We shall discuss the characteristics of these defects in the data together with their sources and methods for correcting them. The experimentally observed properties of the noise and the procedure used to pinpoint the noise source are described in detail in Appendix B. The software used in the data reduction is simple and straightforward and will not be discussed here. (This will be documented in a separate report by TSC.) Appendix C explains the filtering routines used in the data reduction.

2.1 MEASUREMENT AND TEST HARDWARE

In the balloon-aircraft CW multipath experiments, high altitude balloons (100,000 ft) were used to simulate the satellite terminal in a satellite-to-aircraft link. The test signal was transmitted to the balloon from a ground station and then was retransmitted from the balloon to the aircraft where it was measured and recorded. During the tests, the aircraft flew nearly circular paths around the transponding balloon while both were tracked by ground-based radars*. Hence, a fixed elevation angle was maintained in each test run. A series of flight tests was performed to obtain multipath data for various elevation angles ranging from 5° to 15°. All the flight tests were conducted under relatively calm sea conditions.

A broad-beam circular polarized L-Band antenna was installed on top of the aircraft fuselage directly above the wing root. Two low-gain slot dipole circular polarized antennas were also installed 35° to either side of this top-mounted antenna. Since these antennas were relatively well shielded from the sea-reflected signal by the aircraft wings, the signal received using

*Radar tracking was only available in the U.S. West Coast tests.

one of these antennas can be considered as the direct signal from the balloon (i.e., free of multipath). The horizontally and vertically polarized components of the multipath signals, as well as those of the direct signal, were received using one of the broad beam antennas mounted on the side of the fuselage forward of the wing root pointing toward the horizon. The antenna gain was within ±1 dB over the subtended solid angle which included both the direct and multipath returns. This antenna did not appreciably distort either of the signals; therefore we may assume that the antenna is "transparent" (i.e., uniform gain in the direction of all receiver signals).

The receivers on the aircraft were configured as shown in Figure 2-1. A more detailed block diagram of this equipment is shown in Figure 2-2. Receiver 1, connected to either the top mounted or 35° offset antennas, provides a coherent reference for the multipath signal in Receivers 2 and 3. The AGC voltage from Receiver 1, with 500 Hz bandwidth, was recorded digitally at 62.5 samples per second. Receivers 2 and 3, connected to the forward side-looking antennas, translate the horizontally and vertically polarized components of the direct plus multipath signal to a 5 kc IF frequency and also envelope-detect those signals. The IF and detected outputs are sampled and recorded at 4000 and 62.5 samples per second respectively. These receivers, as well as the RF processor, the digital data formatter, the A/D converter and the balloon transponder are described in detail in their respective manuals. Those characteristics that are relevant to our discussions of the data are summarized in Table 2-1. The effects on the data due to oscillator instability, sampling jitters, etc., are discussed in Appendix D.

2.2 GENERAL DESCRIPTION OF DATA

The outputs of the receivers were sampled and recorded digitally. In addition to the signals from Receivers 2 and 3, the AGC voltage of Receiver 1, Receiver 1 lock indicator level, and flight parameters (such as roll, pitch, heading, altitude and airspeed) were recorded at 62.5 samples per second. For purposes of

data reduction, the Receiver 1 lock indicator level was used as the criterion for the usefulness of other data recorded concurrently. That is, we assumed that when this level indicates that Receiver 1 was locked to the direct signal, useful statistics of the multipath channel could be extracted from the recorded signals at the outputs of the receivers.

The 5 kc IF signals of Receivers 2 and 3, after passing through filters of bandwidth 1.8 kc, are recorded at 4000 samples per second. By adjusting the gains of these receivers, the amplitudes of these signals were made to lie in the range of the A/D converter (-1V to 1V). At the output of the A/D converter, their sampled values are represented by 10-bit binary numbers (2's complement).

The detected outputs of the Receivers 2 and 3, on the other hand, are sampled at 62.5 samples per second. Since the power spectral densities of the IF signals (e.g., Figure 2-3) indicate that frequency components of these detected signals can be larger than

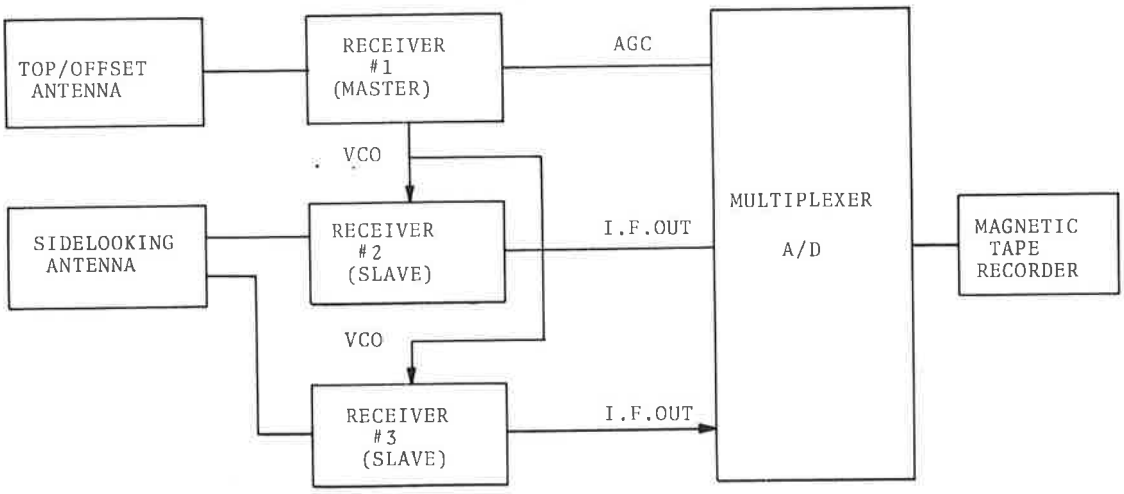

Figure 2-1 Receiver for CW Multipath Measurements

TABLE 2-1 SUMMARY OF EQUIPMENT CHARACTERISTICS

Phase-Lock Receiver	
Carrier Frequency	1550 MHz ± 25 KHz
Nominal Carrier Acquisition Threshold	-135 dBm*
Nominal Carrier Tracking Level	-138 dBm*
Signal Dynamic Range	40 dB
Receiver Noise Figure	6 dB
VCXO Stability (10°C to 40°C)	±10 PPM
Loop Noise Bandwidth, 2B	
Carrier Acquisition	500 Hz
Carrier Tracking	33 Hz
Video Bandwidth	3 MHz
Analog-to-Digital Converter	
Conversion Rate:	100 KHz
Conversion Time:	10 microseconds
Channel Capacity:	16 channels
Accuracy:	±3.0 mv ± 100 μv/C°
Analog Input Range:	± 1 volt
Resolution:	10 bits, 1 part in 1024 (2 mv)
Aperture:	100 nanoseconds plus skew of encode signal
Digital Data Formatter	
Encode Command to A/D Converter:	negative-going edge of 200 ns pulse
Sample Rate:	62.5 Hz except channels 15 & 16 (IF-2 and IF-3 respectively) which are sampled at a 4 KHz rate
Formatter Control Clock:	
a) source:	rubidium frequency standard
b) frequency:	5 MHz
Balloon Transponder (L-Band Portion)	
Maximum Altitude:	125,000 ft
Uplink Frequency:	1650 MHz
Down-link Frequency:	1550 MHz
Input Signal Range:	-90dBm to -50dBm typical
Maximum L-Band Power Amplifier Output:	5 watts
Output Power:	seven levels can be achieved through the use of a remotely controllable output attenuator which covers the range from 0dB to 18dB in 3-dB steps (U.S. West Coast experiment only).

*When preceded by a 20dB gain RF Preamplifier having a 3.5dB noise figure.

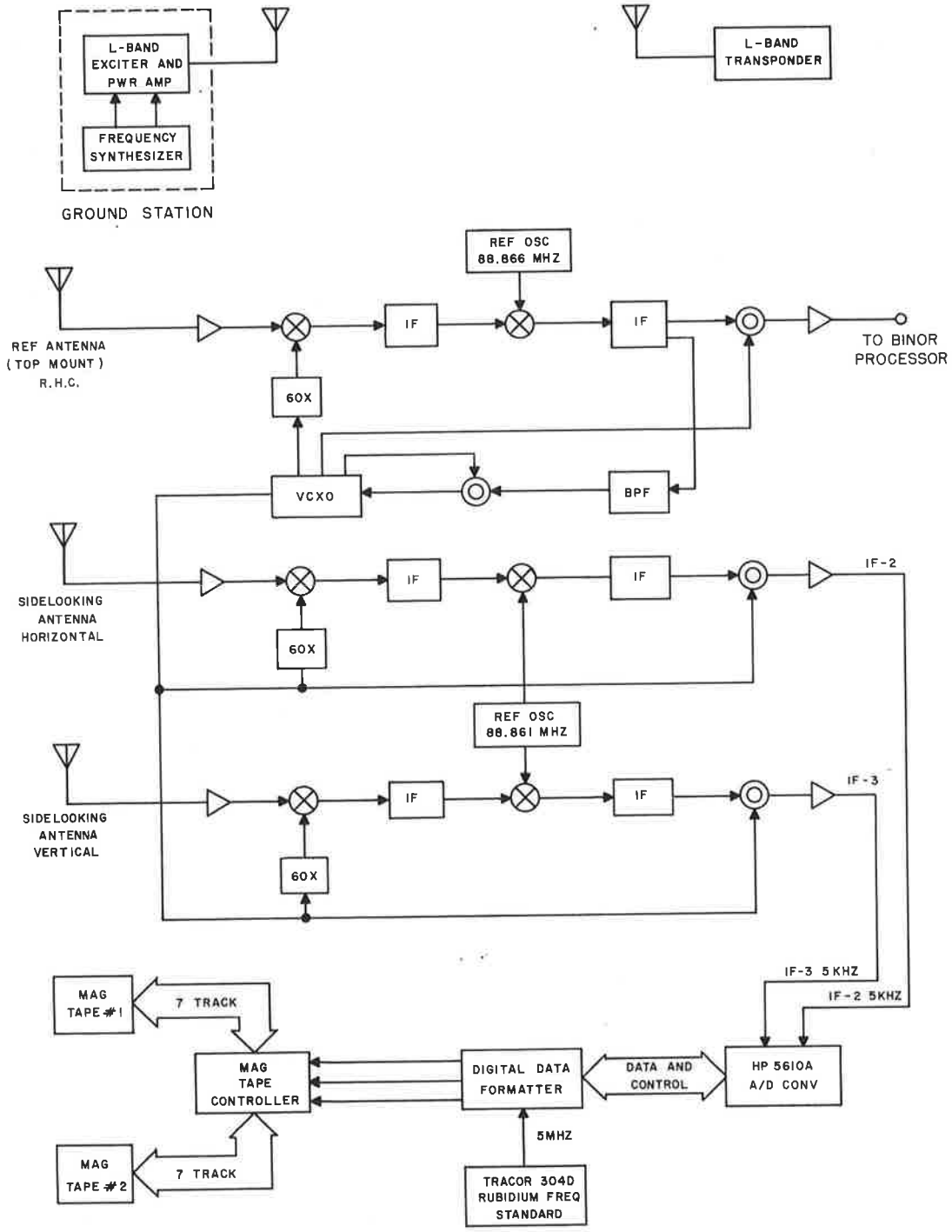

Figure 2-2 Simplified Block Diagram of L-Band Experiment

33 cycles in some cases, the sampled detected signals are at times severely distorted by aliasing. For this reason, we have focused our attention on the processing of the IF signals. Table 2-2 summarizes the volume of data available. To date we have examined the digital recordings of IF 2 and IF 3 taken in all runs in the West Coast test sequence and in most of the French sequence.* In the French test sequences, analog recordings of the IF signals were also made in several runs. The analog data was also processed to obtain power spectral density and amplitude histograms of the multipath signals. This data is presented in Appendix A.

TABLE 2-2 SUMMARY OF DATA VOLUME AVAILABLE

TEST SEQUENCE	ANGLE	VOLUME OF DIGITAL DATA	NUMBER OF RUNS	ANALOG RECORDING
West Coast	9.7°	11 min	1	none
	8-8.3°	48 min 43 sec	2	none
	12°	20 min	1	none
French	5°	50 min 39 sec	4	none
	7°	20 min	2	none
	10°	80 min 40 sec	8	48 min
	12°	41 min 27 sec	4	21 min
	15°	3 min 35 sec	1	4 min 40 sec

2.3 DISTORTION AND NOISE IN DATA

A typical power spectral density of the IF signal is shown in Figure 2-3. The sidebands, such as those at approximately 550 Hz and 450 Hz were also observed to be present most of the time in the data processed to date. The presence of these interfering noises, introducing sidebands in power spectra of the resultant signal, were detected in the calibration signals recorded prior to test runs as well as in the actual multipath data. The exact location of these sidebands varies from 350 Hz to 960 Hz from the

*For the purposes of this report, however, we have restricted the data to samples taken at 5°, 10° and 15° elevation.

5 KHz carrier. Their peak magnitudes vary from -6dB to -20dB relative to the magnitude of the peak at 5 KHz. The variation of their location and relative magnitude throughout the data indicates that the noise source itself drifts in time. The existence of these lines also assures that the 62.5 Hz samples of the IF are aliased.

To understand the exact nature of this noise and its effects on the data, the airborne equipment (L-Band receivers and RF processor) was brought back to Cambridge and made operative in the laboratory. The noise sources were found to be the multiplier chains in Receivers 2 and 3 (see Figure 2-2). The details on the procedure used to pinpoint the noise source and the verification of the noise characteristics are discussed in Appendix B. We will restrict our attention here to the effect of this interference on the data.

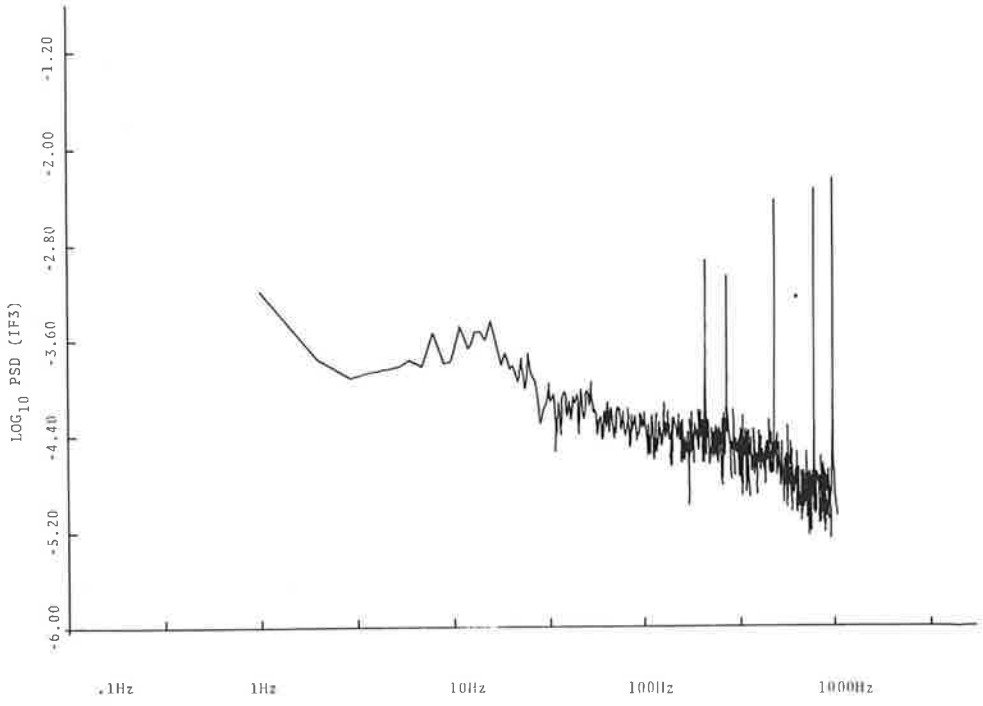

Figure 2-3 Typical Power Spectral Density

As discussed in Appendix B, when the input signal of Receiver 2 (and 3) is a sinusoidal wave, it was observed that the IF output of the receiver (at the output of the bandpass filter), instead of being the expected 5 KHz sine wave, is a modulated wave. Its power spectrum consists of three lines: one at 5 KHz and two sidebands symmetrically displaced in frequency from the carrier (5 KHz). The magnitudes of the sidebands were observed to be equal sometimes and to differ by as much as 6dB relative to each other at other times. The waveform of the output shows that it is amplitude modulated. The fact that the two sidebands have different magnitudes indicates that the carrier is also phase modulated. The width of the sidebands being very narrow suggests that we may assume that the noise itself is a very narrow-band process. In most of the cases observed thus far, it can be considered as a sine wave over time durations on the order of seconds. The source of this interfering noise was verified to be the local oscillator multiplier chains in the receivers (see Figure 2-2). The output became a 5KHz sine wave (no modulation) when a sine wave (1612 MHz) from a signal generator was injected into the first mixer instead of the output of the multiplier chain.

To discuss the effect of this noise on the data and the methods that can be used to separate the noise from the data, let us denote the noise waveform by a(t). Without losing generality in our discussion, let us suppose that its Fourier spectrum is as shown in Figure 2-4. Let the output of the multiplier chain be denoted by x(t). In the absence of noise, it can be written as:

$$x(t) = A \cos 2\pi f_o t$$

where f_o is equal to 1612 MHz and A is a constant. From the results of various tests described in Appendix B, it appears that x(t) in the presence of the noise a(t) can be written either as

$$x(t) = A\left\{\left[1+a(t)\right] \cos 2\pi f_o t + b \cos\left[2\pi f_o t + m a(t)\right]\right\} \quad (2\text{-}1)$$

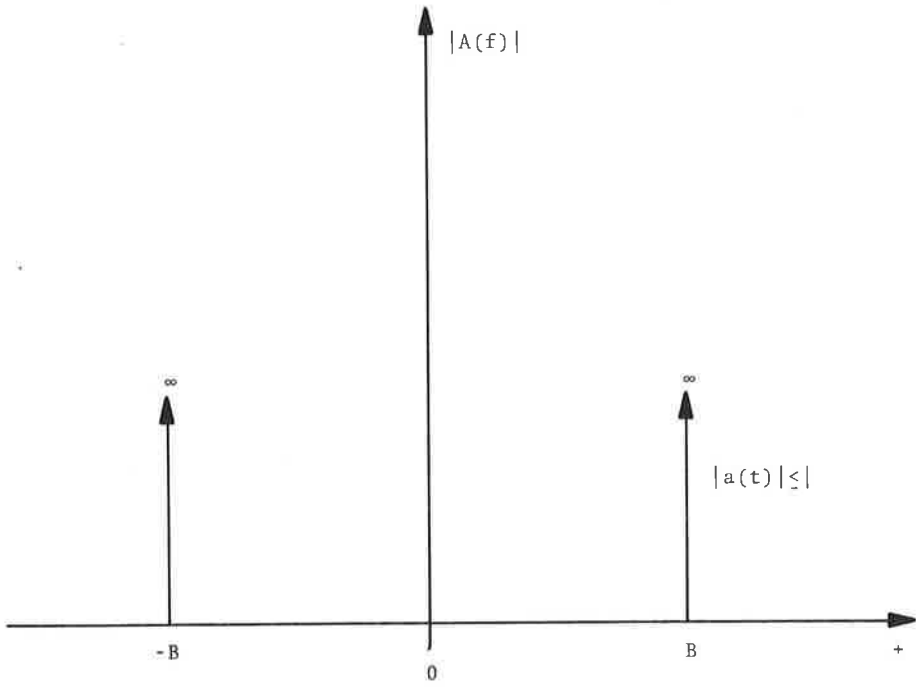

Figure 2-4 Noise Fourier Spectrum of Multiplier Chains

where m is the phase modulation index, or as

$$x(t) = A\left[1+a(t)\right] \cos \left[2\pi f_o t+ma(t)\right] \qquad (2\text{-}2)$$

The Fourier spectra of such signals are shown in Figure 2-5. The exact mixture of phase and amplitude modulations of the 1612 MHz by the noise can be determined by matching the observed spectrum of the output of the multiplier chain to theoretical ones. Nevertheless, by making several assumptions (whose validities are supported by experimental evidence), it is possible to show that the data can be recovered by simply filtering out the unwanted sidebands in any case. Whenever it is possible to do so, there is no need to determine the exact behavior of the distortion generated in the multiplier chain.

Observations were made of the power spectrum of the IF signal at the input of the narrowband filter when the input signal is a sine wave. The fact that there were only a few lines to either

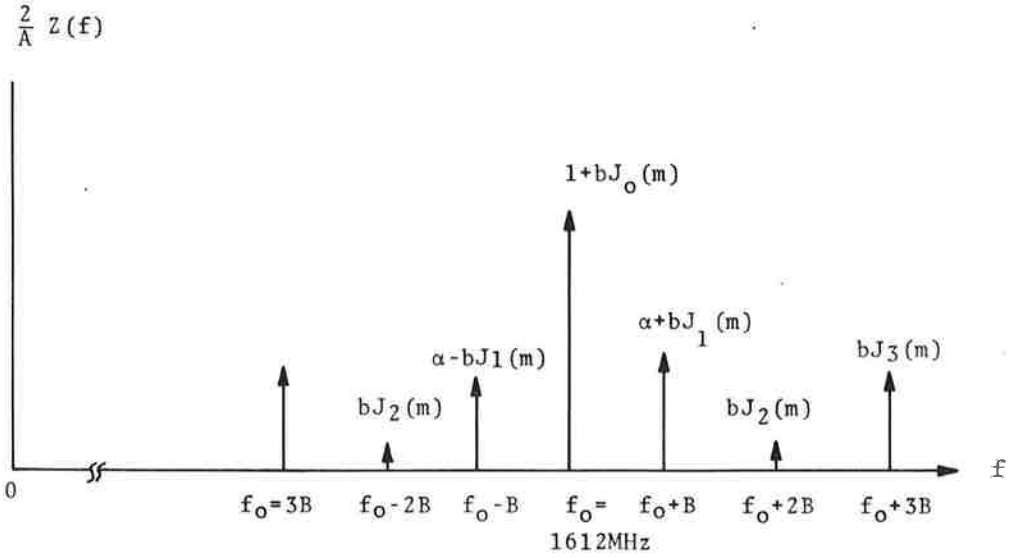

(a), If $x(t) = A\{(1+a(t)) \cos 2\pi f_o t + b\cos[2\pi f_o t + ma(t)\}$

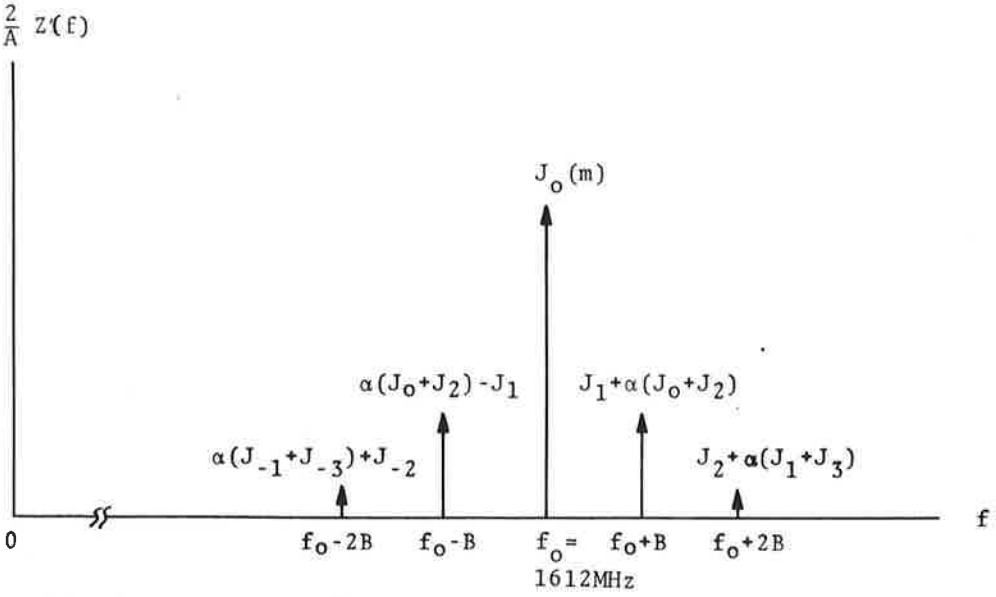

(b) If $x(t) = A(1+a(t)) \cos[2\pi f_o t + ma(t)]$

Figure 2-5 Fourier Spectrum of the Output of the Multiplier Chain x(t)

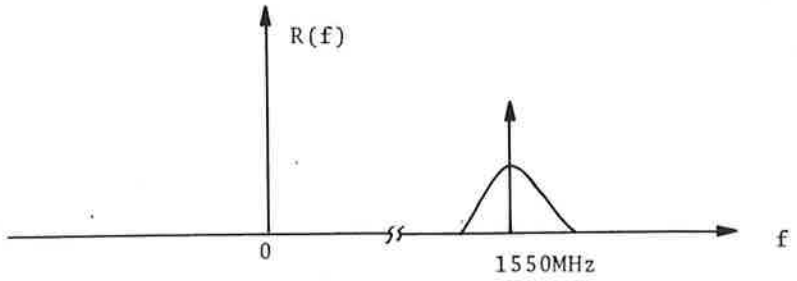

(a) Spectrum of the RF input

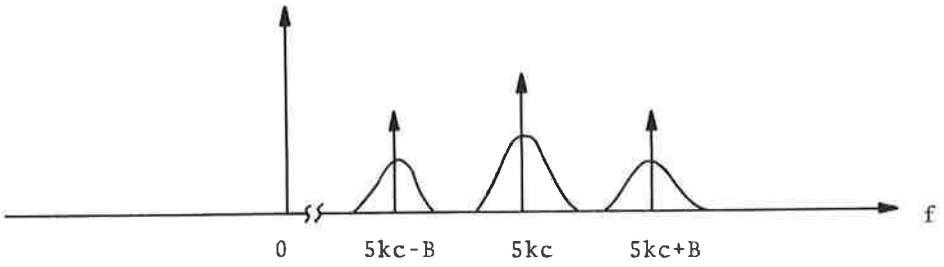

(b) Spectrum of the IF filtered output

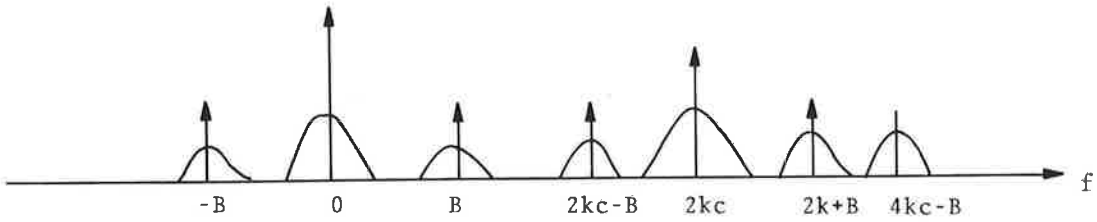

(c) Spectrum of the sampled data

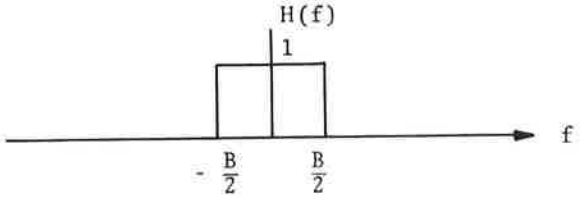

(d) Transfer function of the digital filter

Figure 2-6 The Vertical Fourier Spectrum of Input, Output and Sampled Data

side of the 5 KHz carrier suggested that the phase modulation may be assumed to be narrowband. Furthermore, we may assume that there is no line of significant magnitude in the frequency range 9.1 KHz or more away from the carrier. The assumption is supported by the fact that only the first lines around the carrier were observed at the output of the narrowband filter. (Note that if there are sideband lines of significant magnitude at frequencies which differ from the carrier by more than 9.1 KHz, these lines will fall in the passband of the filter when the signal is down translated.)

In most of the cases that have been observed, the parameter B (see Figure 2-4) is larger than twice the bandwidth of the input signal r(t). Under these assumptions, the Fourier spectrum of the output of the narrowband filter is simply:

$$R(f) + C_1 R(f+B) + C_2 R(f-B)$$

for some constants C_1 and C_2, when the input spectrum is R(f) (see Figure 2-6). Therefore, we can obtain the undistorted version of the signal x(t) by using a digital filter of bandwidth B/2 to suppress the unwanted sidebands.

3. THEORETICAL MODELS

In this section, we will discuss theoretical models of the satellite (balloon)-to-aircraft communication channel. These models give us statistical characterizations of the channel at different levels of completeness and should aid in giving us a better understanding of the experimental data.

Basically, the models considered here can be classified into two types: random process models and channel geometry models. By a random process model we mean a known theoretical random process of which the experimentally observed signal waveform can be considered a sample function. We assume that for the given input signal to the channel, the output signal of the channel is the random process. Thus, the model mathematically characterizes the channel completely. Channel parameters that have been measured are matches to the parameters of the theoretical random process. Those parameters on which there is no experimental data are assumed to be given by the random process. Thus, the model extrapolates from the experimental data channel parameters that are not measured experimentally.

While a random process model of the channel is obtained on the basis of the statistical characteristics of the experimental data, its validity is usually verified (at least in part) by matching its generating physical mechanism to the underlying physical mechanism of the channel. More detailed models of the channel can be obtained by first analyzing the physical characteristics of the channel instead. In our case, the geometric models of the satellite-to-aircraft channel are based on the studies on electromagnetic waves scattered from rough surfaces (such as ocean and land surfaces). For any model of the rough surface, one may calculate for any given input signal and channel geometry the direct plus multipath signal and the output signal of the channel. Thus, we obtain a model which completely characterizes the channel theoretically. In this report, we have not attempted to develop any new models for the reflection characteristics of an electromagnetic

wave off the ocean. While some effort has been expended in this area, the flight profile used in these flights does not accentuate the Doppler profiles and is primarily of use for statistical testing. As we will see, reasonable mathematical models can be equated to the physical conditions.

The satellite (balloon)-to-aircraft channel can be described in general by the block diagram in Figure 3-1. For any given input signal s(t) to the channel, the output signal is a composite of the direct signal d(t) and multipath signal m(t), where the direct signal d(t) is simply a delayed, Doppler-shifted and attenuated version of s(t). The multipath signal m(t) depends on the input signal as well as on the characteristics of the reflecting surface and the relative locations and motions of the transmitter and receiver. In general, it consists of a coherent component and an incoherent component. The former is due to specular reflections off the ocean (or land) surface. The latter is due to diffused scattering by the surface. The magnitude of the coherent component and the statistical characterization of the incoherent component have been subjects of both theoretical and experimental studies.[1,3] We will return to these discussions later in this section.

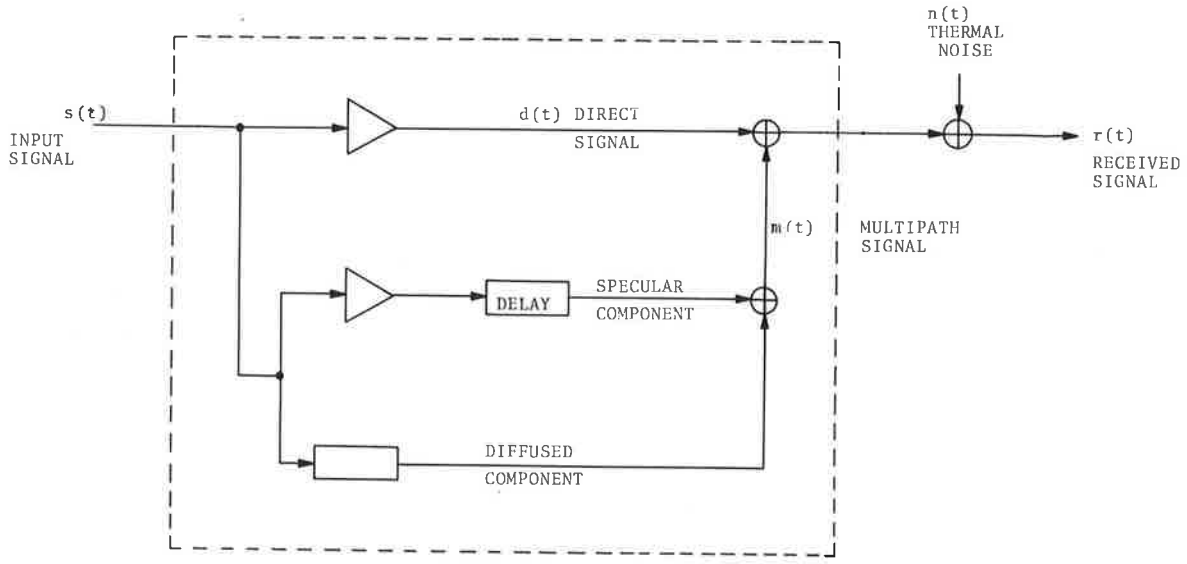

Figure 3-1. Satellite (Balloon)-to-Aircraft Channel

At this juncture, let us consider the special case when the signal input is a sinusoidal wave. To be specific, let

$$s(t) = \cos 2\pi f_o t$$

In this case, the direct signal is simply

$$d(t) = A \cos 2\pi(f_o+f_d)t$$

where the amplitude A depends on the direct path loss and f_d is the direct Doppler frequency. The multipath signal can be written as

$$m(t) = B \cos \left[2\pi(f_o+f_s)t + \phi\right] + g(t)$$

In this expression, f_s is the Doppler frequency of the specular component, ϕ accounts for the unknown relative phase between the direct signal and the specular multipath signal, and amplitude B depends on the specular path loss. The function g(t) is the diffused scattered component. Where the physical dimensions of the surface roughness are large compared to the wavelength of the input signal (as in the case of our experiment), g(t) can be modeled as a narrowband random process with Rayleigh-distributed amplitude and uniform phase. In the presence of the additive white Gaussian thermal noise, the input to the receiver is, therefore,

$$r(t) = A \cos 2\pi(f_o+f_d)t + B \cos\left[2\pi(f_o+f_s)t + \phi(t)\right] + g(t) + n(t) \qquad (3\text{-}1)$$

Equation (3-1) can be rewritten as

$$r(t) = \varepsilon(t) \cos\left[2\pi f_o t + \theta(t)\right]$$

where $\varepsilon(t)$ is the envelope and $\theta(t)$ is the phase of the process r(t).

The probability distributions of the envelope $\varepsilon(t)$ and the instantaneous values of a process such as r(t), consisting of two sine waves of unknown relative phase additively combined with a Gaussian process, have been the subject of a recent study by Esposito and Wilson.[4] For the case where g(t) is stationary, the probability density functions and the cumulative distributions of the envelope have been obtained numerically for several cases of

interest. The cases where the standard deviation of the combined Gaussian process, g(t) + n(t), is equal to 1 are plotted in Figures 3-2 to 3-4. We note that the curve marked A=0, B=0 is simply the Rayleigh distribution, while those waves associated with B=0 are Ricean. In Figure 3-5, we also plot a family of Ricean distributions as a function of A for B=0 and the noise variance set at unity. For the sake of completeness, we note that the mathematical expression for this density is $p_2(r)$ where

$$p_2(r) = r \exp\left[\frac{-r^2}{2}\right] \sum_{m=0}^{\infty} \frac{(-a^2/2)^m}{m!} \, {}_2F_1\left[-m, -m; 1; b^2/a^2\right] L_m(r^2/2) \tag{3-2}$$

where ${}_2F_1$ (a, b; x) is a hypergeometric function and $L_m(\frac{r^2}{2})$ is the Laguerre polynomial, where

$${}_2F_1\left(-m, -m; 1; b^2/a^2\right) = \sum_{n=0}^{m} \left(b^2/a^2\right)^n \binom{m}{n}^2 \tag{3-3}$$

and

$$L_m\left(\frac{r^2}{2}\right) = \sum_{i=o}^{m} (-1)^i \binom{m}{m-i} \frac{\left(r^2/2\right)^i}{i!} \tag{3-4}$$

The cumulative distribution is $C_2(R)$ where

$$C_2(R) = \int_0^R p_2(r)\,dr$$

$$= 1 - \exp\left[\frac{-R^2}{2}\right]\left\{1 - \sum_{m=1}^{\infty} \frac{\left(-a^2/2\right)^m}{m!} \, {}_2F_1\left(-m; -m; 1; \frac{b^2}{a^2}\right)\right.$$

$$\left.\left[L_{m-1}\left(\frac{R^2}{2}\right) - L_m\left(\frac{R^2}{2}\right)\right]\right\} \tag{3-5}$$

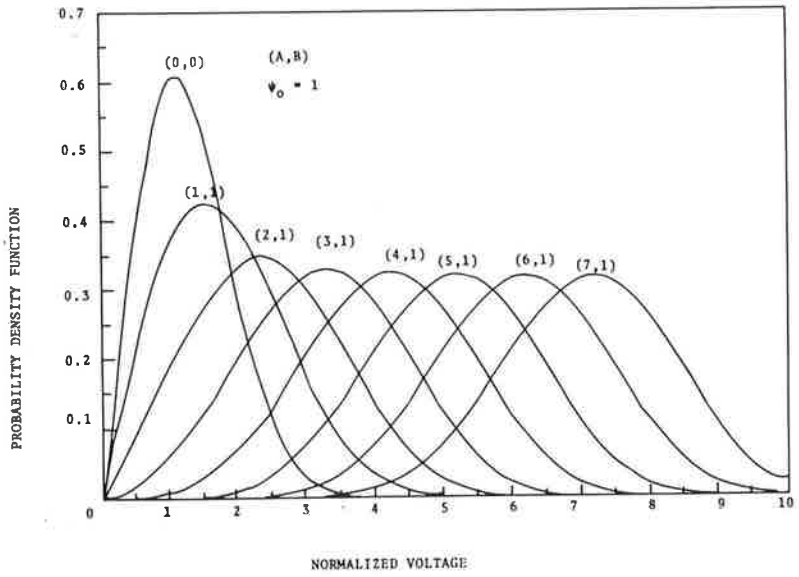

Figure 3-2. Hypergeometric Density for Envelope of Two Sine Waves Plus Additive Gaussian Noise (Case 1)

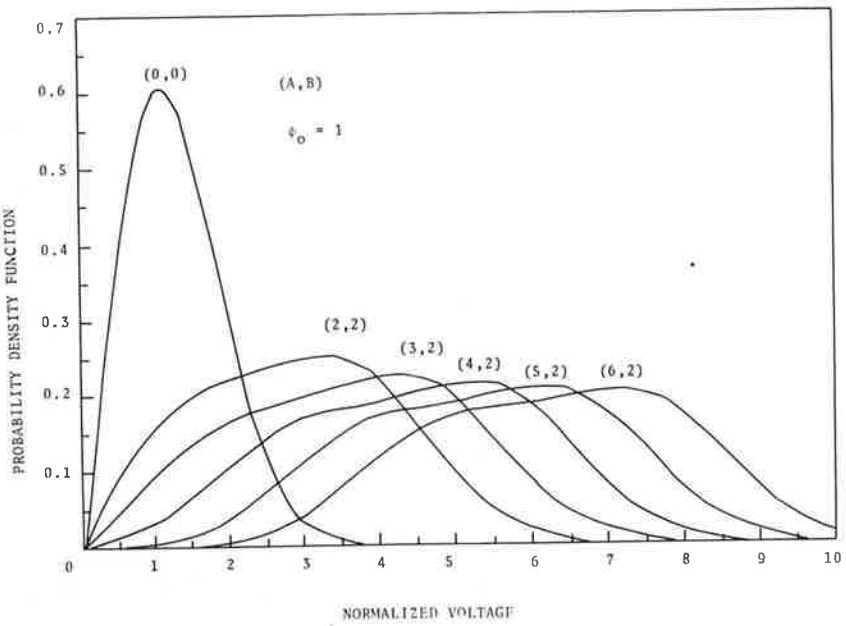

Figure 3-3. Hypergeometric Density for Envelope of Two Sine Waves Plus Additive Gaussian Noise (Case 2)

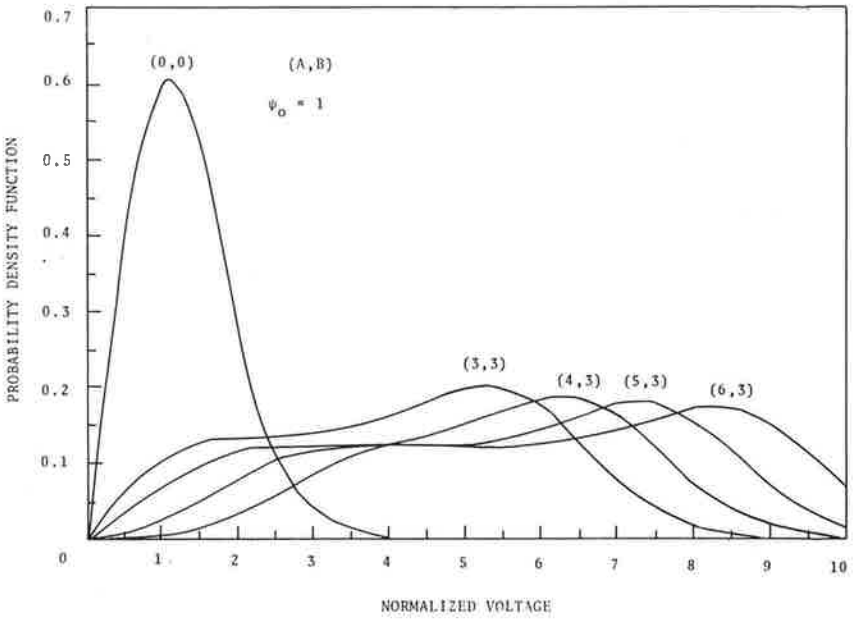

Figure 3-4. Hypergeometric Density for Envelope of Two Sine Waves Plus Additive Gaussian Noise (Case 3)

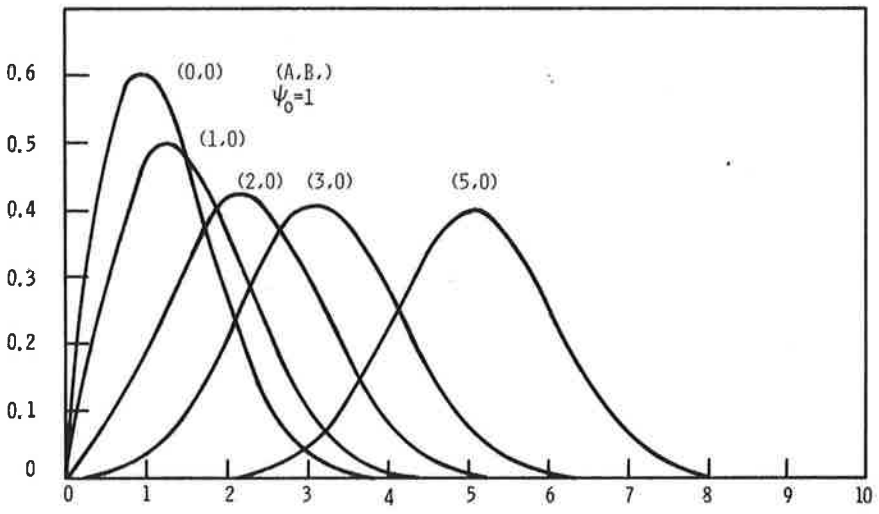

Figure 3-5. Probability Density of Envelope R of $I(t) = P = \cos p^t + {}^{I}N$

The n^{th} moment of the distribution m_n becomes

$$m_n = \int_0^\infty r^n \, p_2(r)\,dr$$

$$= \frac{2^{n/2}\Gamma\left(\frac{n}{2}+1\right)}{\Gamma(-n/2)} \sum_{m=0}^{\infty} \frac{\left(-a^2/2\right)^m}{(m!)^2} \; {}_2F_1\left[-m;\ -m;\ 1;\ \frac{b^2}{a^2}\right] \Gamma\left(m-\frac{n}{2}\right) \qquad (3\text{-}6)$$

As pointed out by Esposito and Wilson[4] these expressions are very difficult to deal with. However, the need to deal with these expressions rests upon the strength of the specular reflection. If the specular term is weak enough, we can assume $B \approx 0$ and use known limiting forms of these expressions. That is, when $B=0$

$$p_2(r) = p(r) = \frac{r}{\psi_o} \exp\left[-\frac{P^2+r^2}{2\psi_o}\right] I_o\left(\frac{rP}{\psi_o}\right)$$

$$C_2(r) = C(r) = Q\left(\frac{P}{\sqrt{\psi_o}},\ \frac{R}{\sqrt{\psi_o}}\right)$$

$$m_n = (2\psi_o)^{n/2}\,\Gamma\left(\frac{n}{2}+1\right) {}_1F_1\left(-\frac{n}{2};\ 1;\ \frac{-P^2}{2\psi_o}\right) \qquad (3\text{-}7)$$

with

$$Q(\alpha,\beta) = \int_0^\beta x \exp\left[-\frac{\left(x^2+\alpha^2\right)}{2}\right] I_o(\alpha x)\,dx \qquad (3\text{-}8)$$

and

$${}_1F_1(a;\ b;\ x) = \sum_{j=0}^{\infty} \frac{(a)_j (x)^j}{(b)_j\ j!}\ ;\quad x_j = x(x+1)\ldots(x+j-1)\ ;\quad x_o = 1 \qquad (3\text{-}9)$$

ψ_o is the noise variance and $I_o(x)$ is the modified Bessel function.

We will make the assumption $B=0$, and then show by statistical tests that the assumption is indeed self-consistent.

4. EXPERIMENTAL RESULTS

The results of the data reduction are presented in this section. We point out again that Receiver 2 was attached to the horizontal antenna and Receiver 3 was attached to the vertical antenna. The data was processed in the following way: first, a best parametric fit was made between the data and the theoretical density derived; next, some portions of the data were viewed during sequential 6-second intervals. Homogeneity tests were made to insure statistical regularity. Finally, power spectral densities (PSD) were calculated for all the data reduced.

All the data processed used the ENV 1 and ENV 2 routines (Appendix C) which filtered the data at 125 Hz and calculated the resulting envelope. Only data which had no significant 60 Hz components were used. The 125 Hz filter was selected as a best compromise since it was verified that receiver noise did not add any appreciable amount to the diffuse component as the bandwidth of the filter was varied.

In the test run, attention was given to the size of the sample. Since the PSD data indicated about a 10 to 20 Hz bandwidth for all the data, the minimum run size used was 6 seconds. This insured that a minimum of 100 data points were used for each estimate. The exact number of independent points to be used in a run of length T seconds with a bandwidth of B Hz is 2BT. It has been shown that the correct way to pick B is by energy content.[5,6,7] Unfortunately, there is no exact way to select B. We have arbitrarily decided to define the bandwidth as that which contains approximately 80% of the energy of the PSD. This should approximate closely the number of degrees of freedom in the signal. It is better to underestimate than overestimate, since the latter would falsely indicate more information than exists. Although this method is not exact, the results are fairly insensitive to the exact value of 2BT.

Calibration curves were run during and after the tests and the results are given in Appendix E.

4.1 GOODNESS OF FIT

The Kolmogorov-Smirnov (K-S) test[8] was used to determine the goodness of fit for the data. In this test, for any data segments containing M samples of the signal amplitude x, the test statistic is

$$Z_s = Z_{sample} = \max_{\{x_i\}} |F_1(x) - F_2(x)|$$

where $F_1(x)$ and $F_2(x)$ are the empirical and theoretical cumulative distributions respectively, and $\{x_i\}$ is the set of quantized sample values of x. The two segments are said to be the same with significance level α (probability of deciding that the two sets are not homogeneous when they are) if Z_{sample} is equal to or less than the threshold

$$Z_\alpha = \lambda_\alpha / \sqrt{M}$$

The value of λ_α is given in Table 4-1 when the sample size M is larger than 40. Figure 4-1 indicates the meaning of α. There are two distributions for the test statistics: $W_1(Z/H_o)$ is the distribution when the correct hypothesis, H_o, is used; $W_1(Z/H_1)$ is the distribution when hypothesis, H_o, is incorrect. The threshold value Z_α divides the test statistic into an acceptance region and a rejection region. If $Z_{sample} < Z_\alpha$ we accept the hypothesis and if $Z_{sample} > Z_\alpha$ we reject it. In general we only know the distribution of the test statistic under the correct hypothesis and hence can only calculate type I error probabilities, α. (When the test for homogeniety is made we merely test one empirical distribution against another to see if they are the same.) If we make a "goodness of fit" test we test a sample distribution against an analytically known distribution. In both cases we accept the hypothesis if $Z_{sample} < Z_\alpha$.

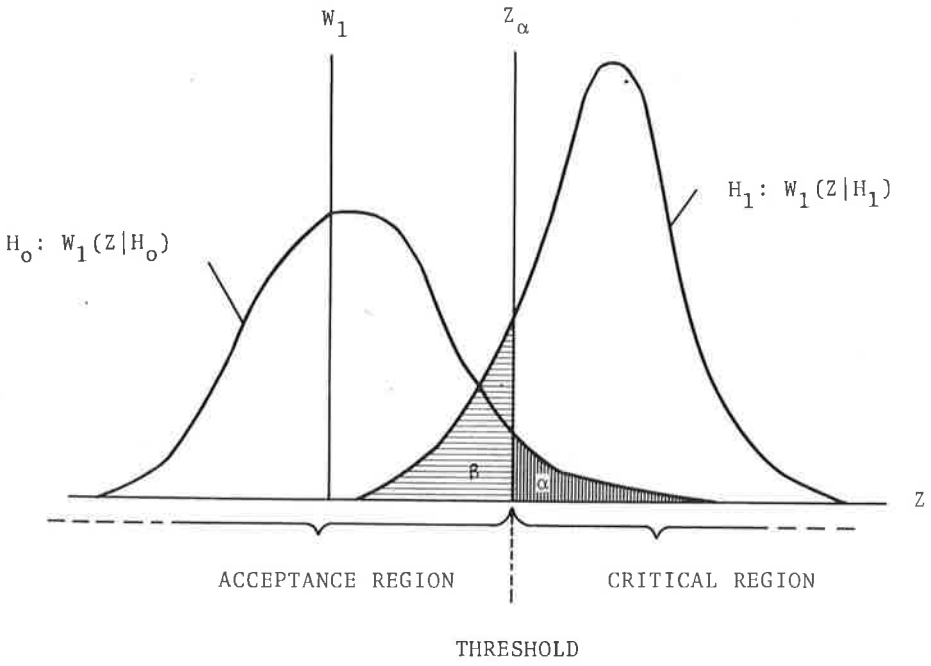

Figure 4-1 Probability Densities of Test Statistic Z_s with Type I and II Error Probabilities (α,β); Z_α = Threshold

We cannot make α arbitrarily small or β will start to increase. Since we cannot calculate β we will restrict our test to a 90% acceptance region or α = 0.1. This will insure a fairly small value for β or a large "power" of the test 1-β.

For $\alpha = .1$, $\lambda_{.1} = 1.22$ and

$$Z_{.1} = \frac{1.22}{\sqrt{M}} \qquad \text{(Goodness of fit)}$$

The results obtained in the K-S test are independent of the exact distribution (non-parametric). The test itself is more powerful than other tests (e.g., x^2-test).

TABLE 4-1 VALUE λ_α WHEN SAMPLE SIZE GREATER THAN 40

LEVEL OF SIGNIFICANCE	λ_α
0.1	1.22
0.05	1.36
0.025	1.4
0.01	1.63
0.0005	1.73
0.0001	1.95

In testing for goodness of fit, we assume the distribution in Equation (3-7):

$$p(r) = \frac{x}{\psi_o} \exp\left[\frac{-(r^2+P^2)}{2\psi_o}\right] I_o\left(\frac{rP}{\psi_o}\right) \; ; \; o \leq r < \infty$$

and calculate the quantities

$$\overline{x^2} = \frac{1}{n}\sum_{i=1}^{n} x_i^2$$

$$\overline{x^4} = \frac{1}{n}\sum_{i=1}^{n} x_i^4$$

Then, as shown in Appendix F, we estimate P^2 and ψ_o by the estimators $\hat{P}^2$ and $\hat{\psi}_o$ where

$$\hat{P}^2 = \overline{x^2}\sqrt{2 - \overline{x^4}/(\overline{x^2})^2}$$

$$\hat{\psi}_o = \frac{\overline{x^2}}{2}\left[1 - \sqrt{2 - \overline{x^4}/(\overline{x^2})^2}\right]$$

Finally we compare the theoretically derived cumulative distribu-

tion function with that of the data. The results are shown in Figures 4-2 through 4-11 which include 1 to 3 minute cumulative results of all the data processed. These results are summarized in Table 4-2.

We have also calculated the correlation coefficient, ρ, defined as

$$\rho = \frac{\frac{1}{n}\sum_{i=1}^{n}(x_i-\bar{x})(y_i-\bar{y})}{\left(\frac{1}{n}\sum_{i=1}^{n}(x_i-\bar{x})^2\right)^{1/2}\left(\frac{1}{n}\sum_{i=1}^{n}(y_i-\bar{y})^2\right)^{1/2}}$$

between the vertical and horizontal channels. The indications are that there is negative correlation between the two channels. This correlation can be identified with the diffuse component by noticing that it generally is associated with the lower direct-to-diffuse ratios.

Notice also that some of the K-S tests were marginal and could be related to the smaller Doppler bandwidths and hence smaller sample size. Unfiltered (ENV 1) envelope Doppler spectra are shown in Figures 4-12 through 4-17.

4.2 HOMOGENEITY

The test for homogeneity is similar to the goodness of fit test. The difference is that the homogeneity test tests one empirical cumulative distribution against another. If the test result is positive, we say that both sets of data come from the same distribution. Hence, the underlying mechanisms generating the two sets of data are the same. If the tests are made for successive instants of time, we conclude that the data is homogenous in time or stationary over a finite segment of time. The test takes the form

$$Z_{sample} \gtrless Z_\alpha = \lambda_\alpha \Big/ \sqrt{\frac{M_1 M_2}{M_1+M_2}}$$

TABLE 4-2 DATA REDUCTION SUMMARY

DATE	RUN	LENGTH OF TIME	ELEV. ANG.	HORIZONTAL $\hat{p}^2$	HORIZONTAL $\hat{\psi}_o$	HORIZONTAL $\frac{\hat{p}^2}{2\hat{\psi}_o}$(db)	VERTICAL $\hat{p}^2$	VERTICAL $\hat{\psi}_o$	VERTICAL $\frac{\hat{p}^2}{2\hat{\psi}_o}$(db)	K-S	ρ
10/1	1	60	15°	.332	.0037	16.56	.313	.0076	13.16	Test Marginal	-.0402
9/27	4	120	5°	.103	.0121	6.29	.089	.0100	6.50	Test Marginal	.1
10/1	5	60	10°	.135	.0206	5.15	.092	.0303	1.82		-.572
9/30	4	180	10°	.111	.0028	13.0	.057	.0021	11.4	Test Marginal	-.247
9/27	1	162	5°	.153	.0339	3.53	.197	.0269	5.64		-.262
9/27	1	60	5°	.192	.0358	4.28	.174	.028	4.91		-.3077
"	1	6	5°	.230	.0306	5.75	.158	.0257	4.87		-.417
"	1	"	"	.192	.0307	4.96	.135	.0231	4.64		-.404
"	1	"	"	.201	.0313	5.07	.138	.0207	5.23		-.457
"	1	"	"	.212	.0404	4.18	.169	.0253	5.24		-.353
"	1	"	"	.258	.034	5.73	.156	.0337	3.64		-.305
"	1	"	"	.205	.0402	4.05	.221	.0314	5.46		-.142
"	1	"	"	.162	.0455	2.51	.196	.0264	5.70		-.285
"	1	"	"	.159	.0315	4.03	.210	.0272	5.87		-.287
"	1	"	"	.137	.0287	3.78	.189	.0247	5.82		-.240
"	1	"	"	.199	.0254	5.92	.203	.0243	6.2		-.265
10/1	5	6	10°	.140	.0233	4.96	.104	.034	1.86		-.517
"	"	"	"	.158	.0177	6.50	.084	.0325	1.09		-.583
"	"	"	"	.173	.0187	6.66	.091	.0287	1.98		-.519
"	"	"	"	.133	.0197	5.29	.083	.028	1.71		-.585
"	"	"	"	.138	.019	5.59	.065	.0282	0.60		-.570
"	"	"	"	.139	.0174	5.98	.070	.0275	1.07		-.647
"	"	"	"	.113	.0184	4.85	.116	.0278	3.18		-.669
"	"	"	"	.119	.0231	4.12	.105	.0263	3.00		-.625
"	"	"	"	.122	.022	4.44	.116	.027	3.33		-.529
"	"	"	"	.125	.0242	4.11	.110	.0326	2.26		-.555
10/1	1	6	15°	.346	.0034	17.1	.261	.0078	12.2		.167
"	"	"	"	.337	.0032	17.2	.239	.0076	12.0		.253
"	"	"	"	.341	.0029	17.7	.257	.0050	14.1		-.0132
"	"	"	"	.340	.0023	18.7	.256	.0045	14.6		.164
"	"	"	"	.290	.0022	18.2	.367	.0054	15.3		.142
"	"	"	"	.317	.0023	18.4	.366	.0035	17.2		.207
"	"	"	"	.327	.0024	18.4	.321	.0054	14.8		.0655
"	"	"	"	.384	.0047	16.1	.336	.0045	15.7		-.133
"	"	"	"	.342	.0040	16.3	.364	.0043	16.2		-.113
"	"	"	"	.3040	.0041	15.7	.412	.0042	16.7		-.077

where M_1 and M_2 are the sample sizes of the two distributions. Since most tests were run only for a few minutes, the homogeneity test was used to check out whether the data was statistically regular in this interval. This was done by looking in detail at three one-minute runs; 5°, 10° and 15°, in 6-second intervals. This data is displayed in Figures 4-18 to 4-81. In each of the three runs the two extreme 6-second segments also passed a K-S test.

HISTOGRAMS OF PROCESSED DATA

- Probability-Density Function (PDF)
- Cumulative Distribution Function (CDF)
- Power Spectral Density (PSD)

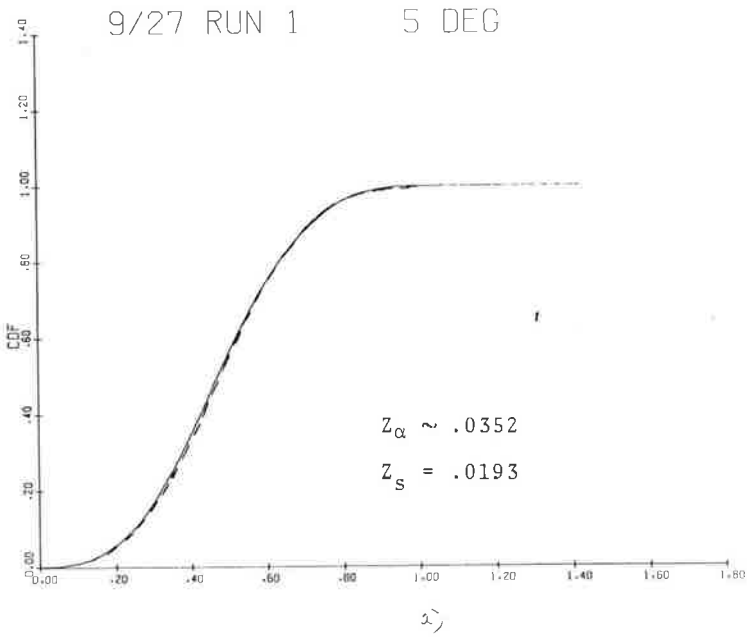

Figure 4-2a RCVR2-IF
ENV2 60 SECS. START=23.57. 9
EXPERIMENTAL

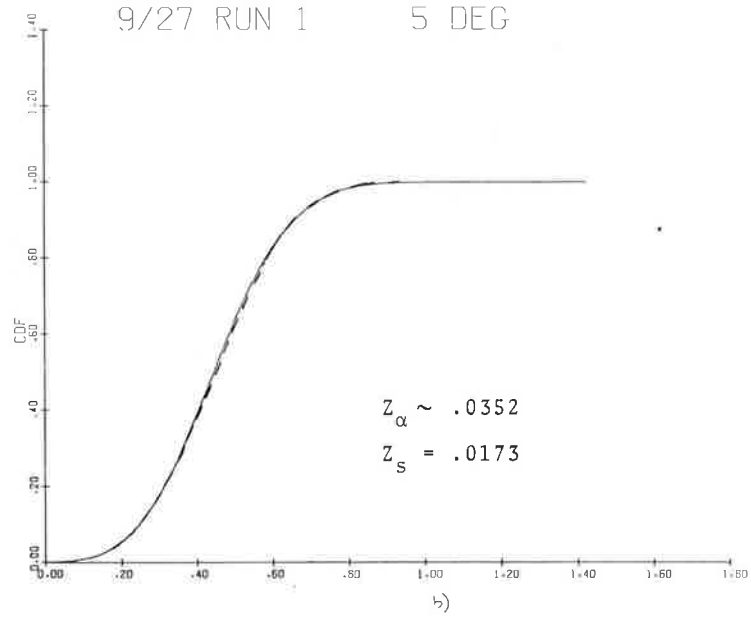

Figure 4-2b RCVR3-IF
ENV2 60 SECS. START=23.57. 9
EXPERIMENTAL

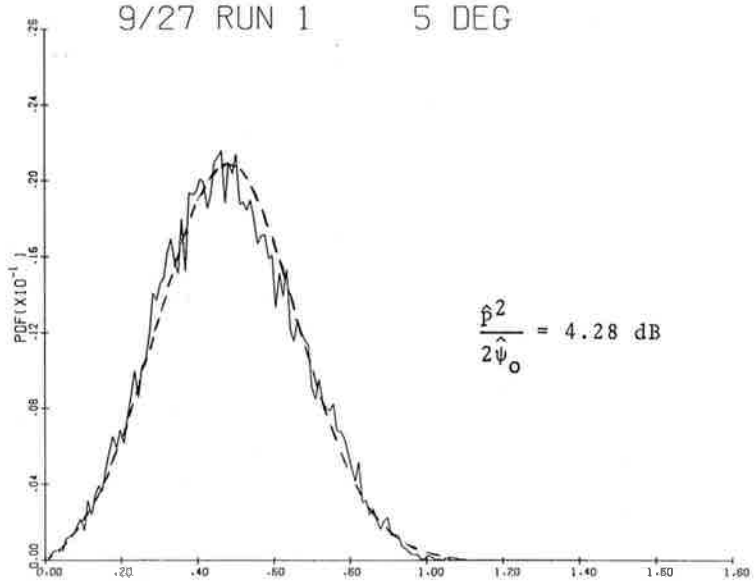

Figure 4-3a RCVR2-IF
ENV2 60 SECS. START=23.57. 9
EXPERIMENTAL

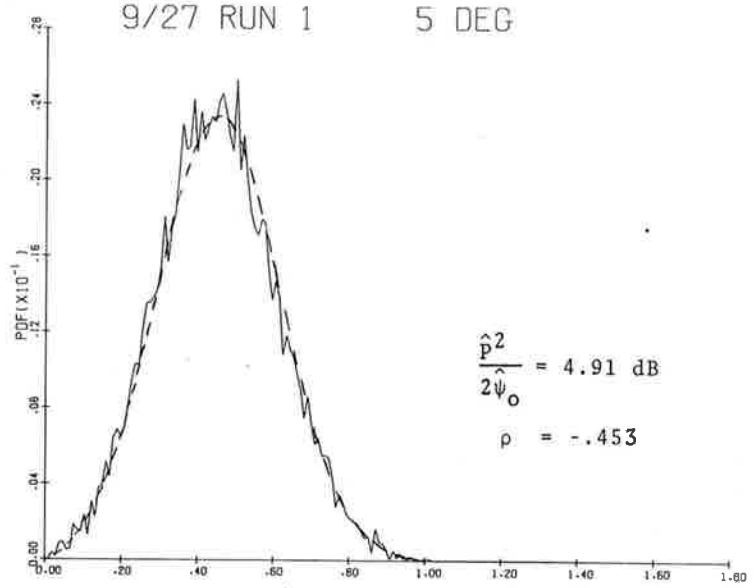

b)

Figure 4-3b RCVR3-IF
ENV2 60 SECS. START=23.57. 9
EXPERIMENTAL

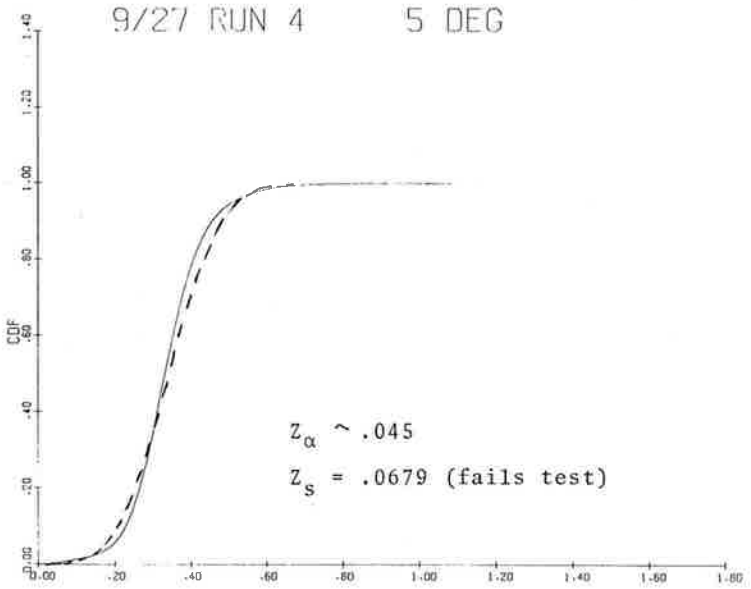

Figure 4-4a RCVR2-IF N= 8
ENV2 120 SECS. START=20.57. 9
EXPERIMENTAL

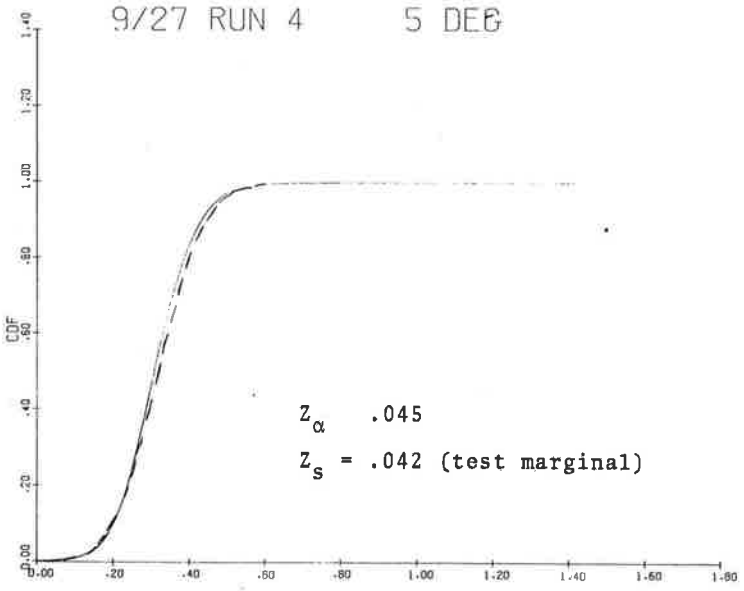

Figure 4-4b RCVR3-IF N= 8
ENV2 120 SECS. START=20.57. 9
EXPERIMENTAL

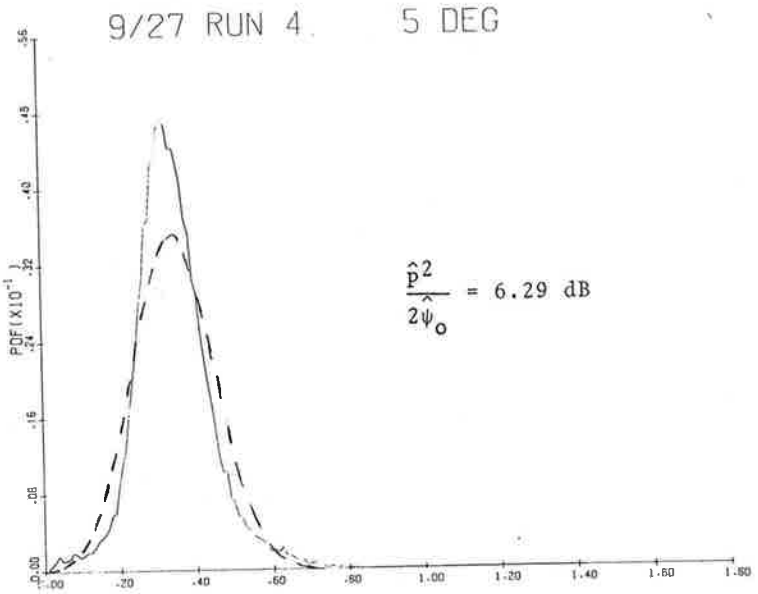

Figure 4-5a RCVR2-IF N= 8
ENV2 120 SECS. START=20.57. 9
EXPERIMENTAL

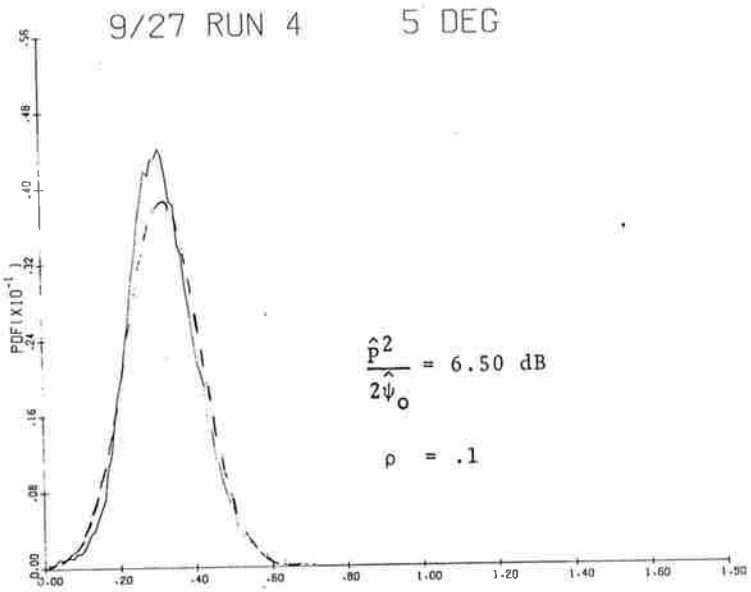

Figure 4-5b RCVR3-IF N= 8
ENV2 120 SECS. START=20.57. 9
EXPERIMENTAL

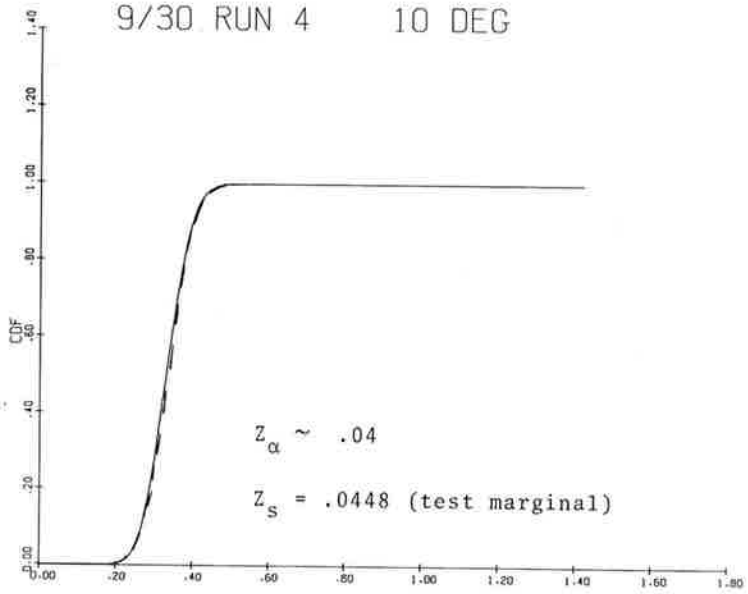

Figure 4-6a RCVR2-IF
ENV2 160 SECS. START= 0.45.14
EXPERIMENTAL

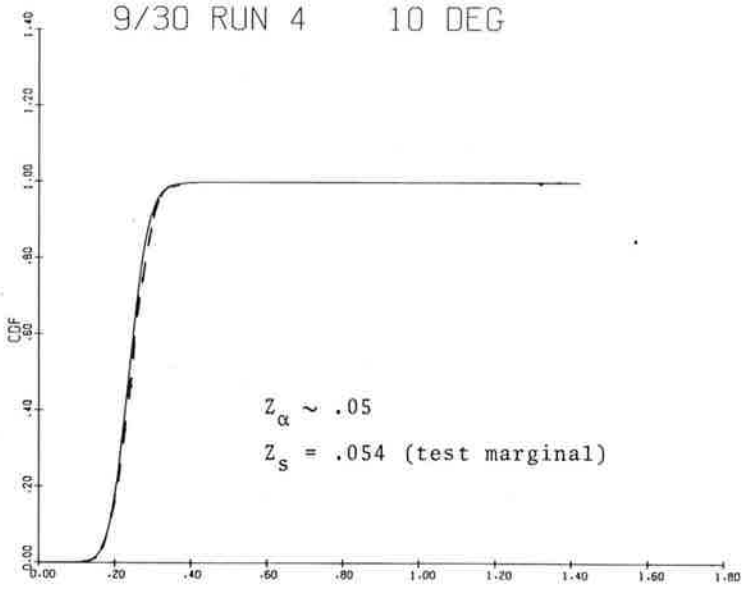

Figure 4-6b RCVR3-IF
ENV2 160 SECS. START= 0.45.14
EXPERIMENTAL

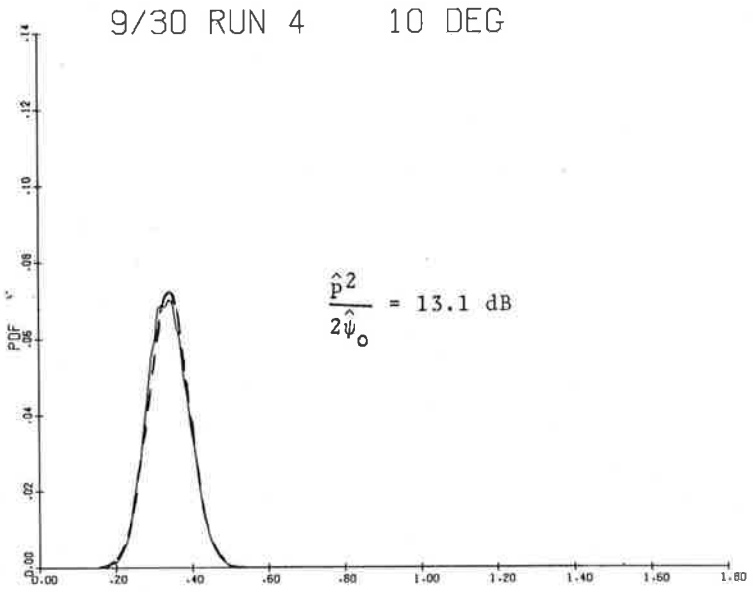

Figure 4-7a RCVR2-IF
ENV2 160 SECS. START= 0.45.14
EXPERIMENTAL

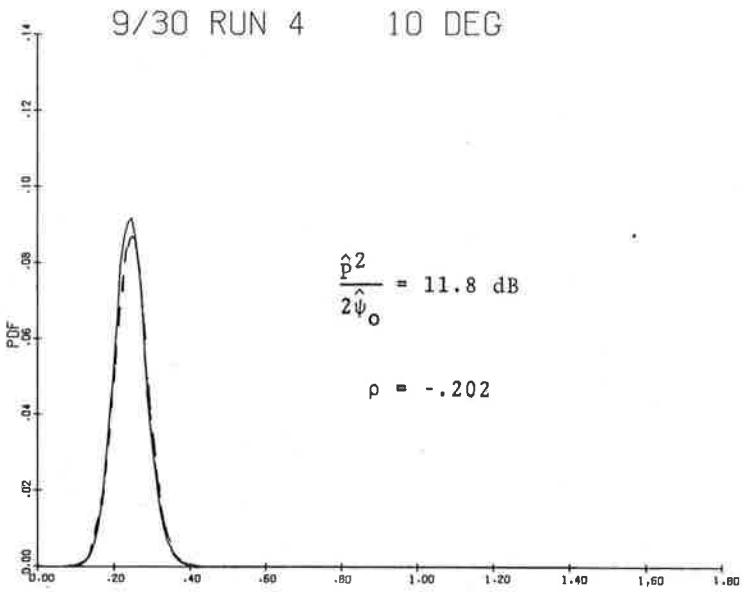

Figure 4-7b RCVR3-IF
ENV2 160 SECS. START= 0.45.14
EXPERIMENTAL

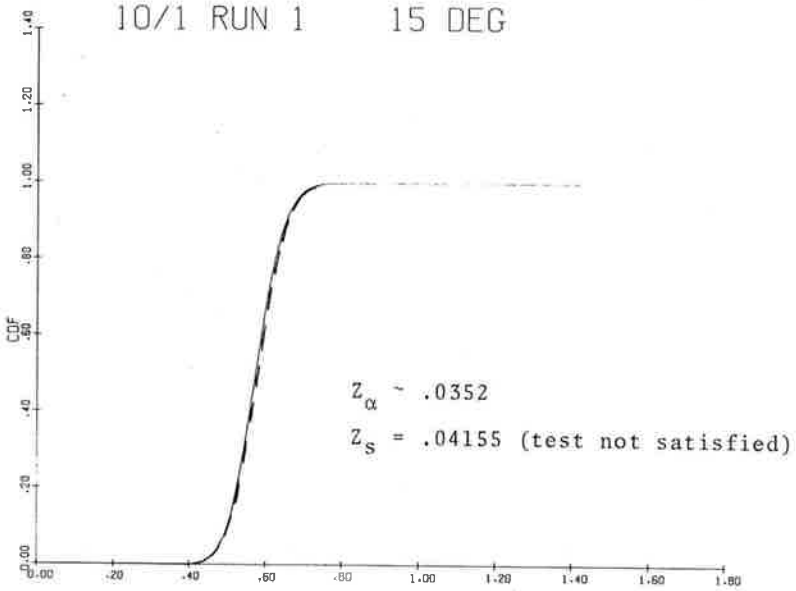

Figure 4-8a RCVR2-IF
ENV2 60 SECS. START= 1.46.31
EXPERIMENTAL

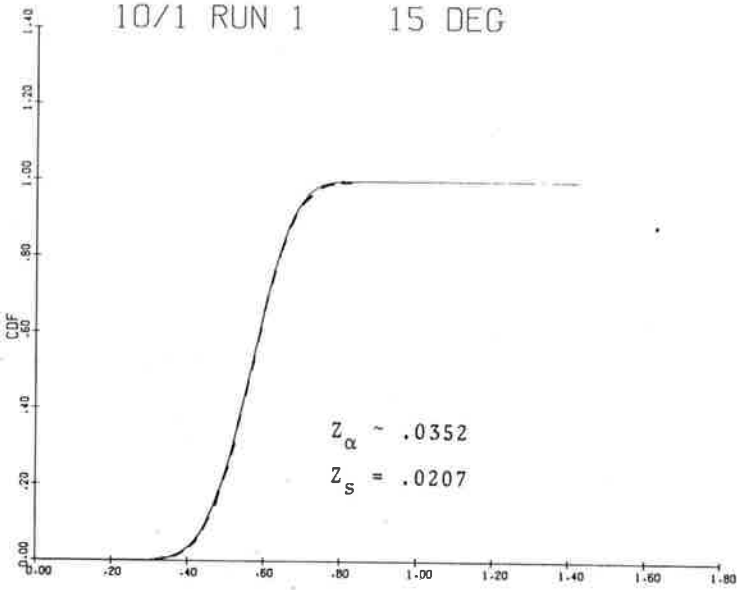

Figure 4-8b RCVR3-IF
ENV2 60 SECS. START= 1.46.31
EXPERIMENTAL

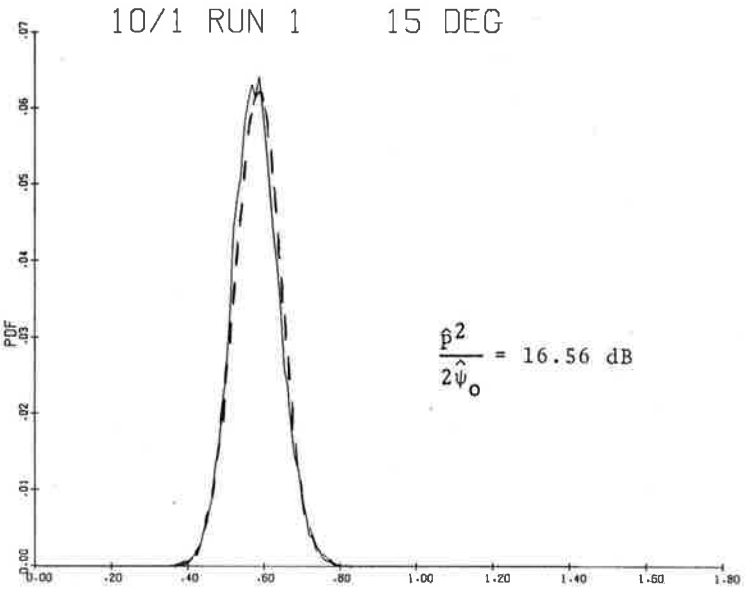

Figure 4-9a RCVR2-IF
ENV2 60 SECS. START= 1.46.31
EXPERIMENTAL

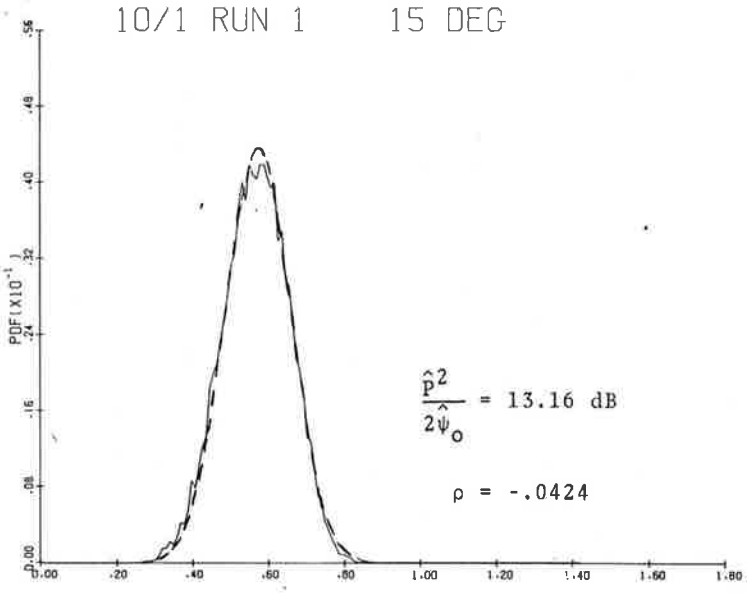

Figure 4-9b RCVR3-IF
ENV2 60 SECS. START= 1.46.31
EXPERIMENTAL

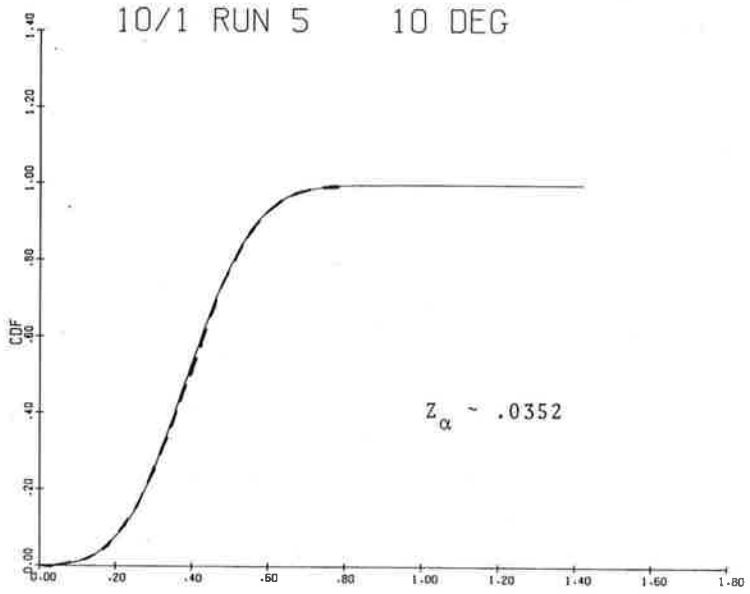

Figure 4-10a RCVR2-IF
ENV2 60 SECS. START=32.54.37
EXPERIMENTAL

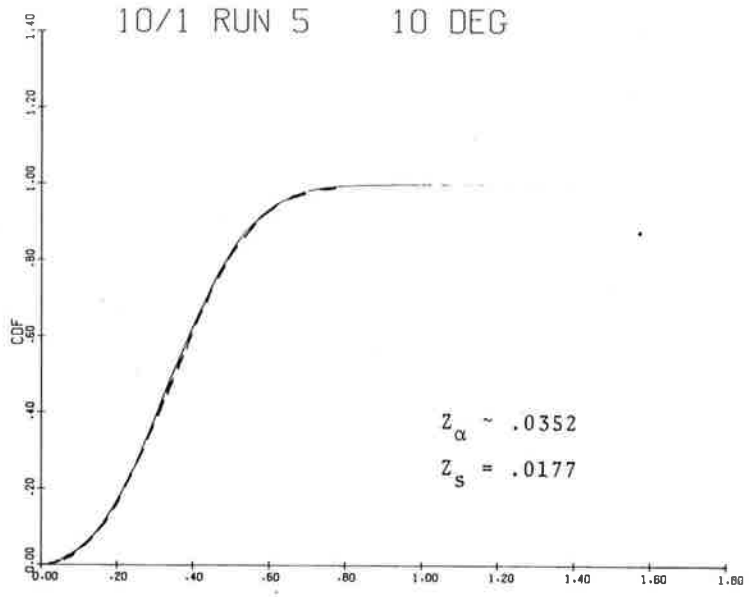

Figure 4-10b RCVR3-IF
ENV2 60 SECS. START=32.54.37
EXPERIMENTAL

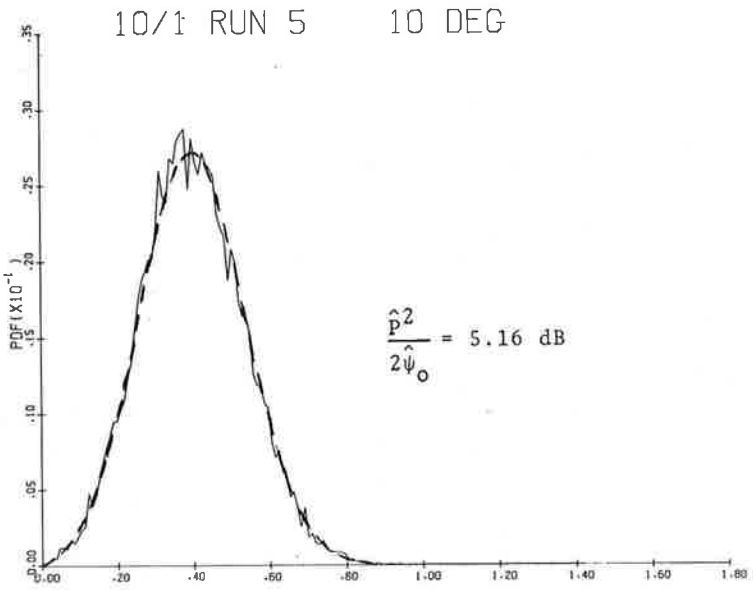

Figure 4-11a RCVR2-IF
ENV2 60 SECS. START=32.54.37
EXPERIMENTAL

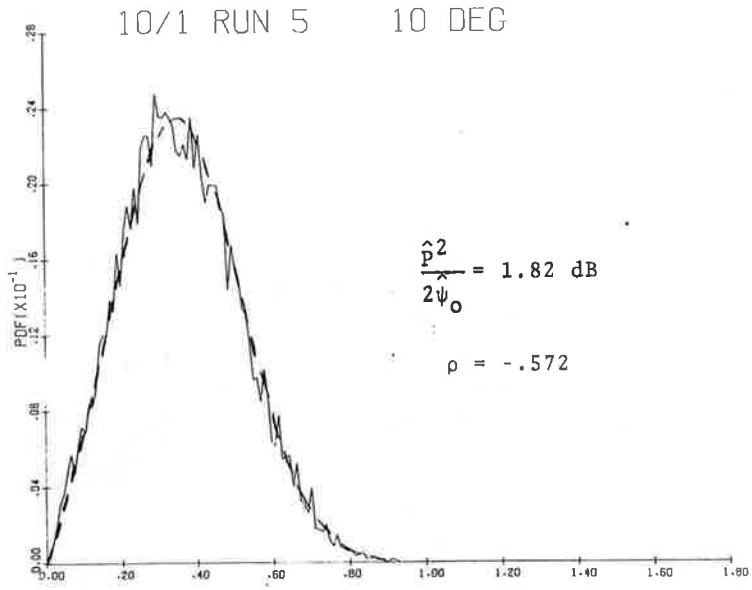

Figure 4-11b RCVR3-IF
ENV2 60 SECS. START=32.54.37
EXPERIMENTAL

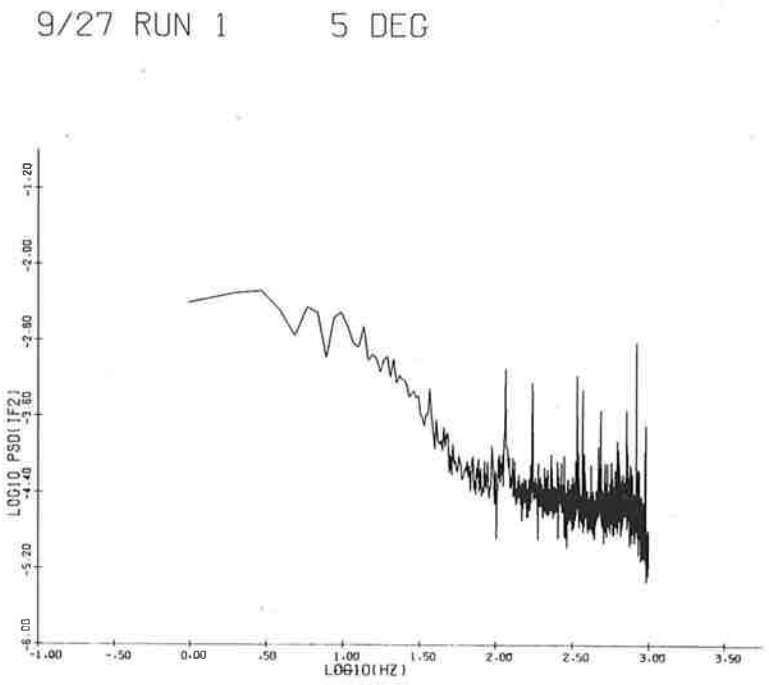

Figure 4-12a ENV1 12 SECS. START=23.57. 9L0

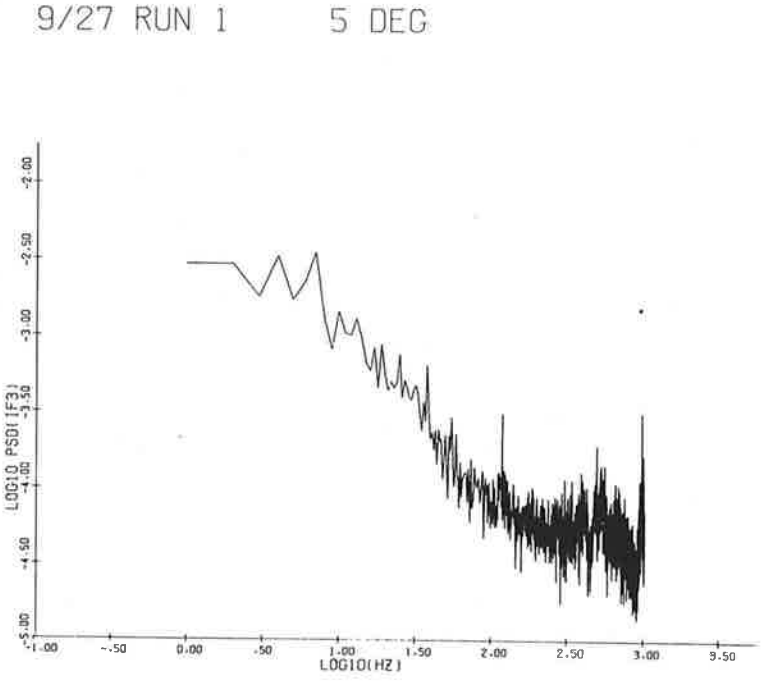

Figure 4-12b ENV1 12 SECS. START=23.57. 9L0

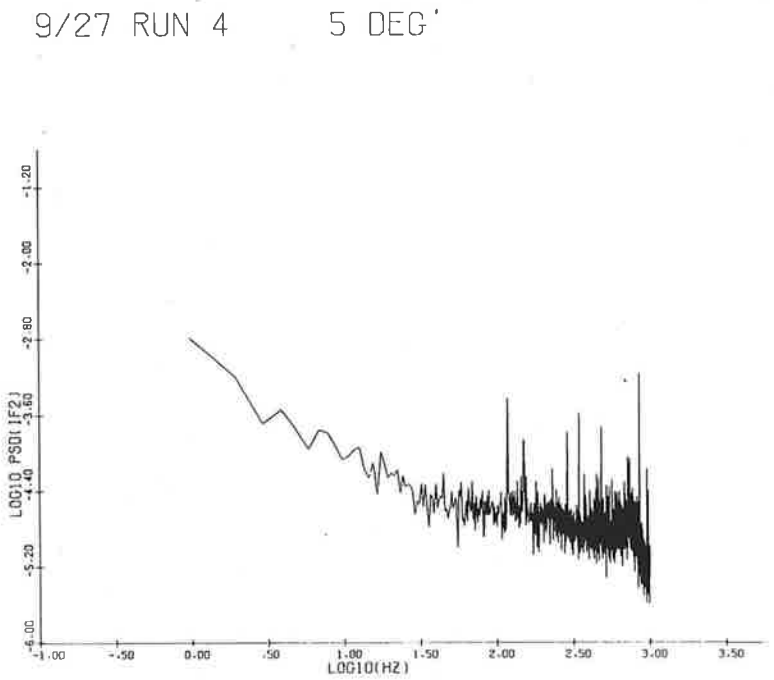

Figure 4-13a ENV1 12 SECS. START=20.57. 9L0

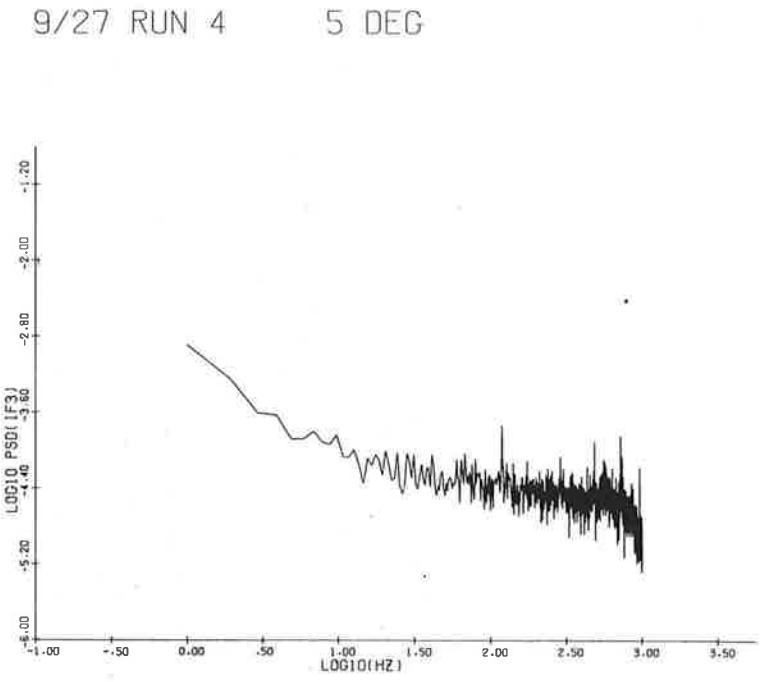

Figure 4-13b ENV1 12 SECS. START=20.57. 9L0

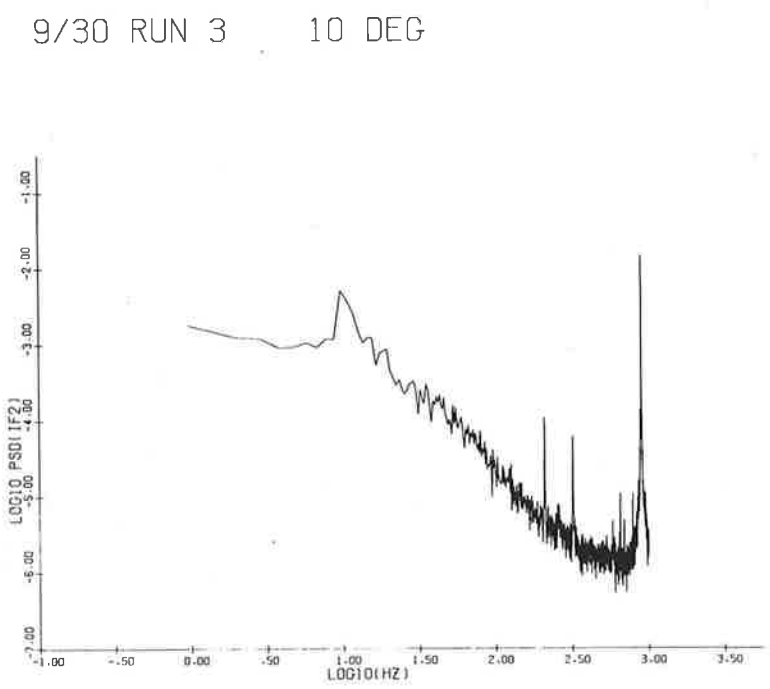

Figure 4-14a ENV1 12 SECS. START=20.28. 2LO

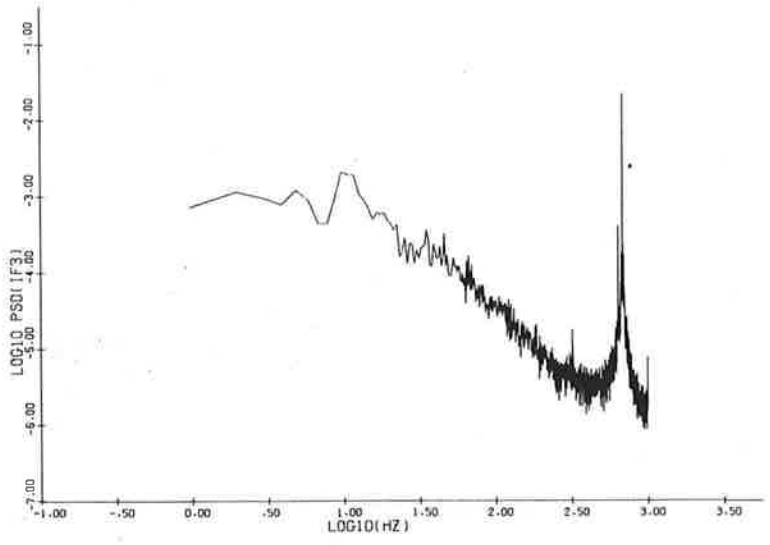

Figure 4-14b ENV1 12 SECS. START=20.28. 2LO

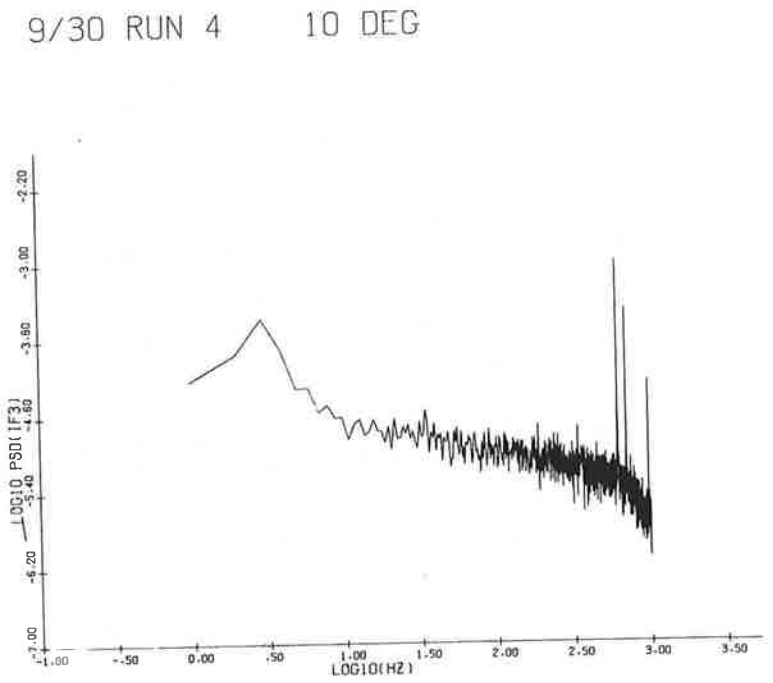

Figure 4-15a ENV1 12 SECS. START= 0.45.14L0

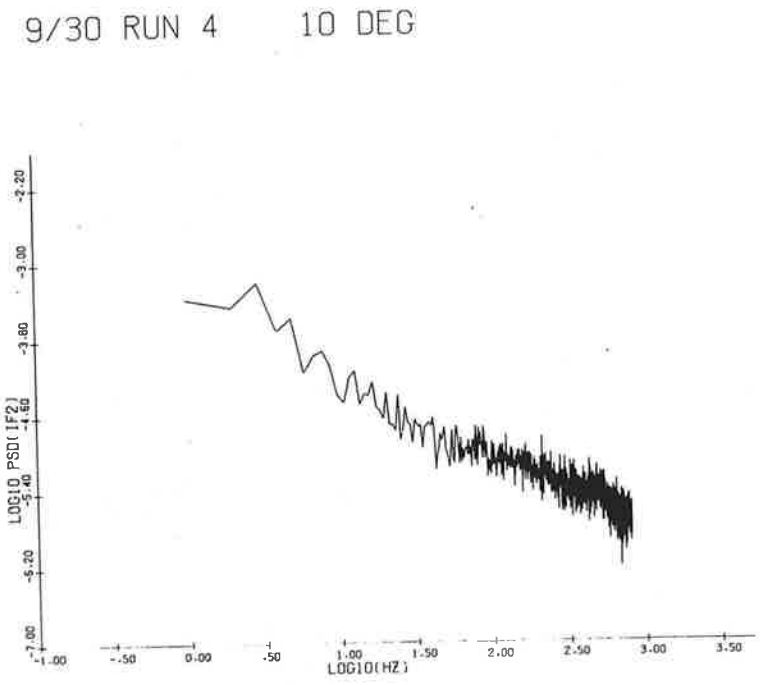

Figure 4-15b ENV1 12 SECS. START= 0.45.14L0

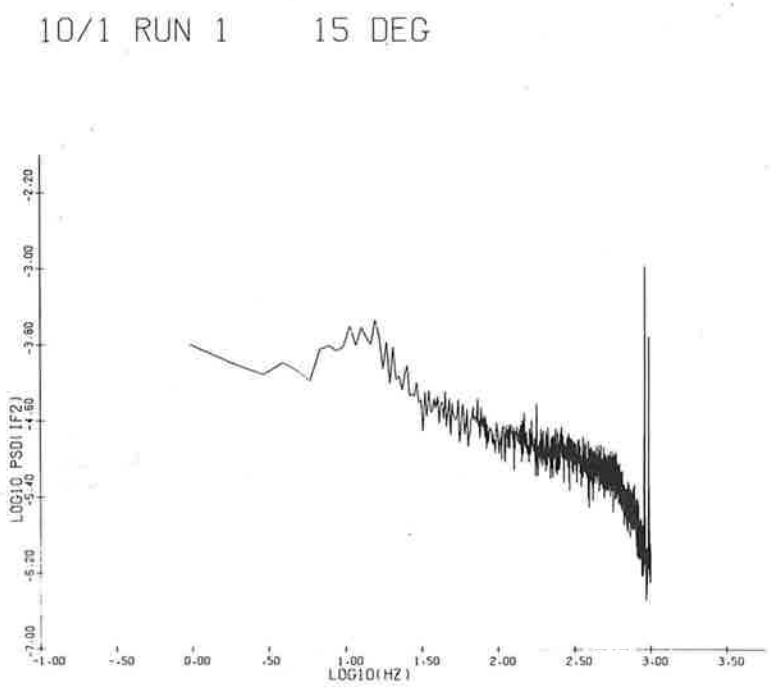

Figure 4-16a ENV1 12 SECS. START= 1.46.31LO

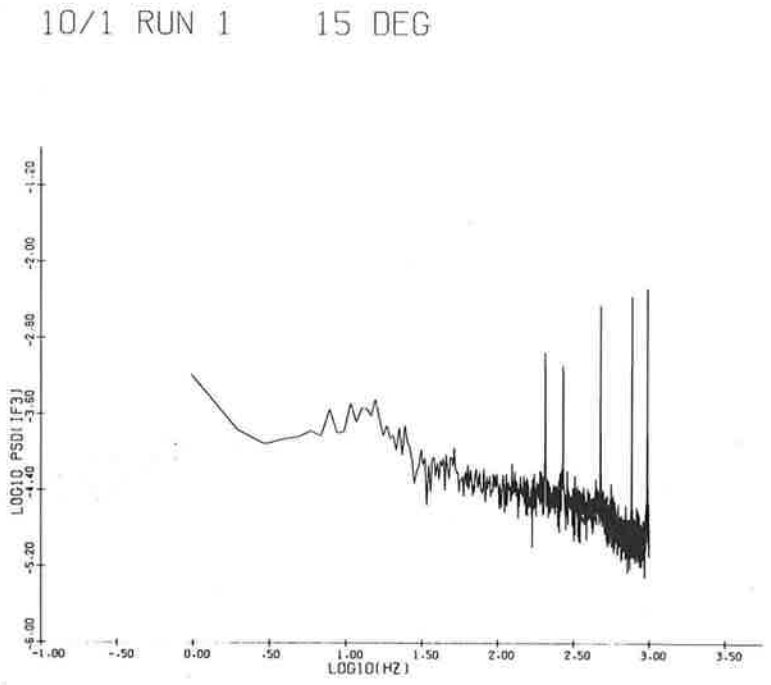

Figure 4-16b ENV1 12 SECS. START= 1.46.31LO

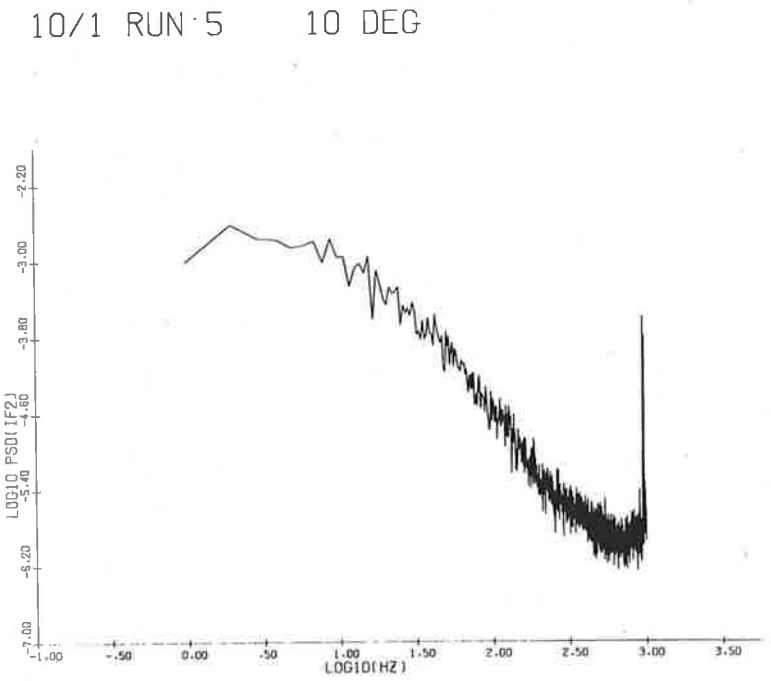

Figure 4-17a ENV1 12 SECS. START=32.54.37LO

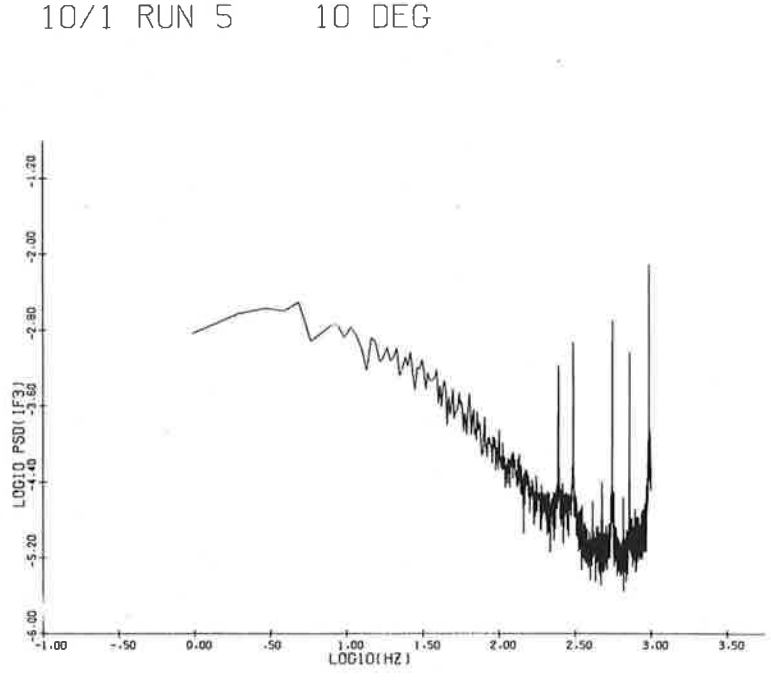

Figure 4-17b ENV1 12 SECS. START=32.54.37LO

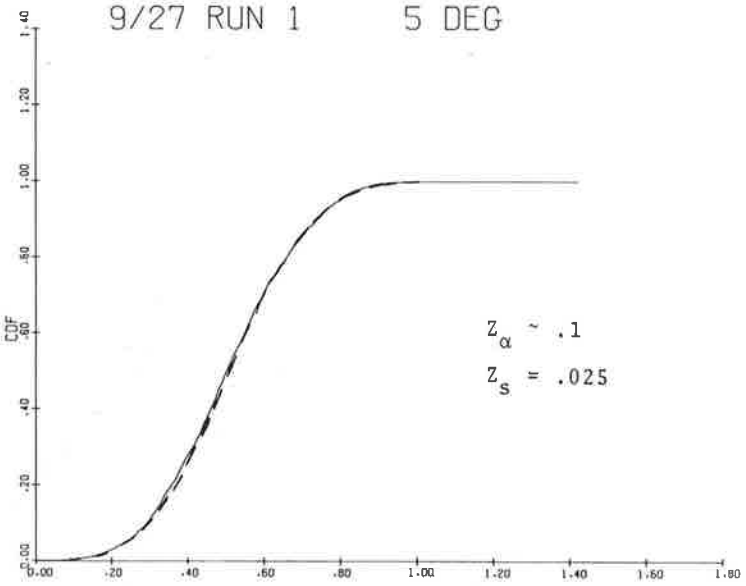

Figure 4-18a RCVR2-IF
ENV2 6 SECS. START=23.57.10
EXPERIMENTAL

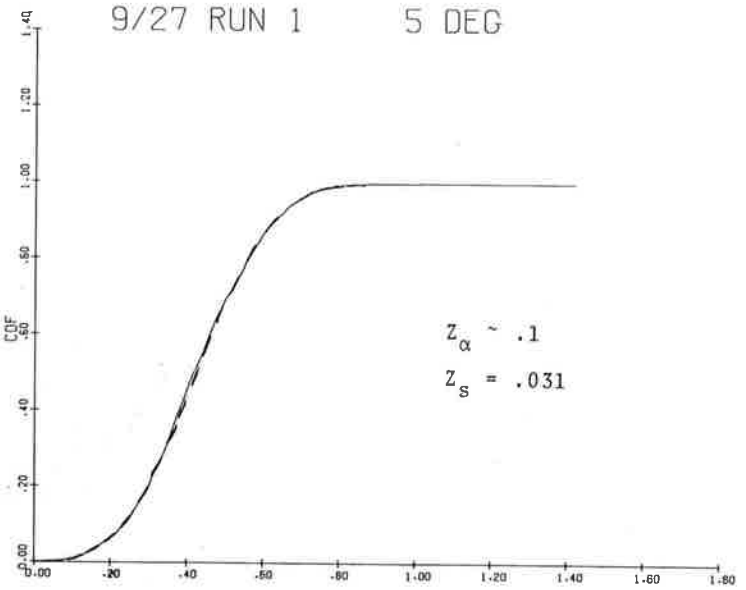

Figure 4-18b RCVR3-IF
ENV2 6 SECS. START=23.57.10
EXPERIMENTAL

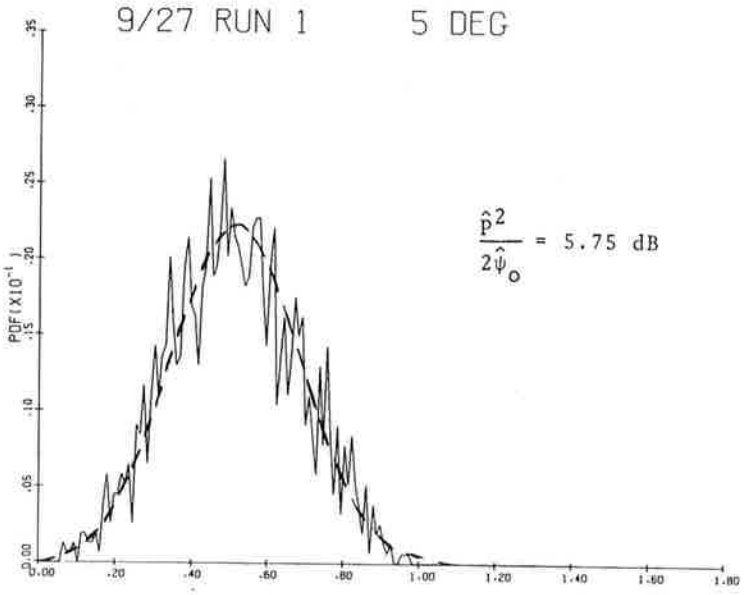

Figure 4-19a RCVR2-IF
ENV2 6 SECS. START=23.57.10
EXPERIMENTAL

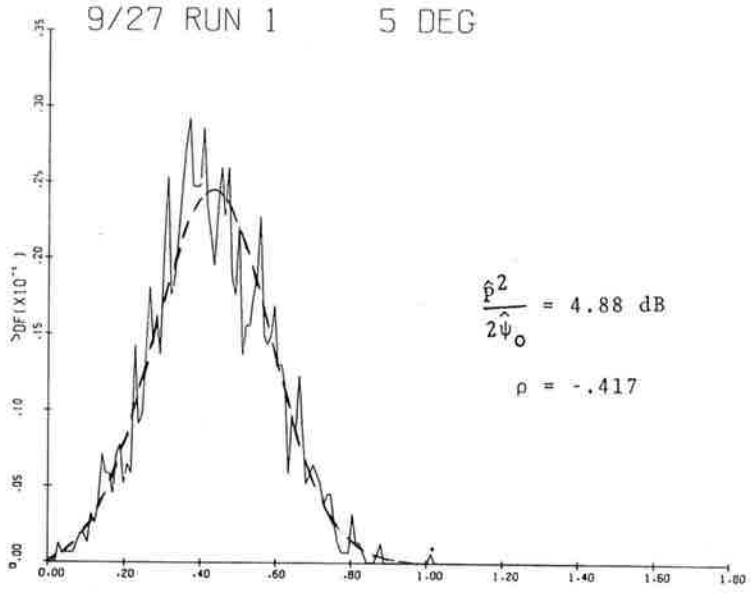

Figure 4-19b RCVR3-IF
ENV2 6 SECS. START=23.57.10
EXPERIMENTAL

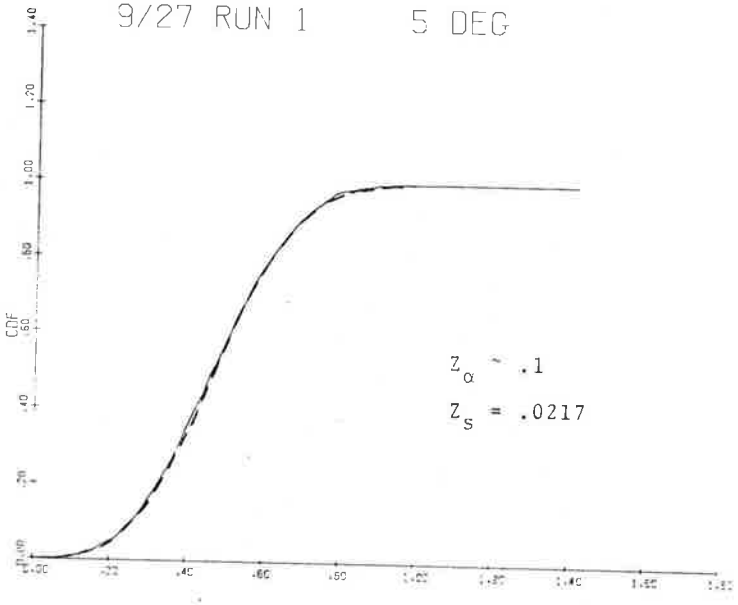

Figure 4-20a RCVR2-IF
ENV2 6 SECS. START=23.57.16
EXPERIMENTAL

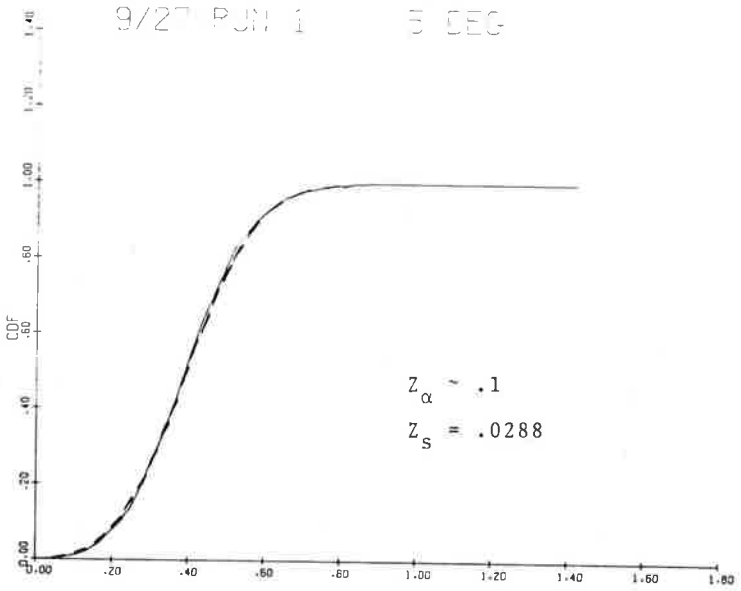

Figure 4-20b RCVR3-IF
ENV2 6 SECS. START=23.57.16
EXPERIMENTAL

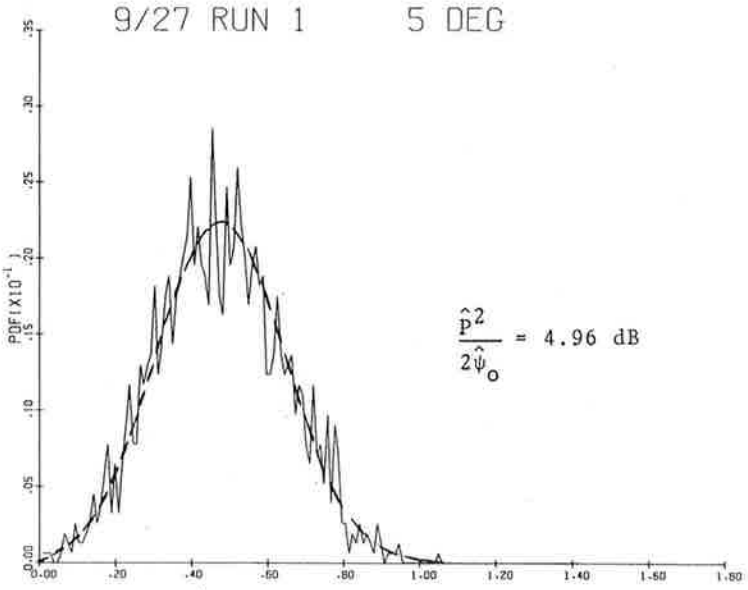

Figure 4-21a RCVR2-IF
ENV2 6 SECS. START=23.57.16
EXPERIMENTAL

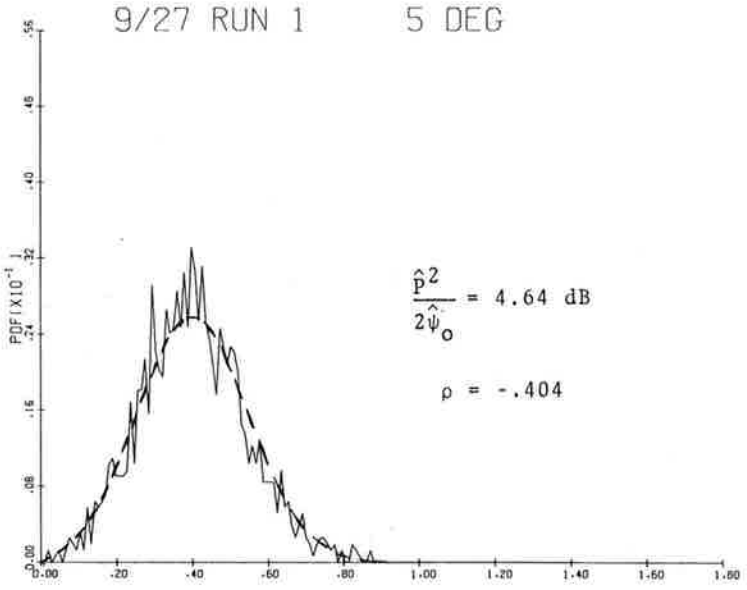

Figure 4-21b RCVR3-IF
ENV2 6 SECS. START=23.57.16
EXPERIMENTAL

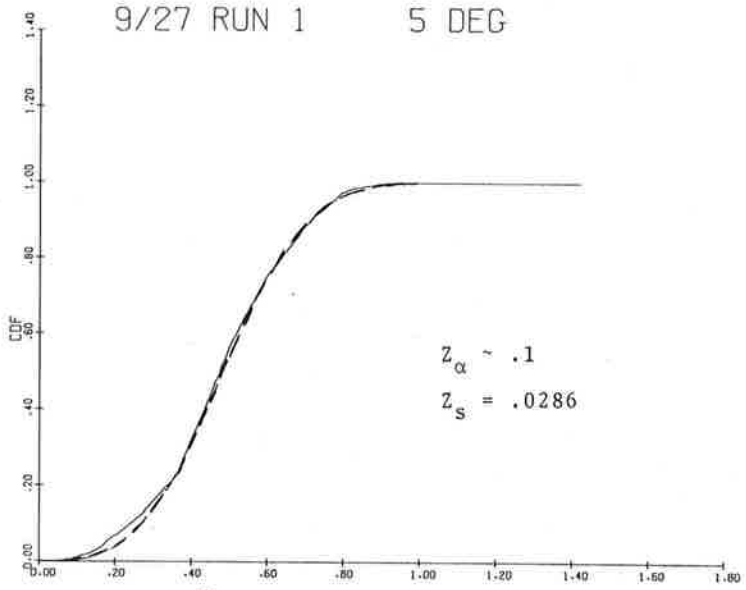

Figure 4-22a RCVR2-IF
ENV2 6 SECS. START=23.57.22
EXPERIMENTAL

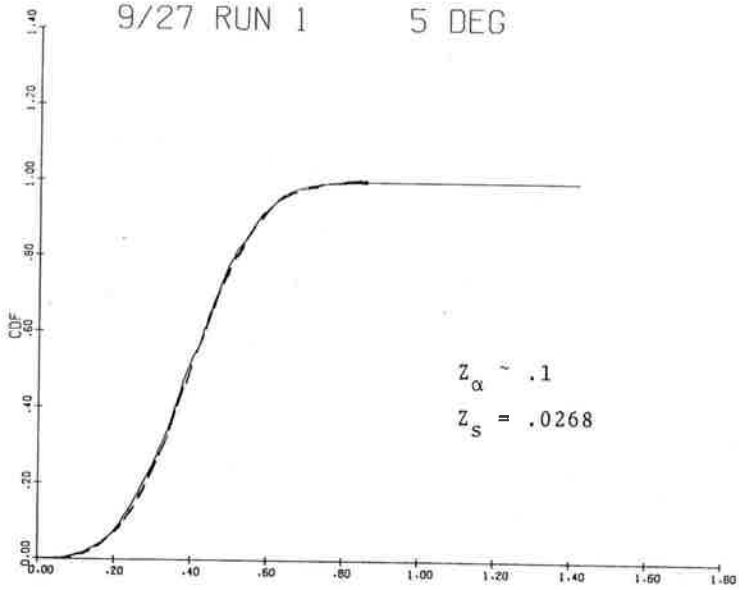

Figure 4-22b RCVR3-IF
ENV2 6 SECS. START=23.57.22
EXPERIMENTAL

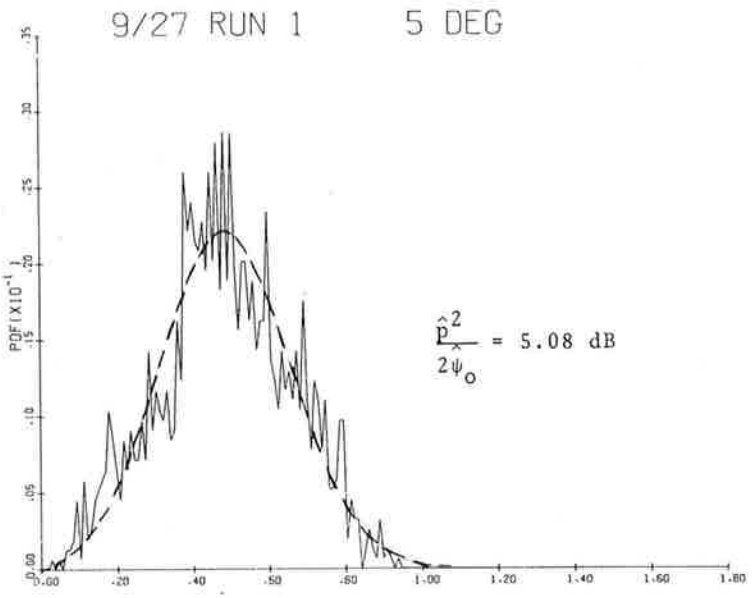

Figure 4-23a RCVR2-IF
ENV2 6 SECS. START=23.57.22
EXPERIMENTAL

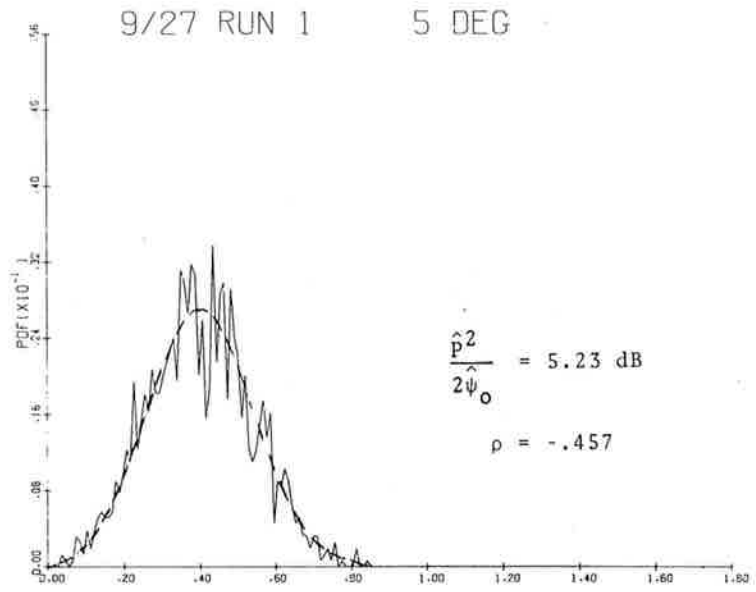

Figure 4-23b RCVR3-IF
ENV2 6 SECS. START=23.57.22
EXPERIMENTAL

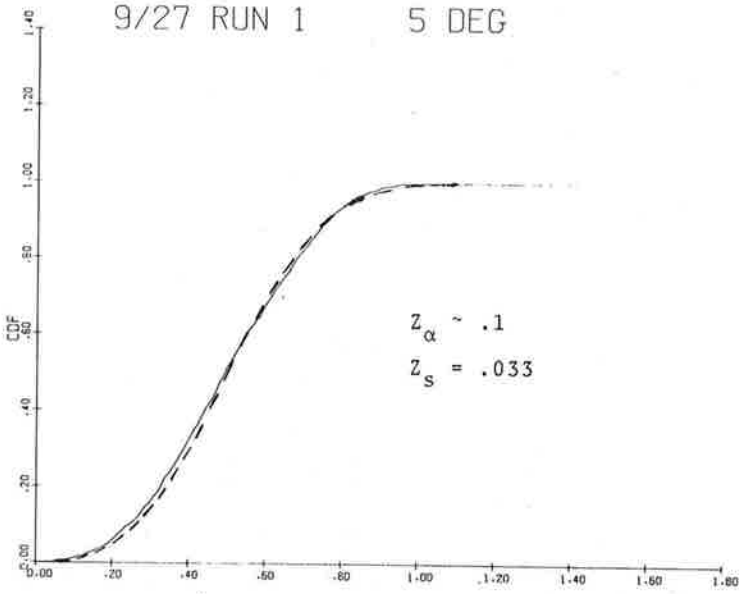

Figure 4-24a RCVR2-IF
ENV2 6 SECS. START=23.57.28
EXPERIMENTAL

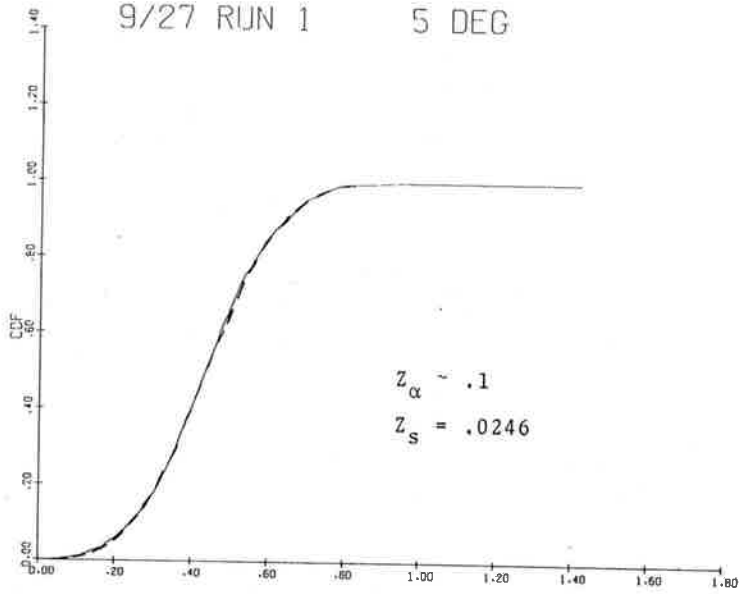

Figure 4-24b RCVR3-IF
ENV2 6 SECS. START=23.57.28
EXPERIMENTAL

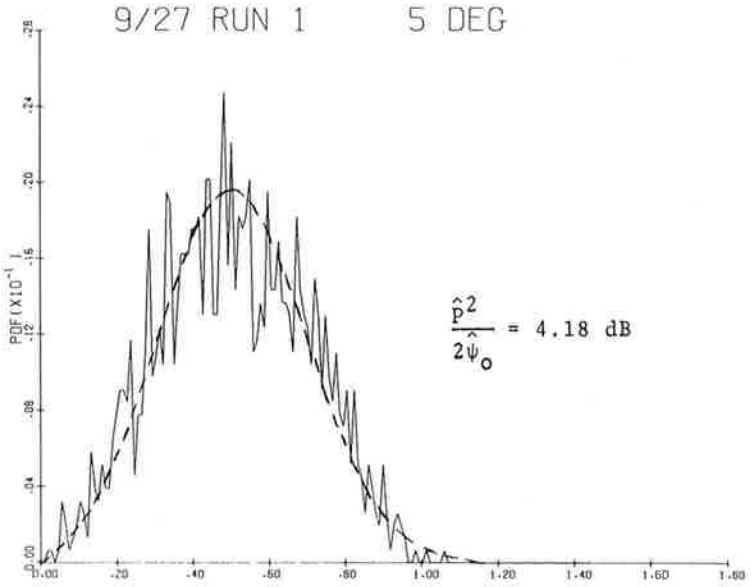

Figure 4-25a RCVR2-IF
ENV2 6 SECS. START=23.57.28
EXPERIMENTAL

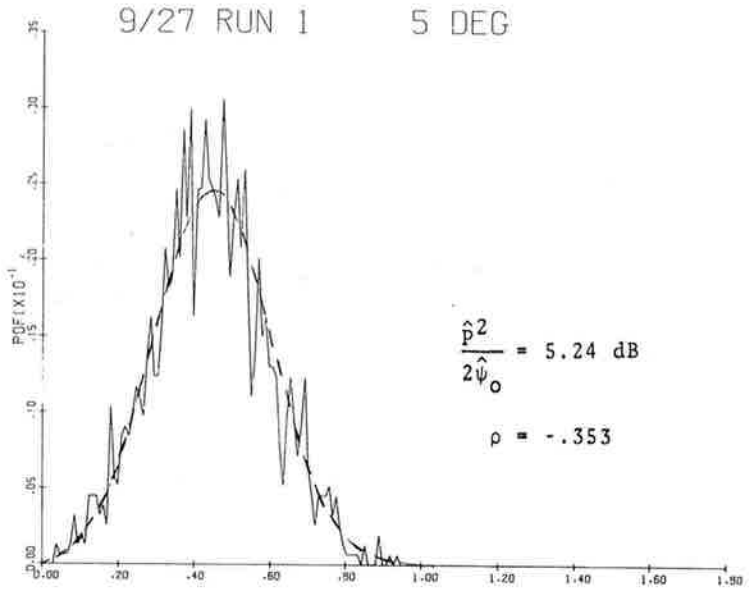

Figure 4-25b RCVR3-IF
ENV2 6 SECS. START=23.57.28
EXPERIMENTAL

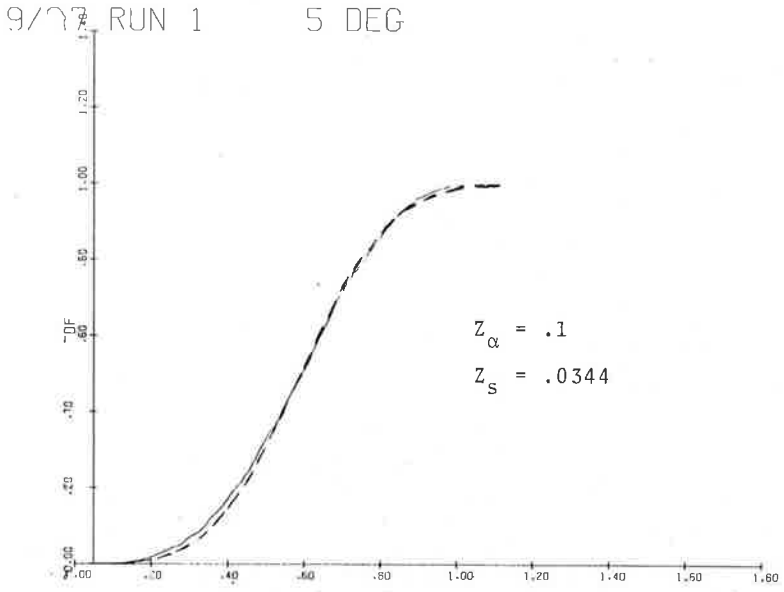

Figure 4-26a RCVR2-IF
ENV2 6 SECS. START=23.57.34
EXPERIMENTAL

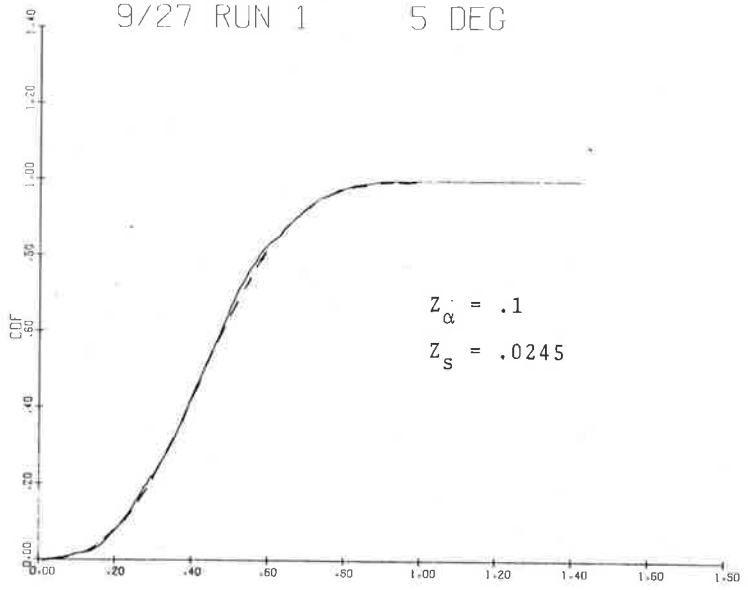

Figure 4-26b RCVR3-IF
ENV2 6 SECS. START=23.57.34
EXPERIMENTAL

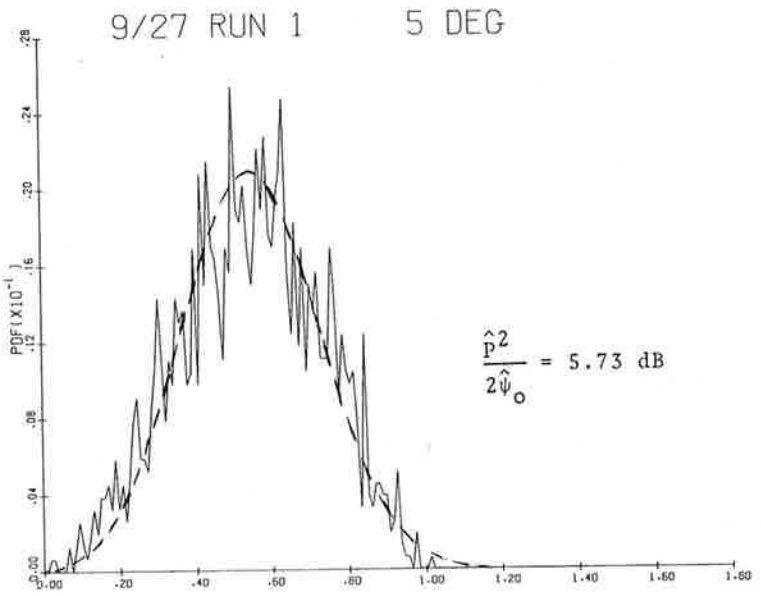

Figure 4-27a RCVR2-IF
ENV2 6 SECS. START=23.57.34
EXPERIMENTAL

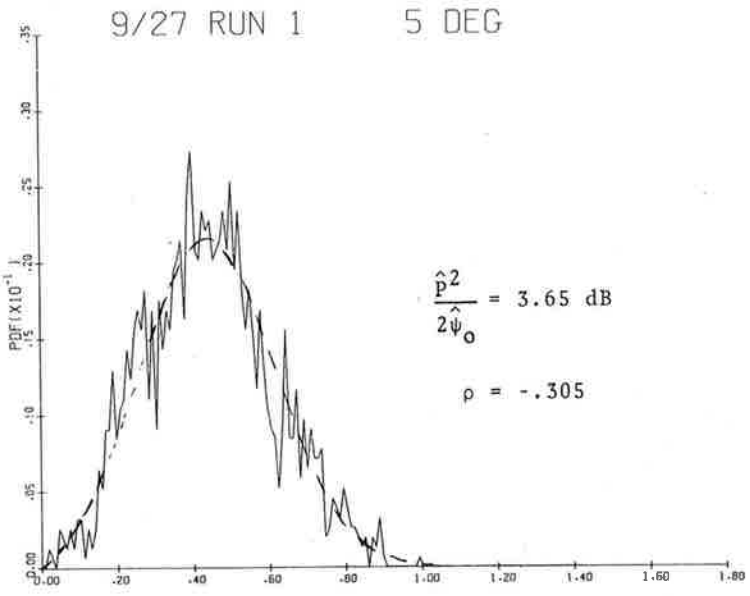

Figure 4-27b RCVR3-IF
ENV2 6 SECS. START=23.57.34
EXPERIMENTAL

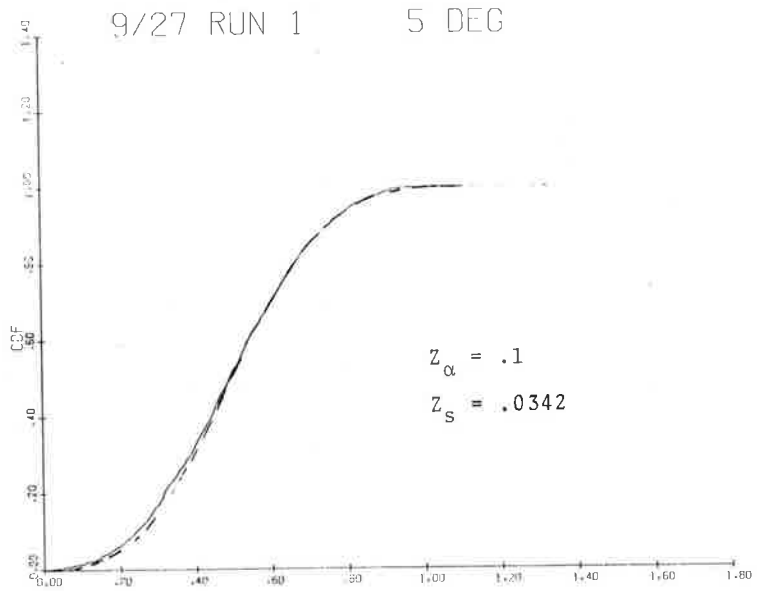

Figure 4-28a RCVR2-IF
ENV2 6 SECS. START=23.57.41
EXPERIMENTAL

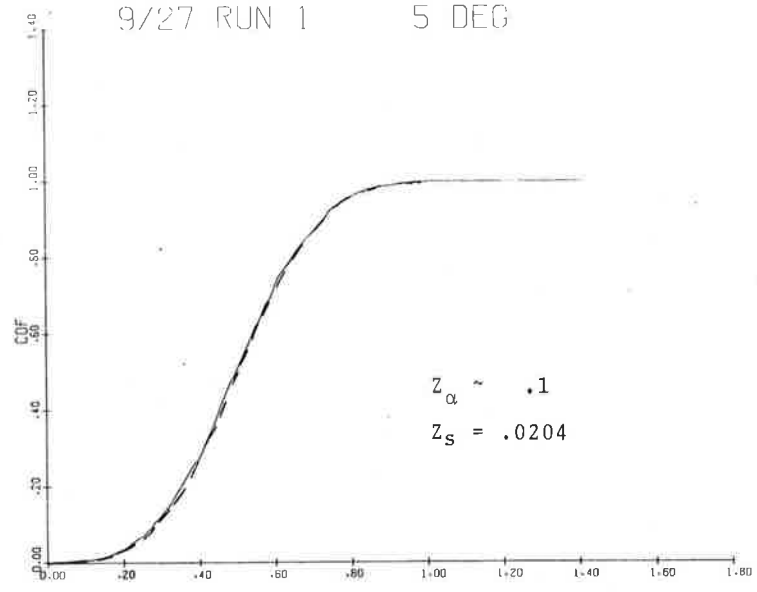

Figure 4-28b RCVR3-IF
ENV2 6 SECS. START=23.57.41
EXPERIMENTAL

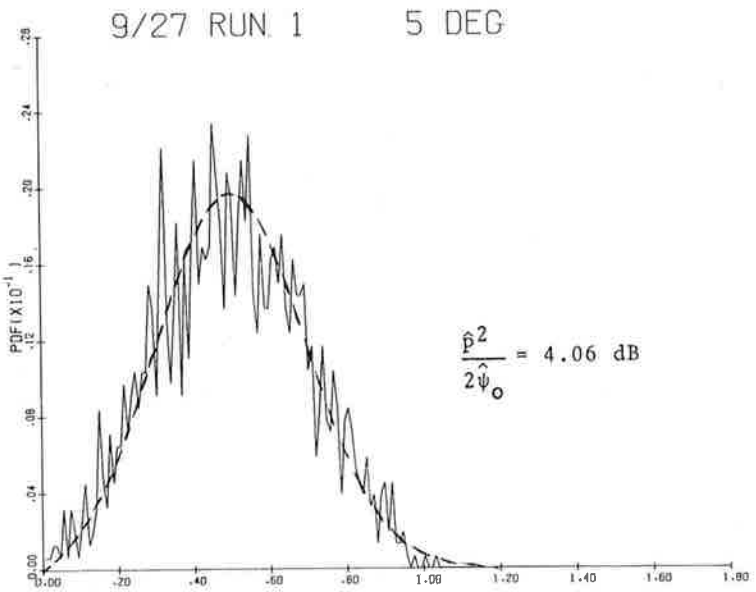

Figure 4-29a RCVR2-IF
ENV2 6 SECS. START=23.57.41
EXPERIMENTAL

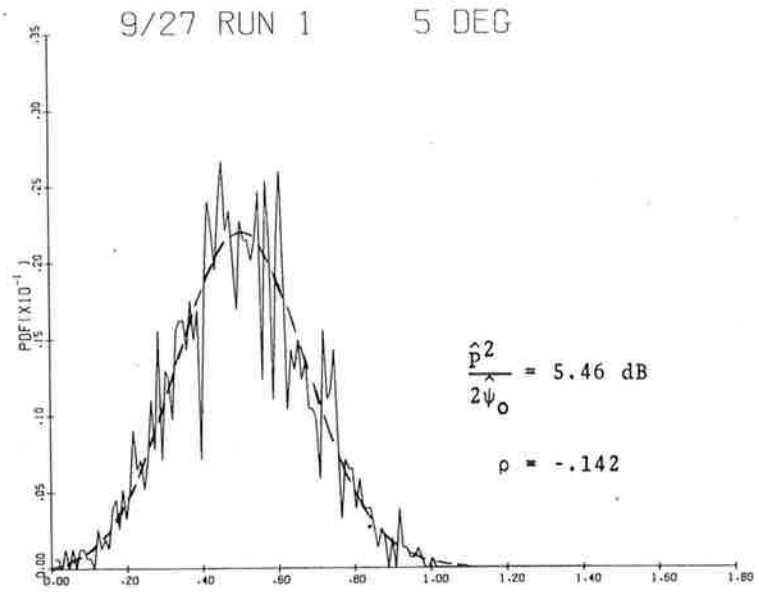

Figure 4-29b RCVR3-IF
ENV2 6 SECS. START=23.57.41
EXPERIMENTAL

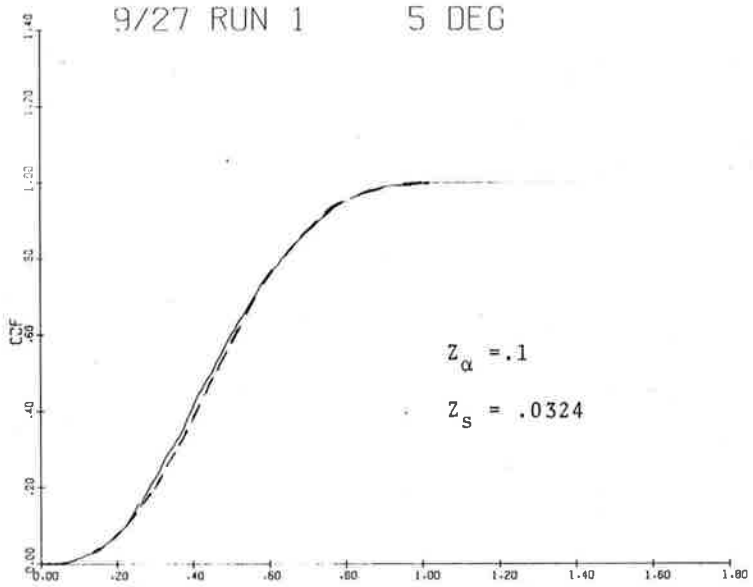

Figure 4-30a RCVR2-IF
ENV2 6 SECS. START=23.57.47
EXPERIMENTAL

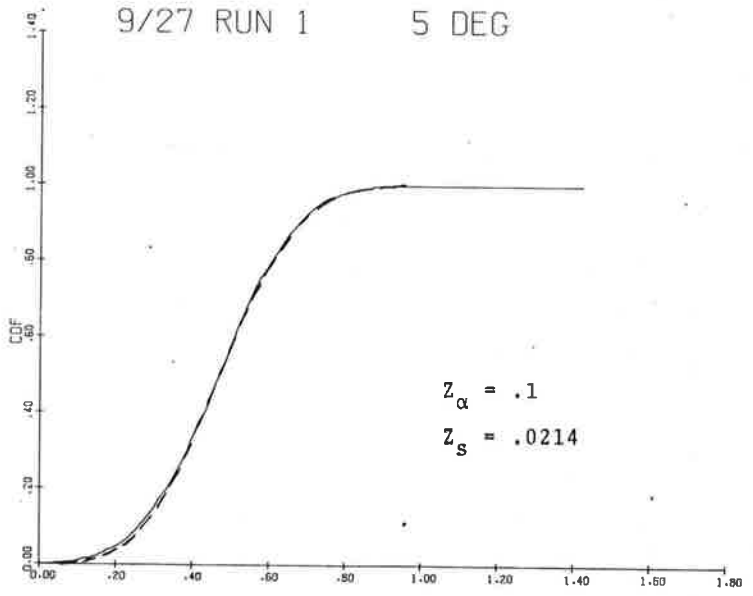

Figure 4-30b RCVR3-IF
ENV2 6 SECS. START=23.57.47
EXPERIMENTAL

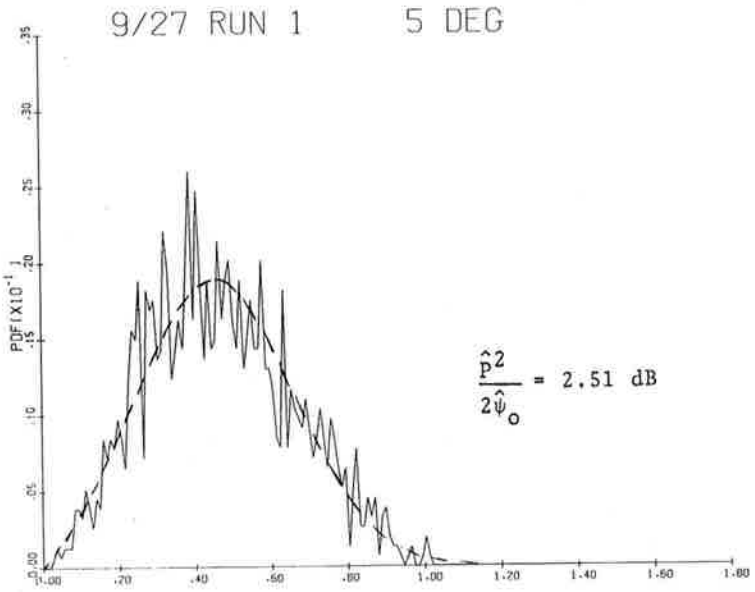

Figure 4-31a RCVR2-IF
ENV2 6 SECS. START=23.57.47
EXPERIMENTAL

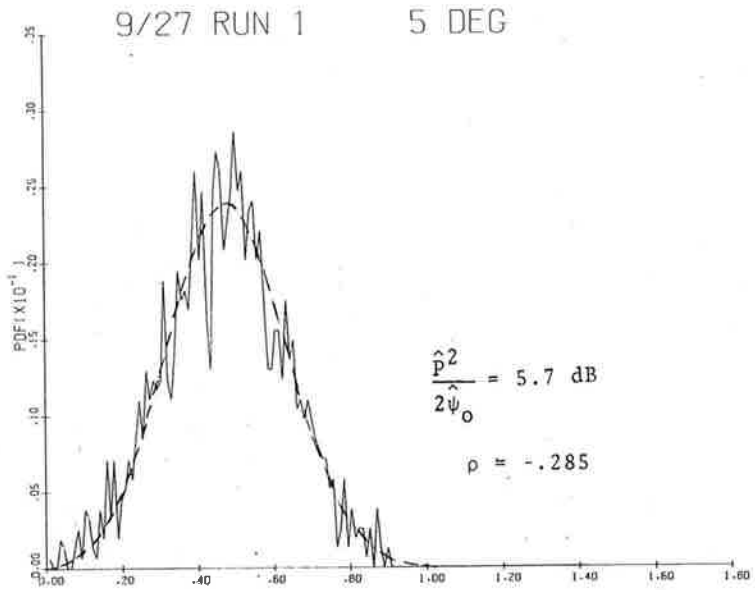

Figure 4-31b RCVR3-IF
ENV2 6 SECS. START=23.57.47
EXPERIMENTAL

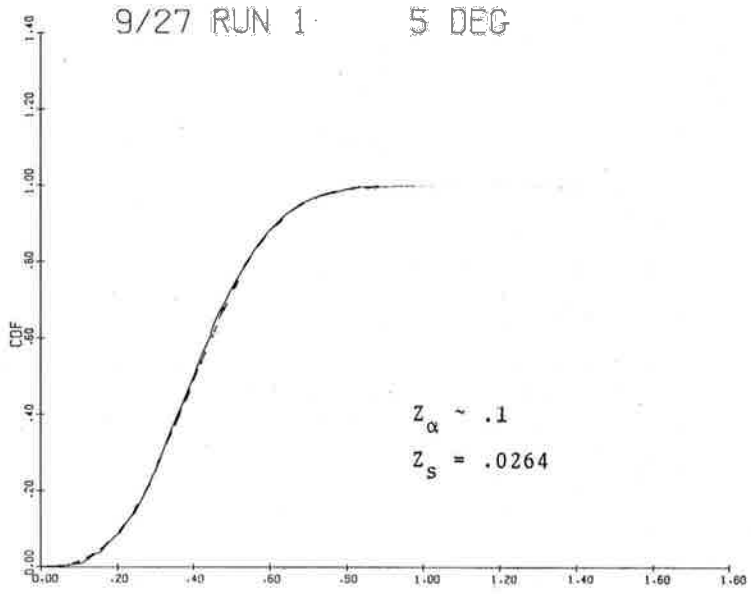

Figure 4-34a RCVR2-IF
ENV2 6 SECS. START=23.57.59
EXPERIMENTAL

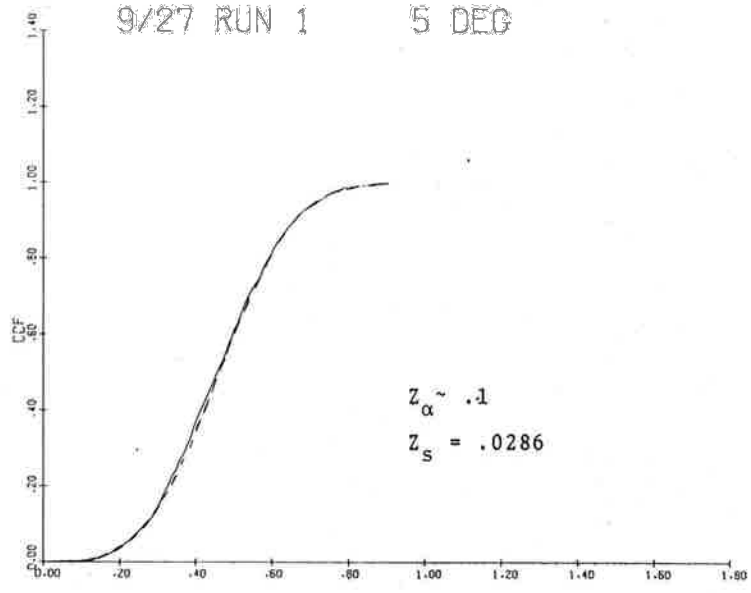

Figure 4-34b RCVR3-IF
ENV2 6 SECS. START=23.57.59
EXPERIMENTAL

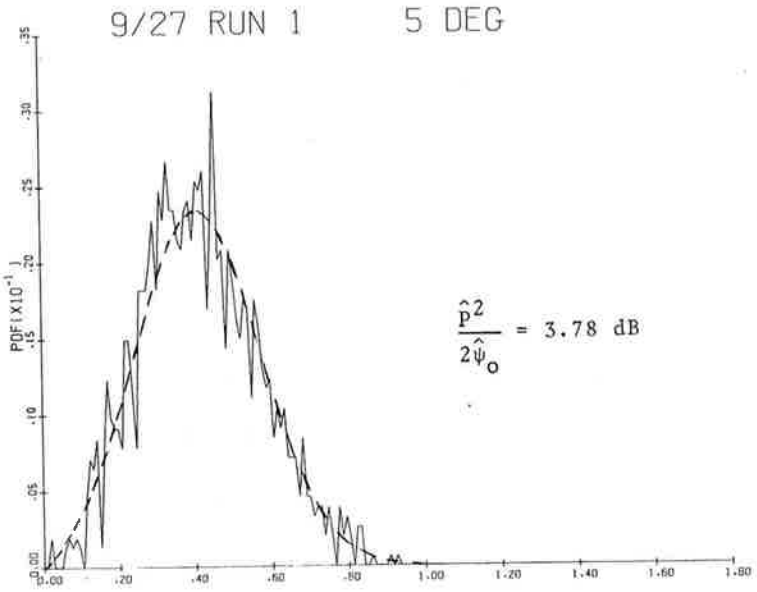

Figure 4-35a RCVR2-IF
ENV2 6 SECS. START=23.57.59
EXPERIMENTAL

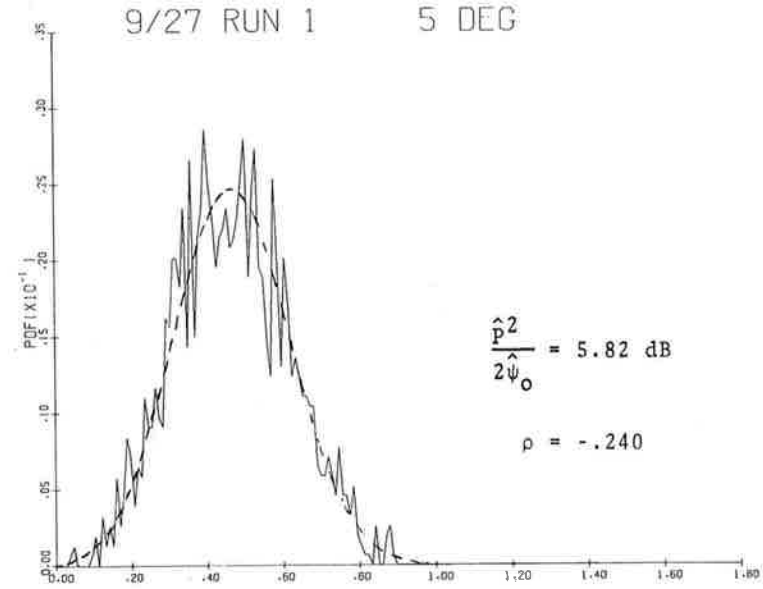

Figure 4-35b RCVR3-IF
ENV2 6 SECS. START=23.57.59
EXPERIMENTAL

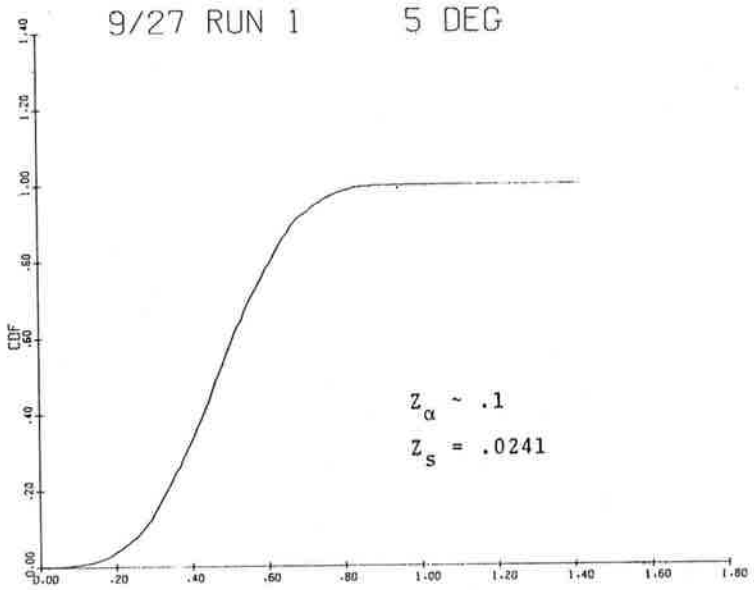

Figure 4-36a RCVR2-IF
ENV2 6 SECS. START=23.58. 5
EXPERIMENTAL

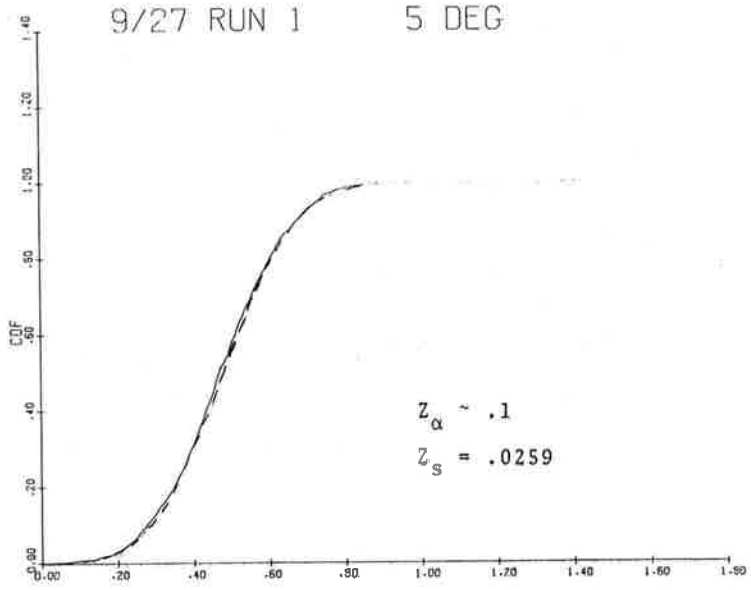

Figure 4-36b RCVR3-IF
ENV2 6 SECS. START=23.58. 5
EXPERIMENTAL

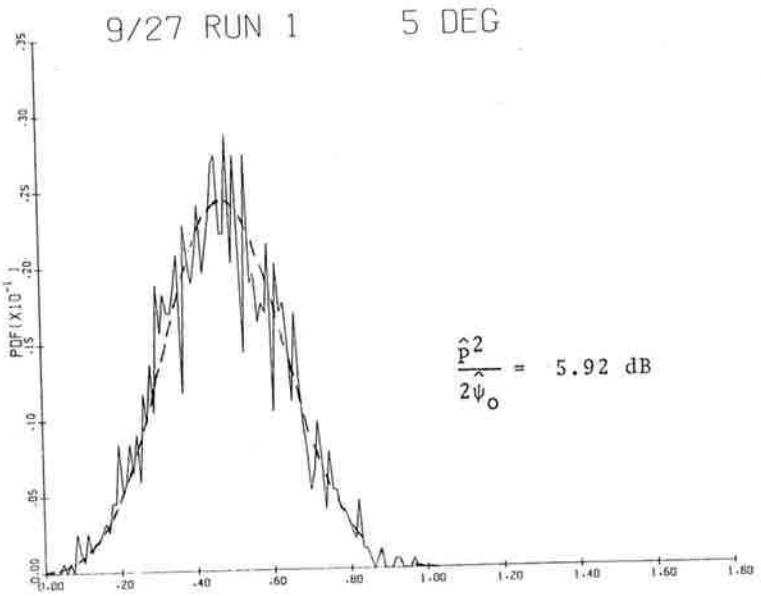

Figure 4-37a RCVR2-IF
ENV2 6 SECS. START=23.58. 5
EXPERIMENTAL

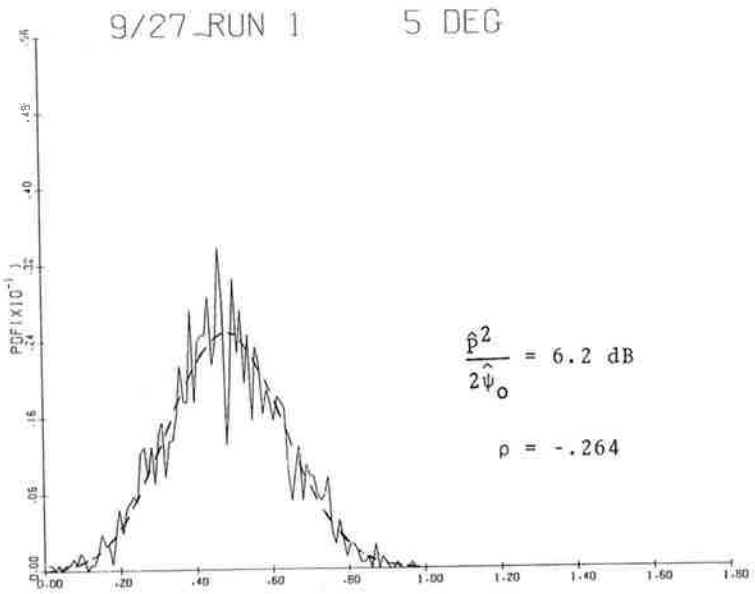

Figure 4-37b RCVR3-IF
ENV2 6 SECS. START=23.58. 5
EXPERIMENTAL

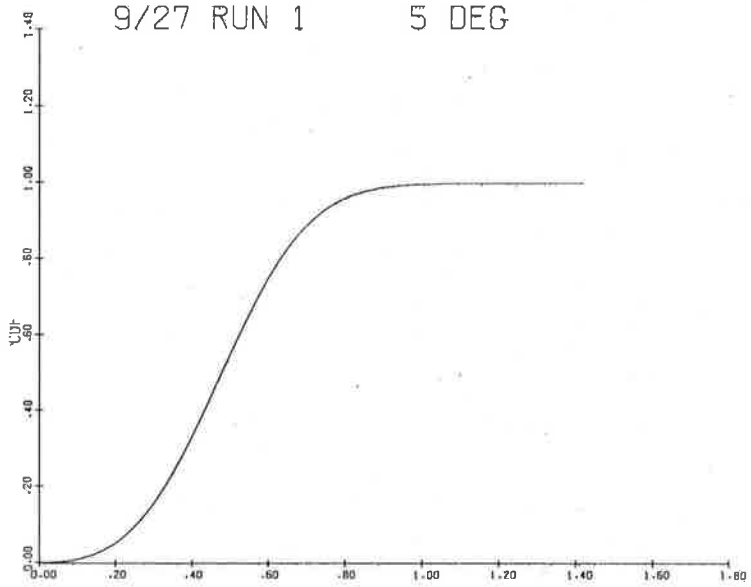

Figure 4-38a RCVR2-IF
ENV2 60 SECS. START=23.57. 9
RICEAN ESTIMATE

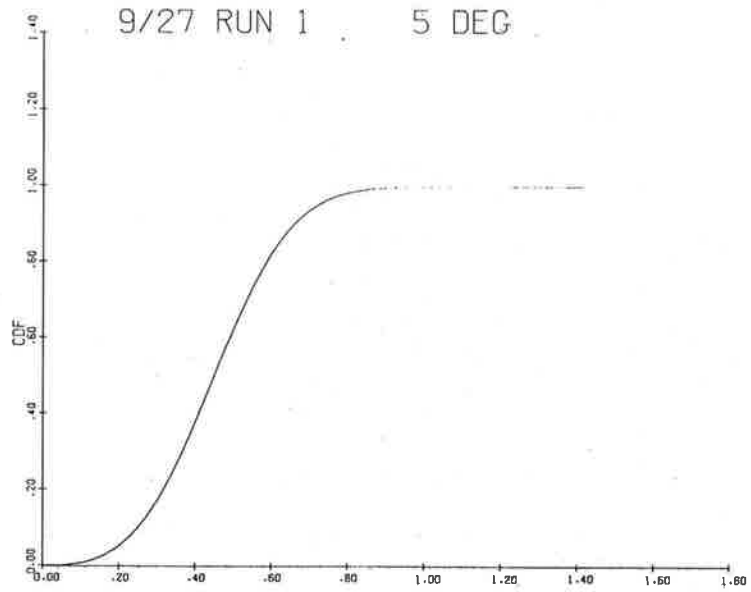

Figure 4-38b RCVR3-IF
ENV2 60 SECS. START=23.57. 9
RICEAN ESTIMATE

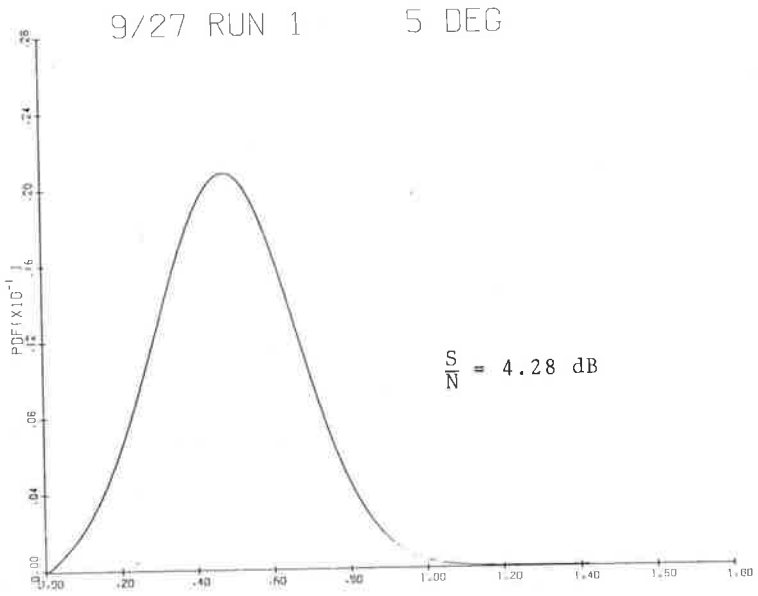

Figure 4-39a RCVR2-IF
ENV2 60 SECS. START=23.57. 9
RICEAN ESTIMATE

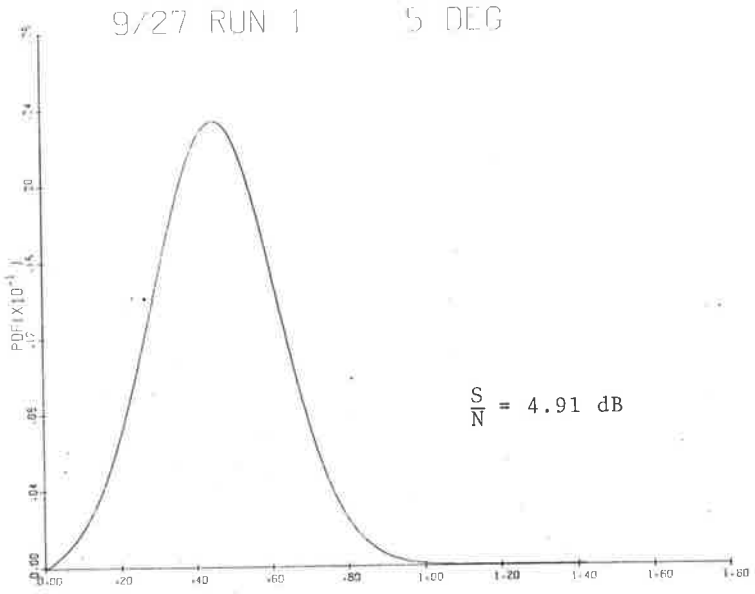

Figure 4-39b RCVR3-IF
ENV2 60 SECS. START=23.57. 9
RICEAN ESTIMATE

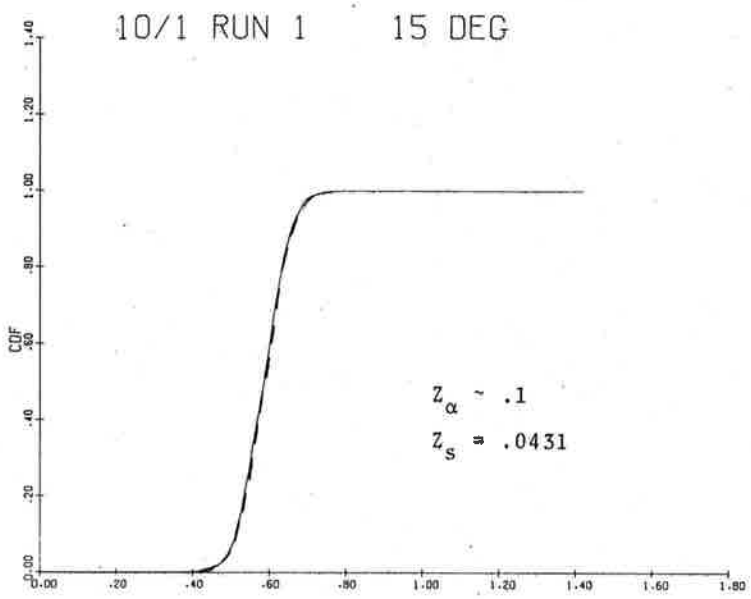

Figure 4-40a RCVR2-IF
ENV2 6 SECS. START= 1.46.32
EXPERIMENTAL

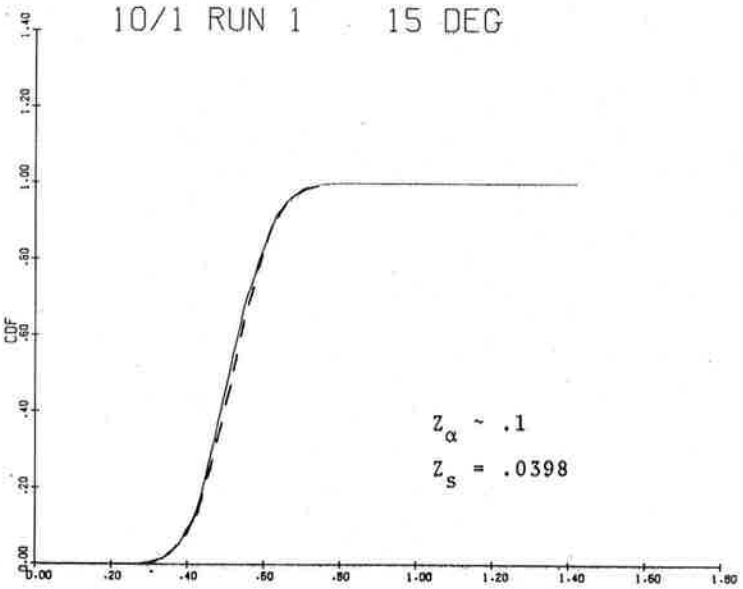

Figure 4-40b RCVR3-IF
ENV2 6 SECS. START= 1.46.32
EXPERIMENTAL

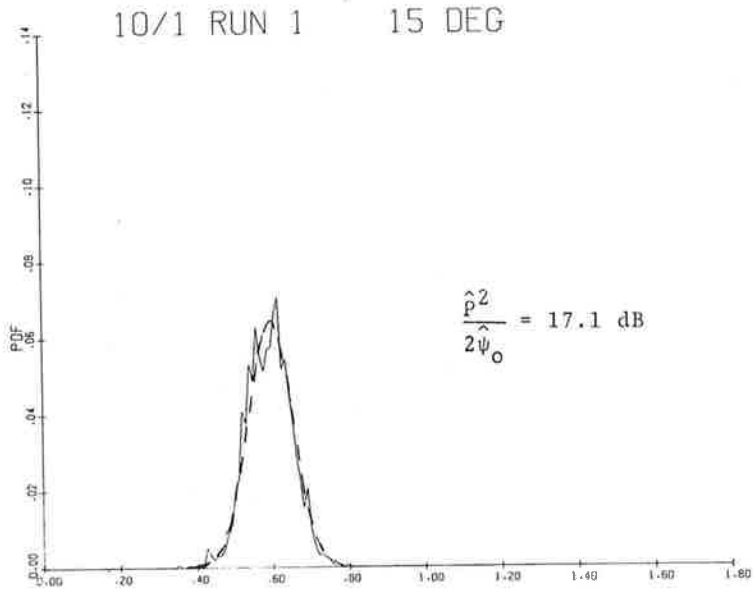

Figure 4-41a RCVR2-IF
ENV2 6 SECS. START= 1.46.32
EXPERIMENTAL

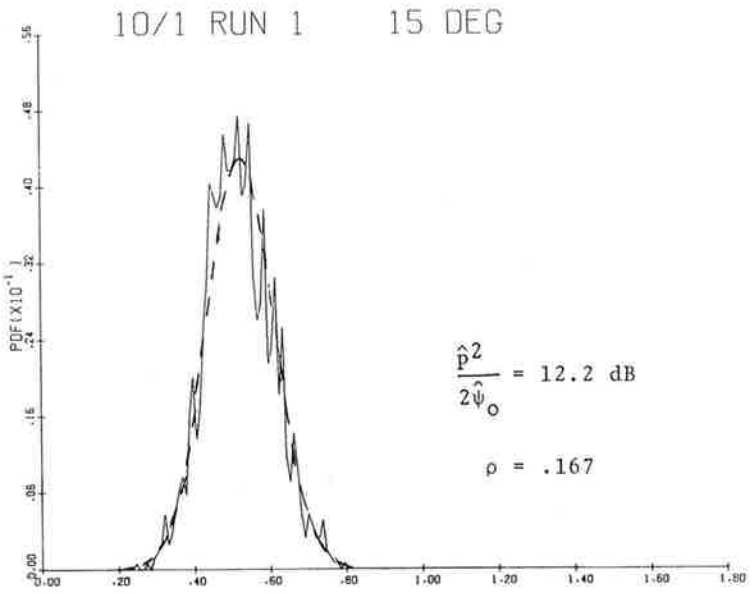

Figure 4-41b RCVR3-IF
ENV2 6 SECS. START= 1.46.32
EXPERIMENTAL

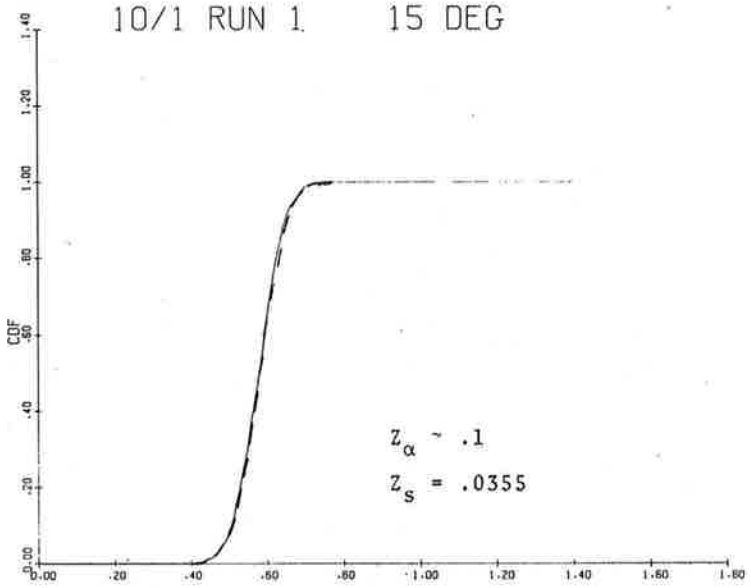

Figure 4-42a RCVR2-IF
ENV2 6 SECS. START= 1.46.38
EXPERIMENTAL

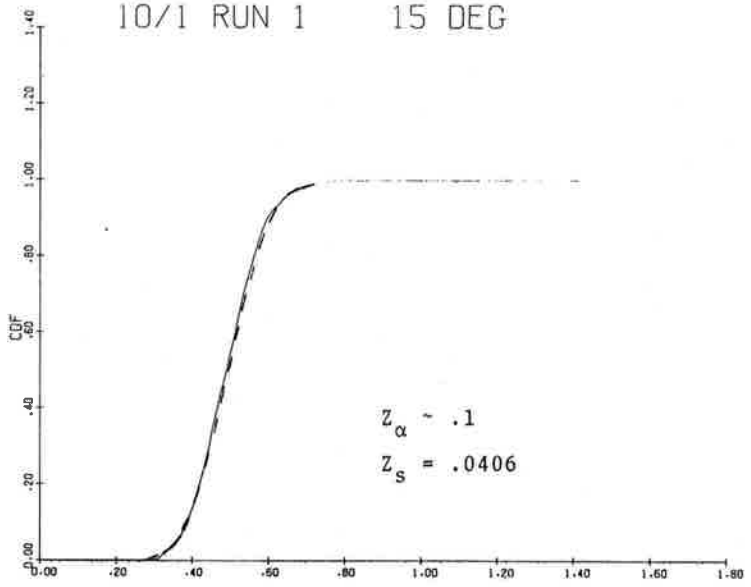

Figure 4-42b RCVR3-IF
ENV2 6 SECS. START= 1.46.38
EXPERIMENTAL

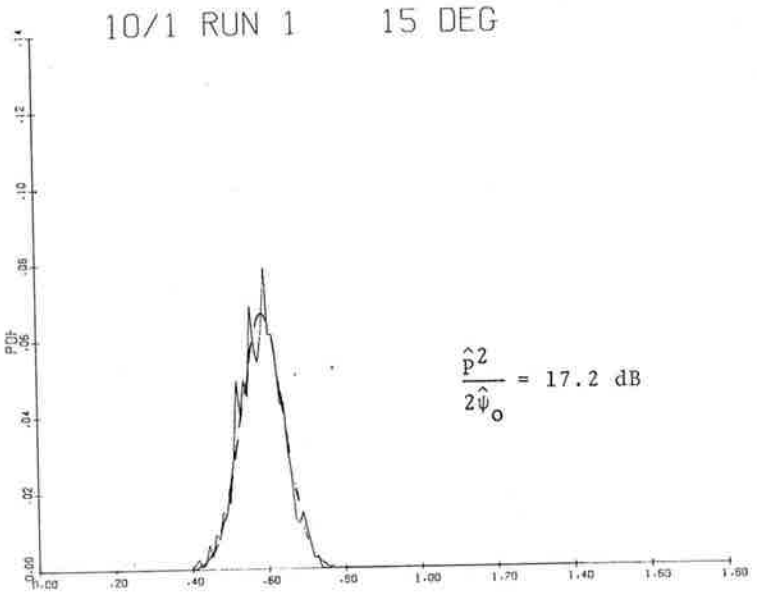

Figure 4-43a RCVR2-IF
ENV2 6 SECS. START= 1.46.38
EXPERIMENTAL

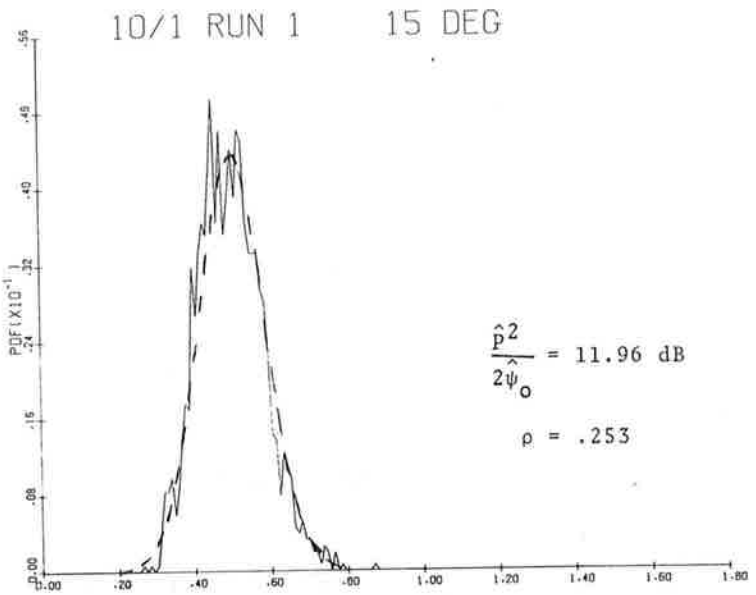

Figure 4-43b RCVR3-IF
ENV2 6 SECS. START= 1.46.38
EXPERIMENTAL

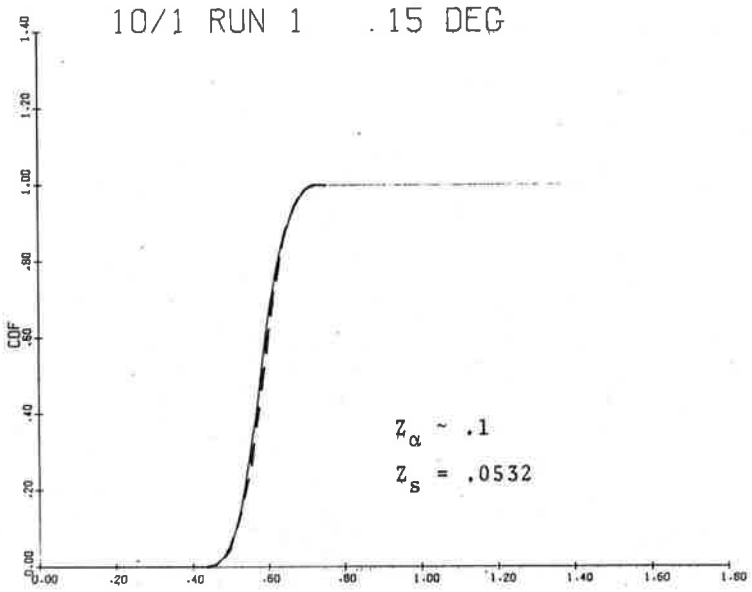

Figure 4-44a RCVR2-IF
ENV2 6 SECS. START= 1.46.44
EXPERIMENTAL

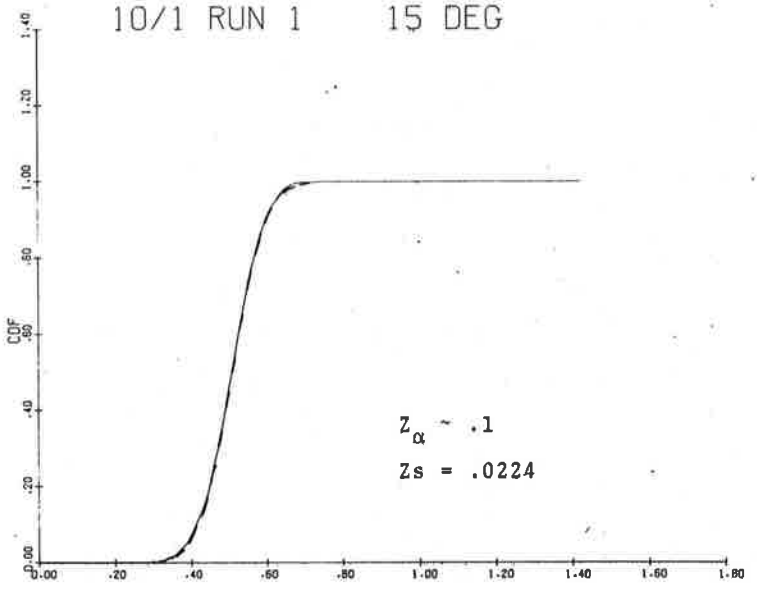

Figure 4-44b RCVR3-IF
ENV2 6 SECS. START= 1.46.44
EXPERIMENTAL

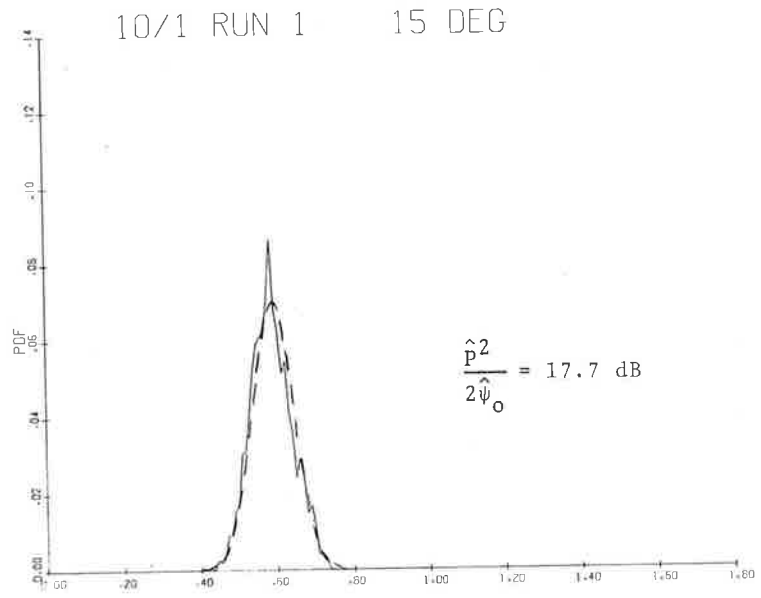

Figure 4-45a RCVR2-IF
ENV2 6 SECS. START= 1.46.44
EXPERIMENTAL

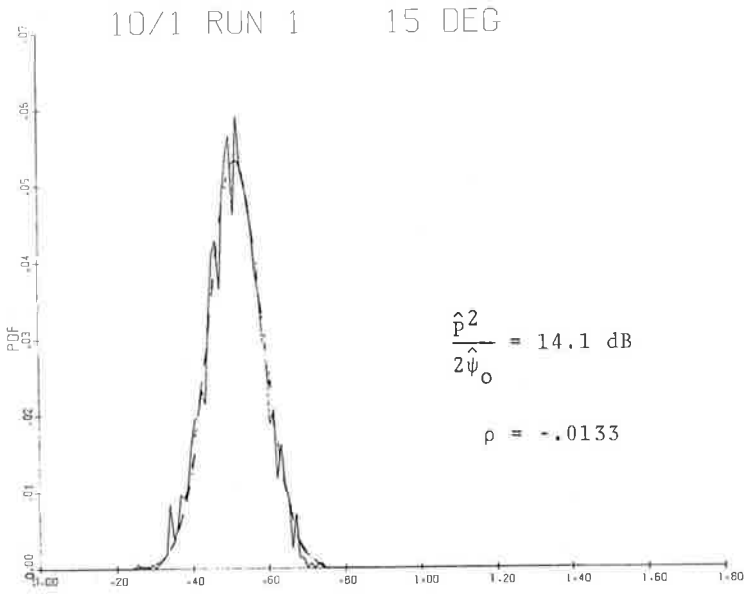

Figure 4-45b RCVR3-IF
ENV2 6 SECS. START= 1.46.44
EXPERIMENTAL

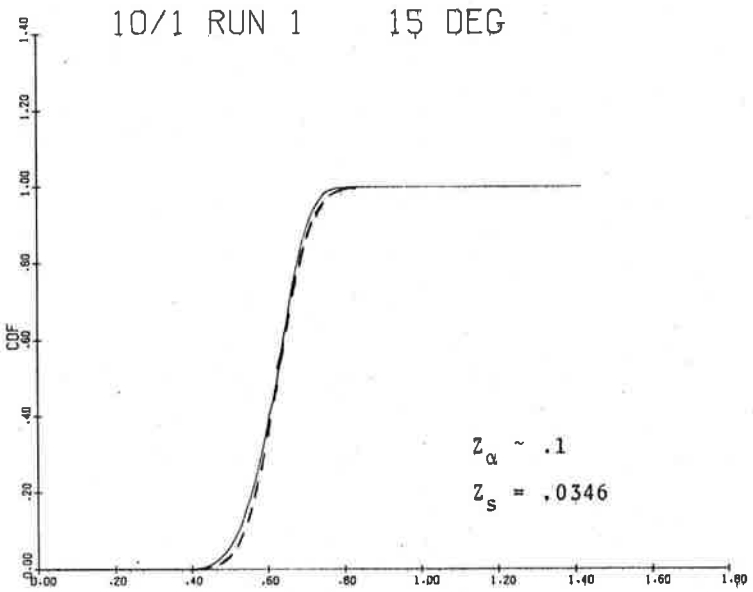

Figure 4-52a RCVR2-IF
ENV2 6 SECS. START= 1.47.15
EXPERIMENTAL

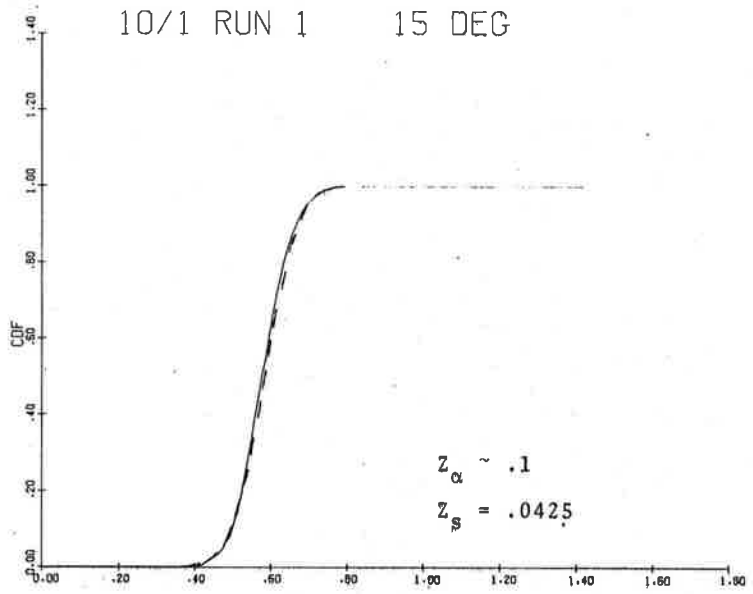

Figure 4-52b RCVR3-IF
ENV2 6 SECS. START= 1.47.15
EXPERIMENTAL

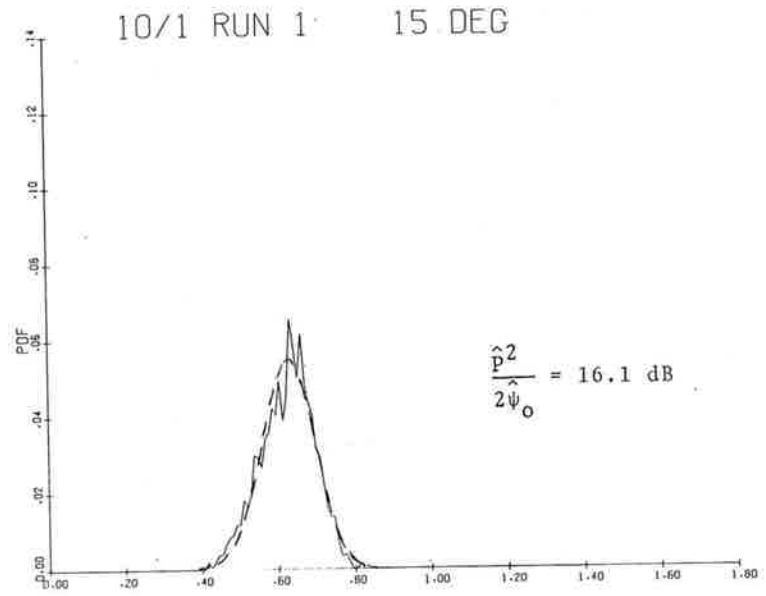

Figure 4-53a RCVR2-IF
ENV2 6 SECS. START= 1.47.15
EXPERIMENTAL

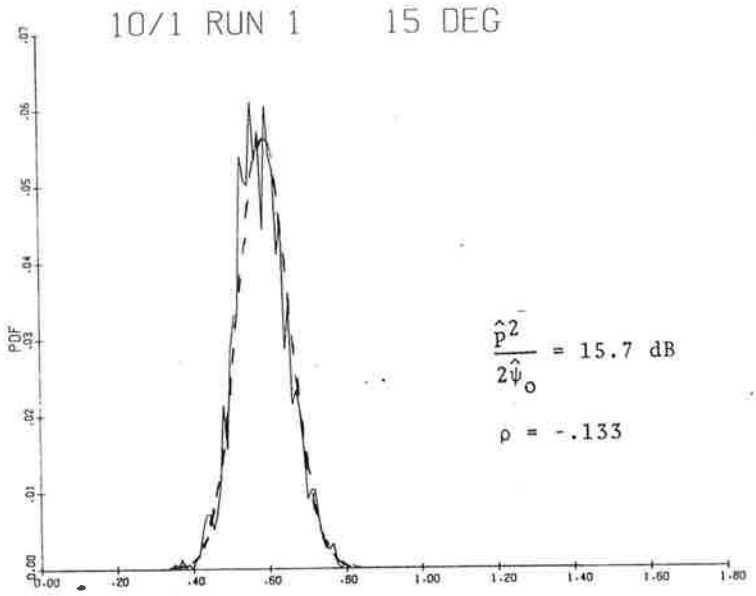

Figure 4-53b RCVR3-IF
ENV2 6 SECS. START= 1.47.15
EXPERIMENTAL

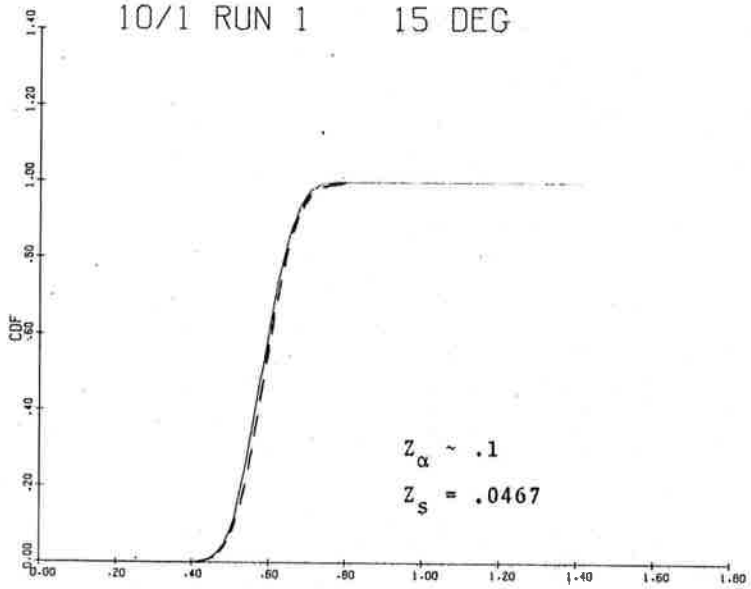

Figure 4-54a RCVR2-IF
ENV2 6 SECS. START= 1.47.21
EXPERIMENTAL

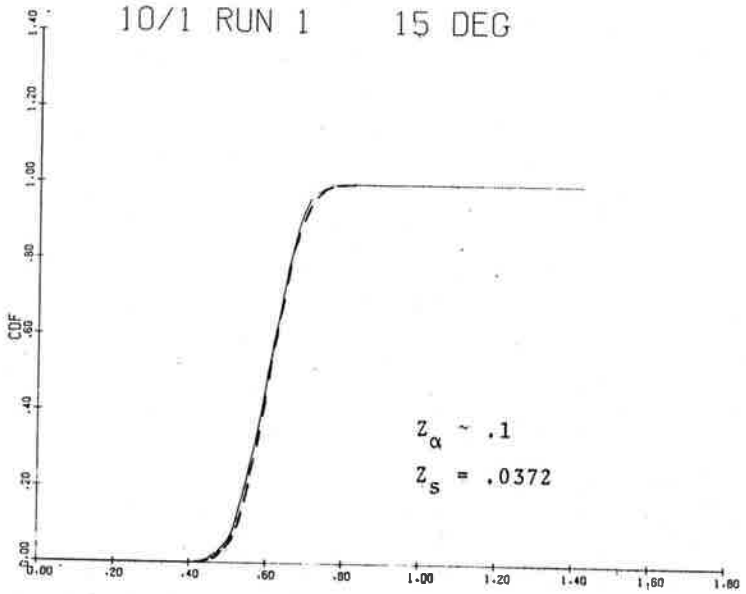

Figure 4-54b RCVR3-IF
ENV2 6 SECS. START= 1.47.21
EXPERIMENTAL

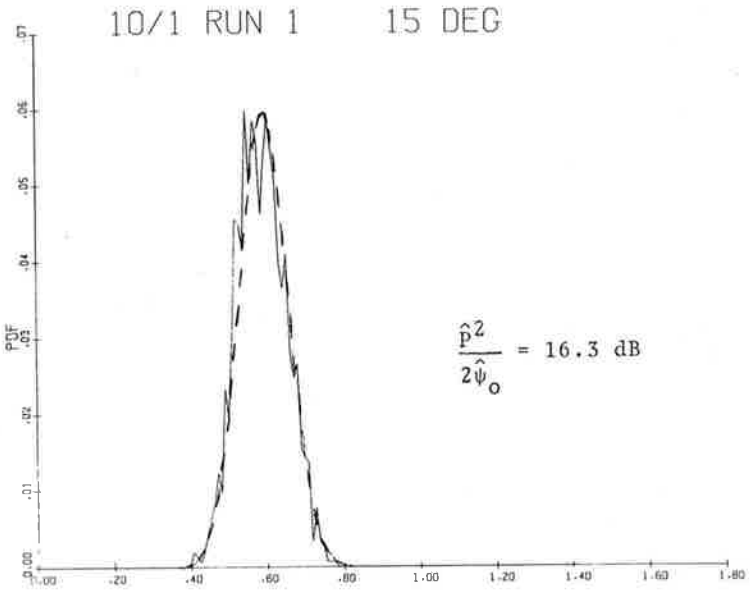

Figure 4-55a RCVR2-IF
ENV2 6 SECS. START= 1.47.21
EXPERIMENTAL

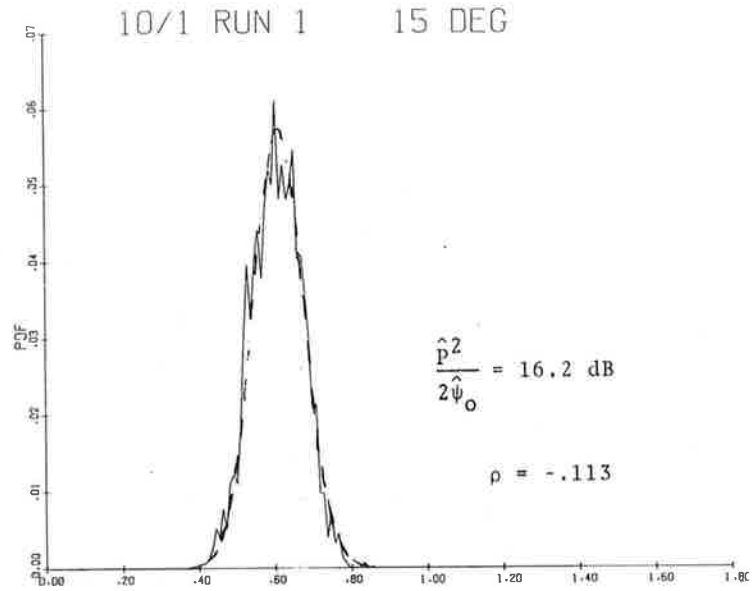

Figure 4-55b RCVR3-IF
ENV2 6 SECS. START= 1.47.21
EXPERIMENTAL

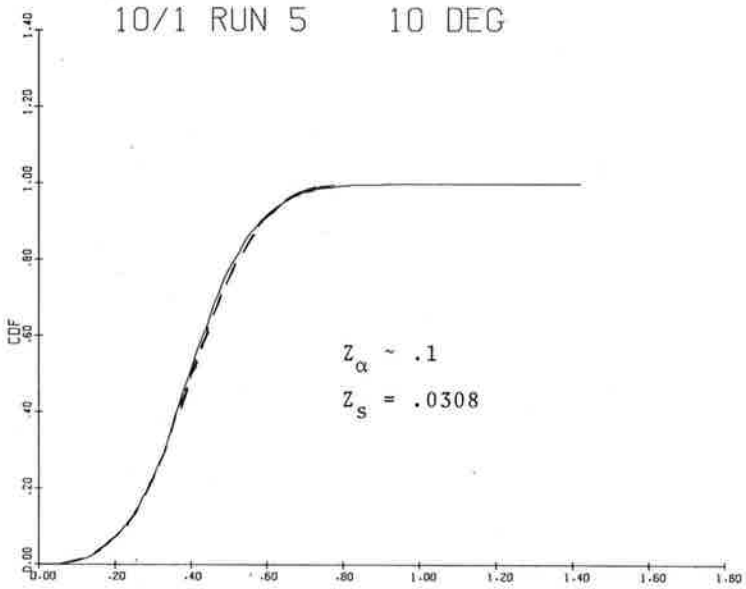

Figure 4-60a RCVR2-IF
ENV2 6 SECS. START=32.54.38
EXPERIMENTAL

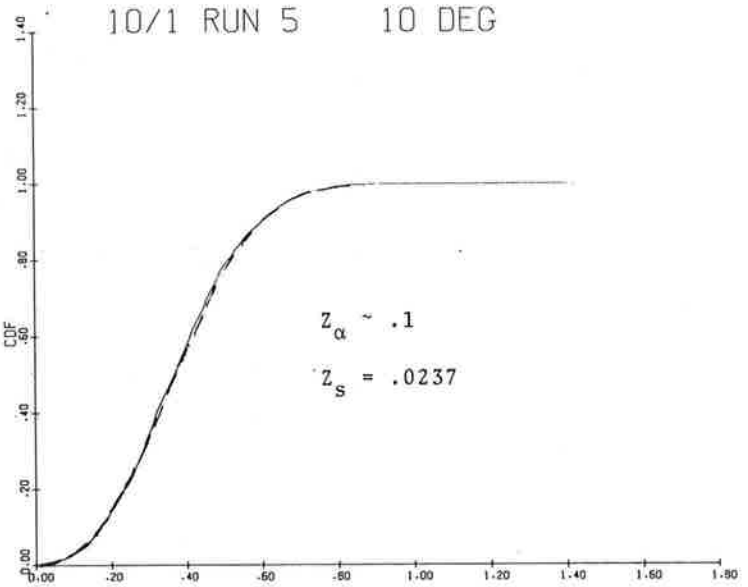

Figure 4-60b RCVR3-IF
ENV2 6 SECS. START=32.54.38
EXPERIMENTAL

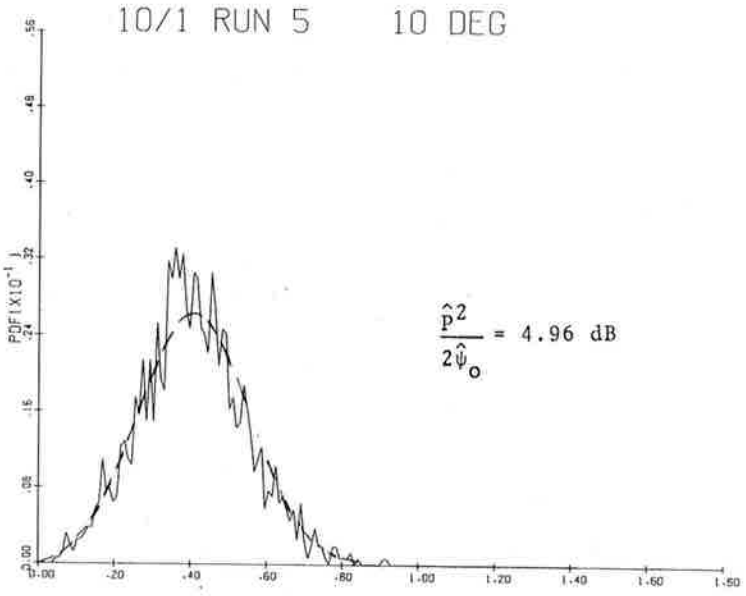

Figure 4-61a RCVR2-IF
ENV2 6 SECS. START=32.54.38
EXPERIMENTAL

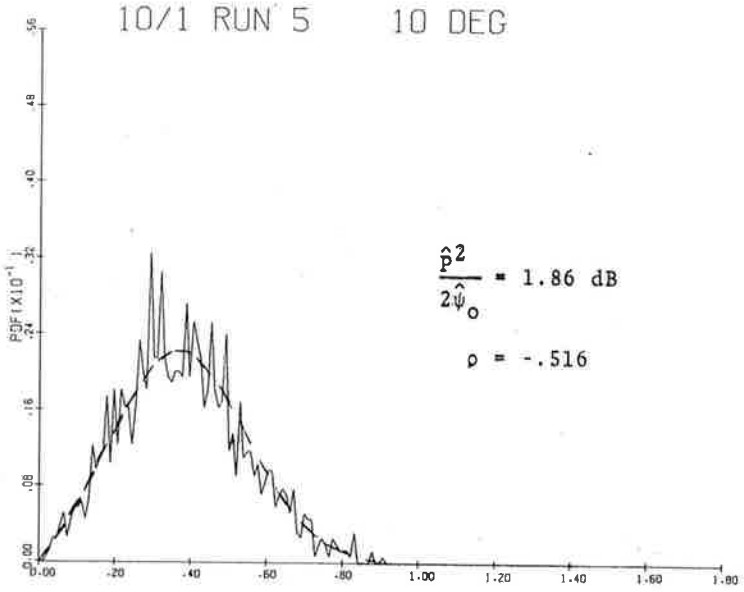

Figure 4-61b RCVR3-IF
ENV2 6 SECS. START=32.54.38
EXPERIMENTAL

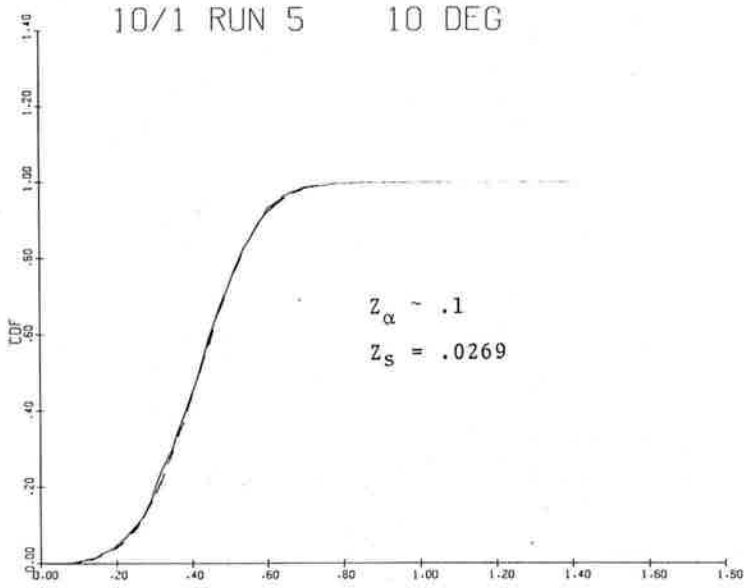

Figure 4-62a RCVR2-IF
ENV2 6 SECS. START=32.54.44
EXPERIMENTAL

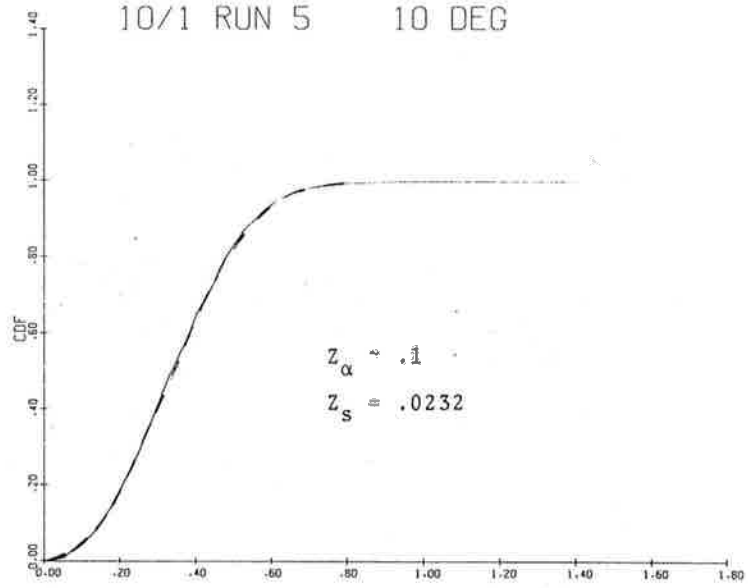

Figure 4-62b RCVR3-IF
ENV2 6 SECS. START=32.54.44
EXPERIMENTAL

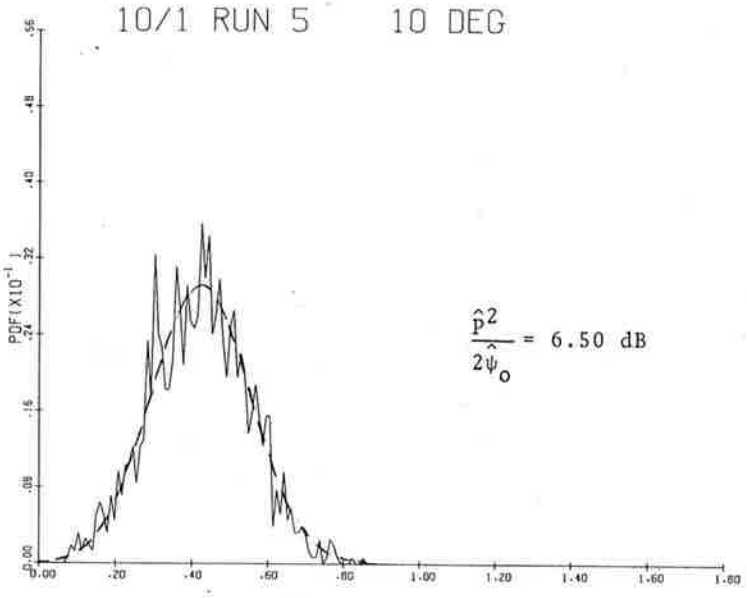

Figure 4-63a RCVR2-IF
ENV2 6 SECS. START=32.54.44
EXPERIMENTAL

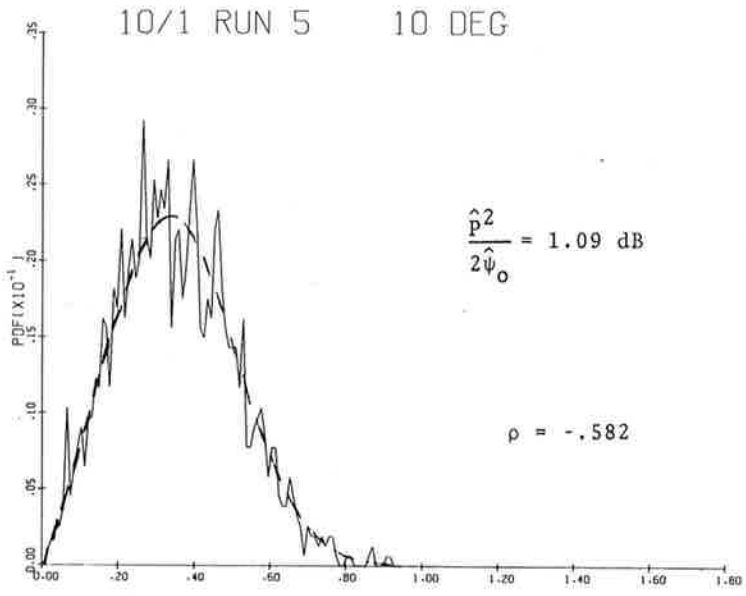

Figure 4-63b RCVR3-IF
ENV2 6 SECS. START=32.54.44
EXPERIMENTAL

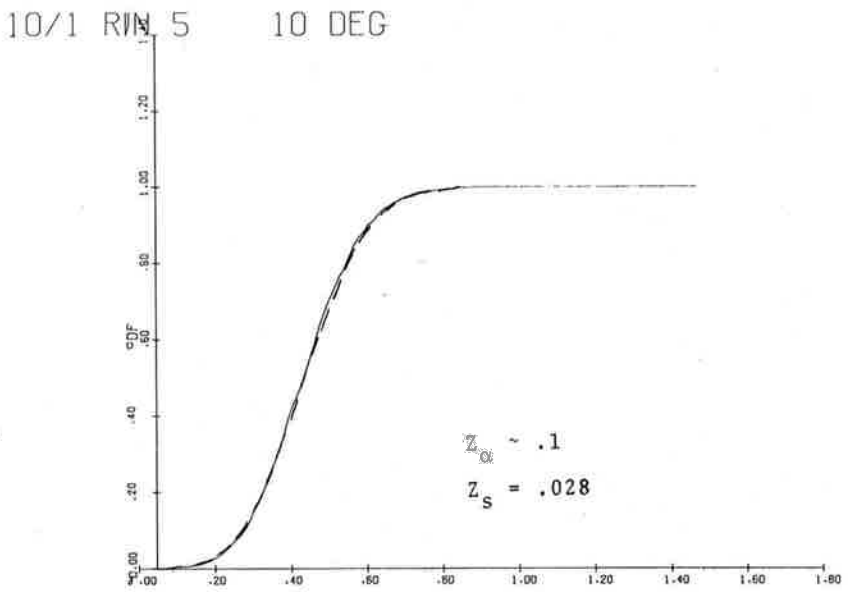

Figure 4-66a RCVR2-IF
ENV2 6 SECS. START=32.54.57
EXPERIMENTAL

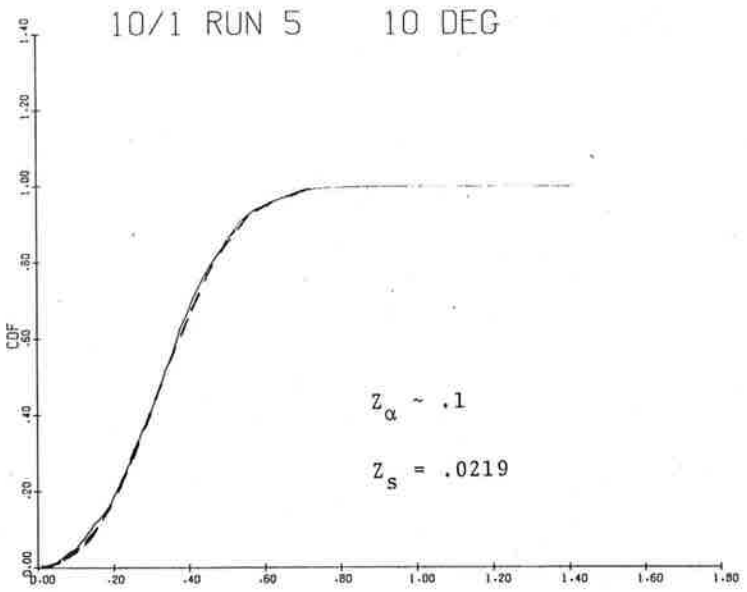

Figure 4-66b RCVR3-IF
ENV2 6 SECS. START=32.54.57
EXPERIMENTAL

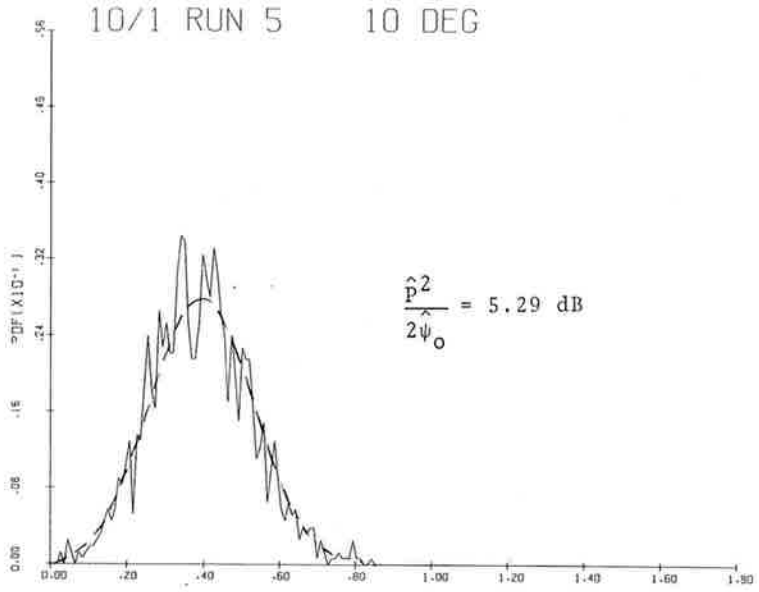

Figure 4-67a RCVR2-IF
ENV26 SECS. START=32.54.57
XPERIMENTAL

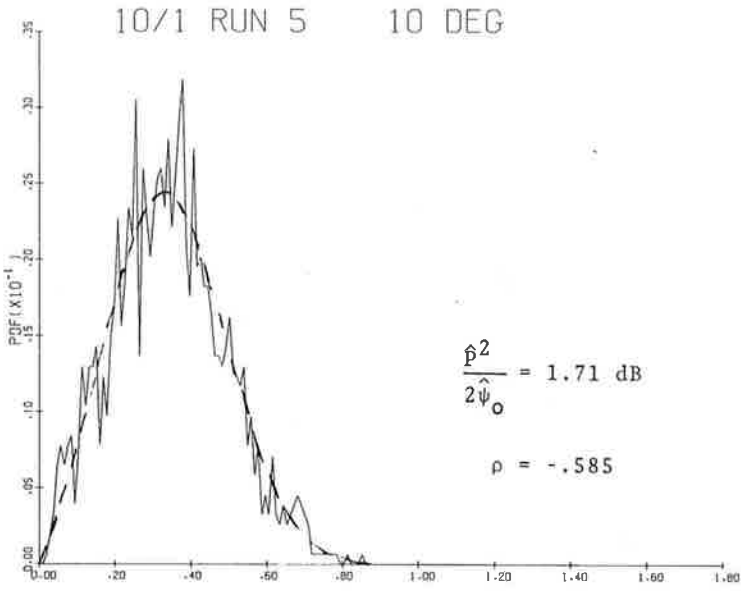

Figure 4-67b RCVR3-IF
ENV2 6 SECS. START=32.54.57
EXPERIMENTAL

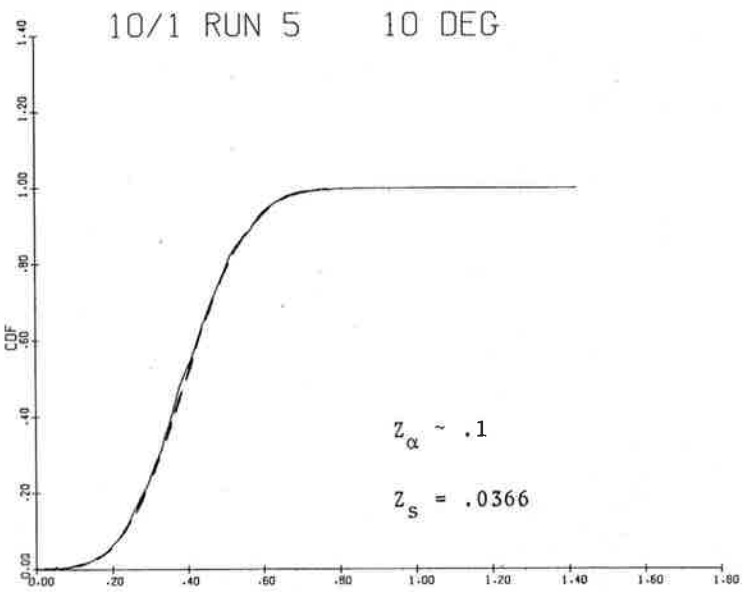

Figure 4-68a RCVR2-IF
ENV2 6 SECS. START=32.55. 4
EXPERIMENTAL

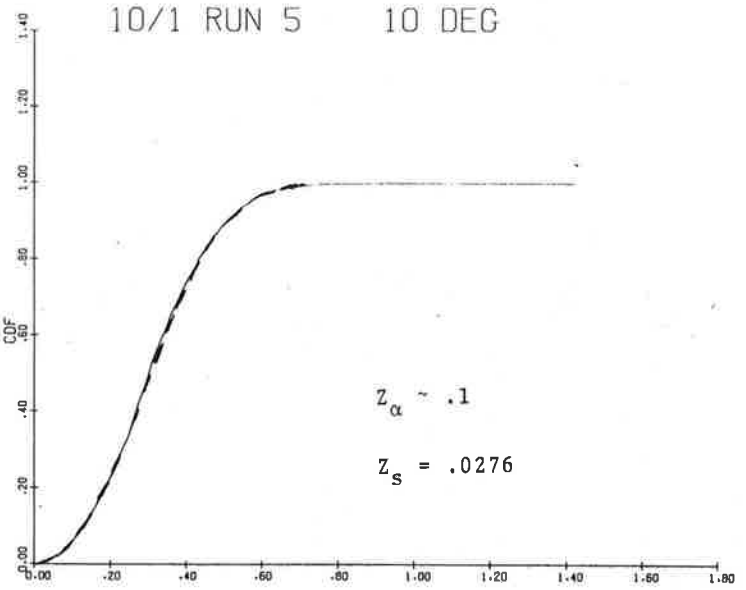

Figure 4-68b RCVR3-IF
ENV2 6 SECS. START=32.55. 4
EXPERIMENTAL

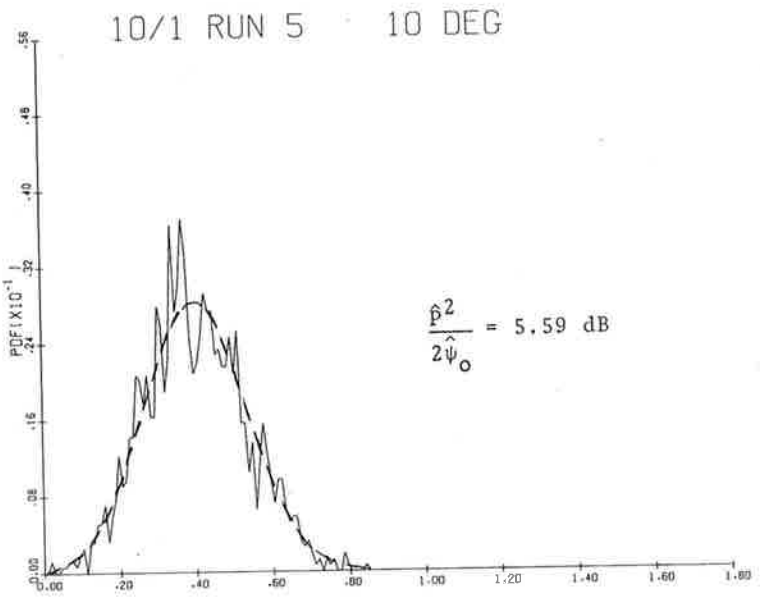

Figure 4-69a RCVR2-IF
ENV2 6 SECS. START=32.55. 4
EXPERIMENTAL

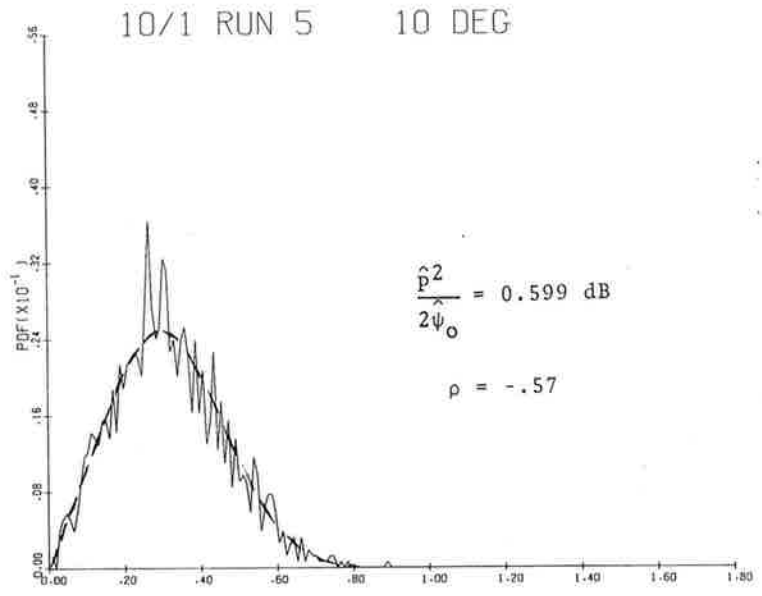

Figure 4-69b RCVR3-IF
ENV2 6 SECS. START=32.55. 4
EXPERIMENTAL

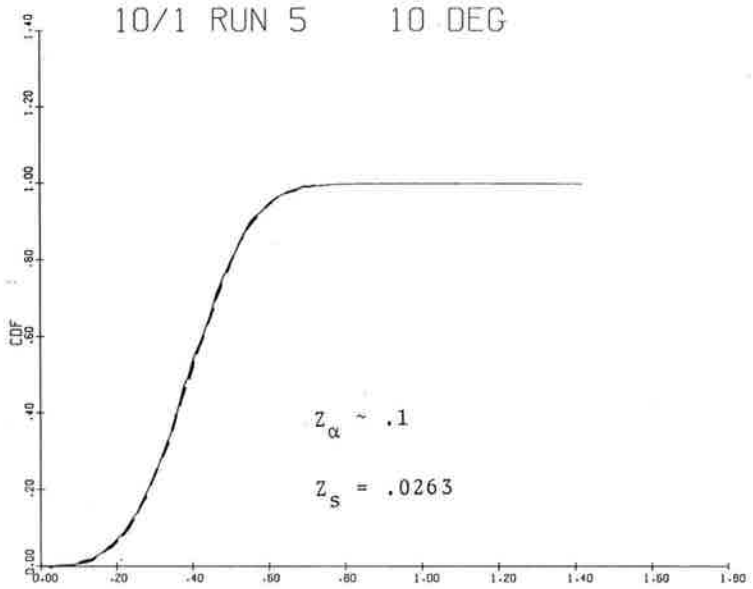

Figure 4-70a RCVR2-IF
ENV2 6 SECS. START=32.55.11
EXPERIMENTAL

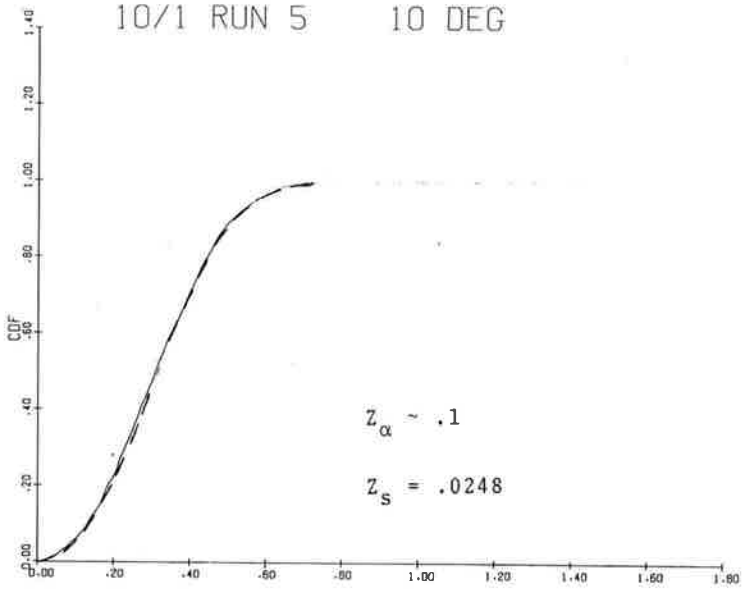

Figure 4-70b RCVR3-IF
ENV2 6 SECS. START=32.55.11
EXPERIMENTAL

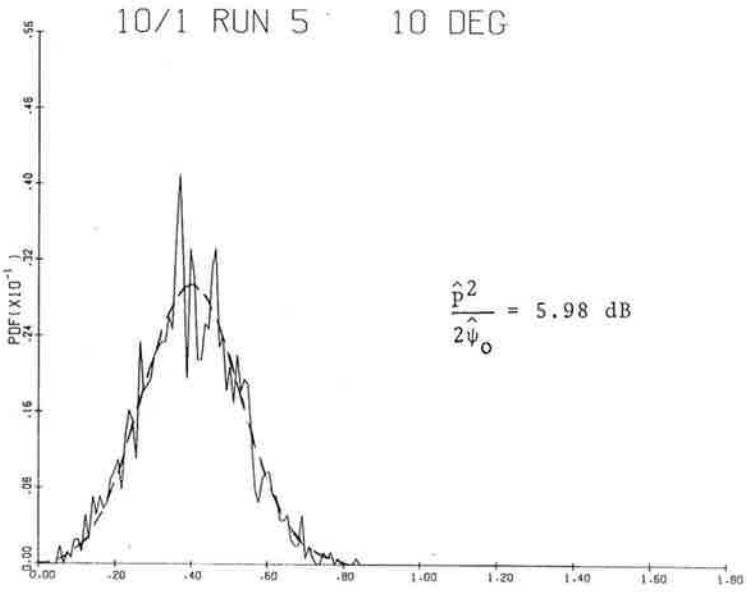

Figure 4-71a RCVR2-IF
ENV2 6 SECS. START=32.55.11
EXPERIMENTAL

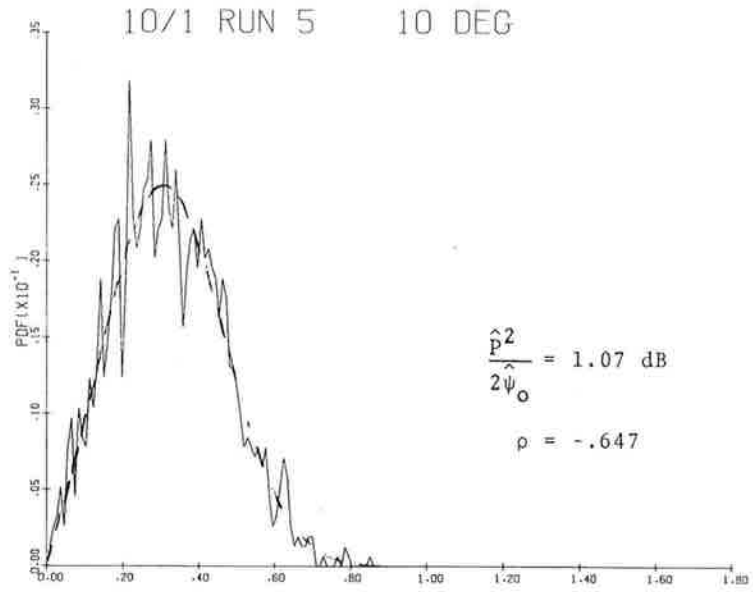

Figure 4-71b RCVR3-IF
ENV2 6 SECS. START=32.55.11
EXPERIMENTAL

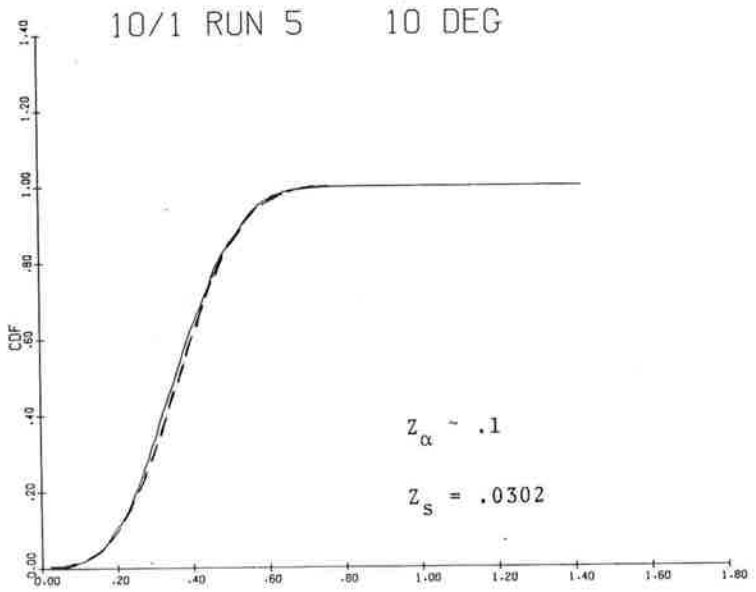

Figure 4-72a RCVR2-IF
ENV2 6 SECS. START=32.55.18
EXPERIMENTAL

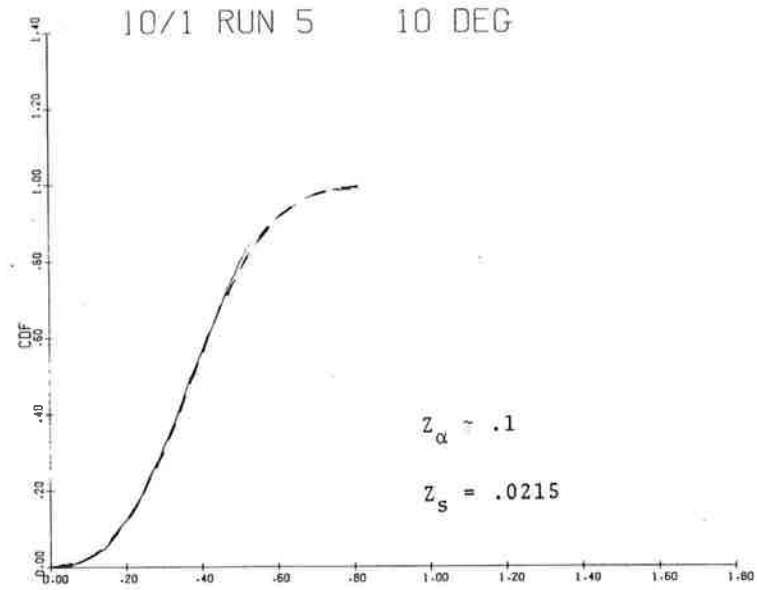

Figure 4-72b RCVR3-IF
ENV2 6 SECS. START=32.55.18
EXPERIMENTAL

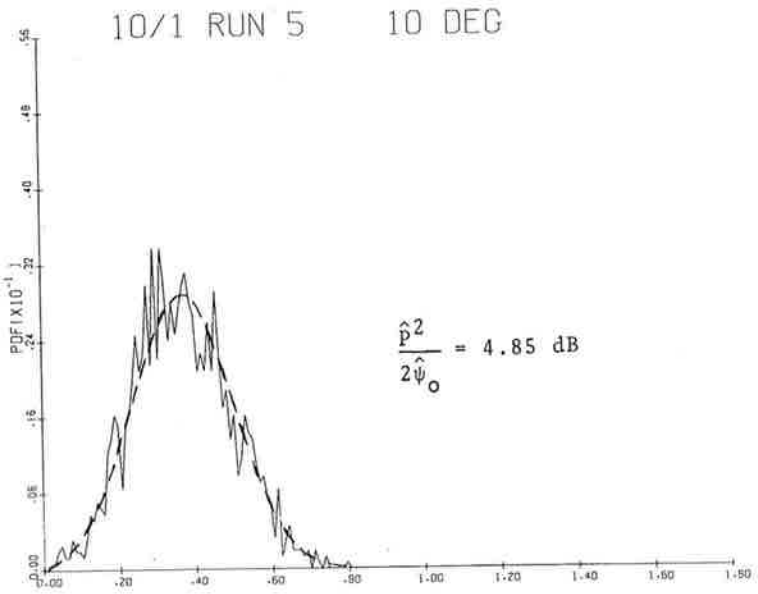

Figure 4-73a RCVR2-IF
ENV2 6 SECS. START=32.55.18
EXPERIMENTAL

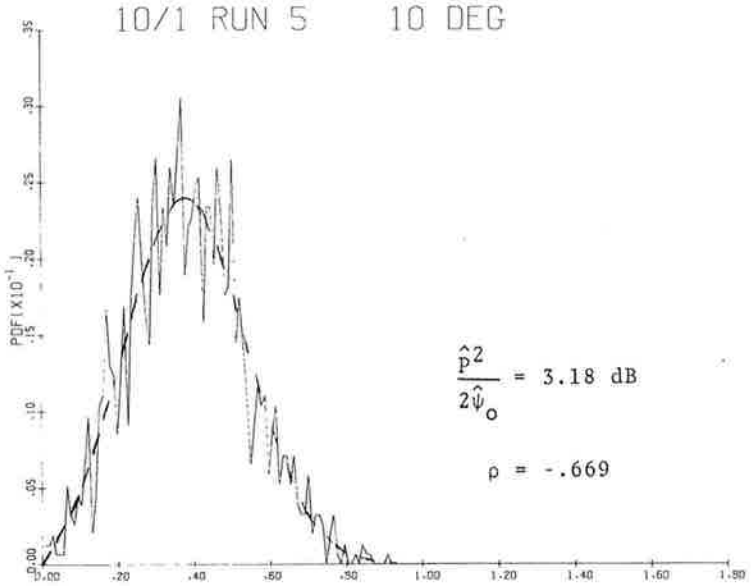

Figure 4-73b RCVR3-IF
ENV2 6 SECS. START=32.55.18
EXPERIMENTAL

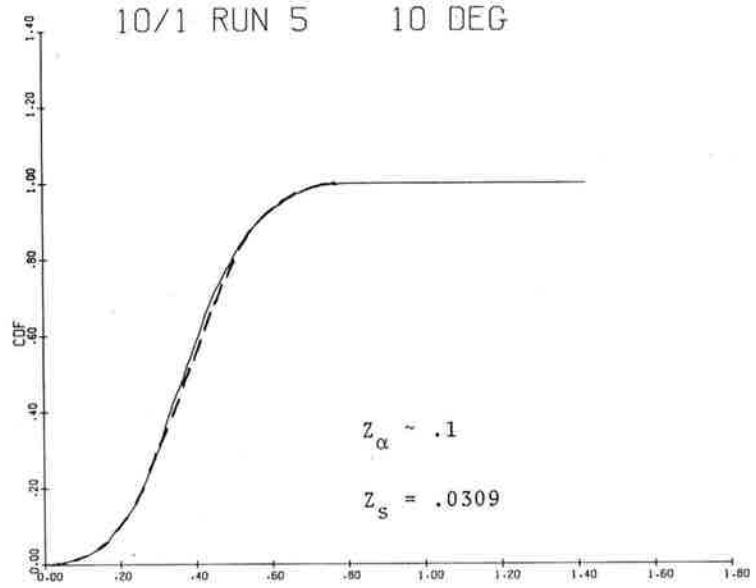

Figure 4-74a RCVR2-IF
ENV2 6 SECS. START=32.55.26
EXPERIMENTAL

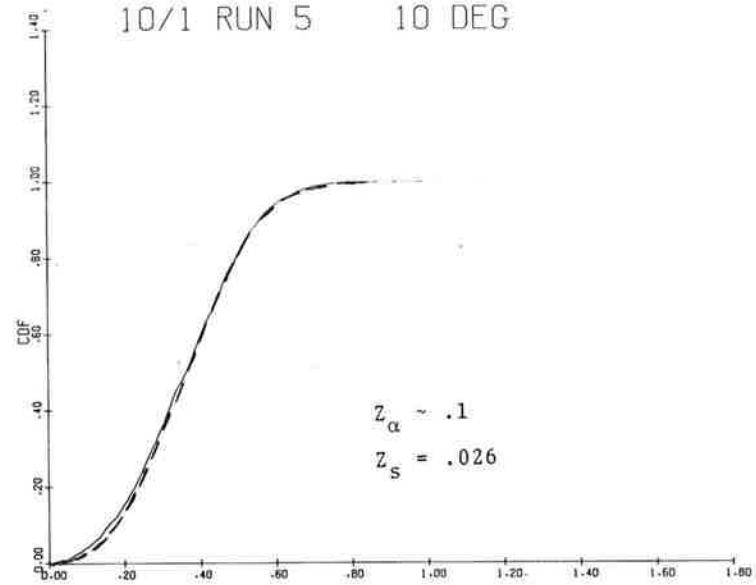

Figure 4-74b RCVR3-IF
ENV2 6 SECS. START=32.55.26
EXPERIMENTAL

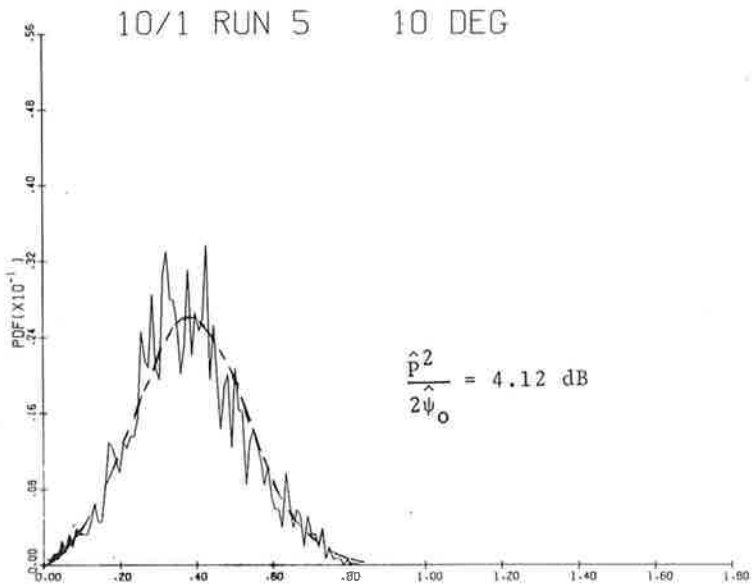

Figure 4-75a RCVR2-IF
ENV2 6 SECS. START=32.55.26
EXPERIMENTAL

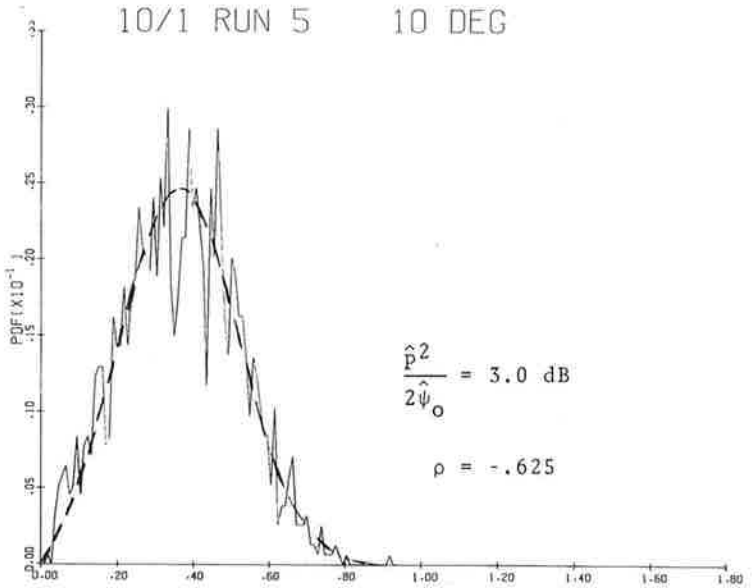

Figure 4-75b RCVR3-IF
ENV2 6 SECS. START=32.55.26
EXPERIMENTAL

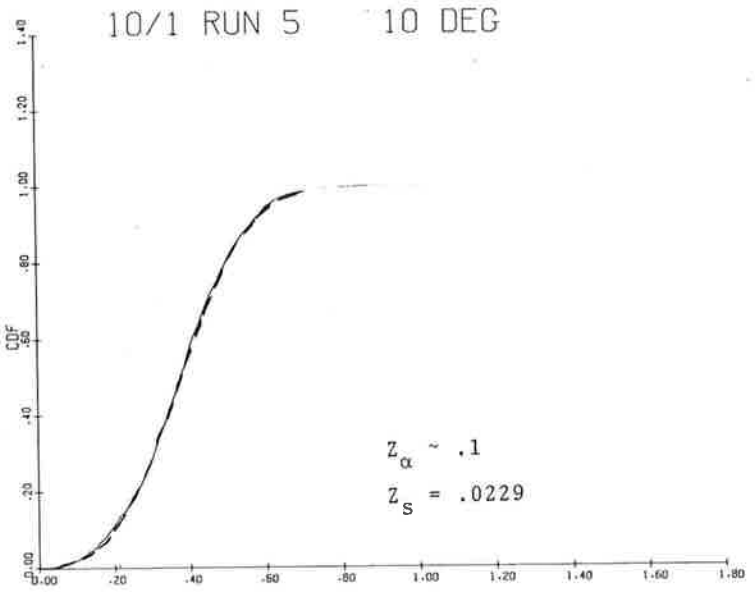

Figure 4-76a RCVR2-IF
ENV2 6 SECS. START=32.55.33
EXPERIMENTAL

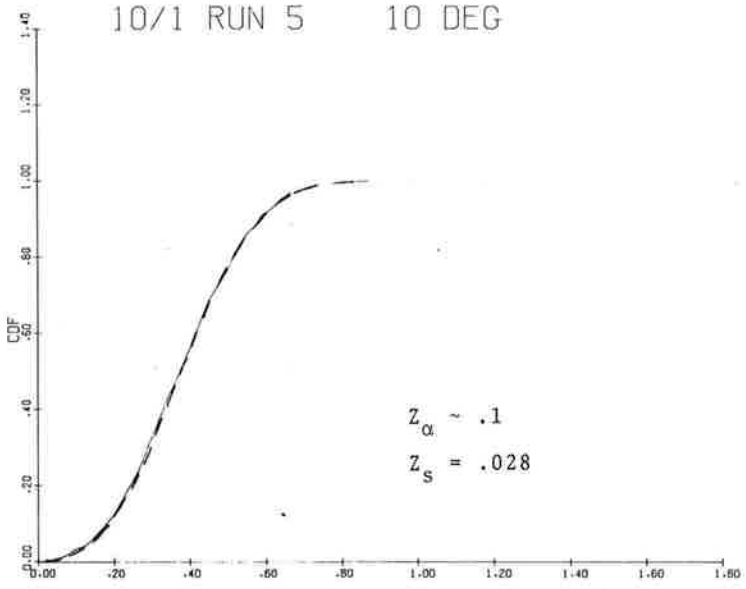

Figure 4-76b RCVR3-IF
ENV2 6 SECS. START=32.55.33
EXPERIMENTAL

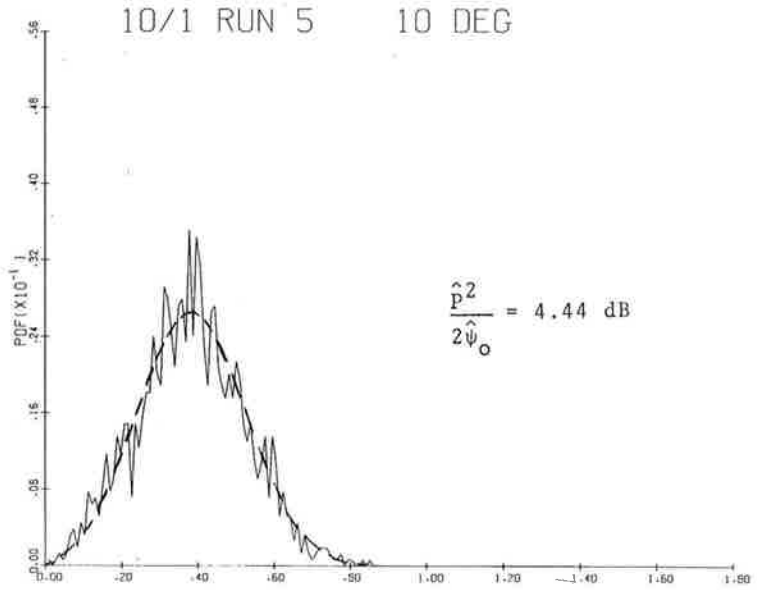

Figure 4-77a RCVR2-IF
ENV2 6 SECS. START=32.55.33
EXPERIMENTAL

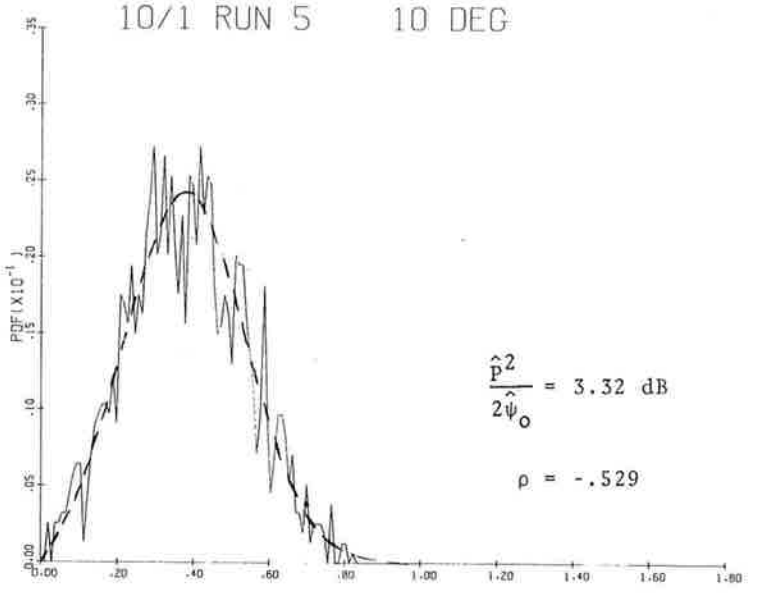

Figure 4-77b RCVR3-IF
ENV2 6 SECS. START=32.55.33
EXPERIMENTAL

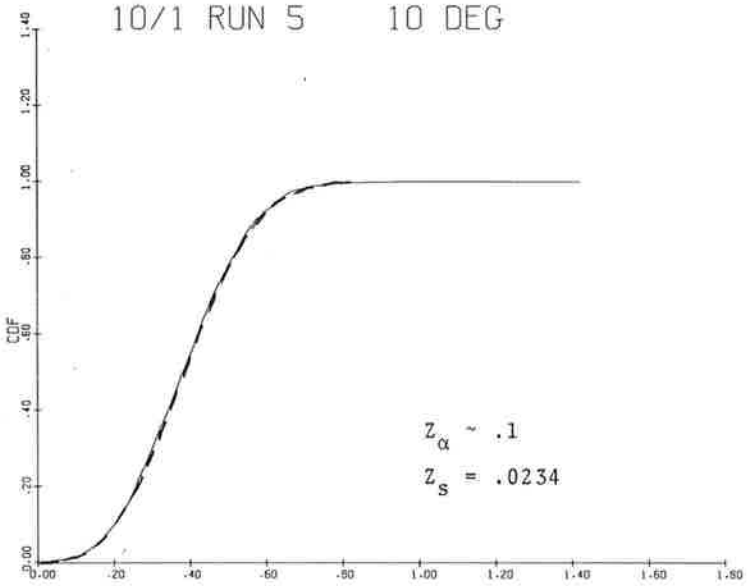

Figure 4-78a RCVR2-IF
ENV2 6 SECS. START=32.55.41
EXPERIMENTAL

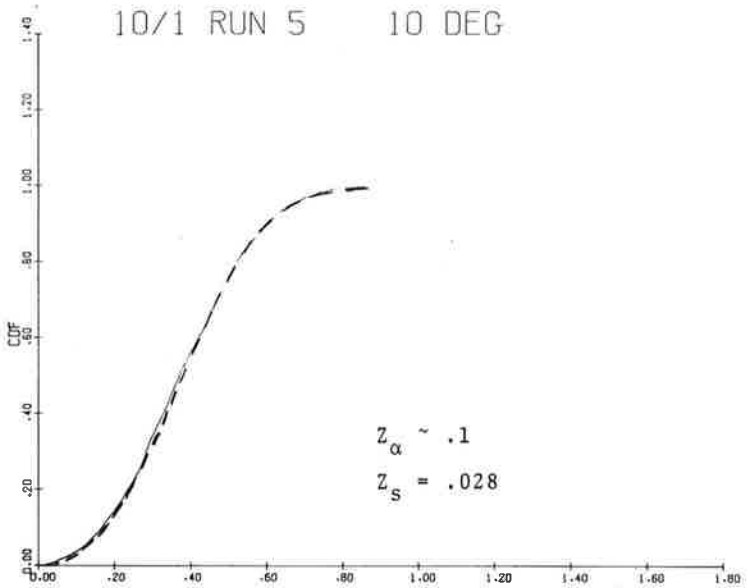

Figure 4-78b RCVR3-IF
ENV2 6 SECS. START=32.55.41
EXPERIMENTAL

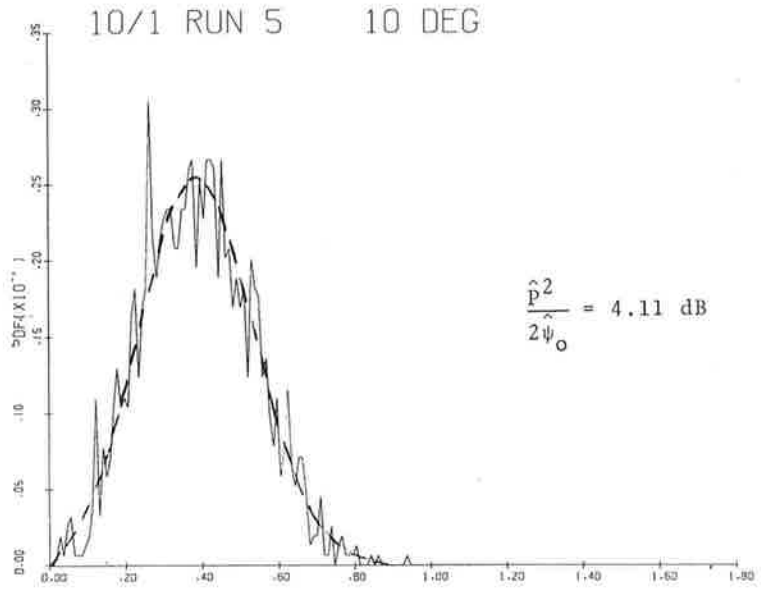

Figure 4-79a RCVR2-IF
ENV2 6 SECS. START=32.55.41
EXPERIMENTAL

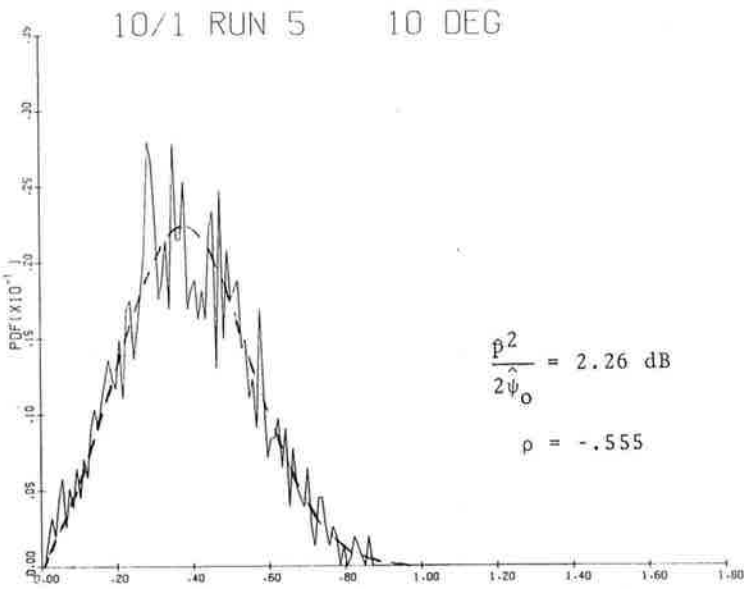

Figure 4-79b RCVR3-IF
ENV2 6 SECS. START=32.55.41
EXPERIMENTAL

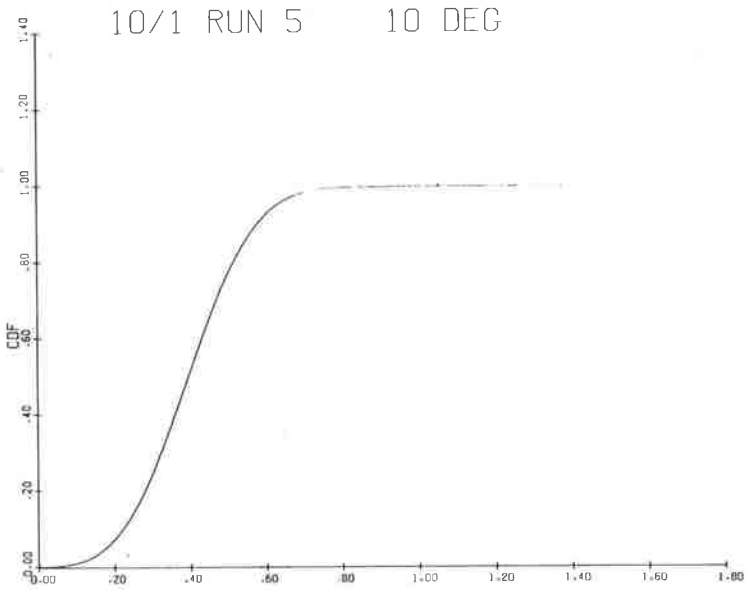

Figure 4-80a RCVR2-IF
ENV2 60 SECS. START=32.54.37
RICEAN ESTIMATE

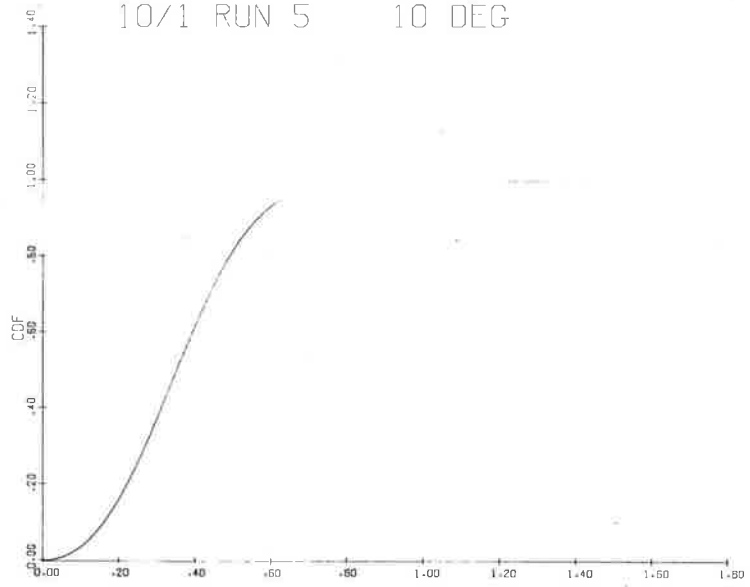

Figure 4-80b RCVR3-IF
ENV2 60 SECS. START=32.54.37
RICEAN ESTIMATE

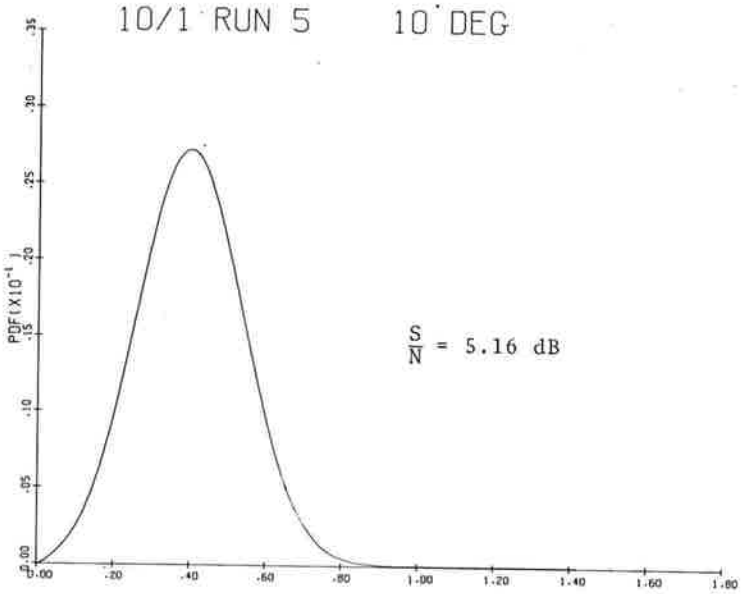

Figure 4-81a RCVR2-IF
ENV2 60 SECS. START=32.54.37
RICEAN ESTIMATE

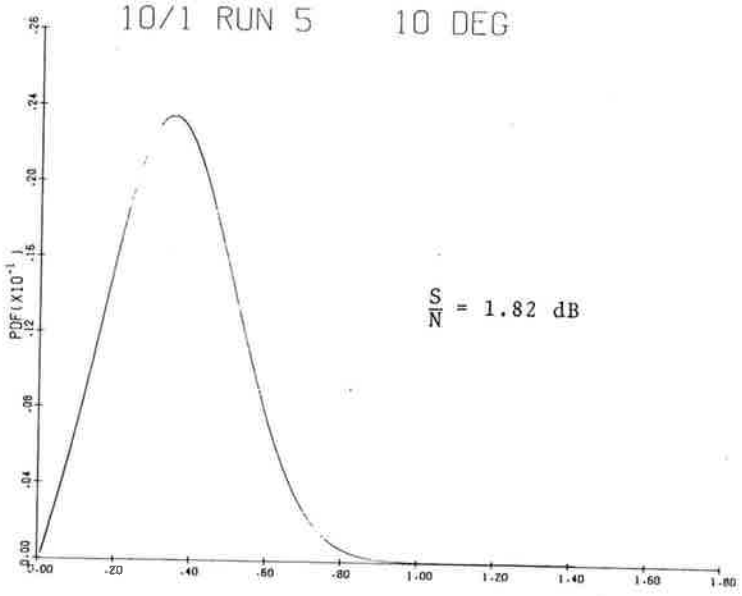

Figure 4-81b RCVR3-IF
ENV2 60 SECS. START=32.54.37
RICEAN ESTIMATE

5. CONCLUSIONS AND RECOMMENDATIONS

There are several conclusions which can be drawn with reasonable confidence from the limited amount of reduction of the CW multipath test data resulting from the experiments conducted over an aircraft-to-balloon simulated satellite link. It should be recalled that only certain segments of the recorded data, about 20 out of 250 minutes, were processed and analyzed in detail. It should also be mentioned that the conditions under which the channel was measured were reasonably constant during the test period; that is, test geometry and sea state did not change appreciably during the test period.

The following conclusions can be made:

a) For the sea states and elevation angles experienced, the specular component of the multipath reflection was not statistically in evidence.

b) The diffuse component of the multipath for the 20 minutes of data analyzed can, with high confidence, be modeled as a Gaussian process. For the test conditions of this experiment, it is felt that analysis of more of the data collected would serve only to support this conclusion. However, as was noted briefly in section 2, other analyses of the data related to the temporal properties of the multipath should be carried out.

c) Direct-to-diffuse ratios (i.e., signal to multipath ratios) range from 0.5 to 18 dB for the data analyzed. This describes the influence of the scattering surface only since for the angular sector considered, the response of the aircraft antenna was practically uniform.

d) Over periods of 1 to 3 minutes, the data appear to be homogeneous which is indicative of the fact that the channel can be modeled by a stationary Gaussian random process for these intervals. However, within these periods, changes in the direct-to-diffuse ratio can vary by several dB.

e) Distortion and noise effects have been removed by the data-reduction subroutines discussed in section 2.3, and have no appreciable effect on the output results or conclusions.

The processed data are also indicative of other tendencies in the scattering process. It is not considered possible on the basis of the available data and the reduction procedures carried out to draw firm conclusions in these areas. However, it is possible to make some preliminary remarks about certain observations.

1) As the sea states become more severe, the specular component should become even less significant (approaching zero), and the diffuse component will remain Gaussian-distributed.

2) Elementary considerations indicate that the horizontal component of the scattered signal suffers less attenuation than the vertical component. Thus, it would be expected that the direct-to-diffuse ratio should be larger for the vertical component of the signal received at the aircraft than for the horizontal. The available data, however, do not support this result. For different observations, both situations have been observed. This implies a depolarization of both vertical and horizontal channels; i.e., energy from one polarization is coupled or scattered into the other polarization under certain conditions. This implication is given some support by observation of an appreciable negative correlation coefficient between the two channels.

3) Changes in "state" of the diffuse component, that is, the emergence of a new sample from the same ensemble, occur in seconds.

4) With reference to Table 4-2, Data Reduction Summary, no special inference can be drawn from the fact that the scattered component of the 15-degree data was small. It should be noted that at 10 degrees, both high-and-low diffuse components are evident. There were not enough 5-

and 15-degree data, so that conclusions relating to elevation angle could not be drawn. In addition, all sea states observed during the test period were relatively smooth; with rough seas, strong scattered reflected components would be expected.

The recommendations are quite straightforward for future research in this area and are in accordance with current and planned work in this area.

a) Additional measurements in support of the channel model should be pursued at different satellite-aircraft geometries and sea states.

b) The existence of a cross-coupling, or negative correlation, phenomenon between the two orthogonal polarizations of the multipath signal should be investigated.

c) In trying to use diversity techniques for communication system improvement, independence of the two components is an adequate condition for improvement. The existence of negative correlation makes possible extended improvement in system design using only a simple antenna configuration. Thus, investigation of the cross-coupling phenomenon should also be carried out for a range of look angles and sea states.

d) Additional analyses of the existing data should be carried out, with emphasis on the temporal properties of the multipath.

6. REFERENCES

1. Boeing Commercial Airplane Group, ATS-5 Multipath/Ranging Experimental Program Interim Results, D6-60149, December 1971.

2. Anon., Test Plan for L-Band ATC Communications Experiment: Part I, Experiment Description, July 28, 1971, Part II, Operations, July 27, 1971. U.S. Department of Transportation, Transportation Systems Center, Electromagnetic Technology Division (Unpublished Data on File).

3. Bello, P.A., "Characterization of Randomly Time-Variant Linear Channels", IEEE Trans. on Comm. Systems, pp. 360-393, December 1963.

4. Esposito, R. and Wilson, L.R., "Statistical Properties of Two Sinewaves in Gaussian Noise", Technical Memorandum T-916, March 23, 1972, Raytheon Co., Research Division.

5. Slepian, D. and Pollak, H.O., "Prolate Spheroidal Wave Functions, Fourier Analysis and Uncertainty- I", Bell System Technical Journal, pp. 44-63, January 1961.

6. Landau, H.J. and Pollak, H.O., "Prolate Spheroidal Wave Functions, Fourier Analysis and Uncertainty-II", Bell System Technical Journal, pp. 65-84, January 1961.

7. Landau, H.J. and Pollak, H.O., "Prolate Spheroidal Wave Functions, Fourier Analysis and Uncertainty-II: The Dimension of the Space of Essentially Time and Band Limited Signals", Bell System Technical Journal, pp. 1295-1336, July 1962.

8. Gnedenko, B.V., The Theory of Probability, 4th Ed., New York, Chelsea, 1967.

9. Norton, K.A., Vogler, L.E., Mansfield, W.V. and Short, P.J., "The Probability Distribution of the Amplitude of a Constant Vector Plus a Rayleigh-Distributed Vector," Proc. of the IRE, pp. 1354-1361, October 1955.

10. McCabe, W.J.,Diamond Antenna and Microwave Corporation, Winchester MA, "A Scale Model Aircraft and Antenna Pattern Test Program," Prepared for U.S. Department of Transportation, Transportation Systems Center, Cambridge MA, November 1971.

APPENDIX A
ANALOG DATA TAKEN IN FRENCH TESTS

In the CW measurements made in France, an analog magnetic tape recorder was added to the aircraft-borne equipment. The analog IF signals at the output of the 5KHz filters were recorded using this analog recorder in addition to being sampled and quantized by the A/D converter for digital recording. The 5KHz IF signals were recorded at 3 3/4 ips on direct channels and the Receiver 1 AGC voltage and flight parameters on FM channels. Also recorded were a servo reference frequency and voice annotation. A limited amount of the IF data was processed to gain relatively quickly some insight into the characteristics of the digital data. These analog data were processed at Johns Hopkins University Applied Physics Laboratory (JHU/APL) using a special purpose computer, the CSS-3. The qualitative study of the analog data provided a valuable guide to the characteristics of the digital data recorded concurrently.

In order to improve repeatability in playback, all analog data were re-recorded on FM channels at JHU/APL and the copies were used in data processing. The re-recording was done as indicated in Table A-1. An IRIG-B time code was recorded on the copy tapes allowing specification of starting times in data processing to increments of one millisecond.

The selection of the data segments for the reduction was based on the display of the envelopes of the two 5 KHz signals, Receiver 1 AGC level and aircraft roll on paper chart recording. As an example, Figure A-1 shows a 15 second segment of the analog data displayed at 1/4 inch per second. This piece of data was chosen to be processed because the roll data indicates that the plane was stable and the relatively constant AGC level of Receiver 1 indicates that Receiver 1 is very likely locked to the direct signal. Three-second and 30-second amplitude histograms of the signal

envelope were obtained for this data segment*. Segments from runs at elevation angles of 10° and 12° were selected. Averaging times of 0.1, 3, and 30 seconds were chosen in obtaining amplitude histograms of the envelopes of the multipath plus direct signals.

TABLE A-1 RE-RECORDING ON FM CHANNELS AT JHU/APL

	Original Recording	Playback at JHU/APL	FM Record at JHU/APL	FM Playback into CSS-3 at JHU/APL
TAPE SPEED	3 3/4 ips	15 ips	60 ips	15, 7 1/2**, and 3 3/4* ips
IF FREQUENCY	5 HHz	20 KHz	20 KHz	5, 2.5, and 1.25 kc

* 15 ips was used initially with CSS-3 sampling controlled by a crystal clock. Tapes were then run at 3 3/4 ips to permit "synchronous" sampling controlled by servo reference frequency originally recorded with the data.

** 7 1/2 ips playback was used to keep input data rate compatible with CSS-3 processing time for the generation of amplitude histograms.

Examination of the power spectral density for both the horizontal and vertical components revealed the symmetric line sidebands discussed earlier in this report and in Appendix B. Sidebands of observable magnitudes were found in all data and also in calibration signals. Figures A-2 through A-4 show several power spectral density plots of the two components of the multipath plus direct signal averaged over 3 seconds and 30 seconds of data. Their characteristics are summarized in Table A-2. By the width of the spectrum in

* The spectra shown here have 6.1 Hz resolution corresponding to 1024 increments between 3.125 KHz and 6.250 KHz. The spectra were generated by using the Fast Fourier Transform Technique. The magnitudes of the Fourier spectra of successive data segments were obtained and averaging was done over 9 segments for the 3 second averages and over 90 segments for the 30 second averages. Note that the averaging times indicate the total duration of the raw data needed to generate the spectra. For example, the 3 second averages consists of 9 non-contiguous segments of data, each of 0.164 second duration, giving a net of only 1.47 seconds of data being processed. The time between successive data segments is devoted to computation. Therefore, the spectra are more accurately said to be 1.47 second and 14.7 second averages.

TABLE A-2 POWER SPECTRAL DENSITY OF 5KHz IF DATA

RUN NUMBER	ELEVATED ANGLE	FWHM IF-2 (Hz)	FW 10% IF-2 (Hz)	FW 10% / FWHM IF-2	FWHM IF-3 (Hz)	FW 10% IF-3 (Hz)	FW 10% / FWHM IF-3
			3 SEC AVERAGE				
2	12°	26	128	5.0	32	173	5.4
3	"	10	48	5.0	10	67	7.0
3	"	22	147	6.6	29	179	6.2
4	"	26	102	4.0	22	134	6.0
4	"	22	112	5.0	26	147	5.8
4	"	26	128	5.0	16	102	6.4
5	10°	77	390	5.1	32	211	6.6
5	"	16	96	6.0	26	138	5.4
5	"	13	45	3.5	16	112	7.0
7	"	10	61	3.8	16	102	6.4
MEAN		25	126	4.9	23	137	6.2
			30 SEC AVERAGE				
2	12°	29	147	5.1	22	205	9.1
3	"	10	58	6.0	10	102	10.7
3	"	22	141	6.3	29	198	6.9
4	"	19	96	5.0	19	90	4.7
4	"	22	125	5.6	26	166	6.5
4	"	19	173	9.0	19	173	9.0
5	10°	74	458	6.2	32	275	8.6
5	"	16	96	6.0	19	144	7.5
5	"	22	77	3.4	19	122	6.3
7	"	16	80	5.0	19	115	6.0
MEAN		25	145	5.76	21	159	7.5
			CALIBRATION				
CAL.	N/A	13	51	4.0	16	58	3.6
CAL.	N/A	13	48	3.8	16	48	3.0

this table, we mean the width of the center line measured at half of its maximum magnitude (FWHM) and also at 10% of its maximum magnitude.

Amplitude histograms of the envelope of the 5 KHz IF signals were made averaging over 0.1, 3, and 30 seconds of data.* Histograms of the data segments with power spectra shown in Figure A-2 through A-4 are shown in Figures A-5 through A-7, respectively. Because the zero reference is not clearly indicated in these plots and because it seems to vary from plot to plot, it is impossible to find meaningful fading statistics from them. For this reason, we used these histograms only as guides in selecting segments of digital data for processing.

---

* The interval from zero to 1.4 volts was divided into 128 quantization levels. Envelope samples were obtained by sampling at the positive peaks of the 5 KHz waveforms. Data was continuously fed to the CSS-3. Hence, for a 3 second histogram, 15000 samples were taken.

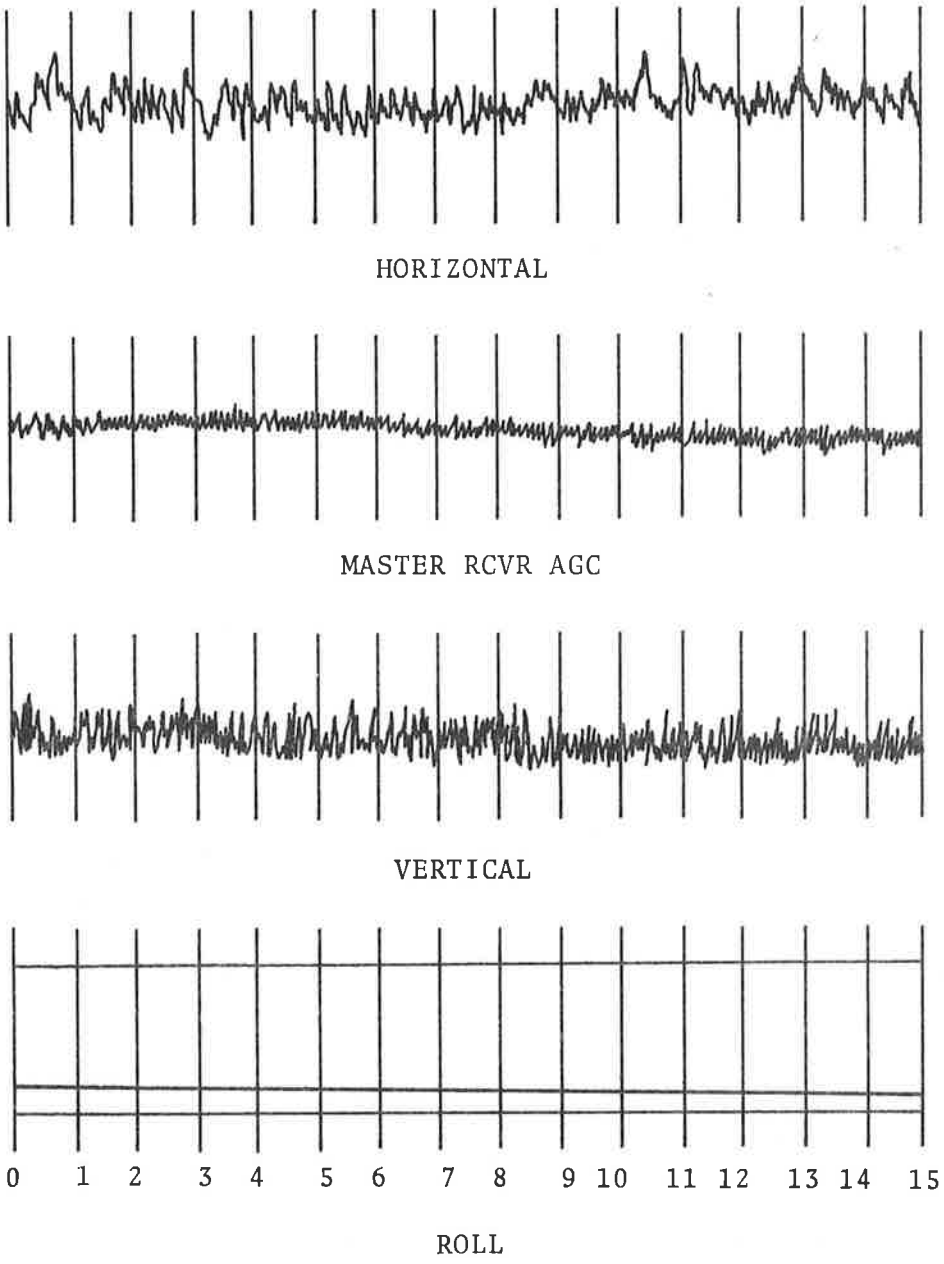

Figure A-1. Strip Chart Record Run No. 4

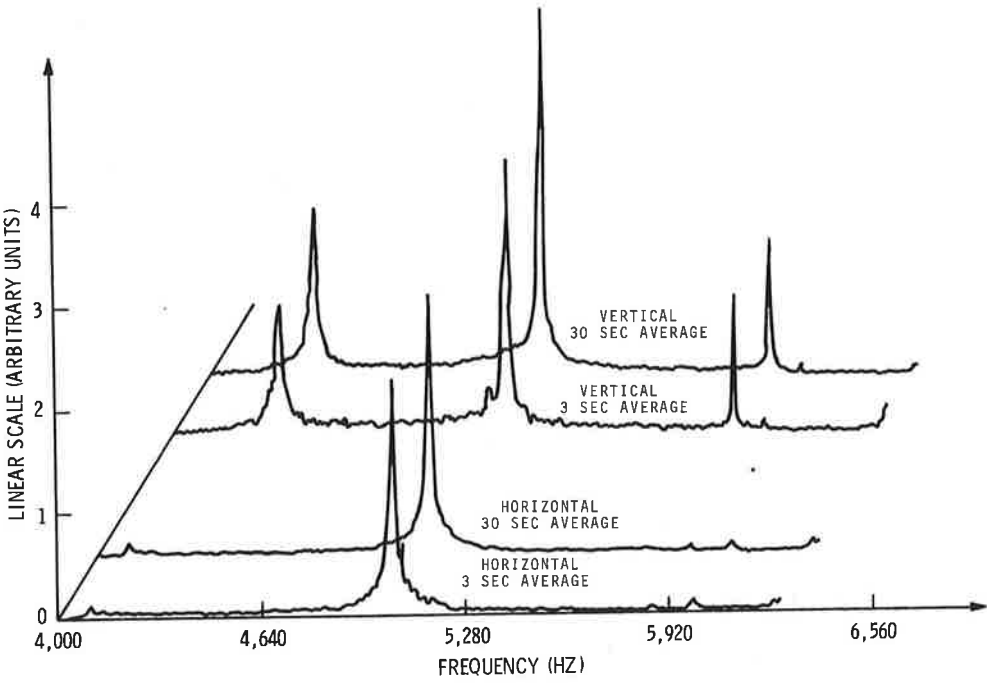

Figure A-2. Amplitude Spectra of 5 KHz IF Data - Run 4 (Typical)

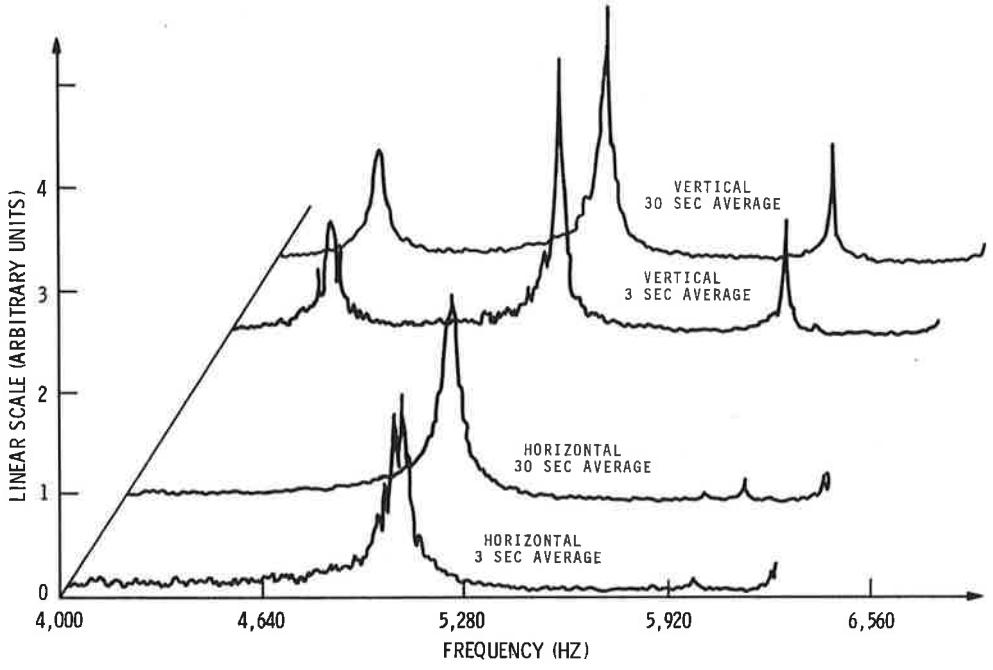

Figure A-3. Amplitude Spectra of 5 KHz IF Data - Run 5 (Broad)

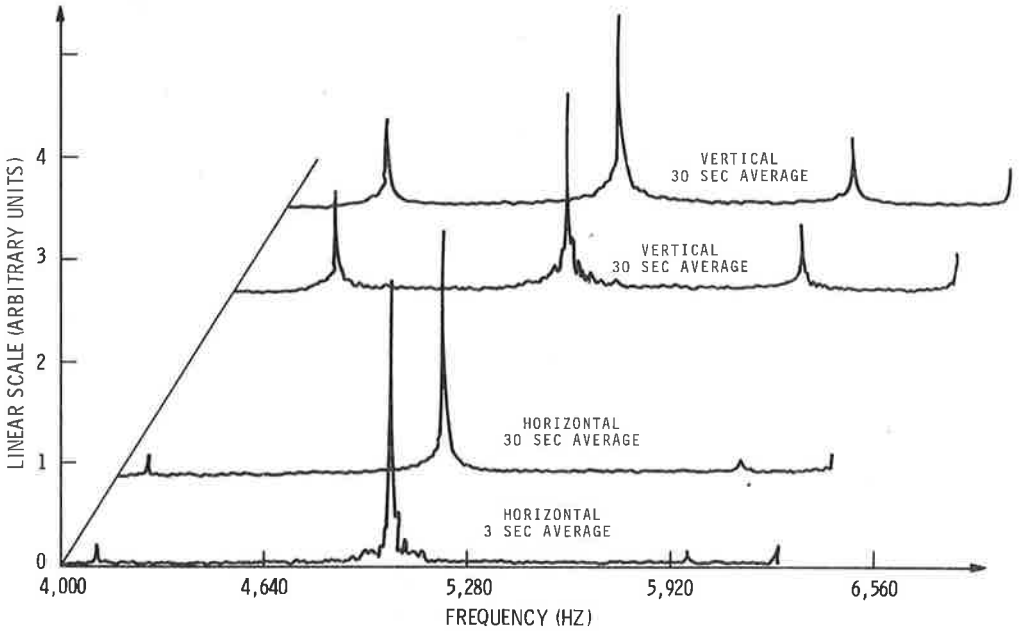

Figure A-4. Amplitude Spectra of 5 KHz IF Data - Run 3 (Narrow)

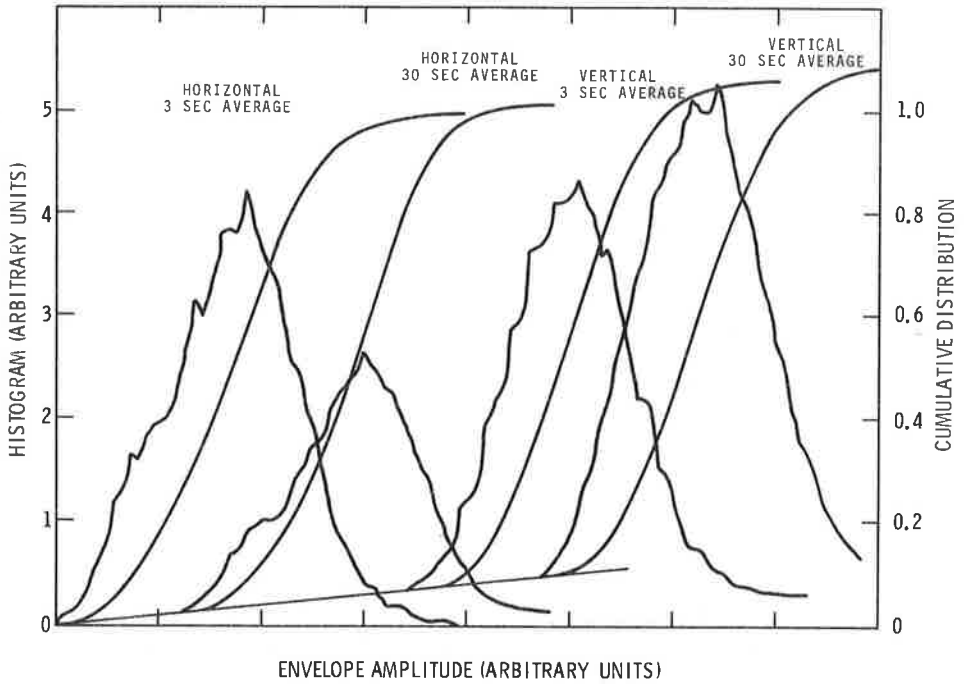

Figure A-5. Amplitude Histogram of Envelope of 5 KHz IF Data - Run 4 (Typical)

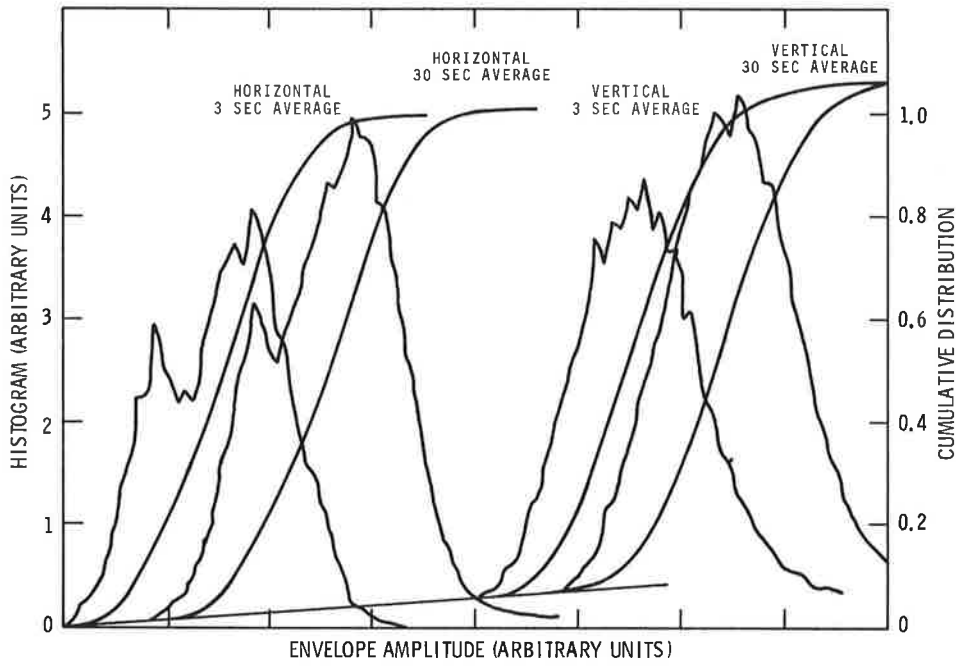

Figure A-6. Amplitude Histogram of Envelope 5 KHz IF Data - Run 5 (Broad)

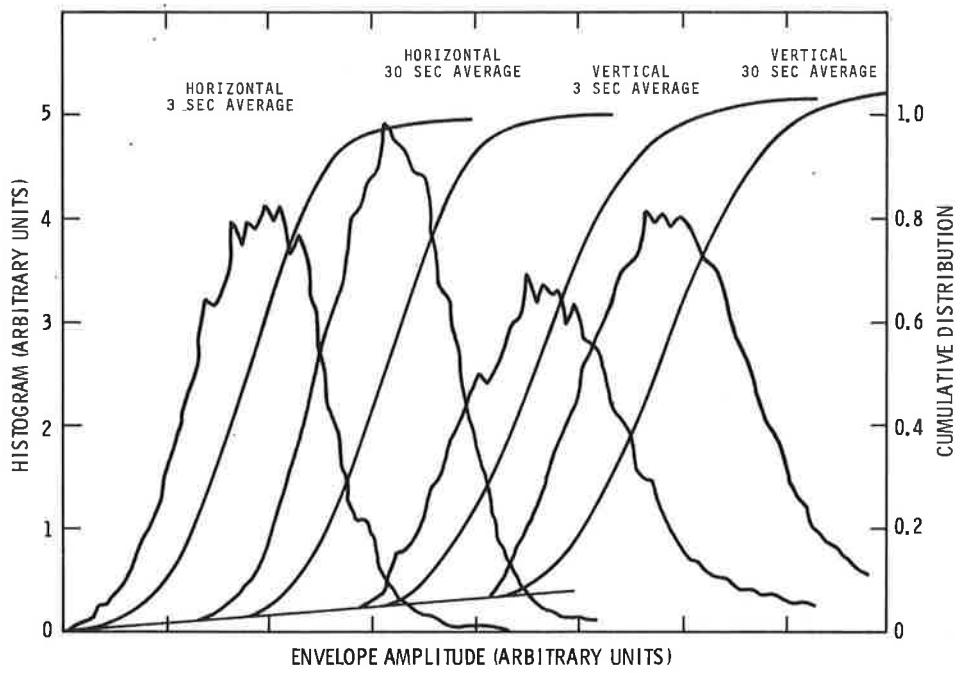

Figure A-7. Amplitude Histogram of Envelope 5 KHz IF Data - Run 3 (Narrow)

APPENDIX B
CHARACTERISTICS OF COHERENT NOISE

This Appendix discusses the characteristics of the coherent noise observed in the West Coast digital data and French analog data. Procedures used to pinpoint the noise source in the receivers are described.

Examination of the West Coast calibration recorded on May 24, shows unexpected apparent amplitude modulation of the 5 KHz IF signals. The spectra of the signal envelope shows relatively weak (-30dB) interfering signals in a band between ± 110 Hz and ± 300 Hz of the carrier in the horizontal channel and a strong (-12dB) interfering signal at approximately ±500 Hz in the vertical channel. Calibration data recorded in France shows relatively weak sidebands in the horizontal channel and rather strong interfering sidebands in the vertical channel. Sideband line-widths (-10dB) were typically 3 to 4Hz. Examination of the multipath data shows substantially the same sideband lines to be present. Table B-1 presents a summary of the observed frequencies and amplitudes of the sidebands relative to the carrier. As will be noted from Table B-1, both the amplitude and frequency of the sidebands vary substantially.

To find the source of this noise, the L-band system was checked out at the FAA/NAFEC facility. The receivers were removed from the aircraft and operated on the bench in the laboratory. The receivers were then installed in the aircraft and operated on 400 Hz power provided by an auxillary ground power unit connected to the aircraft. In each instance the frequencies and relative amplitude of the noise were different. See Table B-1. Since no conclusion on the noise source was reached, the L-band receivers were brought back to DOT/TSC.

TABLE B-1 APPROXIMATE SIDEBAND FREQUENCIES AND LEVELS OF STRONGER SIDEBAND WITH RESPECT TO CARRIER

MEASUREMENT	HORIZONTAL CHANNEL		VERTICAL CHANNEL	
	Frequency	Level	Frequency	Level
West Coast 5-24-71 Run 4	none		±503 Hz	-12dB
France 9-27-71 Run 2	±165 Hz ±937 Hz	-19dB -21dB	-416 Hz +450 Hz +615	-6.8dB -17dB -10dB
9-27-71 Run 4	±942 Hz	-21dB	±715 Hz	-16dB*
10-1-71 Run 1	±906 Hz	-18dB	±752 Hz	-7dB
10-1-71 Run 4	±926 Hz	-21dB	±700 Hz	-6dB
1-19-72 (Receivers in Lab)	±530 Hz	-10dB	±450 Hz	-6dB
FAA/NAFEC 1-20-72 (Receivers in A/C)	±390 Hz	-7dB	±840 Hz	-15dB
DOT/TSC 3-9-72	±625 Hz	-10dB	±580 Hz	-8dB

*Approximately 10 Hz wide noise band.

B-1 MEASUREMENT AT DOT/TSC

The basic elements of the L-band receivers are as shown in Figure 2-2. For the CW multipath measurement, Receivers 2 and 3 are driven by Receiver 1 VCXO in order to provide carrier tracking. Receiver 1 is normally connected to a top-mounted circularly polarized antenna. Receivers 2 and 3 receive their signals from the horizontal and vertical elements of the sidelooking antennas which provide approximately equal gain to the direct and scattered signals. The reference oscillator which feeds the second mixers in

Receivers 2 and 3 is offset by 5 KHz from the Receiver 1 reference oscillator. Consequently, Receivers 2 and 3 operate as down converters rather than phase-locked receivers and provide 5 KHz IF outputs.

On the bench at DOT/TSC, the inputs to all three receivers were connected to an L-band signal generator. As it was under normal operating conditions, the VCXO signal of Receiver 1 was used to drive the L.O. multiplier chain of all three receivers. It was observed with a spectrum analyzer that the interfering signal was present at the outputs of the video, 2nd IF and 1st IF stages of the Receivers 2 and 3. The fact that Receiver 1 was operating properly ruled out the L-band signal generator as a source of the unwanted modulation. We noted that the unwanted modulation disappeared from the output of the Receiver 2 when the L.O. multiplier output from Receiver 1 was used to provide the 1st L.O. signals for both Receiver 1 and 2. At the same time, the noise was still present in the output of Receiver 3 whose 1st mixer was driven by its own L.O. multiplier. A similar L.O. signal substitution eliminated the noise from the Receiver 3. We concluded, therefore, that the L.O. multiplier chains of Receivers 2 and 3 were the sources for the unwanted modulation.

B-2 CHARACTERISTICS OF UNWANTED MODULATION

The noise generated in the L.O. multiplier chains appears to amplitude-modulate and phase-modulate the L.O. signals. The envelope of the IF outputs of Receivers 2 and 3 showed approximately 40% amplitude modulation in both channels, as shown in Figure B-1. The spectra of the IF outputs are shown in Figures B-2 and B-3. To determine the presence of phase modulation, a DEI Model 74 Telemetry Receiver was alternately fed from the L.O. multipliers in Receivers 2 and 3. The 10 MHz IF from the DEI receiver was tapped off after the third stage of limiting in the phase demodulator of the DEI receiver and fed to a spectrum analyzer. The spectrum analyzer showed the same sideband frequencies to be present in the 10 MHz limited signal as were found in the 5 KHz IF outputs of Receivers 2 and 3. See Figures B-4 and B-5.

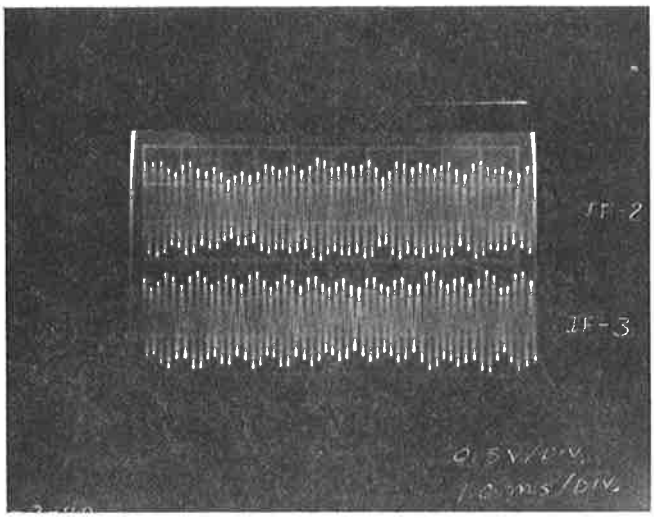

Figure B-1. CRO Display of IF-2 and IF-3

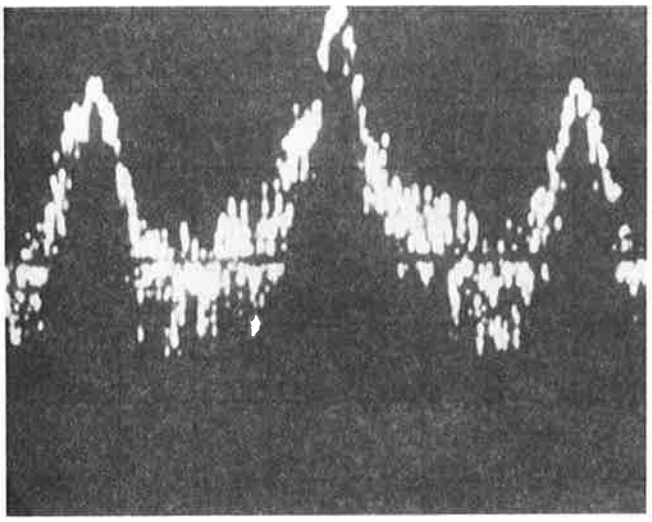

Figure B-2. Spectrum of 5 KHz IF at Output of Bandpass Filter in Receiver 2

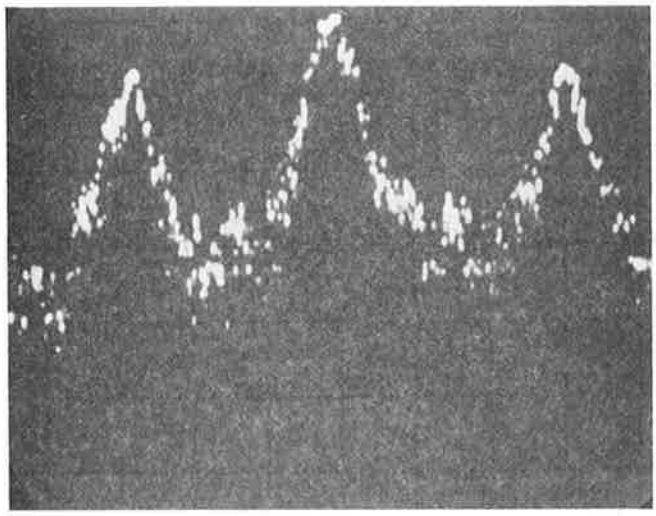

Figure B-3. Spectrum of 5 KHz IF at Output of Bandpass Filter in Receiver 3

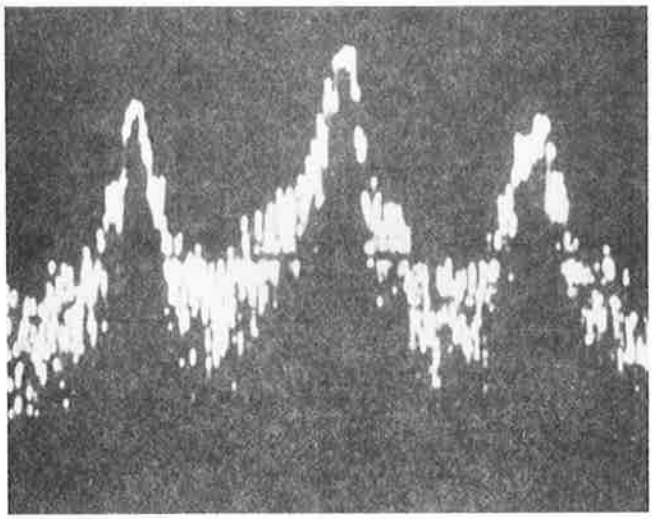

Figure B-4. Spectrum of IF-2 Phase Modulation

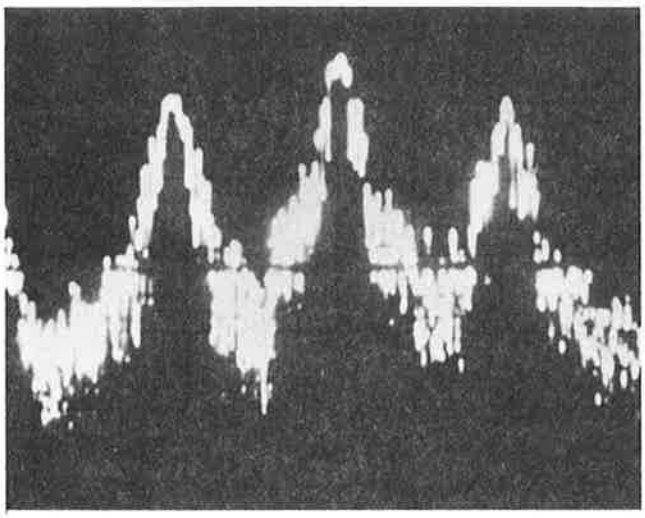

Figure B-5. Spectrum of IF-3 Phase Modulation

As discussed in Section 2, there is no need to determine the relative degrees of amplitude and phase modulation. However, in order for no aliasing to appear in the multipath signal, the phase modulation must be relatively narrowband. That this is indeed the case is shown in Figures B-4 and B-5. Calculation of the power spectral densities of the digitally recorded signals also shows the narrowband nature of the sidebands as was previously pointed out.

We note that in both Receivers 2 and 3, the inputs to the narrowband filters contain no significant sidebands at frequencies 9 KHz from the 5 KHz carrier.

APPENDIX C
LOW-PASS FILTER DATA-REDUCTION SUBROUTINES

This Appendix describes the low-pass filter subroutines available for data reduction. As it will become evident that although these subroutines were written for the specific purpose of generating envelope samples of the IF samples data in the balloon experiment, their derivations are valid for a large class of IF signals. We will describe the characteristics of these low pass filters.

Let $x(t)$ denote a bandlimited IF signal with bandwidth $2w$. The inputs to these subroutines are the Nyquist samples of $x(t)$. That is, the elements of the input array are $x(\frac{k}{4w})$, the values of $x(t)$ at $t = \frac{k}{4w}$ for $k = o, \pm 1, \pm 2, \cdots$. Clearly, in all practical cases there are a finite number of these elements. (In the case of elements in the input array, the number is equal to an integer multiple of 64.)

Being a bandlimited bandpass signal, $x(t)$ can be written as

$$x(t) = x_c(t) \cos 2\pi f_c t + x_s(t) \sin 2\pi f_c t \qquad \text{(C-1)}$$

where $x_c(t)$ and $x_s(t)$ are two low-pass signals of bandwidth w given by

$$x_c(t) = 2 \int_{-\infty}^{\infty} x(t) \cos 2\pi f_c t \cdot \frac{\sin 2\pi w(t-\tau)}{2\, w(t-\tau)}\, d\tau$$

$$x_s(t) = 2 \int_{-\infty}^{\infty} x(\tau) \sin 2\pi f_c t\, \frac{\sin 2\pi w(t-\tau)}{2\, w(t-\tau)}\, d \qquad \text{(C-2)}$$

We claim that

$$x_c\left(\frac{k}{2w}\right) = (-1)^k\, x\left(\frac{k}{2w}\right) \; ; \; k = o, \pm 1, \pm 2 \cdots \qquad \text{(C-3a)}$$

and

$$x_s\left(\frac{2k-1}{4w}\right) = (-1)^{|k|+1}\, x\left(\frac{2k-1}{4w}\right) \quad ; \; k = o, \pm 1, \pm 2 \cdots \qquad \text{(C-3b)}$$

are the Nyquist sample values of $x_c(t)$ and $x_s(t)$, respectively when the carrier frequency f_c is an odd integer multiple of w; that is $f_c = mw$ for some odd integer m. In other words

$$x_c(t) = \sum_{k=-\infty}^{\infty} (-1)^k\, x\left(\frac{k}{2w}\right) \frac{\sin 2\pi w\left(t - \frac{k}{2w}\right)}{2\pi w\left(t - \frac{k}{2w}\right)}$$

and

$$x_s(t) = \sum_{k=-\infty}^{\infty} (-1)^{|k|+1}\, x\left(\frac{2k-1}{4w}\right) \frac{\sin\pi 2\pi w\left(t - \frac{2k-1}{4w}\right)}{2\pi w\left(t - \frac{2k-1}{4w}\right)}$$

As an example, we suppose that the discrete time function $\hat{x}(t)$ shown in Figure C-1a is the Nyquist sample version of x(t)

$$x(t) = \sum_{k=-\infty}^{\infty} x\left(\frac{k}{4w}\right) \mu_o\left(t - \frac{k}{4w}\right) \qquad \text{(C-4a)}$$

then, the Nyquist samples of $x_c(t)$ and $x_s(t)$,

$$x_c(t) = \sum_{k=-\infty}^{\infty} x_c\left(\frac{k}{2w}\right) \mu_o\left(t - \frac{k}{2w}\right) \qquad \text{(C-4b)}$$

$$x_s(t) = \sum_{k=-\infty}^{\infty} x_s\left(\frac{2k-1}{4w}\right) \mu_o\left(t - \frac{2k-1}{4w}\right) \qquad \text{(C-4c)}$$

are as shown in Figures C-1b and C-1c, respectively.

The validity of Equation (C-3) can be easily demonstrated by an example. Suppose that the Fourier spectrum X(f) of x(t) is as

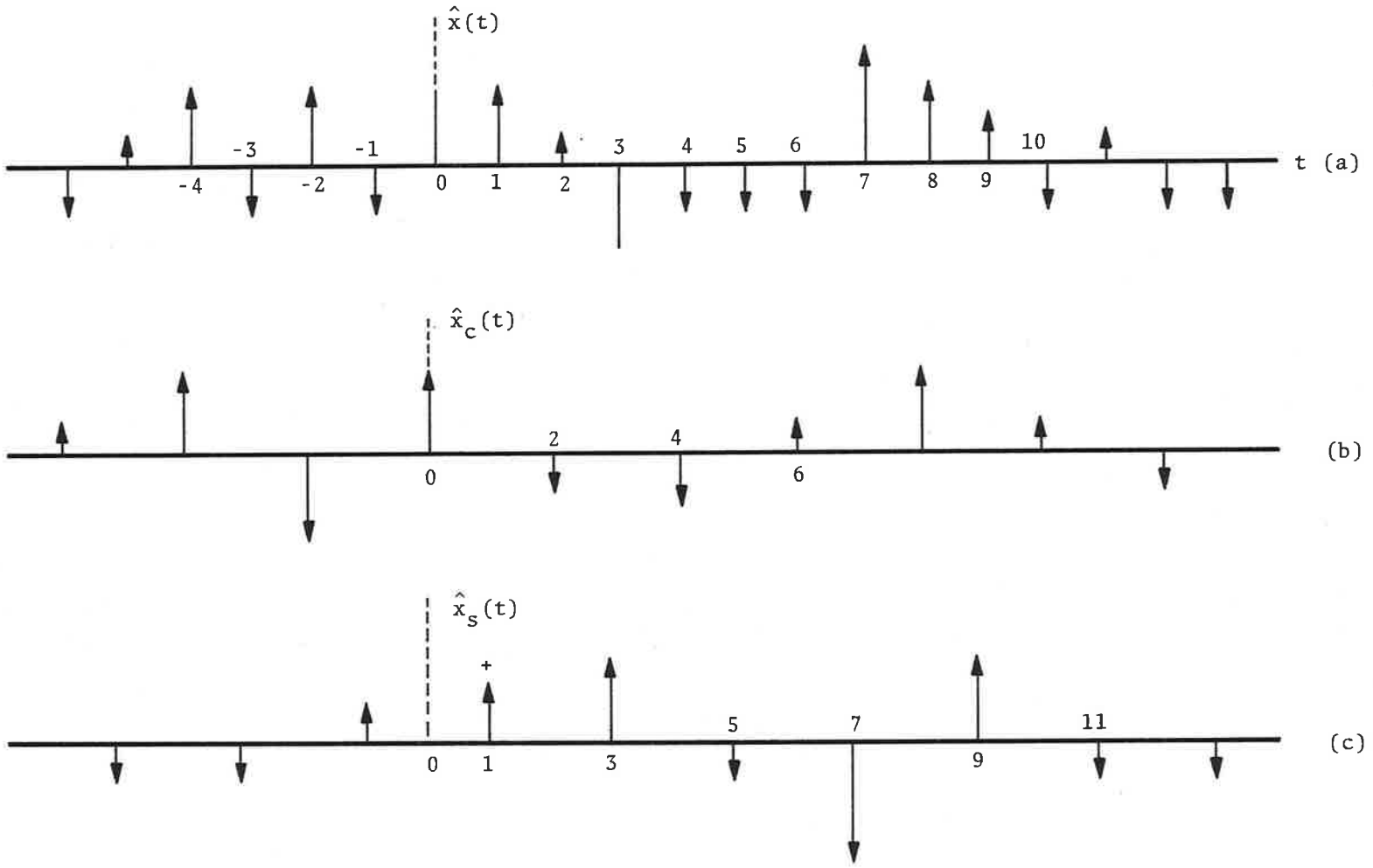

Figure C-1. Discrete Time Functions (Sample 1)

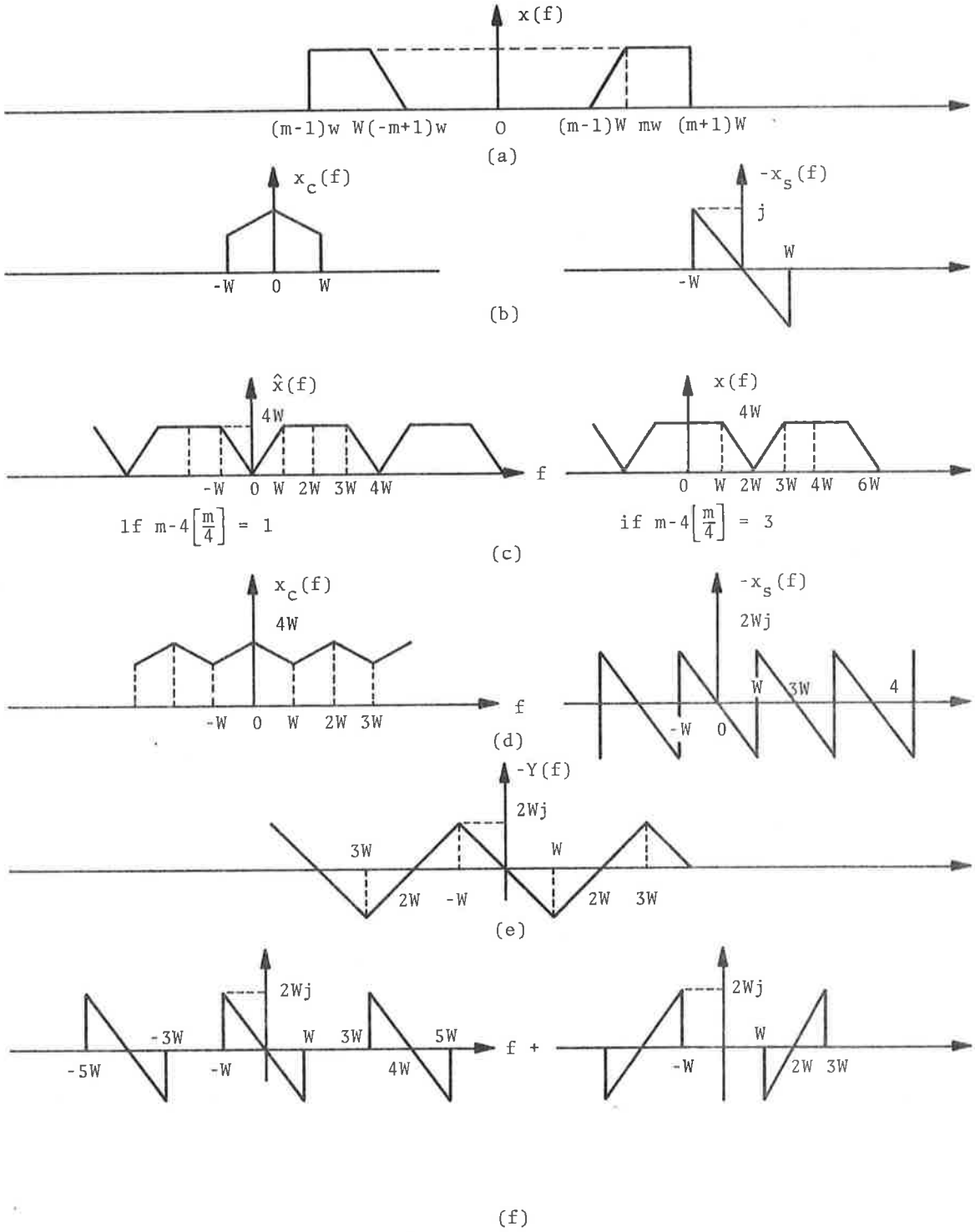

Figure C-2. Discrete Time Functions (Sample 2)

shown in Figure C-2a. For convenience, let us denote by $X^R(f)$ and $X^L(f)$ the portions of $X(f)$

$$X(f)\ \mu_{-1}(f)$$

and

$$X(f)\ \mu_{-1}(-f)$$

respectively. Because of Equation (C-2), we have

$$X_c(f) = X^R\ (f-mw) + X^L\ (f+mw)$$

and

$$jX_s(f) = X^L\ (f+mw) - X^R\ (f-mw)$$

as shown in Figure C-2b. The spectra of $x(t)$, $x_s(t)$ and $x_c(t)$ given by Equation (C-4) are as shown in Figures C-2c and C-2d, respectively. Clearly, we can obtain $X_c(f)$ by convolving $\hat{X}(f)$ with

$$\mu_o(f-w) + \mu_o(f+w)$$

that is

$$\hat{x}_c(t) = \hat{x}(t)\ \cos\ 2\pi wt$$

$$= \sum_{k=-\infty}^{\infty} x\left(\frac{k}{4w}\right)\ \cos\ \frac{\pi k}{2}\ \mu_o\left(t\ -\ \frac{k}{4w}\right)$$

comparing this expression with the right hand side of Equation (C-4b) we have Eq. (C-3a).

To prove Equation (C-3b), let us consider the Fourier spectrum of the signal

$$y(t) = \hat{x}(t) \sin 2\pi wt$$

$$= \sum_{k=-\infty}^{\infty} x\left(\frac{k}{4w}\right) \sin \frac{\pi k}{2} \mu_o\left(t - \frac{k}{4w}\right)$$

$$= \sum_{k=-\infty}^{\infty} (-1)^{|k|} x\left(\frac{2k-1}{4w}\right) \mu_o\left(t - \frac{2k-1}{4w}\right) \qquad \text{(C-5)}$$

For the case $m - 4\left[\frac{m}{4}\right] = 1$, $-Y(f)$ is as shown in Figure C-2e. We note that $Y(f)$ can be expressed as the sum of two spectra shown in Figure C-2f. The sum of the corresponding time functions is

$$-\frac{1}{2} \sum_{k=-\infty}^{\infty} x_s\left(\frac{k}{4w}\right) \mu_o\left(t - \frac{k}{4w}\right) + \frac{1}{2} e^{j4\pi wt} \sum_{k=-\infty}^{\infty} x_s\left(\frac{k}{4w}\right) \mu_o\left(t - \frac{k}{4w}\right)$$

$$= \sum_{k=-\infty}^{\infty} \frac{1}{2} x_s\left(\frac{k}{4w}\right) \left[\cos \pi k - 1\right] \mu_o\left(t - \frac{k}{4w}\right)$$

$$= \sum_{k=-\infty}^{\infty} - x_s\left(\frac{2k-1}{4w}\right) \mu_o\left(t - \frac{2k-1}{4w}\right)$$

Comparing this expression with Equation (C-5), we have Equation C-3b. We note from this derivation that, while the values of $x_s\left(\frac{2K-1}{4w}\right)$ given by Equation C-3b are correct for the case where $m - f\left[\frac{m}{4}\right] = 1$, (e.g., for the balloon data, $m = 5$), they are off from the correct values of $x_s\left(\frac{2k-1}{4w}\right)$ by a minus sign when $m - 4\left[\frac{m}{4}\right] = 3$.* When the sample values of $x_s(t)$ and $x_c(t)$ given by Equation C-3 are used to generate samples of the envelope process

$$E(t) = \left[x_c^2(t) + x_s^2(t)\right]^{1/2} \qquad \text{(C-6)}$$

---

*Note [ ] represents greatest integer value.

of x(t), there is no need to correct for this minus sign. The sample values of the phase process generated by using Equation C-3 differ from the correct values by a constant π.

There are two lowpass filter subroutines available to generate the envelope of x(t) and various filtered versions of x(t). They are described below.

C-1 ENV 1, ENVELOPE DETECTOR: UNFILTERED

ENV 1 is a subroutine for generating the envelope of the IF signal x(t) written as in Equation C-1 when $f_c = mw$ for some odd integer m. (Again, for the balloon experiment data $f_c = 5kc$, $w = 1$ kc.) Specifically, its inputs are the values of x(t) at $t = \frac{k}{4w}$; $k = o, \pm 1, \pm 2 \cdots$. Its outputs are sample values of envelope E(t) at $t = \frac{k}{2w}$; $k = o, \pm 1, \pm 2$

$$E\left(\frac{k}{2w}\right) = \left\{x_c^2\left(\frac{k}{2w}\right) + x_s^2\left(\frac{k}{2w}\right)\right\}^{1/2}$$

The sample values of $x_c(t)$ at $t = \frac{k}{2w}$ are given by Equation C-3a. The sample values of $x_s(t)$, at $t = \frac{k}{2w}$ can be extrapolated from those given by Equation C-3b. According to the sampling theorem, we have

$$x_s\left(\frac{k}{2w}\right) = \sum_{m=-\infty}^{\infty} x_s\left(\frac{2m-1}{4w}\right) \frac{\sin 2\pi w\left(\frac{k}{2w} - \frac{2m-1}{4w}\right)}{2\pi w\left(\frac{k}{2w} - \frac{2m-1}{4w}\right)}$$

Simplifying this expression and substituting Eq. (C-3b), we obtain

$$x_s\left(\frac{k}{2w}\right) = \sum_{m=-\infty}^{\infty} (-1)^{|m|+1}\, x_s\left(\frac{2m-1}{4w}\right) \left\{\frac{2}{\pi} \frac{1}{2k-2m+1} \sin \frac{\pi}{2}\left[2k-m+1\right]\right\}$$

Let $m = k-j$, and note that $\sin \frac{\pi}{2}(2j+1) = (-1)^j$. This expression can be written as

$$x_s\left(\frac{k}{2w}\right) = \sum_{j=o}^{\infty} (-1)^{k+1} \frac{2}{\pi} \frac{1}{2j+1} \left\{x\left(\frac{2(k-j)-1}{4w}\right) - x\left(\frac{2(k+j)+1}{4w}\right)\right\} \qquad (C\text{-}7)$$

In the subroutine ENV1, this infinite series is approximated by

$$\underline{x}_s\left(\frac{k}{2w}\right) = (-1)^{k+1}\,\frac{2}{\pi}\sum_{j=o}^{K}\frac{1}{2j+1}\left\{x\left(\frac{2(k-j)-1}{4w}\right) - x\left(\frac{2(k+j)+1}{4w}\right)\right\} \qquad (C\text{-}8)$$

where the upper limit K is an input parameter of the program. The outputs of the program are

$$\underline{E}\left(\frac{k}{2w}\right) = \left\{x_c^2\left(\frac{k}{2w}\right) + \underline{x}_s^2\left(\frac{k}{2w}\right)\right\}^{1/2} \qquad (C\text{-}9)$$

C-2 ENV2, ENVELOPE DETECTOR: FILTERED

In this filtering routine we simulate an ideal low-pass filter with a frequency response indicated below

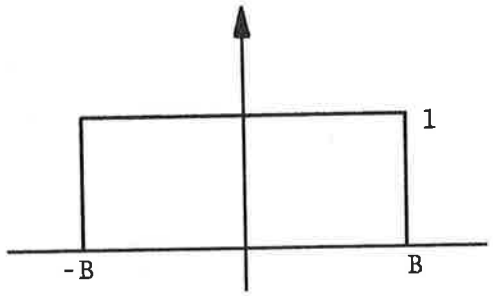

Figure C-3 Ideal Low-Pass Filter

where the cutoff frequency B is related to the IF bandwidth 2w by B = w/n, n is an integer larger than one. The impulse response of this filter is the function sin $2\pi Bt/\pi t$ which is plotted in Figure C-4.

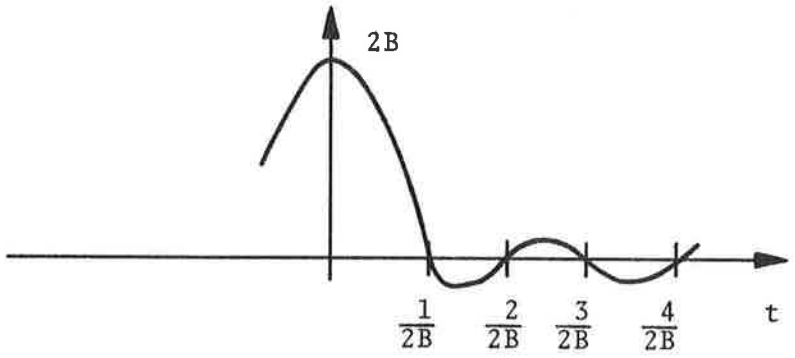

Figure C-4. Sampling Function

The filter is specified by the parameters

n - integer, giving the filter bandwidth

k - the truncation width of the impulse response

ℓ - number of output samples of the envelope generated

$1 \leq \ell \leq n$

The sampled raw data

$$\hat{x}(t) = \frac{1}{4w} \sum_{k=-\infty}^{\infty} x\left(\frac{k}{4w}\right) \mu_o\left(t - \frac{k}{4w}\right)$$

is composed of the inphase signal

$$\hat{x}_c(t) = \frac{1}{2w} \sum_{k=-\infty}^{\infty} x\left(\frac{k}{4w}\right) \cos \frac{k\pi}{2} \mu_o\left(t - \frac{k}{4w}\right)$$

and the quadrature signal

$$\hat{x}_s(t) = \frac{1}{2w} \sum_{k=-\infty}^{\infty} x\left(\frac{k}{4w}\right) \sin \frac{k\pi}{2} \mu_o\left(t - \frac{k}{4w}\right) .$$

If we low-pass filter the two signals we obtain $x_c(t,B)$ and $x_s(t,B)$ where

$$x_c(t,B) = \int_{-\infty}^{\infty} \hat{x}_c(t) \frac{\sin 2\pi B(t-z)}{\pi(t-z)} dz$$

$$= \frac{1}{2w} \sum_{k=-\infty}^{\infty} x\left(\frac{k}{4w}\right) \cos \frac{k\pi}{2} \frac{\sin 2\pi B\left(t - \frac{k}{4w}\right)}{\pi\left(t - \frac{k}{4w}\right)}$$

and

$$x_s(t,B) = \frac{1}{2w} \sum_{k=-\infty}^{\infty} x\left(\frac{k\pi}{4w}\right) \sin \frac{k\pi}{2} \frac{\sin 2\pi B\left(t - \frac{k}{4w}\right)}{\pi\left(t - \frac{k}{4w}\right)}$$

respectively. Now for any sampled time $t = \frac{j}{4w}$,

$$x_c\left(\frac{j}{4w},B\right) = \sum_{k=-\infty}^{\infty} x\left(\frac{k}{4w}\right) \cos \frac{k\pi}{2} \frac{\sin \frac{2\pi w}{n}\left(\frac{j}{4w} - \frac{k}{4w}\right)}{\pi\left(\frac{j}{4w} - \frac{k}{4w}\right)} \cdot \frac{1}{2w}$$

$$= \frac{2}{\pi} \sum_{k=-\infty}^{\infty} x\left(\frac{k}{4w}\right) \cos \frac{k\pi}{2} \frac{\sin \frac{\pi}{2n}(j-k)}{(j-k)}$$

$$x_s\left(\frac{j}{4w},B\right) = \frac{2}{\pi} \sum_{k=-\infty}^{\infty} x\left(\frac{k}{4w}\right) \sin \frac{k\pi}{2} \frac{\sin \frac{\pi}{2n}(j-k)}{(j-k)}$$

Remember for x_c we will only use the even samples and for x_s we will only use the odd samples. The integer ℓ should be large enough so that after filtering we have a sufficient number of output samples. This is satisfied when $1 \leq \ell \leq n$. For $\ell = 1$ every sample is used while for $\ell = n$ every n^{th} sample is calculated, or exactly the Nyquist rate.

The j^{th} sample of the envelope is $\left[x_s^2\left(\frac{j}{4w}\right) + x_c^2\left(\frac{j}{4w}\right)\right]^{1/2}$. The samples of the phase are

$$\ell \text{ even - all samples} = \tan^{-1} \frac{x_s(j/4w)}{x_c(j/4w)}$$

$$\ell \text{ odd - all even } j = \tan^{-1} \frac{x_s(j/4w)}{x_c(j/4w)}$$

$$\text{all odd } j = \cot^{-1} \frac{x_s(j/4w)}{x_c(j/4w)}$$

The filter weights become

k	x_c	x_s
j-9	0	⋮
j-8	$\frac{2}{\pi}\frac{\sin\frac{4\pi}{n}}{8}$	0
j-7	0	$\frac{2}{\pi}\frac{\sin\frac{7\pi}{2n}}{7}$
j-6	$-\frac{2}{\pi}\frac{\sin\frac{3\pi}{n}}{6}$	0
j-5	0	$-\frac{2}{\pi}\frac{\sin\frac{5\pi}{2n}}{5}$
j-4	$\frac{2}{\pi}\frac{\sin\frac{2\pi}{n}}{4}$	0
j-3	0	$\frac{2}{\pi}\frac{\sin\frac{3\pi}{2n}}{3}$
k	x_c	x_s
j-2	$-\frac{2}{\pi}\left[\sin\frac{\pi}{n}\right]\frac{1}{2}$	0
j-1	0	$-\frac{2}{\pi}\sin\frac{\pi}{2n}$

j+0	$1/n$	0
j+1	0	$-\frac{2}{\pi}\sin\frac{\pi}{2n}$
j+2	$-\frac{2}{\pi}\left[\sin\frac{\pi}{n}\right]\frac{1}{2}$	0
j+3	0	$\frac{2}{\pi}\frac{\sin\frac{3\pi}{2n}}{3}$
j+4	$\frac{2}{\pi}\frac{\sin\frac{2\pi}{n}}{4}$	0
j+5	0	$-\frac{2}{\pi}\frac{\sin\frac{5\pi}{2n}}{5}$
j+6	$-\frac{2}{\pi}\frac{\sin\frac{3\pi}{n}}{6}$	0
j+7	0	$\frac{2}{\pi}\frac{\sin\frac{7\pi}{2n}}{7}$
j+8	.	.
	.	.
j+9	.	.

APPENDIX D
OSCILLATOR STABILITY

The effect of oscillator stability on the L-band Experiment can be described with the aid of Figure 2-2. The CW signal originates in the ground station, is frequency-translated in the balloon borne transponder and is received, digitized and recorded in the aircraft. Three receivers are used within the aircraft. The master receiver (Receiver 1) operates as a phase-locked receiver and is used to track out drift, low-frequency instabilities and Doppler shifts in the received signal. The master receiver is fed from a reference antenna which is located on the top of the aircraft fuselage. The antenna is located fore-and-aft in a position which is relatively well shielded by the wing structure from the multipath signal scattered from the ocean. The two slave receivers (Receivers 2 and 3) are operated as frequency translators or down-converters and provide outputs as a 5 KHz IF for A/D conversion and recording. The slave receivers are connected to the horizontal (Receiver 2) and vertical (Receiver 3) elements of side-looking antennas which are located in the window ports well forward of the wings. These antennas provide approximately equal gain to the direct and scattered signals. The master receiver operates with a tracking loop bandwidth of 33Hz and provides signals from its VCXO for Receivers 2 and 3. The reference oscillator for Receivers 2 and 3 is offset in frequency by 5KHz from the reference oscillator for Receiver 1. This frequency offset produces a 5KHz IF in the video outputs of Receivers 2 and 3. Since the master receiver tracks out frequency drift and low-frequency phase instabilities in the received signal these frequency variations are of no particular interest. There are, however, two sources of frequency drift which are not tracked out by the master receiver. The reference oscillator for Receivers 2 and 3 is outside of the phaselocked loop and hence any drift of this oscillator relative to Reference Oscillator 1 shows up directly as a drift in the frequency of the 5KHz IF output from Receivers 2 and 3. Secondly, the 4KHz sampling of the

5KHz IF signals acts as a down conversion to 1KHz. See Appendix C for a detailed description of this process. Any drift in the sampling frequency relative to the 5KHz IF frequency shows up as an apparent shift in the 5KHz IF signal frequency. The significant specifications of the reference oscillators for the receivers are listed in Table D-1.

TABLE D-1 CHARACTERISTICS OF FREQUENCY SOURCES

CHARACTERISTIC	FREQUENCY ELECTRONICS, INC. MODEL FE-30-OPC-1 TCXO	TRACOR MODEL 304D RUBIDIUM FREQUENCY STD.
Nominal Frequency:	88 MHz	5 MHz
Long Term Stability:	$\pm 2 \times 10^{-8}$ per 24 hours	$< 2 \times 10^{-11}$ per month
Short Term Stability:	Typically $\pm 1 \times 10^{-9}$ averaged over one second	$\frac{\Delta f}{f}$ (std.dev.) $< 7 \times 10^{-12}$
Harmonic Distortion:	<5%	Greater than 40 dB down from rated output
Non-harmonic Distortion:	Greater than 50 dB down from rated output	Greater than 80 dB down from rated output
Signal-to-noise Ratio:	Not measured	Greater than 87dB at rated output in 30KHz noise bandwidth

The sampling rate of the analog-to-digital converter is controlled from a stable 5 MHz frequency reference via the Digital Data Formatter (DDF). The 5MHz reference frequency is generated by a Tracor Model 304D Rubidium Frequency Standard and is frequency divided in the DDF to produce a 4KHz clock signal which sets the A/D sampling rate. Since the frequency division process within the DDF is a digital one (no other frequency reference is used) the relative frequency accuracy and drift of the 4KHz sampling

rate is the same as that of the rubidium frequency standard and is negligible. See Table D-1. The drift in the 5KHz IF signals is therefore dominated by the relative drift of the receiver local oscillators (FEI Model FE-30-OPC-1) and may be in the order of ±0.09Hz averaged over one second or ±1.7Hz over 24 hours.

APPENDIX E
CALIBRATION

In this section we shall describe the procedure used to calibrate the CW portion of the L-band experiment and present the results obtained. Calibration files were recorded on all flights, however on certain flights difficulties were encountered which prevented us from generating suitable calibration curves.

The system was operated in the slave mode during all CW data runs and was calibrated in the slave mode. When the system is operated in the slave mode, Receiver 1 (the master receiver) is phaselocked to the direct signal received via one of the reference antennas (zenith or L 35° or R 35°) while Receivers 2 and 3 operate as L-band to 5 KHz down converters for the horizontal and vertical components of the composite signal received from the sidelooking window-mounted antennas. Receiver 1 operates with automatic gain control while Receivers 2 and 3 operate with a manually adjusted gain which remained fixed throughout a particular series of runs or calibration file. In order to determine the gain and linear range of the system, CW signals were fed into the RF preamplifiers associated with the reference and sidelooking antennas. The calibration signal was generated through the use of a General Radio Co. Model 1164-A Coherent Decade Frequency Synthesizer and a multiplier chain (24x). The amplitude of the calibration signal was varied by means of a Hewlett-Packard Model 394A Variable Attenuator. The calibration signal was fed to the RF switching unit where it was power divided and simultaneously injected into the preamplifiers associated with the three receivers. A coaxial relay located at the antenna preamplifier allowed either the antenna or the calibration source to be connected to the preamplifier input. The RF power levels listed on the calibration curves refer to the input power level at the master receiver (Receiver 1) preamplifier. The power level at the input to the Receiver 2 and 3 preamplifiers differs from the value specified

for the master receiver by the differences in cable loss between the RF switching unit and the preamplifiers in question. These cable losses are listed in Table E-1.

TABLE E-1 ONE-WAY CABLE LOSS BETWEEN RF SWITCHING UNIT AND ANTENNA PREAMPLIFIERS

ANTENNA PREAMPLIFIER	ONE-WAY CABLE LOSS (dB)
Zenith	4.2
Right 35°	3.5
Left 35°	3.7
Right horizontal	6.5
Right vertical	5.7
Left horizontal	7.0
Left vertical	6.0

The calibration curves of primary interest are those associated with the envelope of the 5 KHz IF signals derived from the horizontal and vertical elements of the sidelooking antennas. In most cases the mean and standard deviation of the envelope was calculated using an averaging time of 1 second. In those cases where uninterrupted records of one second duration could not be obtained, shorter averaging times were used and are noted. Continuous time records were required in order to avoid introducing interpolation errors in the calculation of the envelope. Appendix C gives a detailed description of the envelope extraction routine.

Calibration curves of secondary interest are those of the Receiver 1 AGC voltage and the Receiver 2 and 3 IF levels. The AGC values of Receiver 1 are sampled at rate of 62.5 samples per second and are representative of the signal strength at the reference antenna preamplifier. The IF levels are also sampled at a 62.5 Hz rate and are representative of the amplitudes of the diode-detected envelopes of the 5 KHz IF signals from Receivers 2 and 3.

While no data is presented based upon either the AGC #1 or level #2 or level #3 measurements, the calibration curves for these functions are presented for completeness.

E-1 WEST COAST CALIBRATION (MAY 24, 1971)

The calibration for the flight of May 24, 1971 was made using the left 35° and left sidelooking antennas. The power spectral density (PSD) of the raw calibration data was calculated in order to characterize the system and to determine the low-pass filter bandwidth to be used in the envelope detection program (ENV-2). The PSD used to characterize the system was the average of ten one-second PSDs. The PSD is representative of the receiver outputs at three different calibration levels (3.8 sec. at -99 dBm, 5.3 sec. at -104 dBm and 0.9 sec. at -109 dBm).

The spectrum of IF-2 shows a clean signal with a 3 dB line width of 2 Hz and a peak at 997 Hz. Note that the PSD shows the carrier to be at 1 KHz (997 Hz) rather than at 5 KHz which is the IF frequency at the receiver output. As pointed out in Appendix C, the 4 KHz sampling of the 5 KHz IF effectively translates the carrier down to 1 KHz as shown by the PSD of the raw data. The line width at -10 dB is approximately 4 Hz and the spectrum width at -20 dB is 8 Hz. The spectrum width at -30 dB is 33 Hz and it reaches a noise floor of -40 dB roughly 50 Hz either side of the carrier. All line components are 33 dB or greater below the carrier.

The spectrum of IF-3 is similar to that of IF-2 except that it has significant sidebands at roughly 500 Hz either side of the carrier. Specifically, the IF-3 spectrum contains a pair of lines 11 dB below the carrier situated 503 Hz on either side of the carrier. Also, there are two pair of 10 Hz wide noise-like bands centered at ± 466 Hz and ± 442 Hz with respect to the carrier. The approximate levels are -20dB (±466 Hz) and -23 dB (±442 Hz) relative to the carrier. All other line or noise components are 25 dB or greater below the carrier.

Figure E-1 shows a plot of the mean and standard deviation of the envelope of 5 KHz outputs from Receivers 2 and 3. The plots represent 2-second time averages of the ENV-2 routine with N=8 (corresponding to a low-pass bandwidth of 125 Hz) and K=150 (corresponding to a truncation width of 150 terms). Figure E-2 shows a plot of the mean and standard deviation of the AGC #1 voltage with a 2-second averaging time.

E-2 FRENCH CALIBRATION

E-2-1 October 1, 1971, Run 1, File 2 Calibration

The calibration for run 1 on 10-1-71 was made using the zenith and right-sidelooking antenna preamplifiers. The power spectral density of the raw IF data was computed on the basis of a 10-second time average which included five different calibration levels. The spectrum of IF-2 (raw data) shows a peak at 1030 Hz. The spectrum broadens to a width of 8Hz at -20 dB and to 26 Hz at -30 dB. The approximate noise floor of -40 dB is reached at a spectrum width of 110 Hz. The only line components about the carrier are situated at ± 906 Hz and are approximately 18 dB below the carrier.

The spectrum of IF-3 (raw data) is similar to that of IF-2 with the exception of its line components. The most significant set of sideband components are located at ± 752 Hz about the carrier. The upper and lower sideband lines are -7.6 dB and -17.4 dB below the carrier. All other sideband line pairs (there are seven) are twenty dB or greater below the carrier and are situated 154 Hz or more from the carrier frequency.

Figure E-3 shows a plot of the mean and standard deviation of the envelope of the 5 KHz outputs from Receivers 2 and 3. The plots represent the output of the ENV-2 routine with N=8 (corresponding to a low-pass filter bandwidth of 125 Hz) and K=150 (truncation width equal to 150 terms). Various averaging times were required due to the lack of continuous 1-second data segments in the data stripped from the original tapes. Table E-2 lists the averaging times used for each calibration level.

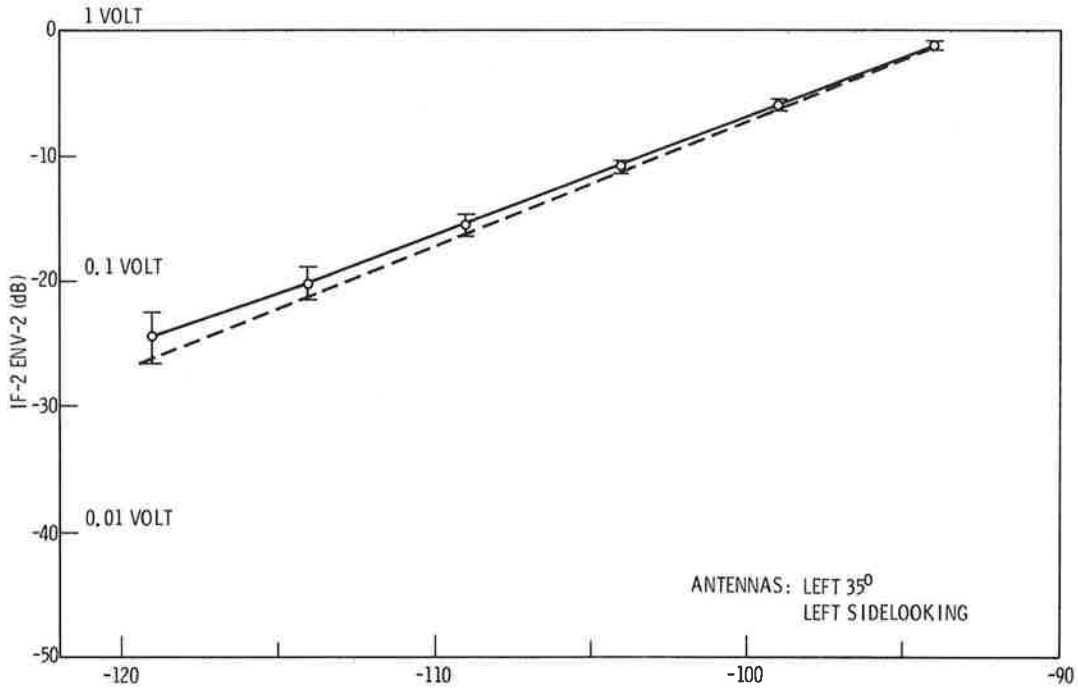

(a) RF INPUT (dBm)

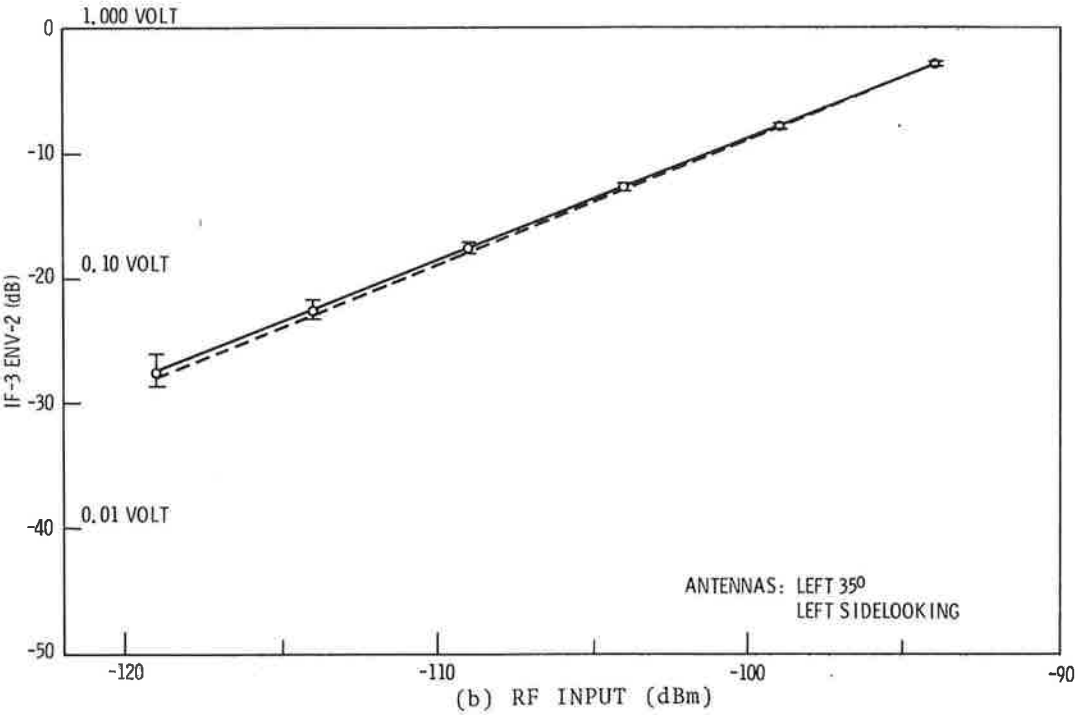

(b) RF INPUT (dBm)

Figure E-1. 5-24-71 Run 4 Calibration, IF-2, 3 ENV-2

TABLE E-2 ENV-2 AVERAGING TIMES FOR 10-1-71
RUN 1, CALIBRATION FILE

LEVEL #	RF INPUT	AVERAGING TIME
1	-100 dBm	0.875 seconds
2	-102	1.000
3	-104	1.000
4	-106	0.375
5	-108	1.000
6	-110	1.000
7	-112	1.000
8	-114	0.750
9	-116	0.625
10	-118	no data
11	-120	0.500
12	-122	0.500
13	-124	1.000
14	-126	0.250
15	-128	1.000

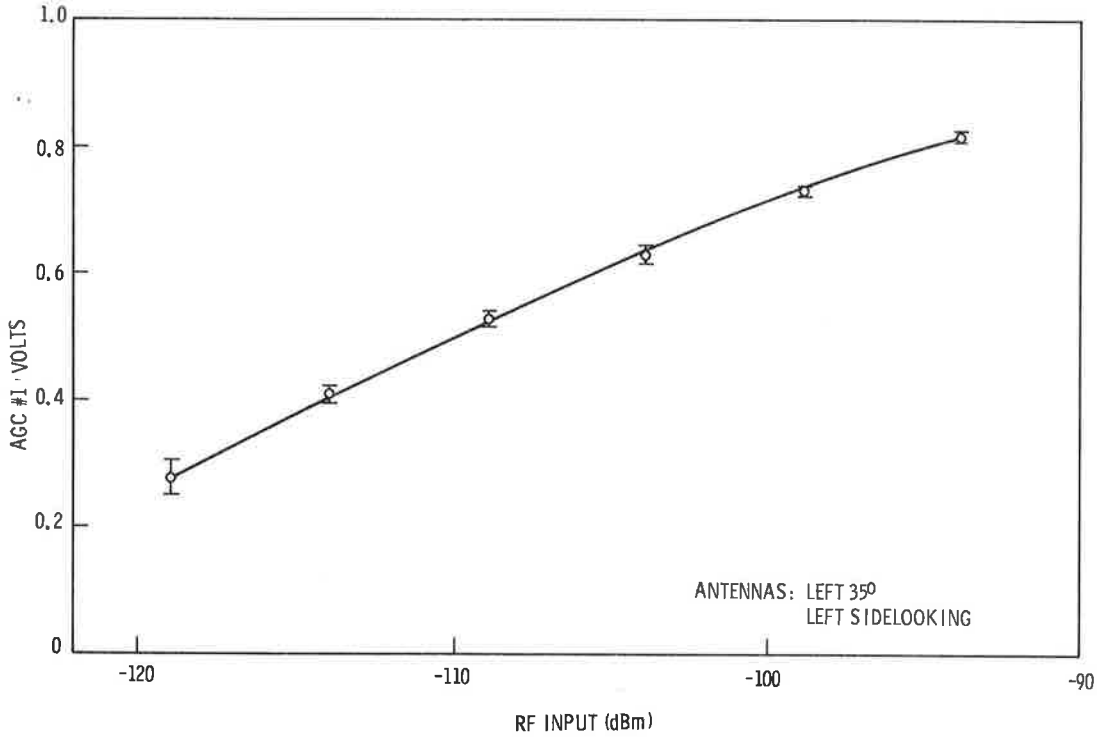

Figure E-2. 5-24-71 Run 4 Calibration, AGC #1

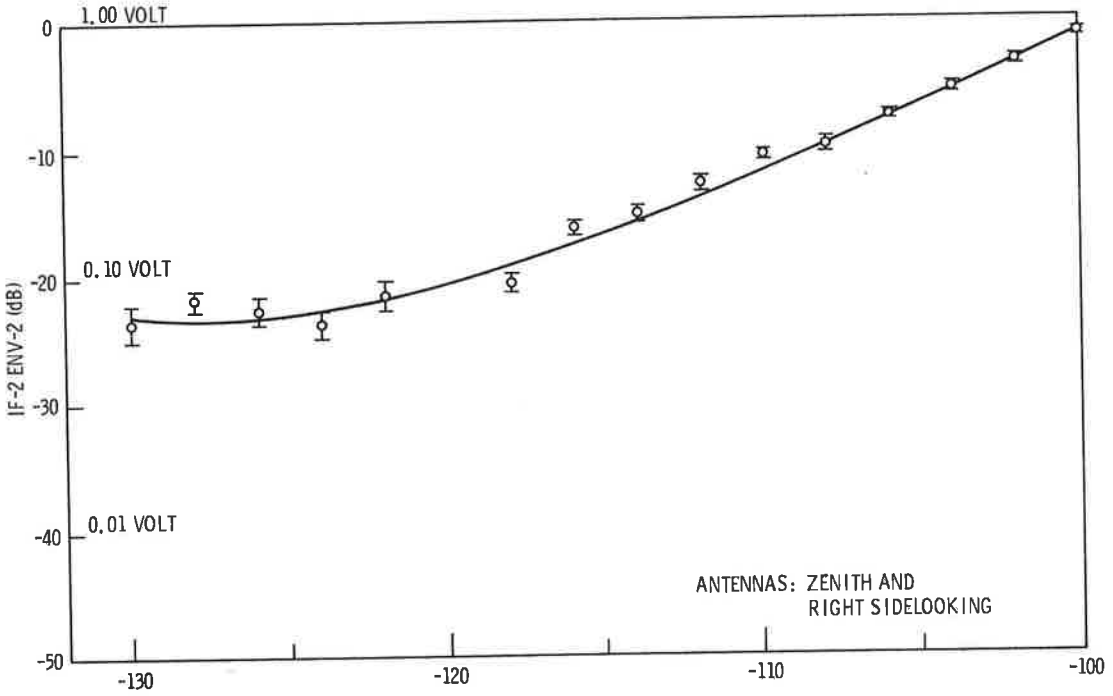

(a) RF INPUT (dBm)

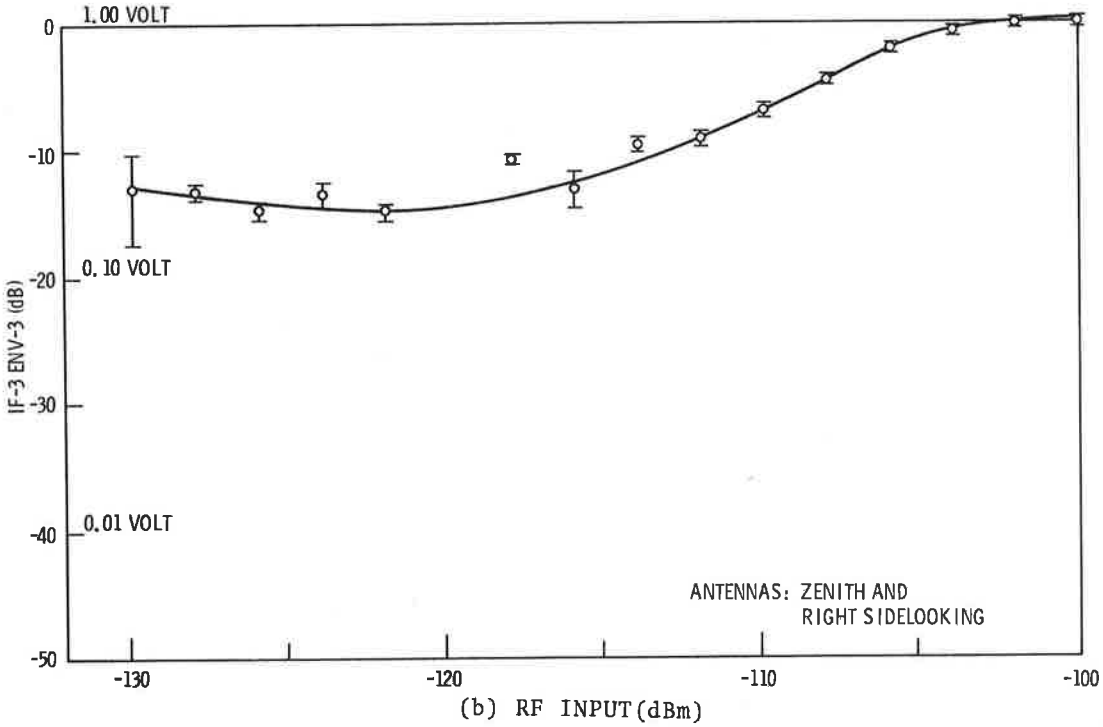

(b) RF INPUT (dBm)

Figure E-3. 10-1-71 Run 1 Calibration, IF-2,3 ENV-2

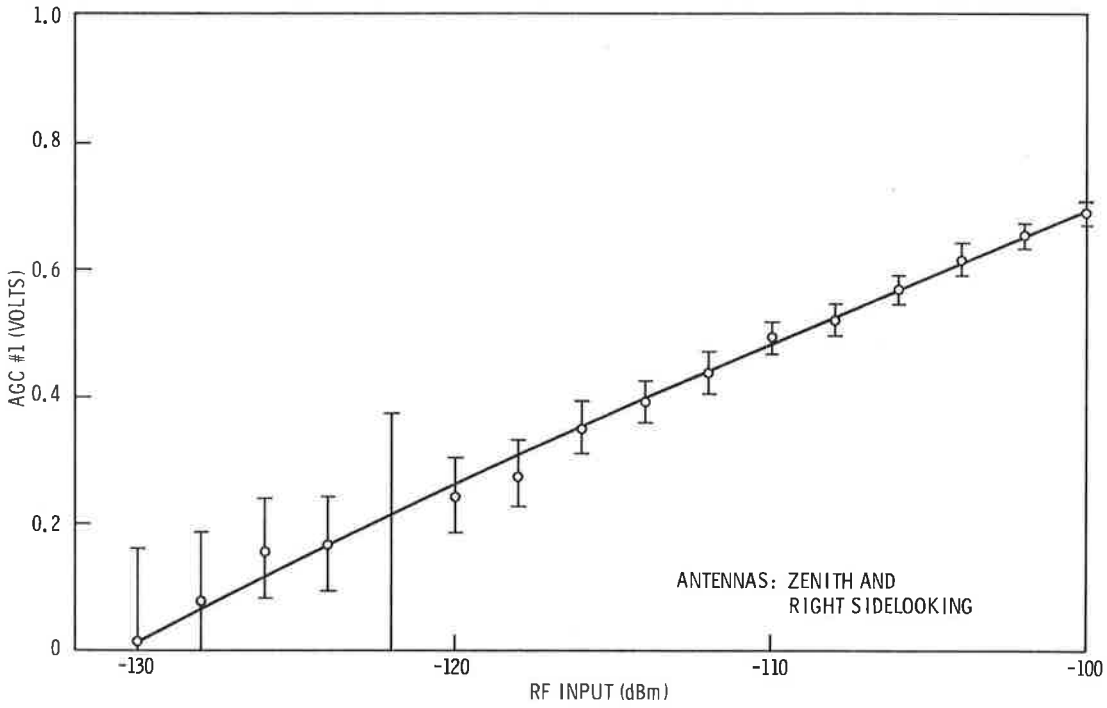

Figure E-4. 10-1-71 Run 1 Calibration, AGC #1

Figure E-4 shows a plot of the mean and standard deviation of the AGC 1 voltage. Figure E-5 shows a plot of the mean and standard deviation of the diode-detected levels of the Receiver 2 and 3 outputs. It will be noted that the first four levels of IF level #3 show saturation at 1.000 volt which is the upper limit of the HP Model 5610A Analog to Digital Converter. The averaging times for the diode-detected levels varied from 2.5 seconds to 3.4 seconds.

A comparison of the calculated envelope values (ENV-2) shown in Figure E-3 shows general agreement with the diode-detected values (level 2 and level 3) shown in Figure E-5. Averages of the positive values of IF-2 and IF-3 (raw data) show the same general characteristic as do Figures E-3 and E-5. The AGC #1 values shown in Figure E-4 do not however confirm the behavior of the IF envelope (ENV-2 values) or of the diode-detected levels. This apparent

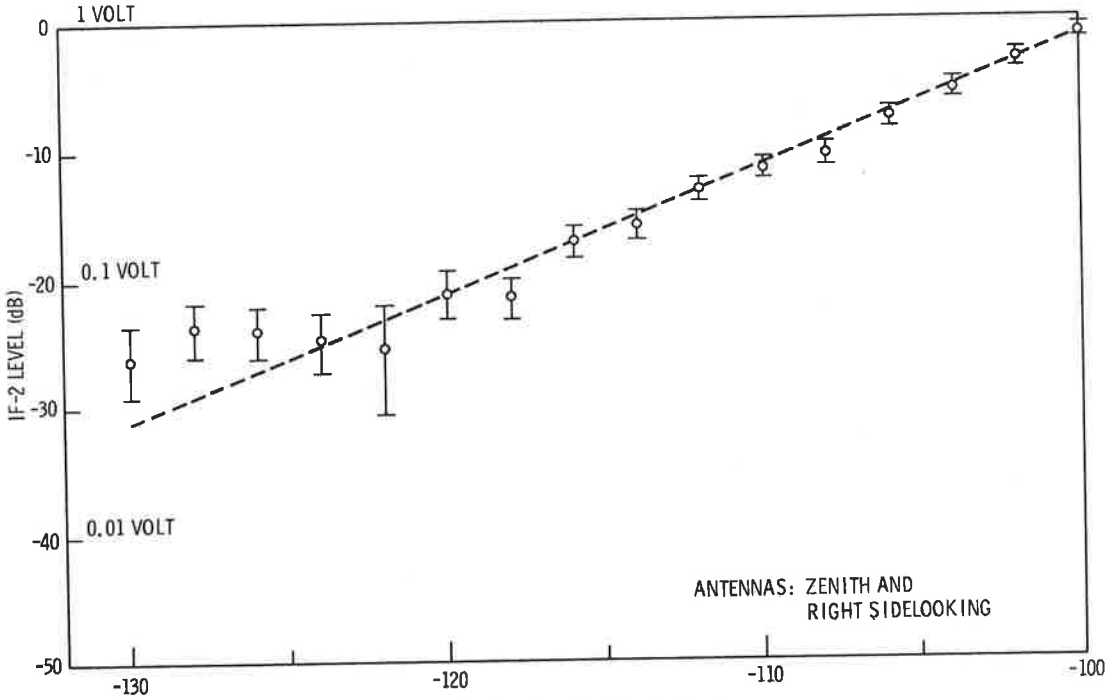

(a) RF INPUT (dBm)

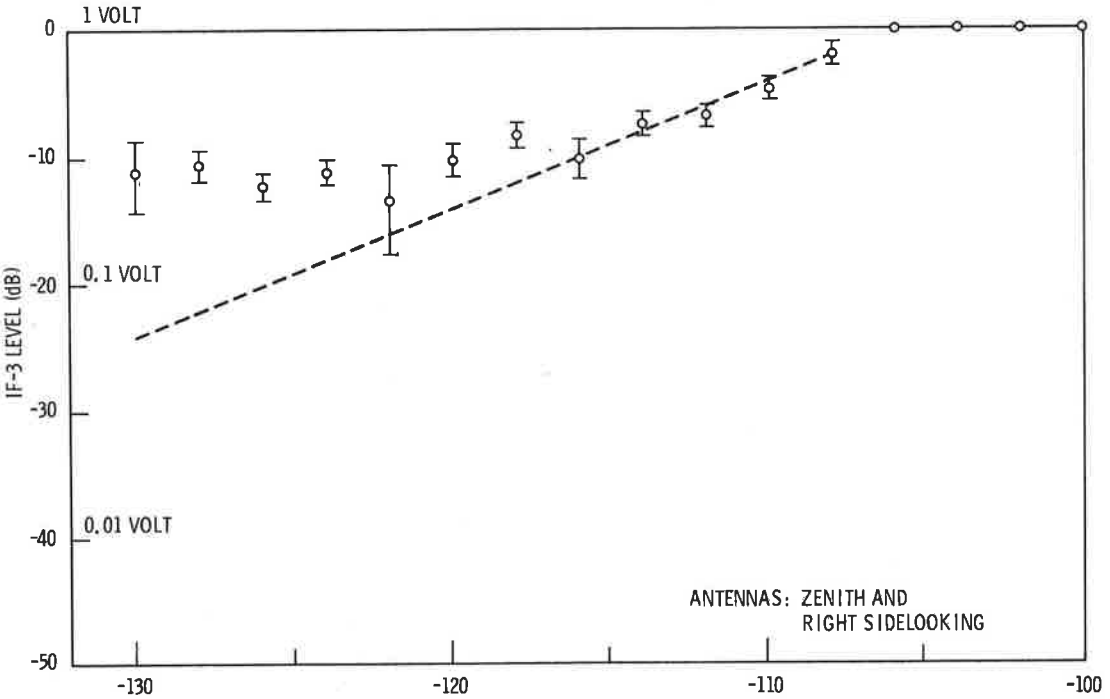

(b) RF INPUT (dBm)

Figure E-5. 10-1-71 Run 1 Calibration, Level 2,3

contradiction has not yet been resolved. Measurements made on the equipment at DOT/TSC indicate that the noise floor of the system should not be reached until the input level reaches approximately -140 dBm (at which point one can expect Receiver 1 to drop out of lock).

E-2-2 10-1-71 Run 4 File 2 Calibration

A power density spectrum was computed for the Receiver 2 and 3 IF outputs. The spectrum is an average of ten spectra, each representing 1 second of calibration data, and spans five different calibration levels.

The spectrum of IF-2 (raw data) shows a peak (carrier) at 1029 Hz with only one pair of sideband lines situated 927 Hz above and below the carrier frequency. The upper and lower sideband levels are -21.8 dB and -21.1 dB respectively with respect to the carrier. The 3 dB carrier linewidth is 2 Hz and the spectrum broadens to 4 Hz at -10 dB, 10 Hz at -20 dB, 31 Hz at -30 dB and finally reaches an approximate noise floor at a width of 111 Hz, 40 dB below the carrier. All other line components are 36 dB or greater below the carrier.

The spectrum of IF-3 (raw data) shows a peak (carrier) at 1029 Hz with a pair of sideband lines located 700 Hz above and below the carrier frequency. The amplitudes of the upper and lower sideband lines are -8.2 dB and -5.9 dB respectively with respect to the carrier. The 3 dB line width the carrier is 2 Hz and the spectrum broadens to 4 Hz at -10 dB, 10 Hz at -20 dB, 30 Hz at -30 dB and finally reaches a width of 110 Hz at an approximate noise floor of 40 dB below the carrier. All other line components are 25 dB or greater below the carrier.

Figure E-6 shows a plot of the mean and standard deviation of the envelope of the 5 KHz IF outputs of Receivers 2 and 3. The plots represent one second time averages with the exception of level 10 (118 dBm) where the averaging time is 0.750 second. The quantity shown is the output of the ENV-2 routine with N=8

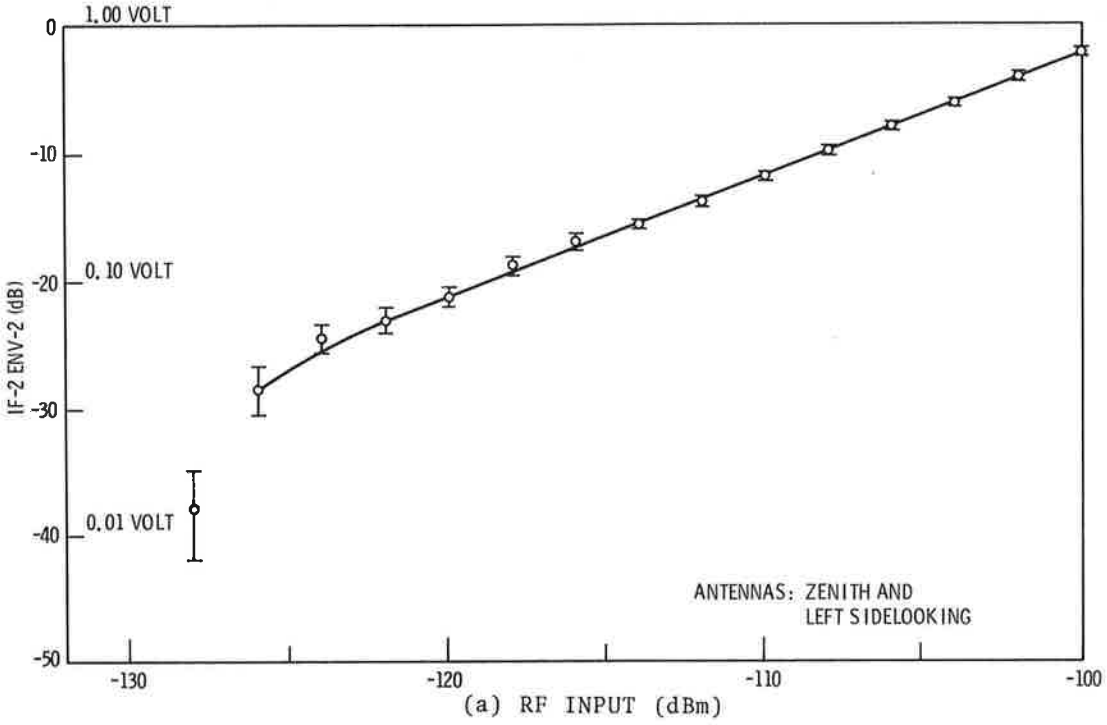

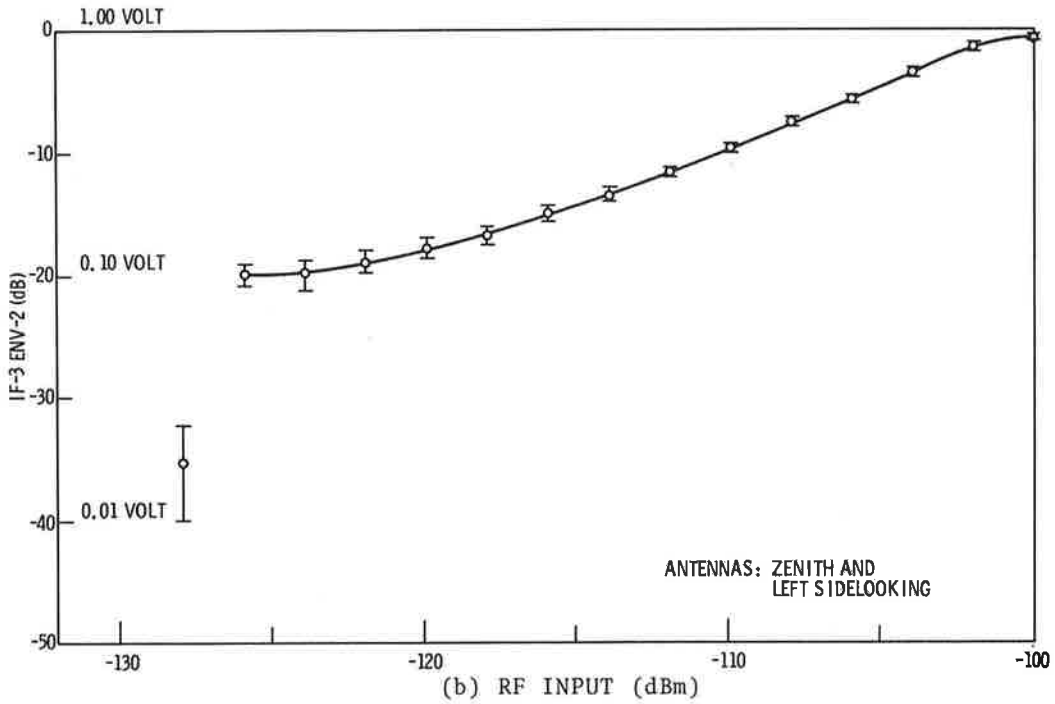

Figure E-6. 10-1-71 Run 4, File 2 Calibration

(125 Hz low-pass bandwidth) and K=150 (truncation width). Figure E-7 shows a plot of the mean and standard deviation of AGC #1 with a 1-second averaging time. Figure E-8 shows plots of the IF-2 and IF-3 diode detected levels. The averaging times for the IF levels vary from 2.5 seconds to 3.4 seconds. As in the case of the calibration for Run 1, we find general agreement between the calculated envelope values (Figure E-6) and the diode-detected levels (Figure E-8). In contrast to Run 1, however there is no agreement between the Receiver 2 and Receiver 3 outputs below a signal level of -120 dBm. The AGC #1 values (Figure E-7) generally confirm the Receiver 2 values. Multiple 100 millisecond time averages of the positive values of the Receiver 2 and 3 outputs (raw data) seem to generally confirm the behavior of the IF envelope (Figure E-6) and diode-detected levels (Figure E-8). Also, there is a lack of agreement at the lower signal levels between the AGC #1 values for Run 1 and the AGC #1 values for Run 4.

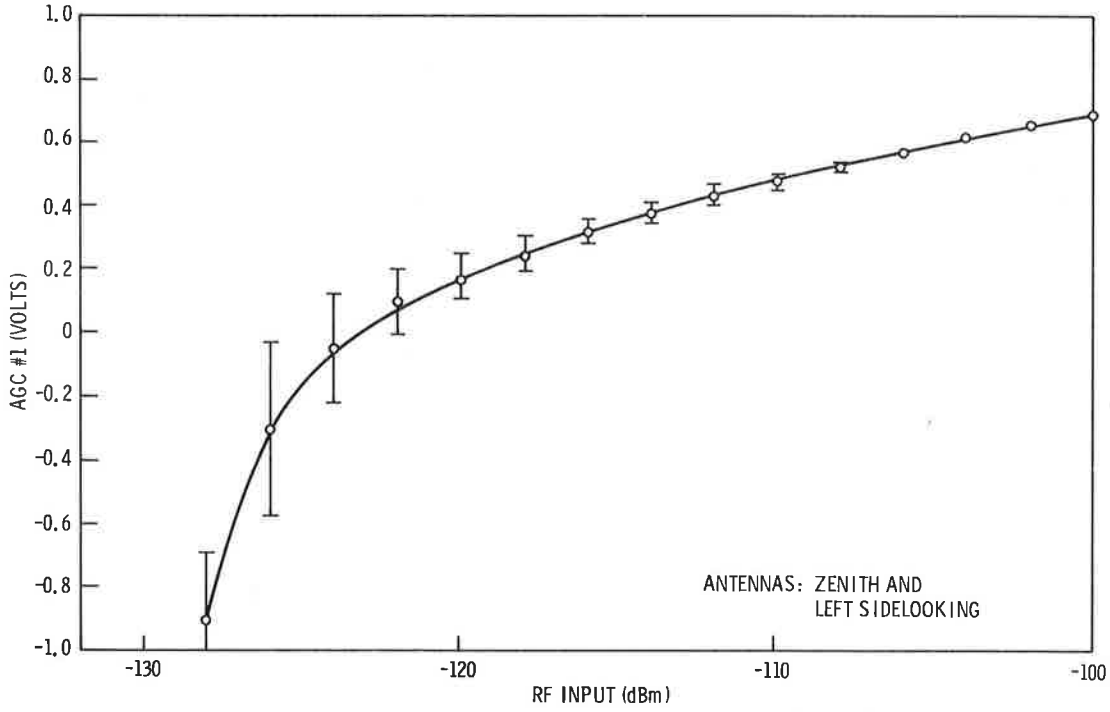

Figure E-7. 10-1-71 Run 4 Calibration, AGC #1

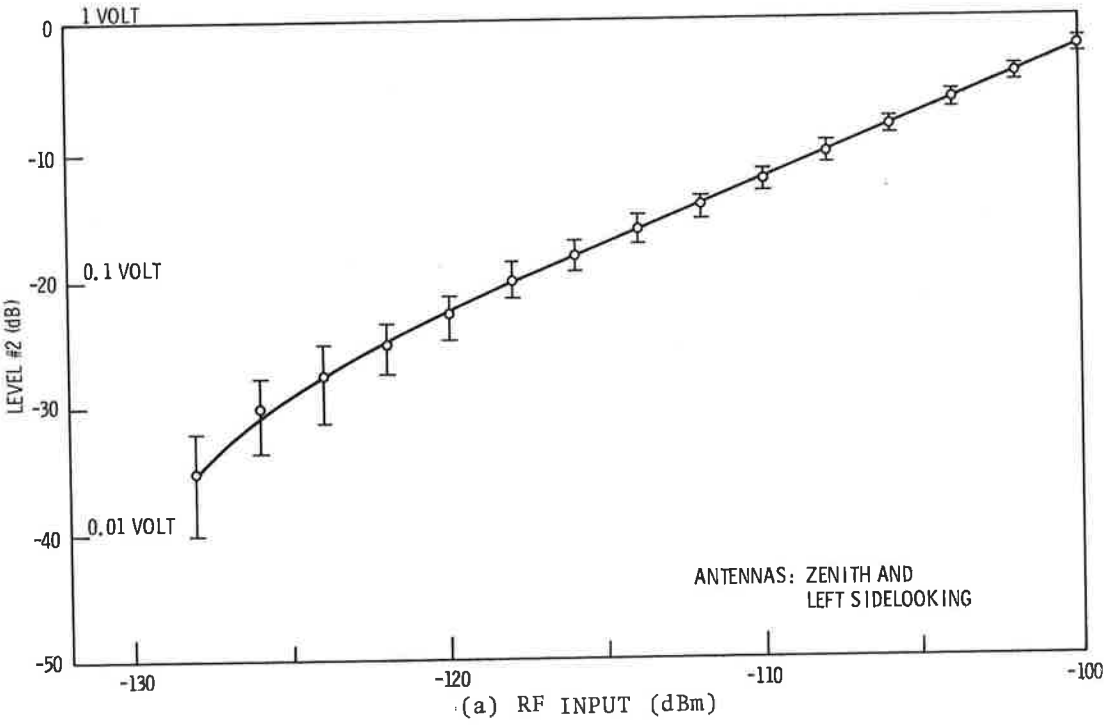

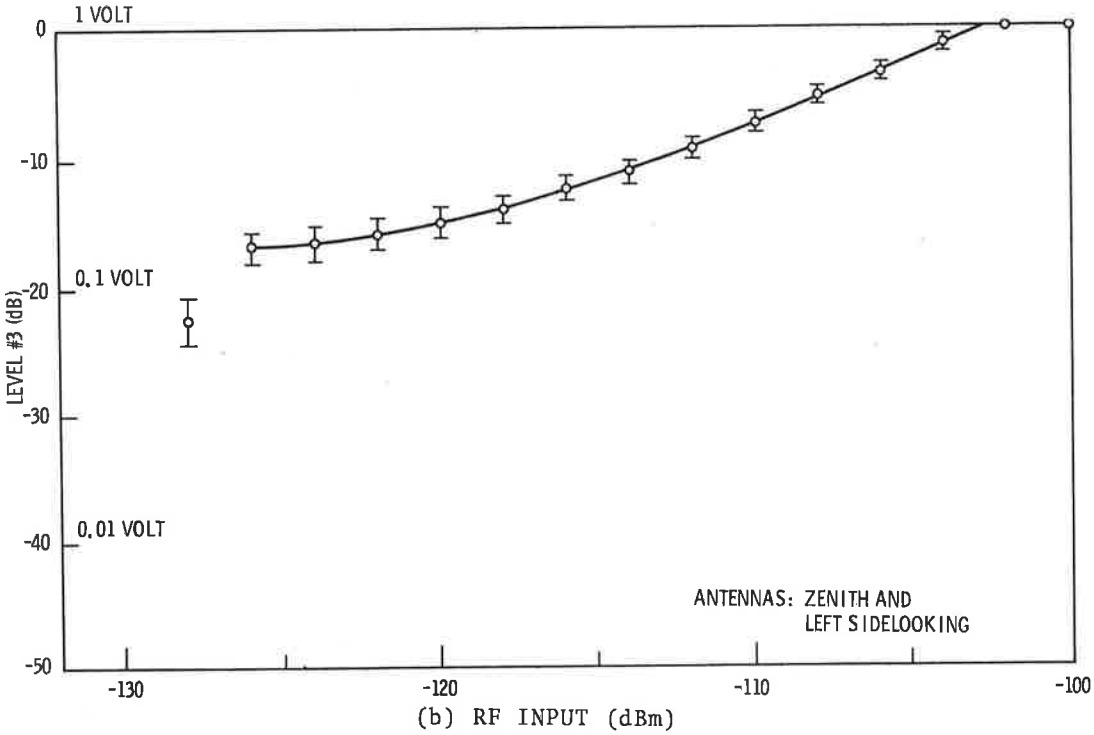

Figure E-8. 10-1-71 Run 4 Calibration, Level 2,3

E-3 CONCLUSIONS

The calibration tests show an acceptable linear receiver performance at all but the low levels. At these levels the samples are generally sparse since the probability is low. Since we do not use the data directly but, rather, test for similarity to a known distribution this weakness in the calibration is not crucial. In fact, since we are continually able to confirm a Ricean density with high confidence we must conclude that there are no significant nonlinearities or other discrepancies in the operation of the system.

APPENDIX F
DATA PARAMETERS PROBABILITY-DENSITY ESTIMATES

The intent of this Appendix is to determine reasonable estimates from the data of the parameters of a probability density when it is assumed to be Ricean, that is when

$$p(x) = \frac{x}{\psi_o} e^{-\left[\frac{x^2+p^2}{2\psi_o}\right]} I_o\left(\frac{xp}{\psi_o}\right) ,$$

It is known that the n^{th} moment $\overline{x^n} = E\left[x^n\right]$ takes the form

$$\overline{x^n} = (2\psi_o)^{n/z}\ \Gamma\left(\frac{n}{2}+1\right)\ {}_1F_1\left[-\frac{n}{2};\ 1;\ \frac{-p^2}{2\psi_o}\right]$$

where $\Gamma(x)$ is the gamma function and ${}_1F_1(\ )$ is the confluent hypergeometric function. Because of the awkward form of $p(x)$ it is extremely difficult to obtain a maximum likelihood estimate of the parameters. In addition all the odd moments can be shown to be alternating infinite series. However, the even moments take on the more useable form of

$$\overline{x^{2m}} = (2\psi_o)^m\ \Gamma(m+1)\ {}_1F_1\left[-m;\ 1;\ \frac{-p^2}{2\psi_o}\right]$$

$$= (2\psi_o)^m\ (m!)\ L_m\left(-\frac{p^2}{2\psi_o}\right)$$

where

$$L_m(x) = \sum_{i=o}^{m} (-1)^i \binom{m}{m-1} \frac{1}{i!}\, x^i$$

is the Laguerre polynomial. From this we see that

$$\overline{x^2} = (2\psi_o)\left[1 + \frac{p^2}{2\psi_o}\right] = 2\psi_o + p^2 \qquad \text{(F-1)}$$

$$\overline{x^4} = (2\psi_o)^2\, 2! \left[1 + 2\left(\frac{P^2}{2\psi_o}\right) + \frac{1}{2}\left(\frac{P^2}{2\psi_o}\right)^2\right]$$

$$= 2(2\psi_o)^2 + 4(2\psi_o)P^2 + (P^2)^2 \qquad \text{(F-2)}$$

It is known using the method of moments that by solving Equations F-1 and F-2 for ψ_o and P^2 we can derive asympototically efficient estimator $\hat{\psi}_o$ and $\hat{P}^2$ in terms of the sample moments $\overline{x_s^2}$ and $\overline{x_s^4}$. Thus

$$\hat{\psi}_o = \frac{\overline{x_s^2}}{2}\left[1 - \sqrt{2 - \frac{\overline{x_s^4}}{\left(\overline{x_s^2}\right)^2}}\right]$$

$$\hat{P}^2 = \overline{x_s^2}\sqrt{2 - \frac{\overline{x_s^4}}{\left(\overline{x_s^2}\right)^2}}$$

The sample moments $\overline{x_s^n}$ are defined as

$$\overline{x_s^n} = \frac{1}{N}\sum_{i=1}^{N} x_i^n$$

where x_i is the i^{th} sample and N is the sample size. The cumulative for the Ricean density then becomes

$$C(x) = \int_o^x \frac{x'}{\hat{\psi}_{o'}} e^{-\frac{x^2+\hat{P}^2}{2\hat{\psi}_o}} I_o\left[\frac{x'(\hat{P}^2)^{1/2}}{\hat{\psi}_o}\right] dx'$$

$$= \int_o^{\frac{x}{\sqrt{\hat{\psi}_o}}} r\, e^{-\frac{\left[r^2 + \left(\frac{\hat{P}^2}{\hat{\psi}_o}\right)\right]}{2}} I_o\left[r\left(\frac{\hat{P}^2}{\hat{\psi}_o}\right)^{1/2}\right] dr$$

$$= 1 - Q\left[\left(\frac{\hat{P}^2}{\hat{\psi}_o}\right)^{1/2}, \frac{x}{\sqrt{\hat{\psi}_o}}\right]$$

APPENDIX G
ANTENNAS

The Convair CV-880 aircraft used in the L-band experiment was equipped with five L-band antennas which were used to make multipath measurements. The antennas were of two general types insofar as use is concerned. A reference antenna provides a signal relatively free of multipath effects to the master receiver (Receiver 1) which is phase locked to the signal. See Section 2.1 for a detailed description of system operation. A two-element sidelooking antenna provides composite signals with approximately equal gain in the direct and indirect paths from the balloon. The signals from the horizontally polarized and vertically polarized elements of the sidelooking antenna are fed to Receivers 2 (horizontal) and 3 (vertical) which operate as L-Band to 5 KHz frequency translators. The master receiver (Receiver 1) provides a frequency reference to Receivers 2 and 3, thereby tracking out Doppler and low-frequency instabilities in the direct signal. The 5 KHz IF signals from Receivers 2 and 3 are the signals of primary interest in this report.

G-1 ANTENNA TYPES AND LOCATION

The reference antenna is selected from one of three right-hand circularly polarized antennas mounted on the top of the fuselage. One antenna is located on the top centerline of the aircraft and offset antennas are located 35° to the right and left of the centerline. The three reference antennas are located fore-and-aft about mid-way over the wings at station 803.5 as shown in Figure G-1. The sidelooking antennas are located on either side of the aircraft in the forwardmost window ports at station 422.8 (see Figure G-1). Boresight for the sidelooking antennas is 78° down from zenith. During the West Coast series of measurements the three reference antennas (zenith and 35° offset) were Diamond Antenna and Microwave Corp., Model DIC-6980 circularly polarized slot antennas. The 78° sidelooking antennas were Boeing Co. orthogonal mode slot antennas. In the French test series, a Boeing orthogonal mode slot antenna was used at the zenith position

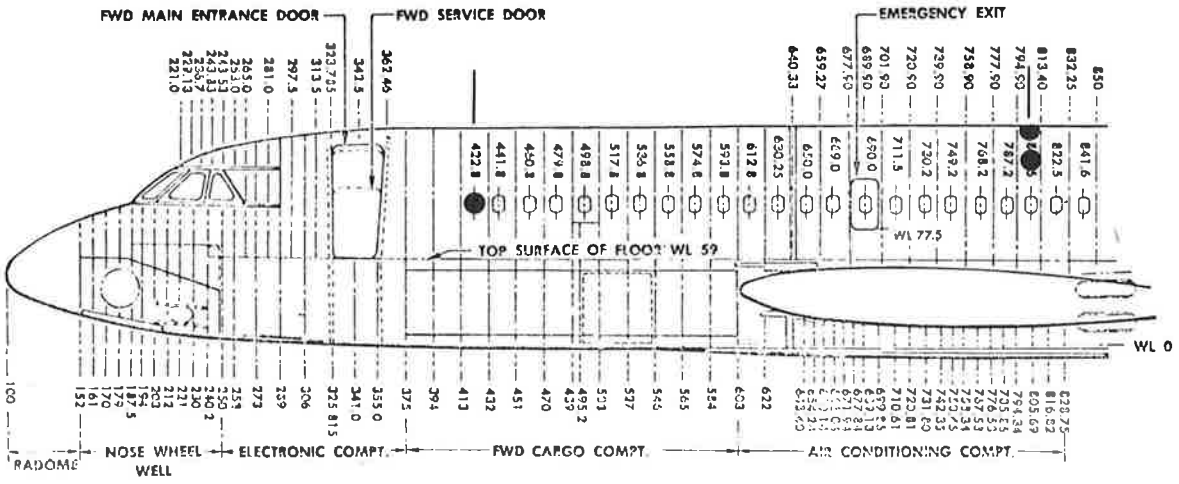

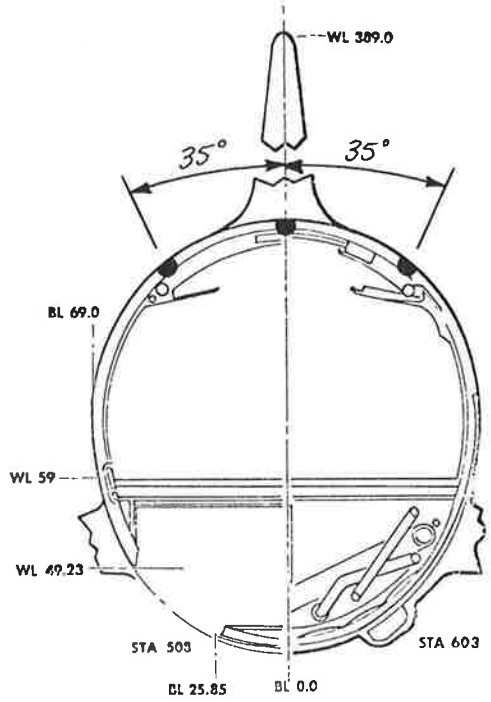

Figure G-1, Fuselage Station Locations CV-880[10]

replacing the Diamond antenna. In this instance the "horizontal" and "vertical" outputs of the Boeing Antenna are combined in a hybrid to provide an output sensitive to right hand circular polarization. The Diamond Antennas were oriented such that the major axis of the 35° offset antenna patterns was along the pitch axis (slot length dimension parallel to the roll axis of the aircraft) while the opposite is true of the zenith antenna. This arrangement provides broad coverage in the pitch plane for the zenith antenna with broad coverage in the roll plane for the 35° offset antennas. In the case of the Boeing antenna, the pattern is symmetric and hence there is no preferred orientation for the zenith antenna.

G-2 ANTENNA PATTERNS

G-2-1 Zenith

Figures G-2 and G-3 show the radiation patterns of the Diamond antenna for the zenith position. The patterns were made using a 1/10 scale model of a Convair CV-880 aircraft and at a frequency of 15.5 GHz. The scale is in dB and it will be noted that the gain at $\theta = 80°$ (10° above the horizon) is from 6 to 8 dB greater than the gain at $\theta = 100°$ (10° below the horizon) at $\phi = 90°, 270°$. With the aircraft flying roughly circular patterns about the balloon, Figure G-3b indicates a 7 dB discrimination against the multipath signal (for a balloon elevation angle of 10° and an aircraft roll angle of 2°) for right-hand circular polarization. Some additional discrimination against the multipath signal can be expected due to polarization reversal and de-polarization upon reflection and scattering from the ocean surface. Figures G-4 and G-5 show similar patterns for the Boeing antenna located at zenith. In the case of the Boeing antenna, the patterns were made at a frequency of 32 GHz using a 1/20 scale model of a Boeing 707 aircraft. The antenna was located on the top centerline of the model at a position equivalent to station 820 on the Convair CV-880. Examination of Figure G-5b shows a discrimination of between 5 dB and 7 dB for a balloon elevation angle of 10° for right-hand circular polarization. In this instance we have assumed

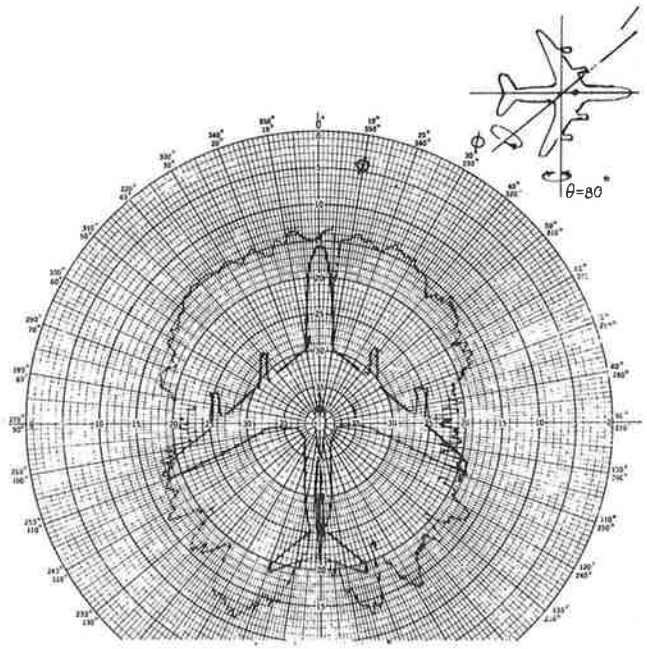

θ = 80°

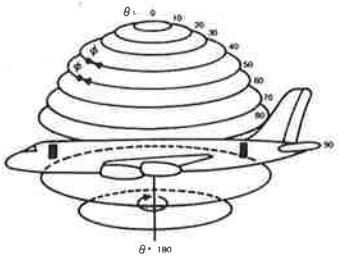

Antenna Location - Station 803.5
Angular Location from Zenith - 0°
Transmitter Polarization - RHC
Frequency - 15.5 GHz

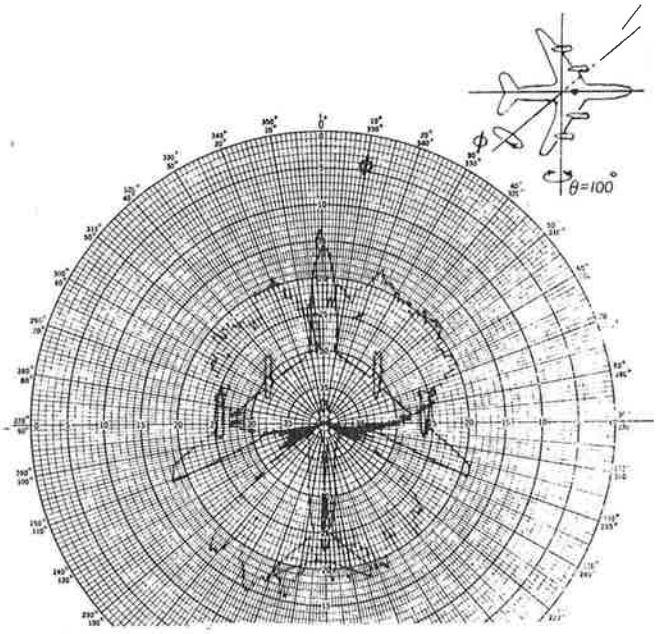

θ = 100°

Figure G-2. One-Tenth Scale Model CV-880, Diamond Model DIC-6980[10]

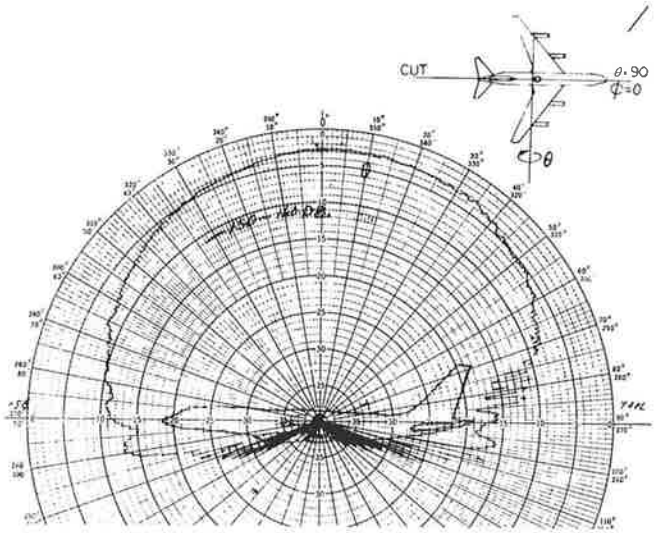

Antenna Location - Station 803.5
Angular Location from Zenith - 0°
Transmitter Polarization - RHC
Frequency - 15.5 GHz

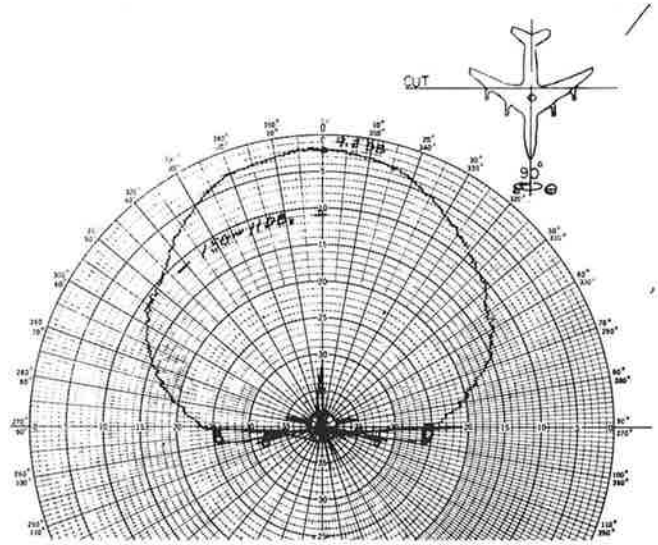

Figure G-3. One-Tenth Scale Model CV-880, Diamond Model DIC-6980 Circularly Polarized Slot Antenna[10]

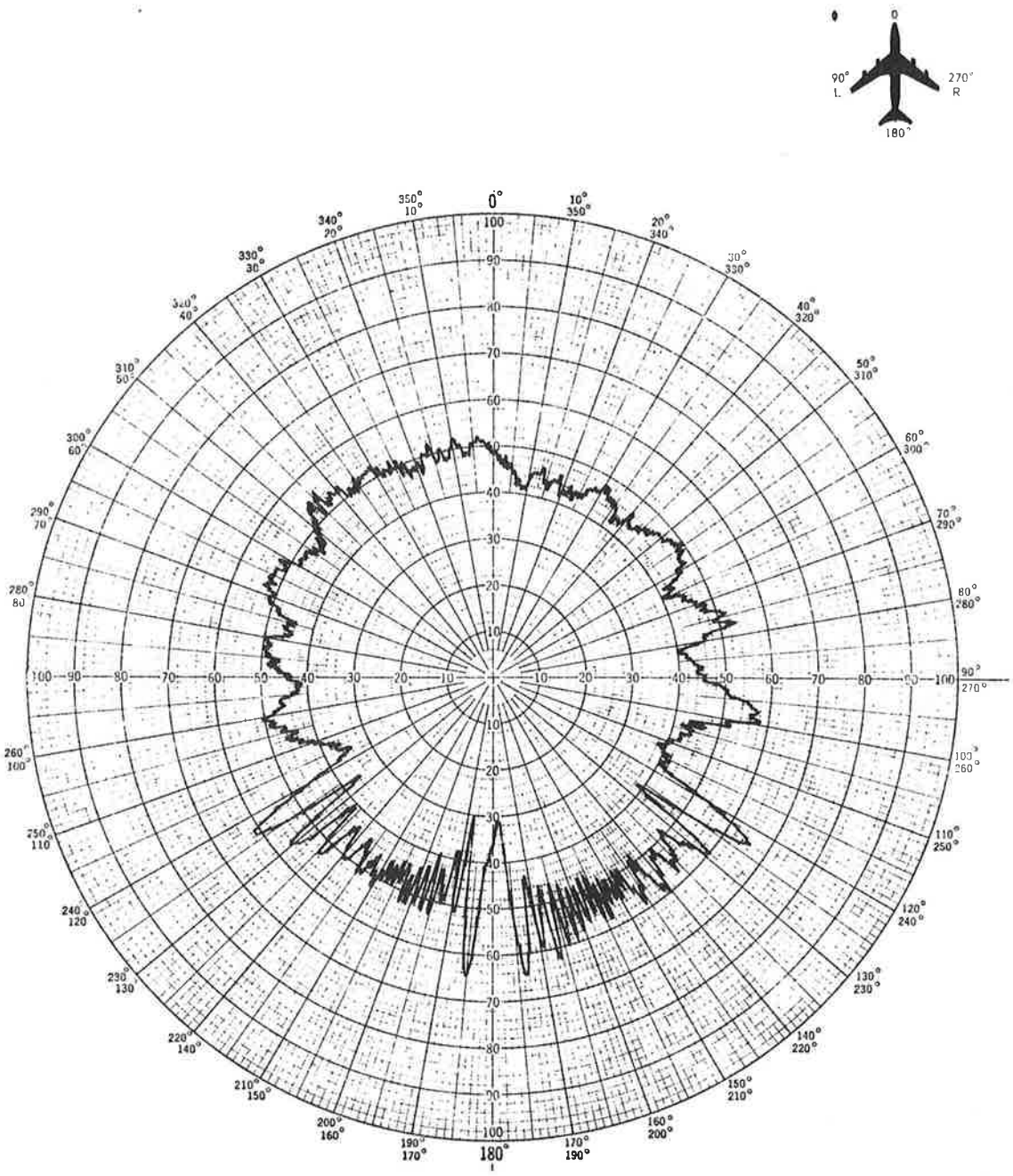

Figure G-4a. One-Twentieth Scale Model Boeing 707, Boeing Orthogonal Mode Slot Antenna, Station 820 Top C.L., RHC

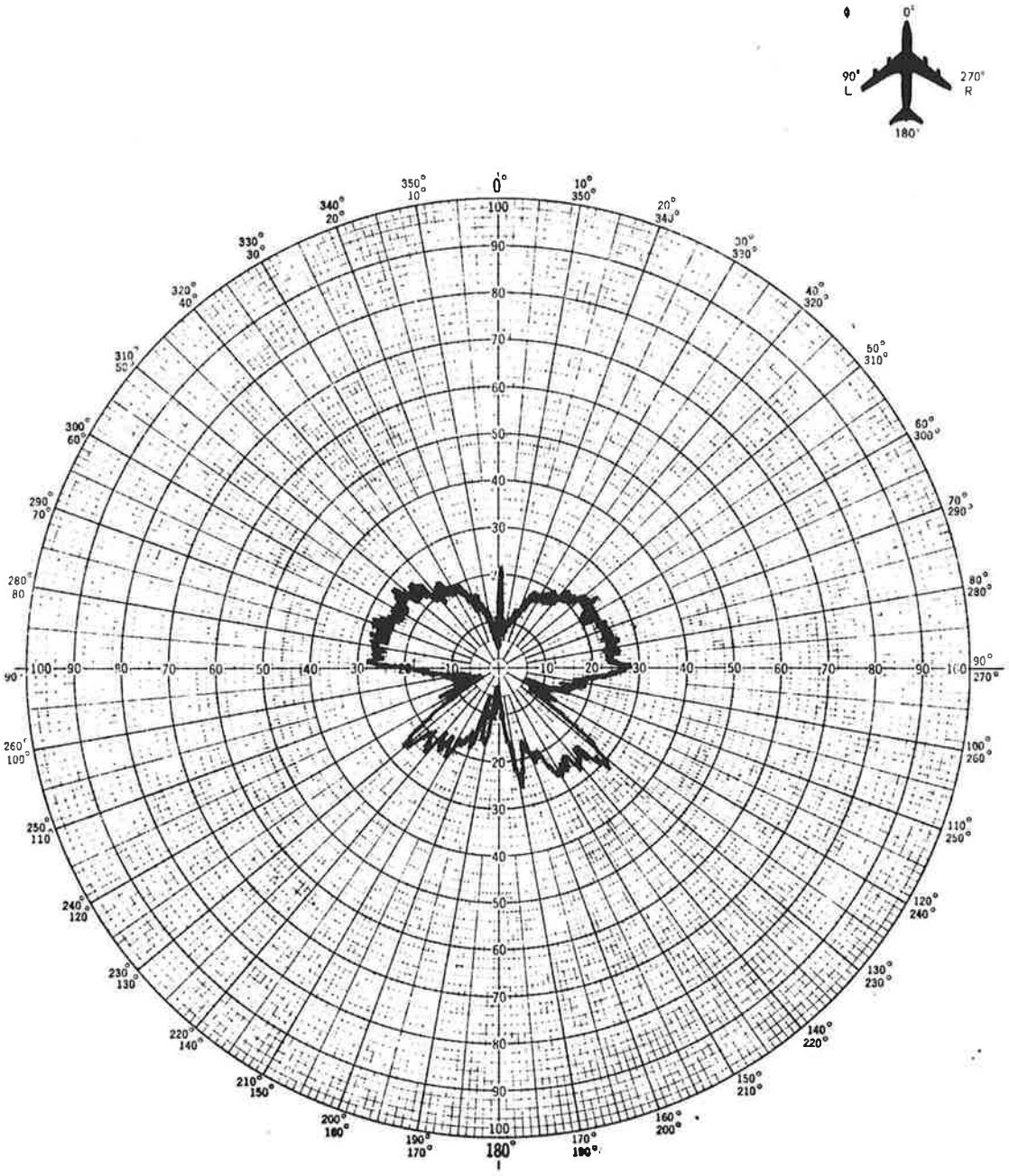

Figure G-4b. One-Twentieth Scale Model Boeing 707, Boeing Orthogonal Mode Slot Antenna, Station 820 Top C.L., RHC

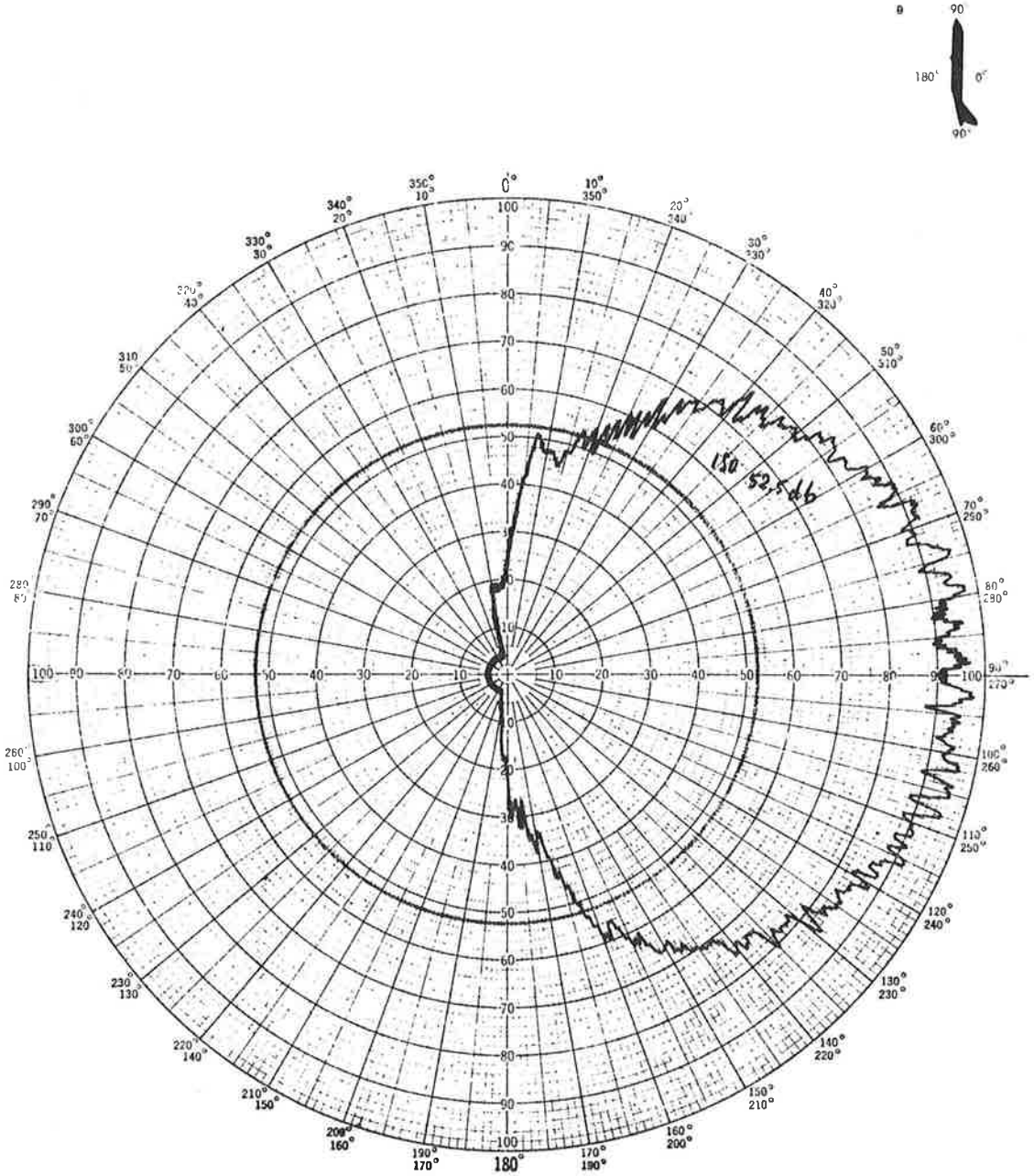

$\phi = 0°$

Figure G-5a. One-Twentieth Scale Model Boeing 707, Boeing Orthogonal Mode Slot Antenna, Station 820 Top C.L., RHC

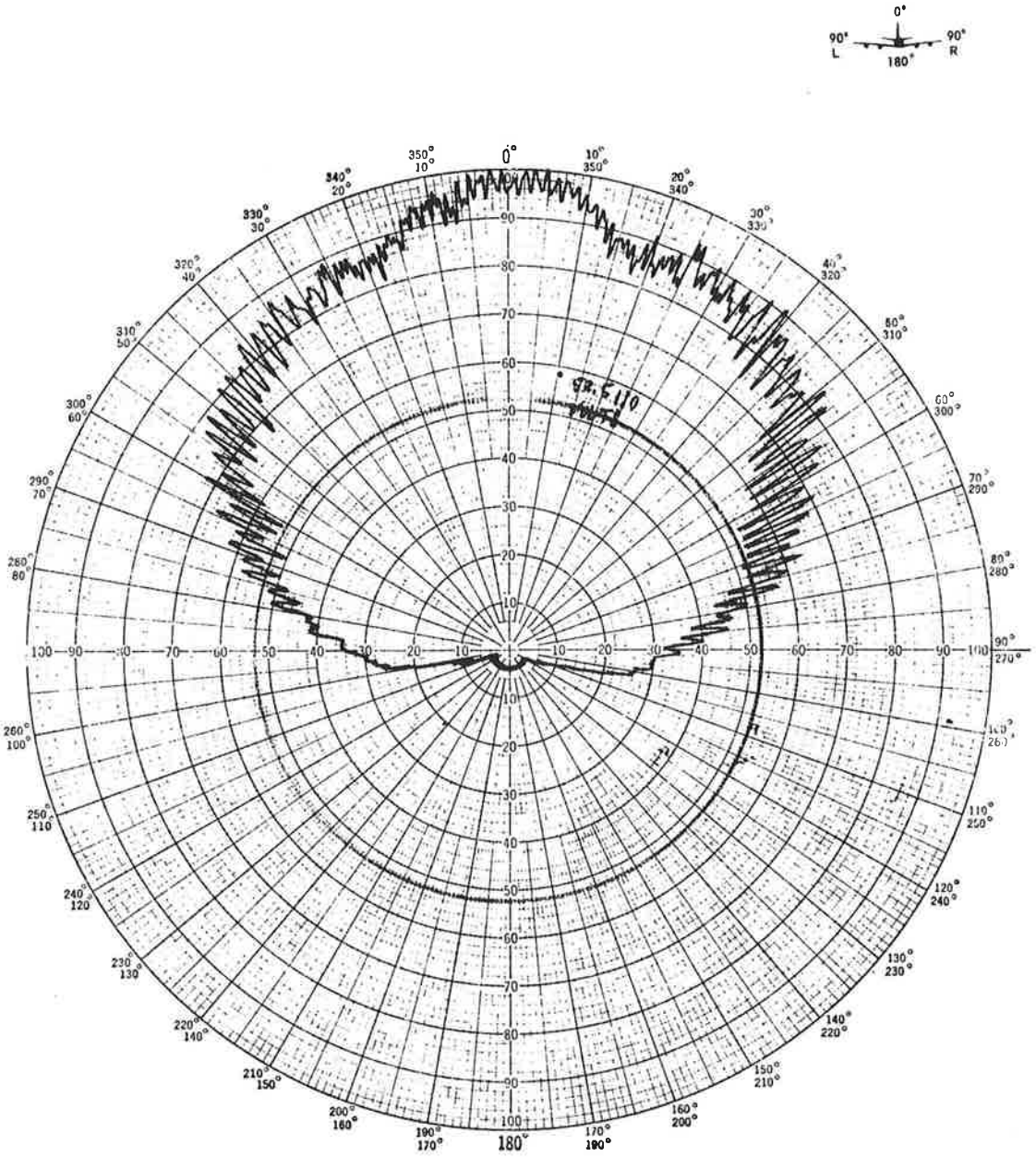

Figure G-5b. One-Twentieth Scale Model Boeing 707, Boeing Orthogonal Mode Slot Antenna, Station 820 Top C.L., RHC

the aircraft roll angle to be zero since the aircraft was flown along a number of straight line tracks which approximated a circular path about the balloon in the French tests where this antenna was used.

G-2-2 35° Offset Antenna

Figures G-6 and G-7 show the radiation patterns of the Diamond slot-antenna for the 35° position. Again if we assume a balloon elevation angle of 10° (2° aircraft roll angle) we note from Figure G-7b that one can anticipate approximately 4 dB rejection of the multipath signal neglecting any additional discrimination due to polarization reversal or depolarization of the multipath signal.

G-2-3 78° Sidelooking Antennas

Now let us consider the antennas used to provide signals to Receivers 2 and 3; i.e., the sources of the 5 KHz IFs (IF-2 and IF-3) which are digitized at a 4 KHz rate and upon which the data reduction in this report is based. As previously mentioned, the sidelooking antennas are the Boeing orthogonal mode slot antenna which was used as a zenith reference antenna in the French tests.

G-3 HORIZONTAL POLARIZATION

Figures G-8 and G-9 show the radiation patterns (conical pattern polar diagrams) for the vertical slot which is sensitive to horizontal polarization. The pattern shown in Figure G-8 corresponds to a cone 10° above the horizon (neglecting aircraft roll), while the pattern shown in Figure G-9 corresponds to a cone 10° below the horizon neglecting aircraft roll. The possible effects of small changes in aircraft heading relative to the balloon are evident these figures. Note for example, that a ± 5° change in balloon bearing from the aircraft (from 265° to 275°) can produce a maximum change in antenna gain of approximately 2 dB in the balloon-to-aircraft path (see Figure G-8). Since the fine structure in the pattern has a periodicity of approximately 2° we may experience variations of nearly 2 dB with a heading change of ± 1° relative to the balloon. Examination of the Figure G-9 shows a

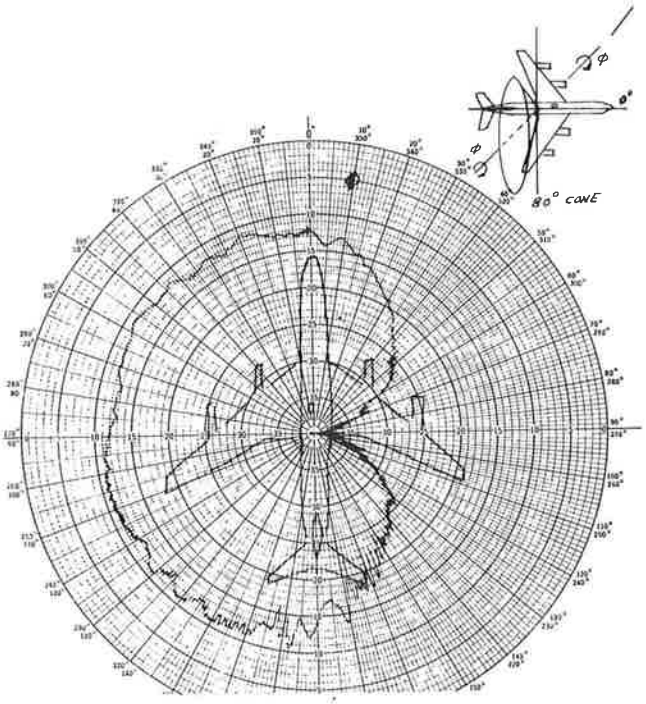

θ = 80°

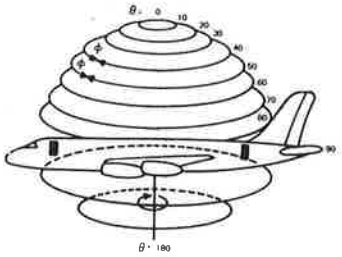

Antenna Location - Station 803.5°
Angular Location from Zenith -
35° Down Port Side
Transmitter Polarization - RHC
Frequency - 15.5 GHz

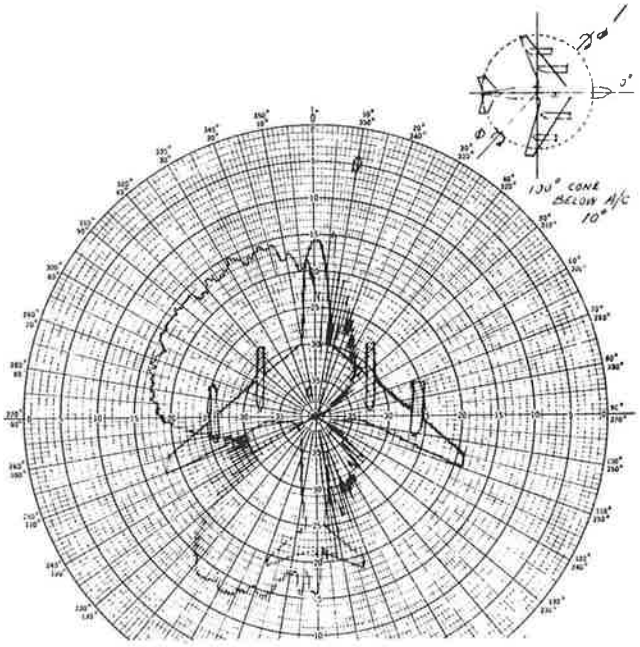

θ = 100°

Figure G-6. One-Tenth Scale Model CV-880, Diamond Model DIC-6980 Circularly Polarized Slot Antenna[10]

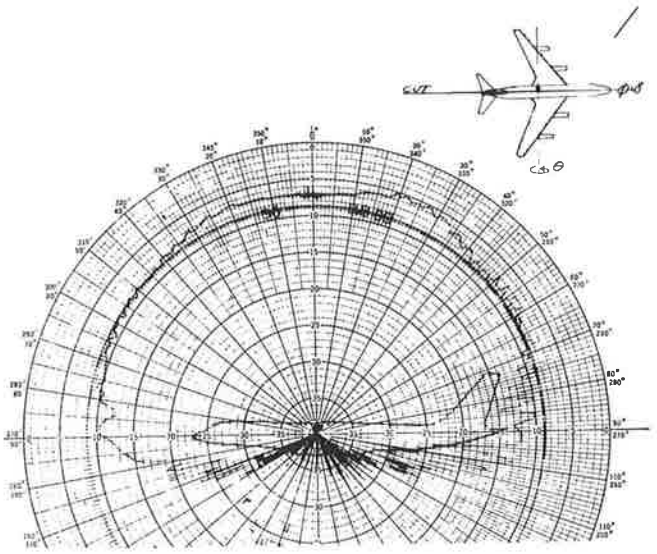

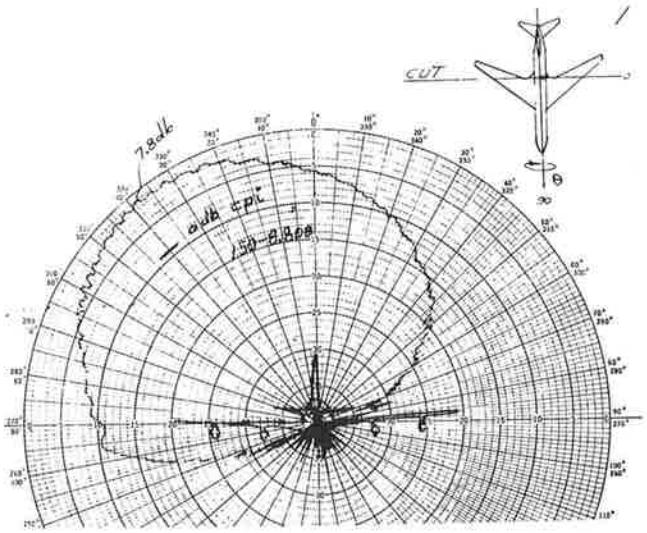

Antenna Location - Station 803.5°
Angular Location from Zenith -
35° Down Port Side
Transmitter Polarization - RHC
Frequency - 15.5 GHz

Figure G-7. One-Tenth Scale Model CV-880, Diamond Model DIC-6980 Circularly Polarized Slot Antenna[10]

somewhat less severe situation in the case of the multipath scattering. Here the gain variation is only 1.4 dB over a ± 5° relative balloon bearing change (265° to 275°). In considering these patterns, however, one must keep in mind the fact that they were made on a 1/20 scale model and that the scattered (multipath) power comes not from a point source, but from an extended source on the ocean surface. It is also perhaps worth noting that the average gain difference over a ± 5° sector between the patterns of Figure G-8 and G-9 is only about 0.25 dB. Let us now consider the great circle pattern shown in Figure G-10. This figure shows the pattern in a plane whose normal is parallel to the longitudinal axis of the aircraft. In the West Coast measurements, the aircraft was flying a circular pattern around the balloon and hence we must add the aircraft roll angle to the balloon elevation in using the plots. Consider a roll of 2° (typical of the West Coast flight) and balloon elevation angles of 8°, 10°, and 12° (also corresponding to the West Coast flight). Figure G-10 shows that the antenna gain in the direction of indirect path is equal to the gain in the direction of the direct path. In the French test series, the aircraft approximated a circular path by flying a number of straight-line segments. If we assume a zero aircraft roll angle for this case and use balloon elevation angles of 5°, 10°, and 15° (corresponding to the data presented in this report), we have indirect to direct relative gains of 0.5 dB, -0.7 dB and -.06 dB respectively (see Figure G-10).

G-4 VERTICAL POLARIZATION

Figures G-11 and G-12 show the corresponding conical patterns for the horizontal slot which responds to vertically polarized waves. In this case we find a variation of approximately 1.1 dB over a ± 5° change in balloon relative bearing for both the direct path (Figure G-11) and the indirect path (Figure G-12). The average antenna gain over ± 5° (265° to 275°) in the indirect path (Figure G-12) relative to that in the direct path (Figure G-11) is less than 0.1 dB for the case of a 10° balloon elevation angle neglecting aircraft roll. The relative antenna gains for the indirect path to the direct path are -0.3 dB, 0.1 dB and -0.3 dB for balloon

Antenna Location - Station 422.8
Angular Location from Zenith - 78° Down Port Side
Frequency - 32 GHz
Polarization - Horizontal (E_ϕ)

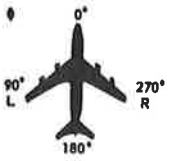

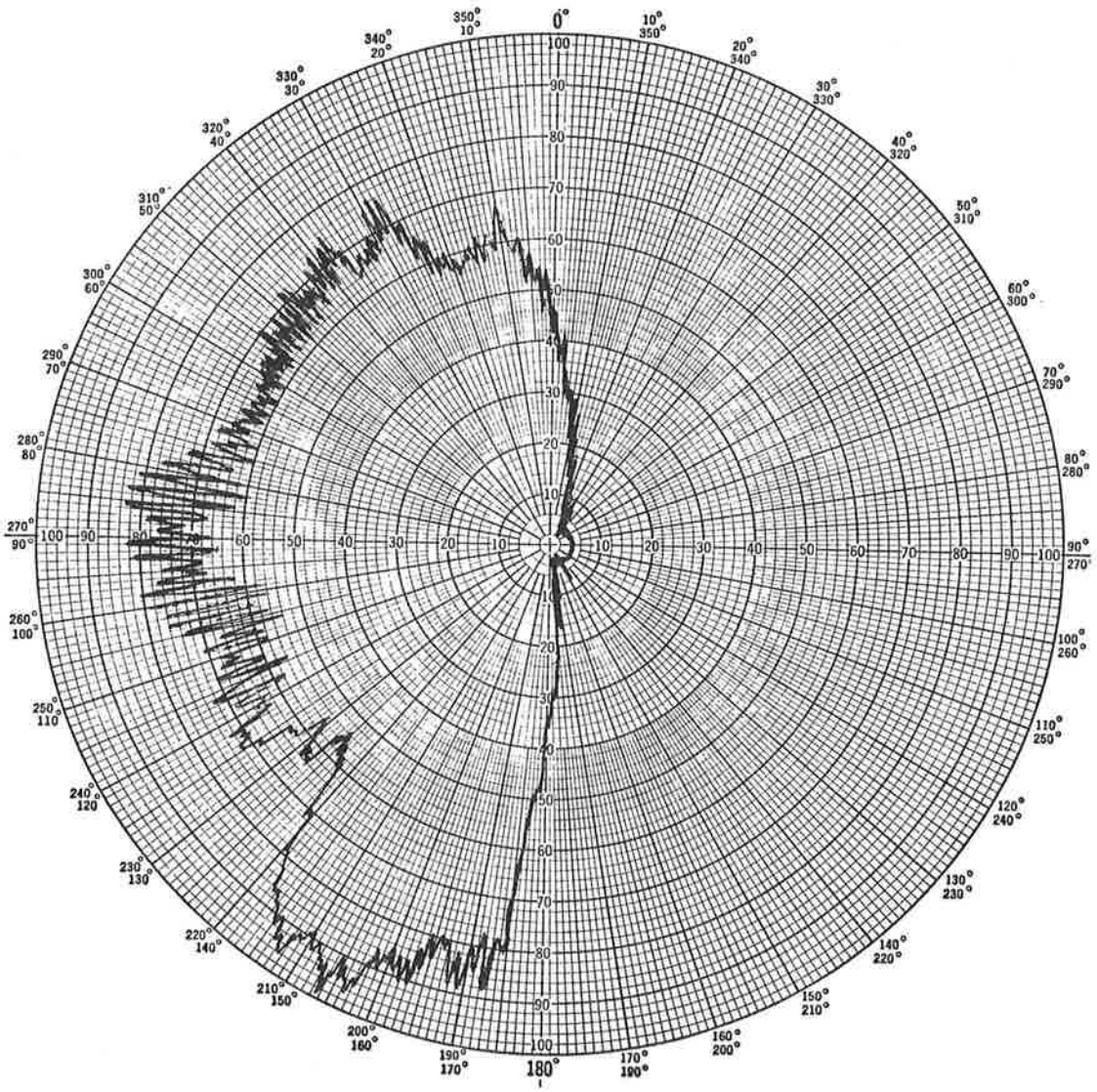

$\theta = 80°$

Figure G-8. One-Twentieth Scale Model Boeing 707, Boeing Orthogonal Mode Slot Antenna, Slot Vertical

Antenna Location - Station 422.8
Angular Location from Zenith - 78° Down Port Side
Frequency - 32 GHz
Polarization - Horizontal (E_ϕ)

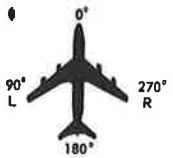

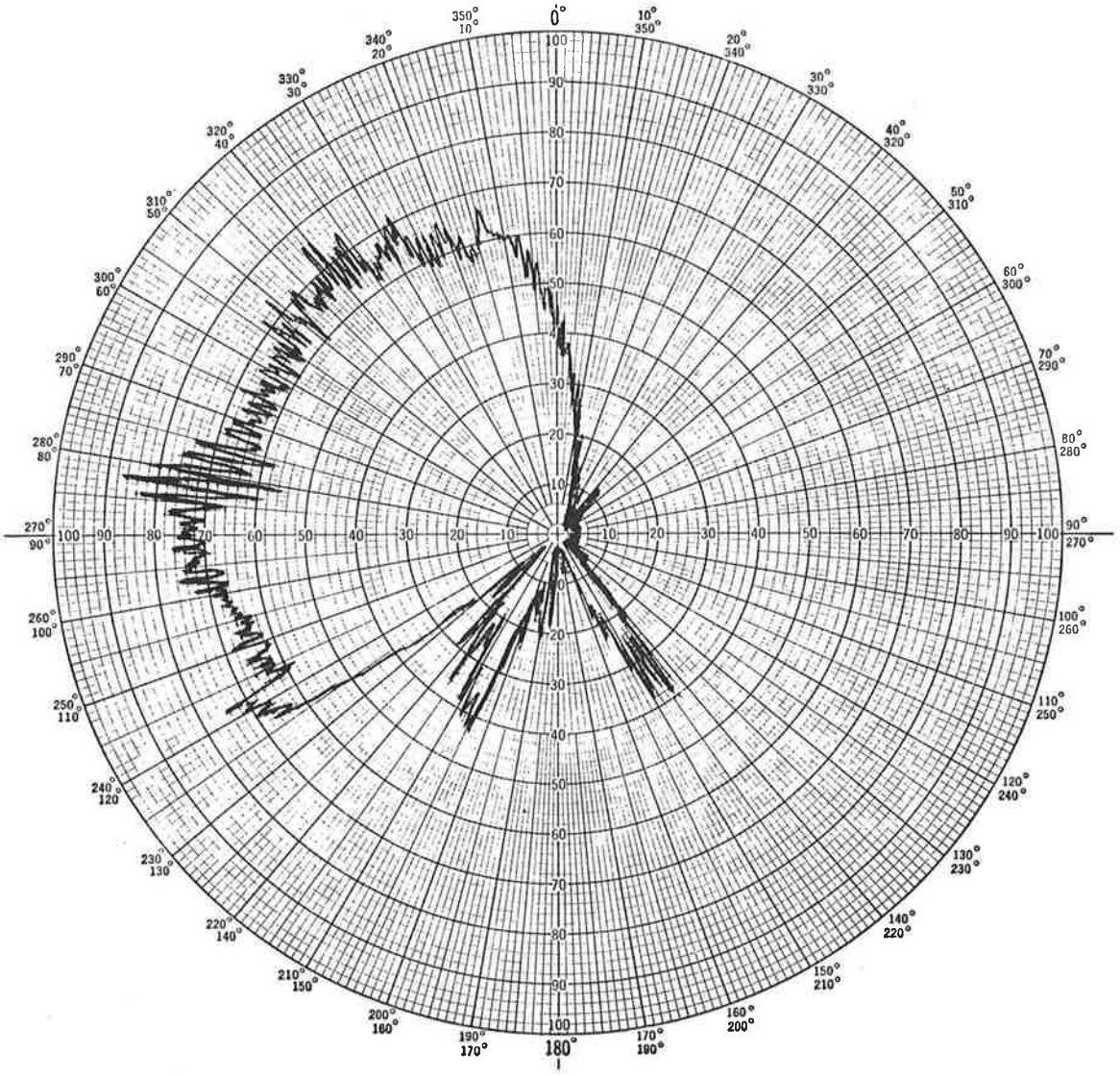

θ = 100°

Figure G-9. One-Twentieth Scale Model Boeing 707, Boeing Orthogonal Mode Slot Antenna, Slot Vertical

Antenna Location - Station 422.8
Angular Location from Zenith - 78° Down Port Side
Frequency - 32 GHz
Polarization - Horizontal (E_ϕ)

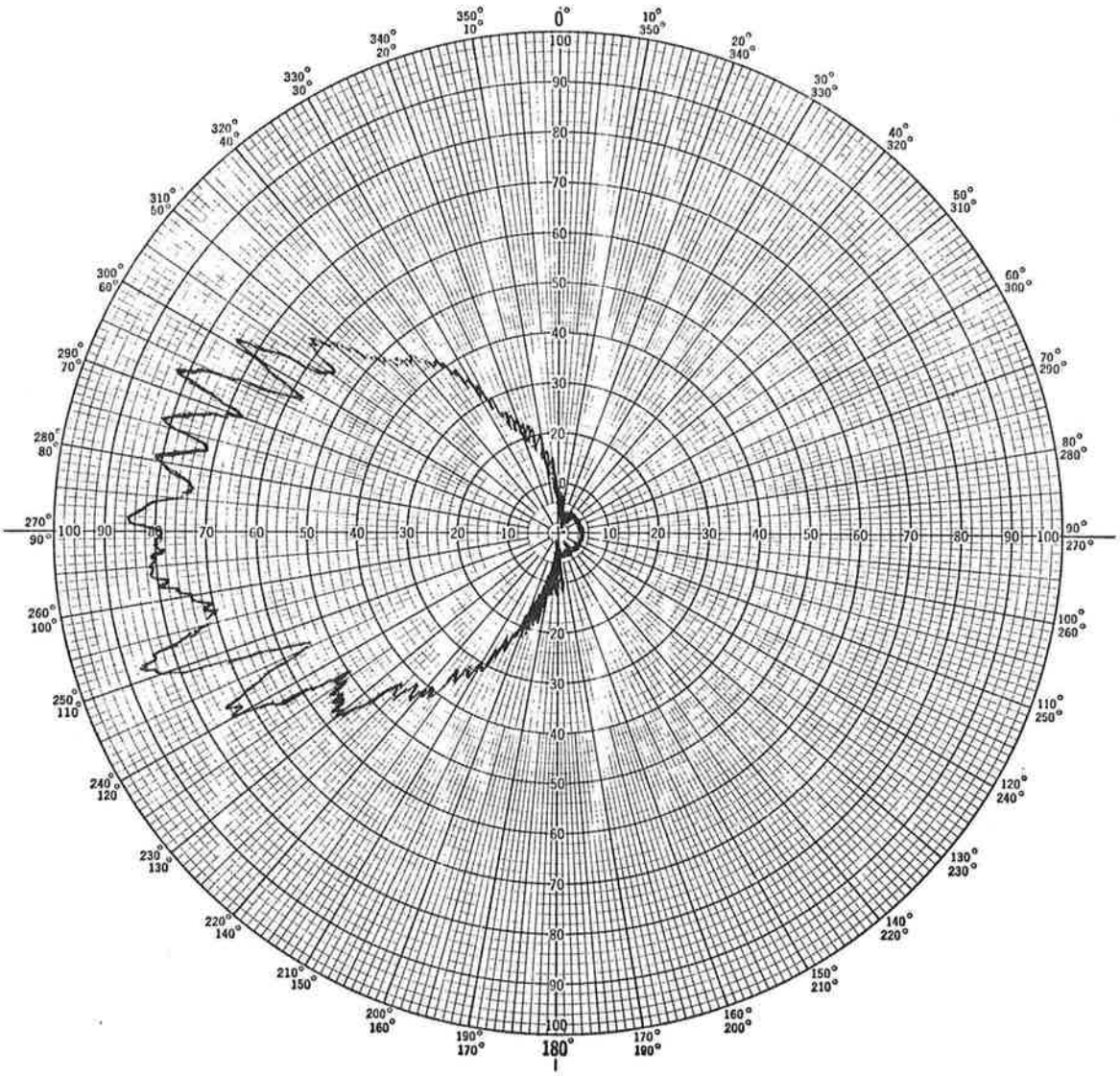

Figure G-10. One-Twentieth Scale Model Boeing 707, Boeing Orthogonal Slot Antenna, Slot Vertical

Antenna Location - Station 422.8
Angular Location from Zenith - 78° Down Port Side
Frequency - 32 GHz
Polarization - Vertical (E_θ)

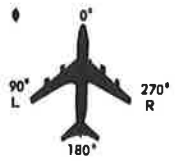

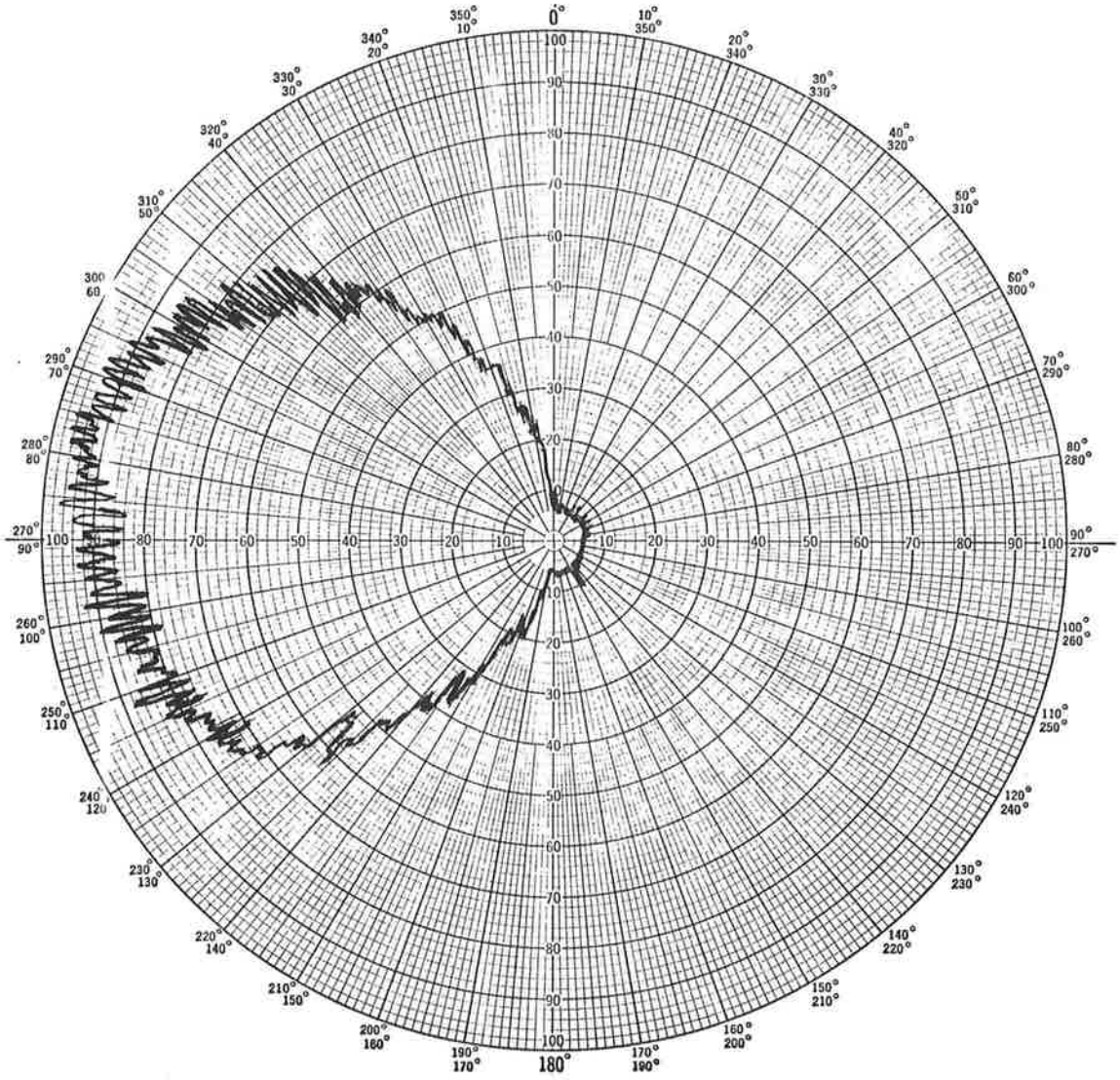

θ = 80°

Figure G-11. One-Twentieth Scale Model Boeing 707, Boeing Orthogonal Mode Slot Antenna, Slot Horizontal

Antenna Location - Station 422.8
Angular Location from Zenith - 78° Down Port Side
Frequency - 32 GHz
Polarization - Vertical (E_θ)

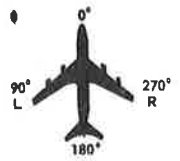

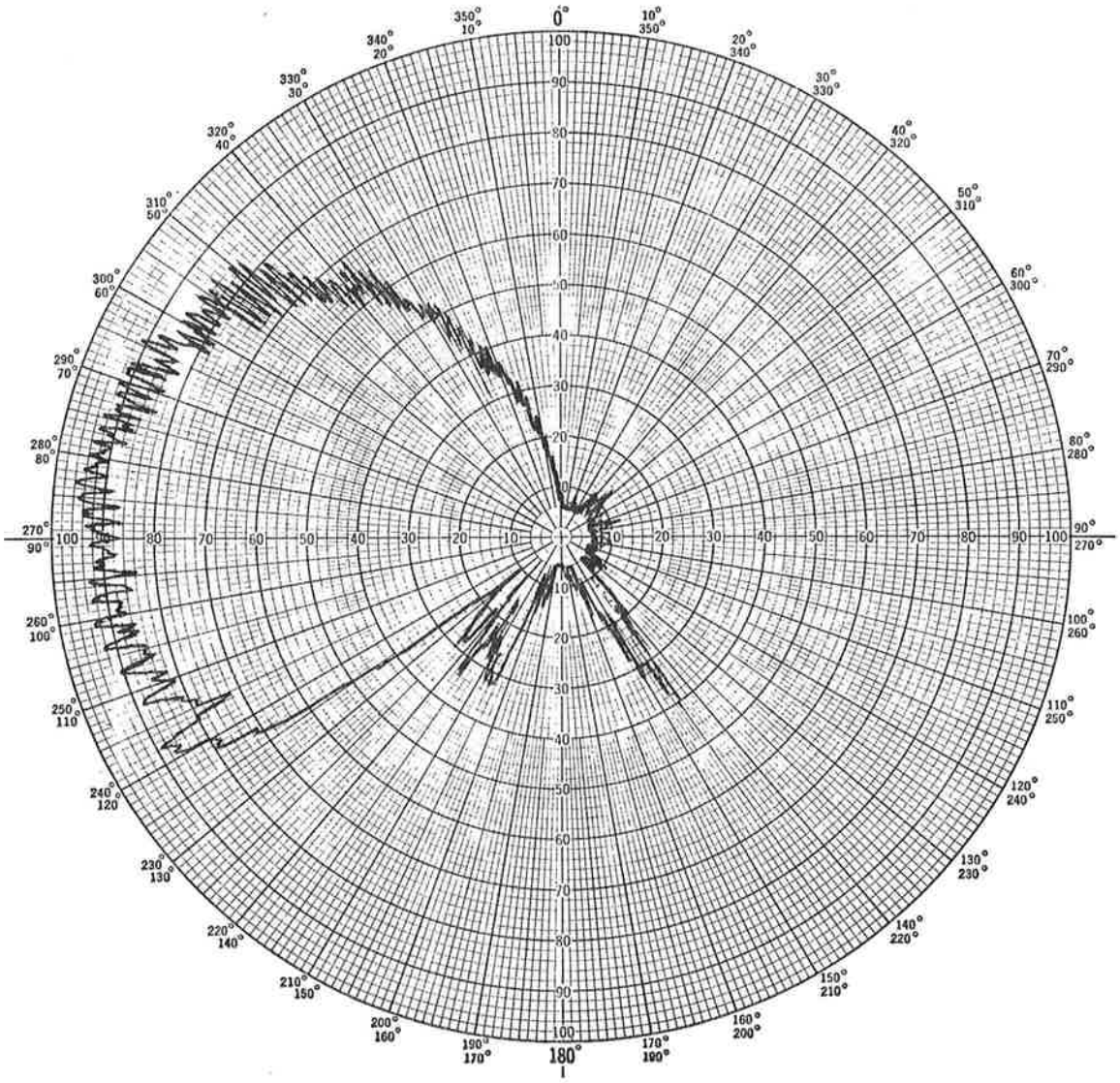

$\theta = 100°$

Figure G-12. One-Twentieth Scale Model Boeing 707, Boeing Orthogonal Mode Slot Antenna, Slot Horizontal

Antenna Location - Station 422.8
Angular Location from Zenith - 78° Down Port Side
Frequency - 32 GHz
Polarization - Vertical (E_θ)

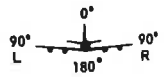

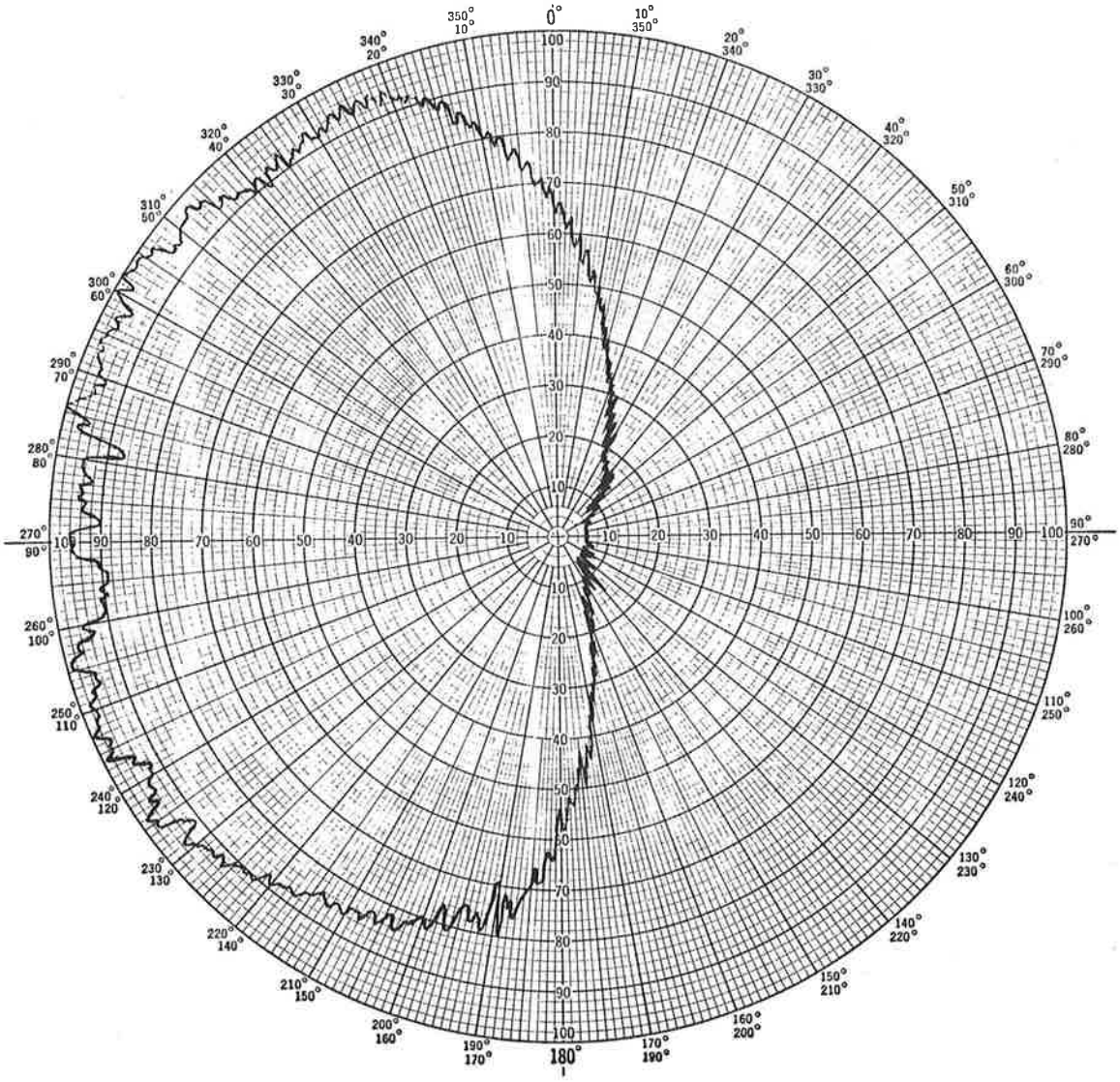

ϕ = 90°

Figure G-13. One-Twentieth Scale Model Boeing 707, Boeing Orthogonal Mode Slot Antenna, Slot Horizontal

elevation angles of 8°, 10°, and 12° (assumed aircraft roll equal to 2°), corresponding to the West Coast flight and -0.4 dB, 0.1 dB and 0.1 dB for balloon elevation angles of 5°, 10°, and 15° (aircraft roll equal to 0°), corresponding to the flights in France (see Figure G-13). We must once again caution the reader that these values are based upon antenna patterns taken on a 1/20 scale model of a Boeing 707 aircraft and not actual measured data on the Convair CV-880. Also, we have neglected the fact that the scattered power density in the indirect path must be integrated over the solid angle subtended by the scattering region. The values presented in this Appendix assume a point source for the multipath located below the aircraft by the magnitude of the balloon elevation angle. The intent of this Appendix is not to provide antenna corrections for the data but rather to present a qualitative description of the aircraft antenna installation.

APPENDIX H
VERIFICATION OF CHANNEL MODEL

Some of the conclusions indicated in section 5 bear on problems of current interest in satellite-system design. The most important fact appears to be that the character of the multipath for this narrowband channel implies a "clutter" model with Gaussian statistics. Thus, the nature of the random process can be completely characterized by second-moment theory. Hence, detailed measurements of the delay Doppler scatter function are all that should be needed for system design. Furthermore, a synthetic channel simulator will provide a complete representation of the channel characteristics when Gaussian noise is properly introduced into the taps. Since the multipath is Gaussian, the envelope statistics are Ricean.* Consequently, all information on envelope-fade statistics can be obtained from table H-1[9] once the direct-to-diffuse ratio is known. An example is given in figure H-1, where the threshold is related to the median. In addition, any antenna discrimination can be added as an increase of the direct-to diffuse ratio.

* The first-order density of the phase was computed to be uniformly distributed for every run measured, both long-and-short term.

TABLE H-1. RESULTANT AMPLITUDE (THRESHOLD) FOR A GIVEN FADE PROBABILITY (P) AS FUNCTION OF SIGNAL-TO-NOISE RATIO ($P^2/2\psi_0$) IN DECIBELS
(From Reference 9)

$P^2/2\psi_0$ \ P	0.0001	0.0002	0.0005	0.001	0.002	0.005	0.01	0.02
+40	0.2257	0.2150	0.2000	0.1880	0.1752	0.1570	0.1419	0.1254
+35	0.3976	0.3789	0.3528	0.3318	0.3094	0.2775	0.2511	0.2221
+30	0.6958	0.6636	0.6186	0.5823	0.5437	0.4884	0.4425	0.3920
+25	1.2035	1.1496	1.0738	1.0124	0.9470	0.8529	0.7745	0.6880
+20	2.0431	1.9560	1.8328	1.7327	1.6254	1.4703	1.3401	1.1955
+18	2.5063	2.4021	2.2548	2.1346	2.0056	1.8183	1.6607	1.4851
+16	3.0582	2.9351	2.7604	2.6177	2.4639	2.2399	2.0506	1.8390
14	3.7091*	3.5653*	3.3606*	3.1928*	3.0115*	2.7464*	2.5214*	2.2688*
+12	4.4682*	4.3022*	4.0654*	3.8705*	3.6593*	3.3492*	3.0847*	2.7863*
+10	5.3424*	5.1535*	4.8830*	4.6598*	4.4170*	4.0589*	3.7520*	3.4038*
+8	6.3361*	6.1424*	5.8198*	5.5676*	5.2925*	4.8847*	4.5334*	4.1329*
+6	7.4510*	7.2164	6.8787*	6.5980*	6.2908*	5.8334*	5.4373*	4.9832*
+4	8.6844*	8.4288*	8.0596*	7.7518*	7.4138*	6.9085*	6.4689*	5.9624*
+2	10.0318*	9.7570*	9.3590*	9.0263*	8.6599*	8.1103*	7.6301*	7.0742*
0	11.4856*	11.1939*	10.7708*	10.4159	10.0245*	9.4355*	8.9190*	8.3192*
-2	13.0362*	12.7304*	12.2858*	11.9125*	11.5000*	10.8778*	10.3309*	9.6942*
-4	14.6734*	14.3562*	13.8945*	13.5065*	13.0773*	12.4289*	11.8583*	11.1931*
-6	16.3869*	16.0610*	15.5866*	15.1875*	14.7466*	14.0789*	13.4915*	12.8068*
-8	18.1666*	17.8345*	17.3513*	16.9450*	16.495 *	15.8161*	15.2184*	14.5218*
-10	20.0023*	19.6665*	19.1779*	18.7671*	18.3127*	17.6266	17.0229*	16.3205*
-12	21.8840*	21.5462*	21.0546*	20.6414	20.184 *	19.4947	18.8882	18.1823*
-14	23.8017*	23.4628	22.9697	22.5554	22.097	21.4057	20.7978	20.0905
-16	25.7460*	25.4066	24.9129	24.4980	24.039	23.3470	22.7385	22.0305
-18	27.7092*	27.3696	26.8755	26.4604	26.001	25.3088	24.7001	23.9918
-20	29.6852*	29.3455	28.8513	28.4361	27.976	27.2842	26.6754	25.9670

$P^2/2\psi_0$ \ P	0.05	0.1	0.2	0.5	0.8	0.9	0.95	0.98
+40	0.1006	0.0786	0.0518	0.0002	-0.051	-0.0788	-0.1014	-0.1268
+35	0.1785	0.1359	0.0921	0.0007	-0.091	-0.1404	-0.1808	-0.2265
+30	0.3158	0.2475	0.1640	0.0022	-0.162	-0.2503	-0.3232	-0.4060
+25	0.5565	0.4381	0.2924	0.0069	-0.288	-0.4469	-0.5799	-0.7322
+20	0.9741	0.7725	0.5220	0.0217	-0.509	-0.8001	-1.0479	-1.3355
+18	1.2189	0.9675	0.6583	0.0343	-0.6379	-1.0110	-1.3317	-1.7073
+16	1.5116	1.2101	0.8303	0.0543	-0.7976	-1.2783	-1.6963	-2.1920
+14	1.8755*	1.5106	1.0472	0.0859	-0.9943	-1.6169	-2.1667	-2.8297
+12	2.3187*	1.8811	1.3202	0.1356	-1.2342	-2.0452	-2.7763	-3.6787*
+10	2.8544*	2.3354	1.6631	0.2136	-1.5212	-2.5839*	-3.5684*	-4.8236*
+8	3.4956*	2.8882*	2.0920	0.3354	-1.8533	-3.2507*	-4.5933*	-6.3817*
+6	4.2554*	3.5548*	2.6252*	0.5241	-2.2133*	-4.0473*	-5.8818*	-8.4491*
+4	5.1445*	4.3496*	3.2829*	0.8130*	-2.5480*	-4.8971*	-7.3086*	-10.7055*
+2	6.1709*	5.2856*	4.0853*	1.2490*	-2.7280*	-5.5384*	-8.3788*	-12.2200*
0	7.3393*	6.3726*	5.0524*	1.8944*	-2.5527*	-5.6323*	-8.6609*	-12.6457*
-2	8.6504*	7.6169*	6.2007*	2.8081*	-1.9064*	-5.1993*	-8.1924*	-12.2190*
-4	10.1014*	9.0195*	7.5376*	4.0058*	-0.8327*	-4.0674*	-7.1818*	-11.2215*
-6	11.6834*	10.5713*	9.0512*	5.4480*	0.5591*	-2.6906*	-5.8126*	-9.8566*
-8	13.3801*	12.2516*	10.7119	7.0767	2.1674	-1.0879*	-4.2126	-8.2582
-10	15.1689*	14.0324*	12.4837	8.8348	3.9175	0.6595*	-2.4657	-6.5118
-12	17.0266	15.8863*	14.3338	10.6792	5.7589	2.5000*	-0.6256	-4.6720
-14	18.9330	17.7911*	16.2369	12.5799	7.6583	4.3995	1.2734	-2.7730
-16	20.8721	19.7287*	18.1747	14.5169	9.594	6.3358	3.2097	-0.8368
-18	22.8330	21.6904	20.1351	16.4769	11.554	8.2956	5.1694	1.1229
-20	24.8081	23.6653	22.1100	18.4516	13.5292	10.2702	7.1440	3.0975

$P^2/2\psi_0$ \ P	0.99	0.995	0.998	0.999	0.9995	0.9998	0.9999
+40	-0.1438	-0.1594	-0.1784	-0.1917	-0.2043	-0.2200	-0.2312
+35	-0.2572	-0.2853	-0.3194	-0.3435	-0.3663	-0.3948	-0.4153
+30	-0.4616	-0.5129	-0.5754	-0.6195	-0.6614	-0.7138	-0.7516
+25	-0.8352	-0.9305	-1.0475	-1.1305	-1.2096	-1.3092	-1.3813
+20	-1.5327	-1.7172	-1.9461	-2.1103	-2.2683	-2.4694	-2.6163
+18	-1.9671	-2.2118	-2.5177	-2.7389	-2.9532	-3.2278*	-3.4301*
+16	-2.5388	-2.8688	-3.2859*	-3.5909*	-3.8890*	-4.2757*	-4.5639*
+14	-3.3013*	-3.7563*	-4.3412*	-4.7760*	-5.2074*	-5.7763*	-6.2035*
+12	-4.3359*	-4.9832*	-5.8367*	-6.4883*	-7.1506*	-8.0509*	-8.7567*
+10	-5.7697*	-6.7316*	-8.0522*	-9.1060*	-10.2248*	-11.8333*	-12.9142*
+8	-7.8064*	-9.3032*	-11.4979*	-13.3510*	-15.4376*	-18.5400*	-21.1370*
+6	-10.5731*	-12.8953*	-16.0274*	-19.0233*	-21.8850*	-25.7680*	-28.7447*
+4	-13.4416*	-16.2887*	-20.1592*	-23.2154*	-26.0831*	-30.3797*	-33.0950*
+2	-15.1768*	-18.1583*	-22.1189*	-25.1288*	-28.1261*	-32.1323*	-35.1176*
0	-15.6568*	-18.6674*	-22.6467*	-25.6571*	-28.6674*	-32.6468*	-35.6572*
-2	-15.2446*	-18.2625*	-22.2463*	-25.2583*	-28.2693	-32.2513	-35.2616
-4	-14.2515*	-17.2716*	-21.2569*	-24.2691*	-27.2810*	-31.2606	-34.2709
-6	-12.8881	-15.9085*	-19.8946	-22.9069*	-25.9181	-29.8984	-32.9087
-8	-11.2902	-14.3113	-18.2971	-21.3096	-24.3209	-28.3010	-31.3113
-10	-9.5440	-12.5652	-16.5511	-19.5636	-22.5749	-26.5550	-29.5653
-12	-7.7042	-10.7254	-14.7113	-17.7238	-20.7352	-24.7153	-27.7256
-14	-5.8053	-8.8265	-12.8125	-15.8249	-18.8363	-22.8164	-25.8267
-16	-3.8691	-6.8903	-10.8763	-13.8887	-16.9001	-20.8802	-23.8905
-18	-1.9094	-4.9306	-8.9165	-11.9290	-14.9404	-18.9204	-21.9307
-20	0.0652	-2.9560	-6.9419	-9.9544	-12.9658	-16.9458	-19.9561

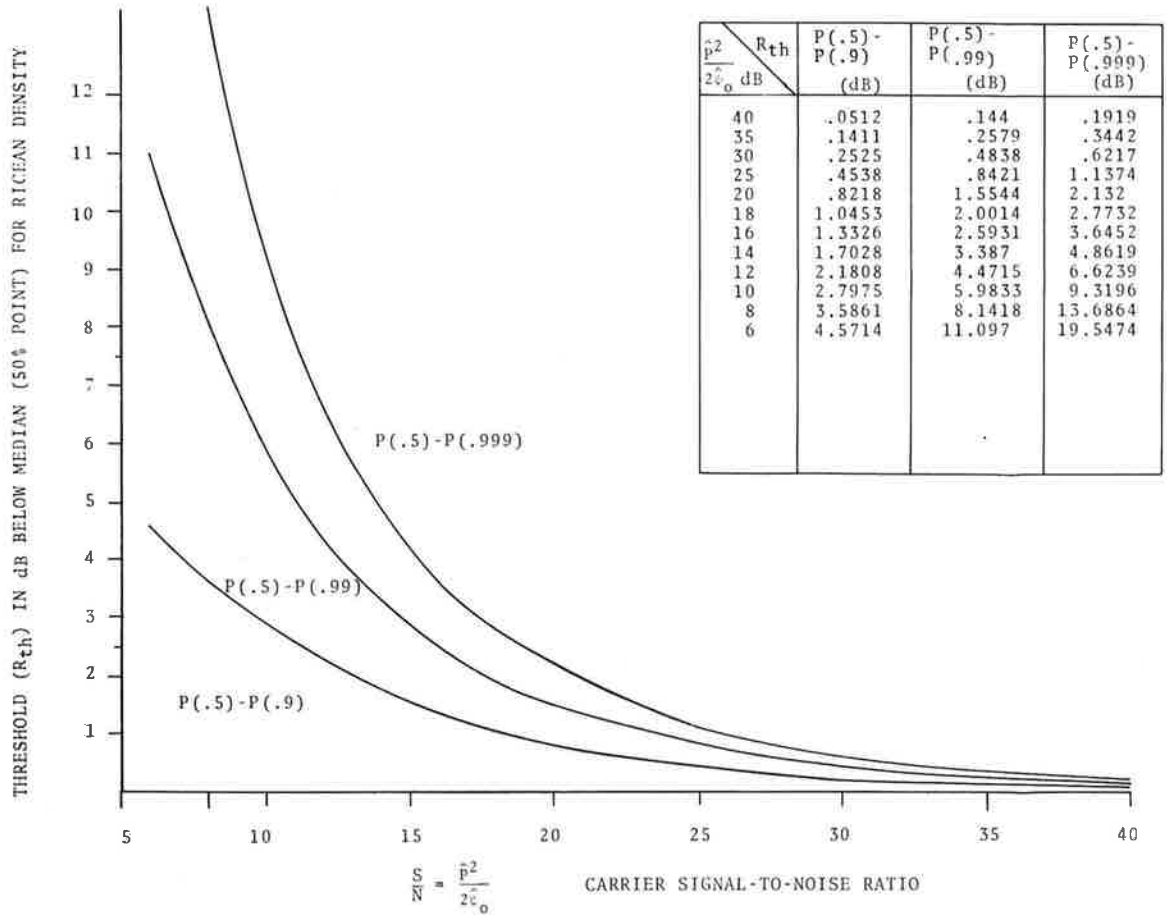

$\frac{\hat{P}^2}{2\hat{\sigma}_o^2}$ dB \ R_{th}	P(.5)-P(.9) (dB)	P(.5)-P(.99) (dB)	P(.5)-P(.999) (dB)
40	.0512	.144	.1919
35	.1411	.2579	.3442
30	.2525	.4838	.6217
25	.4538	.8421	1.1374
20	.8218	1.5544	2.132
18	1.0453	2.0014	2.7732
16	1.3326	2.5931	3.6452
14	1.7028	3.387	4.8619
12	2.1808	4.4715	6.6239
10	2.7975	5.9833	9.3196
8	3.5861	8.1418	13.6864
6	4.5714	11.097	19.5474

Figure H-1. Relationship Of Threshold To Median